Ni/ScCeSZ Anode-Supported Cell Manufacturing and Development of Carbon Tolerant Anodes for Methane-Fuelled SOFCs

By

ZEYU JIANG

A thesis submitted to the University of Birmingham for the degree of
DOCTOR OF PHILOSOPHY

Centre for Fuel Cell and Hydrogen Research
School of Chemical Engineering
College of Engineering and Physical Sciences
University of Birmingham
May 2023

ABSTRACT

Solid oxide fuel cells (SOFCs) are highly efficient energy conversion devices with flexible fuel choices. However, SOFCs suffer thermal degradation from the high operating temperature (> 600°C) and display a coking issue at the anode when operating with hydrocarbon fuels. To overcome these issues, it is crucial to reduce the operating temperature and develop carbon-tolerant anode materials. This thesis aims to optimise the fabrication process for intermediate operating temperature (600 to 800°C) SOFCs and develop carbon-tolerant anode materials for operation under dry methane reforming conditions.

This thesis presents a comparative study of different cell fabrication approaches for anode-supported SOFC button cells with a ScCeSZ-GDC bi-layer electrolyte. Sequential tape casting coupled with spin coating were found to be the most appropriate techniques for fabricating defect-free SOFC single cells. It was found that sintering the ScCeSZ and GDC layers at different temperatures was necessary to avoid the interdiffusion of Zr and Ce during co-sintering. The successfully prepared bi-layer electrolyte SOFC showed promising electrochemical performance in hydrogen operation, with maximum power densities (P_{max}) of 1.10, 1.00, and 0.80 W•cm^{-2} at 800°C, 750°C, and 700°C, respectively. The cell also exhibited good operational stability with hydrogen operation at current densities of 0.2 and 1.0 A•cm^{-2} for 1200 and 500 hours, respectively. Electrochemical impedance spectroscopy (EIS), scanning electron microscopy (SEM), and energy dispersive X-ray spectroscopy (EDS) were used to investigate the main factors causing performance degradation. It was found that Ni coarsening at the anode and migration of Sr from the LSCF cathode to the ScCeSZ electrolyte were the main contributions to cell performance degradation.

In this study, 1wt.% of Sn, Ag, Cu, or Fe dopant (with respect to Ni content) was infiltrated into the porous Ni/ScCeSZ anode to modify its catalytic activity and carbon resistivity under dry methane reforming conditions (CH_4, CO_2 and N_2). The concentration of dopant on the anode surface was found to be higher than 1wt.%, suggesting that the dopant preferentially remained on the anode surface after the infiltration process. Electrochemical performance of the 1wt.% Sn, Ag, Cu, and Fe-doped cells operated with simulated biogas was further evaluated at 750°C. Adding Sn to the Ni/ScCeSZ anode showed a significantly improved electrochemical performance in biogas operation at 750°C, with a P_{max} of 0.963 $W \cdot cm^{-2}$. However, no obvious enhancement on the power output of the Ag and Cu-doped cells was observed in biogas operation, suggesting unchanged catalytic activity towards dry methane reforming. Notably, modifying the Ni/ScCeSZ anode with 1wt.% of Fe showed a negative impact on the cell performance with hydrogen operation compared to other dopants. This was largely attributed to the accumulation of Fe dopant on the anode surface and the presence of low electrically conductive NiFe-ZrO_2 catalyst.

All metal-infiltrated cells showed stable voltage output with simulated biogas operation for 120 hours. No carbon formation on the anode surface was identified from the Sn, Ag, and Cu-doped cells after biogas operation, resulting from stable operation in biogas. However, fibrous carbon was found on the Fe-doped cells after 120 hours of operation in simulated biogas. Raman spectroscopy results suggested that the carbon deposited on the Fe-doped cell had a lower graphitisation degree than on the undoped cells. The reduced formation of graphitic carbon suppressed the dissolution of carbon into the Ni catalyst, resulting in an improved operational stability of the Fe-doped cell in simulated biogas.

ACKNOWLEDGEMENT

To my supervisor Prof Robert Steinberger-Wilckens, I would like to massively thank you for providing me the MRes and PhD opportunities in fuel cell and hydrogen research group. I appreciate the support, encouragement, and knowledge you offered!

I would like to thank my co-supervisors Dr Ahmad El-kharouf and Dr Bernardo Sarruf for the helpful guidance you provided on my PhD pathway and future career. I could not complete my PhD without your support.

To my beloved parents, I would like to express my sincere appreciation. Thank you for your unconditional love and support through the entire journey. I cannot wait to share my success and achievement with you!

To Dr Zhilin Guo, it is my pleasure to have you being my best friend since 2017 in Birmingham. The support, encouragement and memes have always been a constant source of inspiration and motivation. I would like to acknowledge the support from my friends, Enbang Ti, Xuan Huang, Xinkai Zhou, and particularly Ke Liu.

To Dr Kun Zhang, Dr Nor Anisa Arifin, and Dr Lina Troskialina, Dr Artur Majewski, Dr James Courtney, John Hooper, Chris, Abby, Abu, Pushpa, Liam, Naser, Bhargav, Alan, Oujen, Yang, Yichang, Recep, Ahmed, Melissa, Chyntol, Manzo, and everyone from the Birmingham Centre for Fuel Cell and Hydrogen Research, thank you for your support over the last few years.

Finally, I am also grateful to the staff at the School of Chemical Engineering, who provided me academic and administrative supports.

“很惭愧，就做了一点微小的工作”

PUBLICATIONS

- Z. Jiang, B. J. M. Sarruf, A. El-kharouf, R. Steinberger-Wilckens, Preparation of gadolinium-doped ceria barrier layer for intermediate temperature solid oxide fuel cells by spin coating and evaluation of performance degradation by impedance analysis. (To be submitted)
- Z. Jiang, AL. Snowdon, A. Siddiq, A. El-kharouf, R. Steinberger-Wilckens, Optimization of a ScCeSZ/GDC bi-layer electrolyte fabrication process for intermediate temperature solid oxide fuel cells. Ceram. Int. 2022; 48: 32844-32852
- AL. Snowdon, Z. Jiang, R. Steinberger-Wilckens, Five-layer reverse tape casting of IT-SOFC. Int J Appl Ceram Technol. 2022; 19: 289– 298
- Z. Jiang, A. El-Kharouf, R. Steinberger-Wilckens, Effect of Sn, Cu, and Ag Modification on Electrochemical Performance and Carbon Tolerance of Biogas-Operated Ni/YSZ and Ni/ScCeSZ SOFC Anodes. ECS Trans. 2021; 103: 1557

CONFERENCES

- 15th European SOFC & SOE Forum, Lucerne (2022) – Oral presentation
- 17th International Symposium on Solid Oxide Fuel Cells (2021) – Oral presentation
- 14th European SOFC & SOE Forum, Lucerne (2020) – Poster

NOMENCLATURE

Abbreviation	**Definition**
AFL	Anode functional layer
AS	Anode substrate
ASR	Area specific resistance
DRT	Distribution of relaxation times
EDS	Energy dispersive X-ray spectroscopy
EIS	Electrochemical impedance spectroscopy
GDC	Gadolinium-doped ceria
IT-SOFC	Intermediate temperature SOFC
OCV	Open circuit voltage
P_{max}	Maximum power density
R_{ohm}	Ohmic resistance
R_p	Electrode/polarisation resistance
ScCeSZ	Scandia-ceria-stabilised zirconia
SEM	Scanning electron microscopy
SOFC	Solid oxide fuel cell
TEC	Thermal expansion coefficient
TGA	Thermogravimetric analysis
TPB	Triple phase boundary
XPS	X-ray photoelectron spectroscopy
XRD	X-ray diffraction

TABLE OF CONTENTS

LIST OF FIGURES

LIST OF TABLES

CHAPTER 1: INTRODUCTION

1.1 Fuel cells

Greenhouse gases released from burning fossil fuels can cause many environmental problems, including air pollution, global warming, and ozone depletion. To reduce greenhouse gas emissions, using renewable energy sources such as solar, wind, geothermal, hydro, and biomass to replace fossil fuels for power generation is extremely important [1-3].

Over the last few decades, considerable efforts have been made to generate power from renewable sources more sustainably, effectively, and affordably [3-6]. Complimenting these renewable energy technologies, fuel cells are electrochemical devices that directly convert chemical energy from fuels into electrical energy. Compared to traditional internal combustion engines, fuel cells have higher efficiency (40–60%) and cause far less air pollution [1, 7]. For hydrogen-fuelled fuel cells, the output products are electricity, water, and heat. For a typical fuel cell, the fuel and oxidant (oxygen/air) are fed to the anode and cathode, respectively. The electrochemical reactions take place at the electrodes and then produce electric current through the external load circuit [8, 9].

The most investigated fuel cells are the polymer electrolyte membrane fuel cell (PEMFC), the direct methanol fuel cell (DMFC), the alkaline fuel cell (AFC), the phosphoric acid fuel cell (PAFC), the molten carbonate fuel cell (MCFC), and the solid oxide fuel cell (SOFC). Based on the operating temperature, fuel cells can be classified into low-temperature and high-temperature types. The details of each type of fuel cell are summarised in Table 1-1 and Figure 1-1.

Table 1-1: Fuel cell types [9, 10].

Fuel cell type	Classification	Fuel	Oxidant	Ion transfer	Operating temperature	Efficiency
PEMFC	Low temperature fuel cell	H_2	O_2, air	H^+	60 to 80°C	40-45%
DMFC		CH_3OH	O_2, air	H^+	80 to 100°C	25–30%
AFC		H_2	O_2, air	OH^-	80 to 200°C	50–60%
PAFC		H_2	O_2, air	H^+	200°C	40–45%
MCFC	High temperature fuel cell	$H_2/CO/CH_4$	O_2, air	CO_3^{2-}	650°C	50–55%
SOFC		$H_2/CO/CH_4$	O_2, air	O^{2-}	600 to 850 °C	50–60%

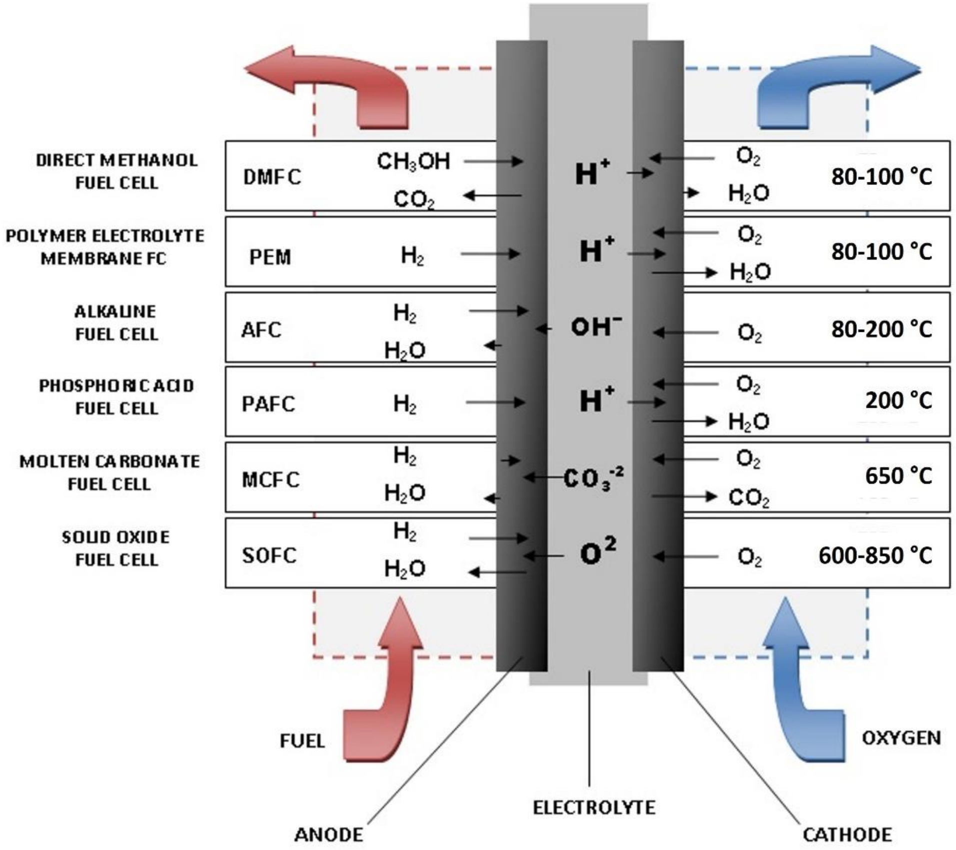

Figure 1-1: Operating principle of different type of fuel cells [11].

1.2 Fuel cell electrical efficiency

The electrical efficiency, η_e, of a fuel cell refers to the fraction of chemical energy in fuel that is converted to electrical energy. This value can be calculated by dividing the produced electricity by higher heating value (HHV) of the fuel, shown as Eq.(1).

$$\eta_e = \frac{Produced\ electricity}{HHV\ of\ fuel\ used} \tag{1}$$

As fuel cells are not heat engines that relies on internal fuel combustion, hence, their efficiency is not restricted by the Carnot cycle. This feature leads to the high electrical efficiency of fuel cells. For hydrogen fuel cell system, the maximum achievable electrical efficiency, $\eta_{e,max}$, (also known as reversible fuel cell efficiency) is can be determined by dividing the Gibbs free energy by HHV, shown as Eq.(2).

$$\eta_{e,max} = \frac{Gibbs\ free\ energy\ of\ H_2}{HHV\ of\ H_2} = \frac{-237.2\ kJ/mol}{-285.8\ kJ/mol} = 0.83 \tag{2}$$

The HHV considers the water produced in the reaction to be in the liquid phase. Conversely, lower heating value (LHV) considers that the reaction produces water in the form of vapour or steam. For hydrogen, the HHV is around 18% higher than its LHV. When using the LHV for calculations, the obtained efficiency is always higher compared to calculation using the HHV. It is important to highlight which value is used for electrical efficiency calculation [12]. In a low-temperature fuel cell, where liquid phase water is produced, the HHV should be used for electrical efficiency calculation. On the other hand, the LHV should be used for calculating the electrical efficiency of a high-temperature fuel cell.

A more convenient way to describe the fuel cell efficiency is to evaluate the voltage efficiency, η_V, defined as Eq.(3):

$$\eta_V = \frac{V_{actual}}{V_{ideal}} \tag{3}$$

To describe the electrical efficiency of a fuel cell, the reversible fuel cell efficiency, $\eta_{e,max}$, and fuel utilisation, U_f, need to be considered. Therefore, the electrical efficiency, η_e, of a fuel cell can be also described as Eq.(5):

$$U_f = \frac{m_{fuel,consumed}}{m_{fuel,inlet}} = \frac{m_{fuel,inlet} - m_{fuel,outlet}}{m_{fuel,inlet}} \qquad (4)$$

$$\eta_e = \eta_{e,max} * \eta_V * U_f \qquad (5)$$

For a fuel cell with hydrogen as fuel and oxygen as oxidant, the thermodynamic voltage, E^0, (also known as ideal voltage) of it at the standard conditions (25°C and 101.325 kPa) can be calculated as follow:

$$E^0 = \frac{-\Delta G^0}{2F} = \frac{237200\, J/mol}{2 * 96485\, C/mol} = 1.229\, V \qquad (6)$$

Using the obtained thermodynamics voltage, the Eq.(5) can be defined as follows:

$$\eta_e = 0.83 * \frac{V_{actual}}{1.229} * U_f = 0.675 * V_{actual} * U_f \qquad (7)$$

For example, for a fuel cell with 0.8 V operating voltage and 80% fuel utilisation, the electrical efficiency is 43.2%.

1.3 Solid oxide fuel cell (SOFC)

Among the various types of fuel cells, solid oxide fuel cell (SOFC) is constructed with all ceramic materials. They possess several benefits over other fuel cell types, such as low environmental impact, high electrical efficiency, fuel flexibility, and high-quality exhaust heat [10, 13, 14]. An SOFC typically has three components: a porous anode, a porous cathode, and a dense electrolyte. SOFCs are usually operated in the temperature range of 600 to 850°C, because adequate ionic conductivity of the electrolyte and low impedance losses in both electrodes can only be ensured at such high temperatures [15]. The operating principles of SOFCs consists of oxygen reduction at the cathode, diffusion of oxide ions (O^{2-}) through the ionically conductive electrolyte, and finally fuel oxidation at the anode. Electrons are generated from the reaction of fuel and oxygen ions at the anode, which completes the external electrical circuit [9, 10]. The main chemical reaction in a hydrogen-operated SOFC is illustrated by the following equation, Eq.(8).

$$H_2\,(g) + \frac{1}{2}O_2(g) \rightarrow H_2O(l) \qquad\qquad \Delta H = -285.8\;kJ/mol \qquad (8)$$

The main reaction can be divided into two half reactions as shown in Eq.(9) and Eq.(10). On the cathode side, O^{2-} ions are produced from the reduction of molecular oxygen. Oxygen ions are collected by the cathode and then transferred through the electrolyte to the anode. On the anode side, hydrogen molecule reacts with an oxygen ion to form a water molecule and thereby releases two electrons. Figure 1-2 illustrates the operating principle of a hydrogen-operated SOFC.

$$Cathode\colon \frac{1}{2}O_2 + 2e^- \rightarrow O^{2-} \qquad (9)$$

$$Anode\colon H_2 + O^{2-} \rightarrow H_2O + 2e^- \qquad (10)$$

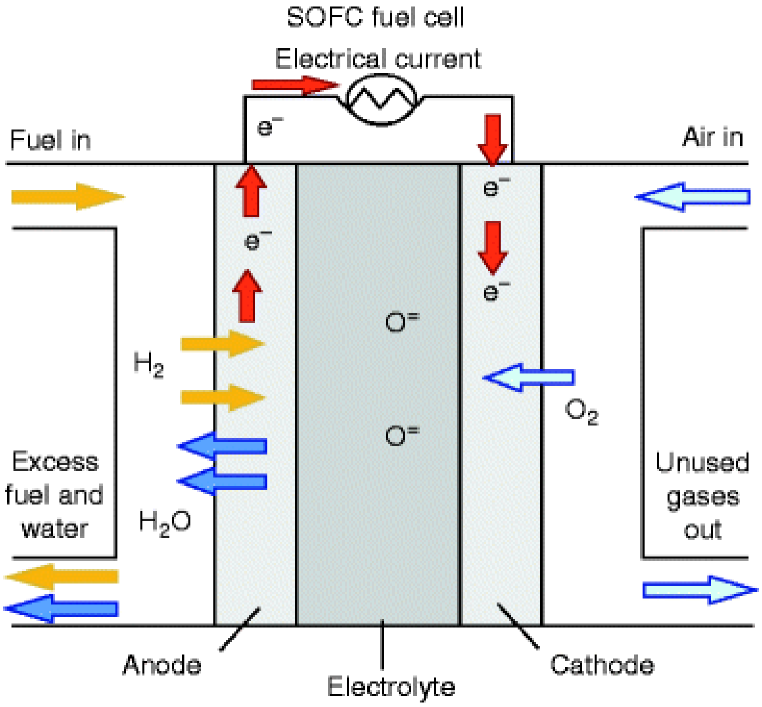

Figure 1-2: Schematic operating principle of a hydrogen fuelled SOFC. Reprinted from Ref. [16] with permission from Springer Nature.

1.3.1 SOFC materials

- Electrolyte

The electrolyte is the most important component of the SOFC. It plays a critical role in the SOFC, preventing the diffusion of electrons produced from the electrode reaction and crossover of fuel and oxidant gases [17-19]. The electrolyte material must possess high ionic conductivity (0.01 to 0.1 S•cm^{-1}) to allow the oxygen ions to travel through [20]. Mechanical stability and chemical compatibility with other cell components is also important for cell fabrication and operation [3]. Zirconia-based electrolyte is usually applied in high temperature SOFC (HT-SOFC) applications due to its high ionic conductivity and stability at such temperatures (800 to 1000°C), especially yttria-stabilised zirconia (YSZ) is used [21-23].

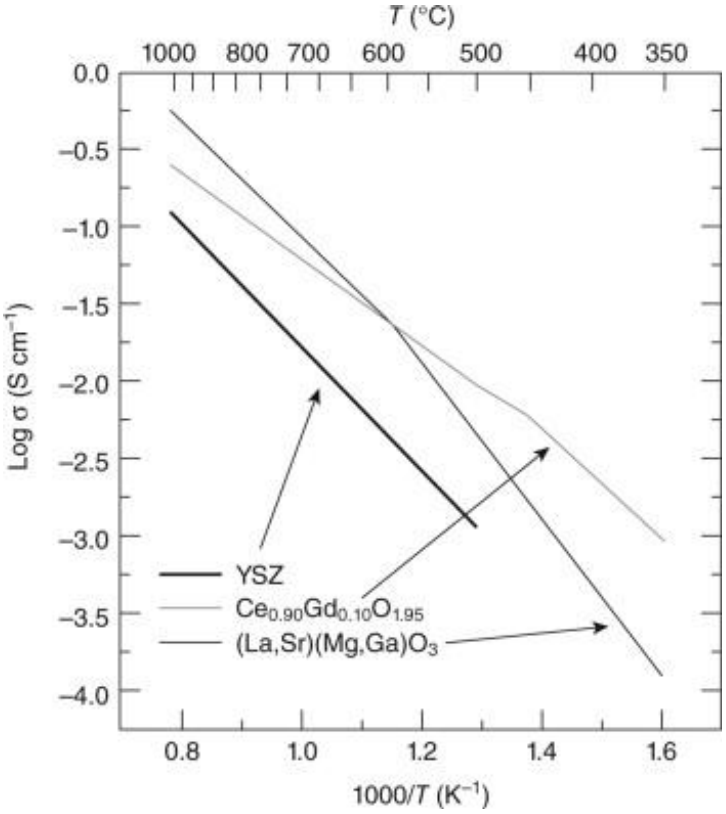

Figure 1-3: Ionic conductivity of YSZ, GDC, and LSGM as a function of temperature. Reprinted from Ref. [24] with permission from Elsevier.

Figure 1-3 shows the ionic conductivity of some commonly used SOFC electrolyte materials as a function of temperature. The conductivity of gadolinium-doped ceria (GDC) is superior to YSZ at all temperatures, particularly at the lower temperatures (below 700°C). Ceria-based materials are reported to have purely ionic conductivity at high oxygen partial pressures and low temperatures. Due to this feature, doped-ceria has been widely investigated as the electrolyte material for low-temperature SOFC (LT-SOFC). Nevertheless, it develops electric conductivity from the partially reduced Ce^{4+} at low oxygen partial pressure, which can lead to internal short circuiting and decrease in cell efficiency [17, 25-27].

- Anode

The anode is where the fuel reacts with oxygen ions to produce water, among other products, such as CO and CO_2, depending on the fuel used. Electricity is produced from the electrochemical reactions at the triple-phase boundary (TPB) of the anode [10]. Therefore, the main requirement of the anode material is to provide high ionic conductivity, high electronic conductivity, and high catalytic activity for fuel oxidation during the cell operation. Ni/YSZ anodes were first developed by Spacil [28] in 1970 and have been widely used as anode materials for SOFCs. As nickel is commonly used as catalyst for industrial steam reforming of hydrocarbons, Ni/YSZ anode enables internal reforming of hydrocarbons and water gas shift reactions on the anode side of an SOFC [13, 29]. More importantly, Ni can provide sufficient catalytic activity for anode reactions, such as hydrogen oxidation, meanwhile the existence of YSZ can prevent the agglomeration of Ni during operation and alleviate the mismatch of thermal expansion coefficient (TEC) between anode and electrolyte materials [30].

Ni from the conventional Ni/YSZ cermet anodes is generally prepared in the form of nickel oxide, which increases the compatibility of the ceramic materials during the cell manufacturing process. NiO in the manufactured cells is easily reduced to metallic Ni in the H_2-rich atmosphere at SOFC operating temperatures. The reduction of NiO not only gives sufficient catalyst active sites for anode reactions, but also greatly increases the anode porosity through the loss of oxygen ions during reduction. The increased porosity leads to more gas flow channels through the anode, which is beneficial for fuel oxidation reactions [10]. According to the percolation theory, the electrical conductivity of Ni/YSZ cermet anode is largely related to the size and shape of the particles, as well as the volumetric fraction of metallic nickel phase [31-33]. Hence, the porosity and composition of the Ni/YSZ cermet anode need to be carefully adjusted to provide sufficient electrical conductivity from the interconnected Ni particles.

Although Ni/YSZ anode materials possess many advantages, there are a few issues yet to be solved, such as carbon deposition and sulphur poisoning on using hydrocarbons, and nickel coarsening/agglomeration after long-term operation [34-37]. Ni catalyst can promote internal reforming process for the hydrocarbon-operated SOFCs, whereas it also promotes carbon formation [38, 39]. Carbon deposition on nickel is one of the main reasons of catalyst deactivation in any SOFC operated with hydrocarbons. Catalyst deactivation leads to drastically reduced catalytic activity towards fuel oxidation and then rapid degradation of cell performance [29, 40, 41]. The detailed mechanism of carbon deposition on Ni-based anodes is explained in Chapter 2.2.

- Cathode

The SOFC cathode is composed of oxide ceramic materials with good catalytic activity towards oxygen reduction reaction (ORR) and high electronic conductivity at SOFC operating temperatures [18, 42]. Perovskite oxides with the formula of ABO_3 are the most commonly used cathode materials for SOFC, such as lanthanum strontium manganite (LSM) and lanthanum strontium cobaltite (LSC), including modified composition such as lanthanum strontium cobalt ferrite (LSCF). LSM is widely used in the commercial SOFCs due to its moderate electronic conductivity at high temperatures and excellent compatibility with YSZ electrolyte and other cell components. However, LSM cannot transport ions well and has drastically reduced electrocatalytic activity at lower temperatures (below 700°C). Therefore, LSM/YSZ composite is usually used as the SOFC cathode material to provide adequate ionic conductivity. Compared with the electronic conducting LSM, LSC and LSCF are mixed ionic and electronic conductors (MIECs) that have higher oxygen ion conduction capacity, high oxygen surface exchange coefficient, and more active sites for the ORR. At lower operating temperatures (≤ 750°C), LSC and LSCF-based cathodes are more superior to LSM-based cathodes due to its outstanding electrochemical performance. Although LSC and LSCF cathodes are generally incompatible with YSZ electrolytes due to the undesired interdiffusion across cathode/electrolyte interfaces, a diffusion barrier layer (e.g. GDC) can effectively prevent the formation of resistive compound at the interfaces without negatively affecting the electrochemical performance. Hence, LSC and LSCF have been considered as potential cathode materials for SOFC operated at lower temperatures (≤ 750°C) [43, 44].

1.3.2 SOFC design

Two types of SOFC design have been extensively investigated over the past decades, the planar and tubular designs [1, 3]. Figure 1-4 shows the configuration of planar and tubular cells with anode, cathode, electrolyte, and interconnect. Due to the low fabrication cost and relatively simple fabrication process, mass production has been applied in the industries for planar SOFCs. A stack composed of planar cells is usually suitable for portable and transportation applications [20, 45]. Compared with the planar SOFCs, tubular SOFCs can offer high mechanical strength and good sealing during cell operation. It is claimed that a stack made with tubular SOFC can produce higher volumetric power densities than the stack made with planar SOFC, which is beneficial for large scale applications, such as stationary power generation, but will depend more on the stack design than the shape of the cells [46-48]. Comparison of planar and tubular SOFC designs are summarised in Table 1-2.

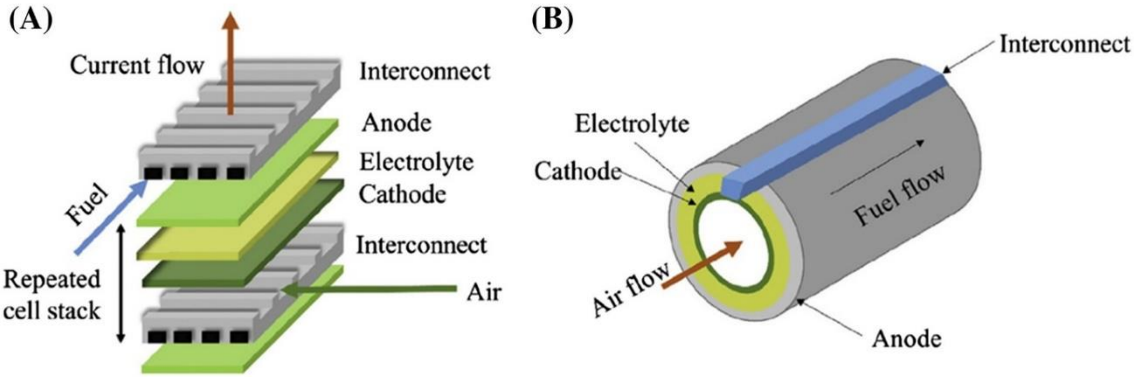

Figure 1-4: Planar SOFC (a) and tubular SOFC (b) designs. Reprinted from Ref. [20] with permission from Wiley.

Table 1-2: Comparison between planar and tubular SOFC designs.

	Benefits	**Drawbacks**
Planar design	High power density Low fabrication cost	Low mechanical strength for large cells Difficult to have a gas-tight sealing
Tubular design	High mechanical strength Gas-tight sealing	High fabrication cost Low power density

Both planar and tubular SOFCs can be configured as either self-supporting or externally supported structures. In a self-supporting SOFC, one of the cell components is designed to serve as the structural support, typically comprising the thickest layer in a single cell. Therefore, self-supporting SOFCs are commonly configured as electrolyte-supported, anode-supported, and cathode-supported structures. On the contrary, an external supporting SOFC has thin cell components that are fabricated on an interconnect or substrate, enabling gas diffusion. The schematic illustrations of various single cell configuration are shown in Figure 1-5.

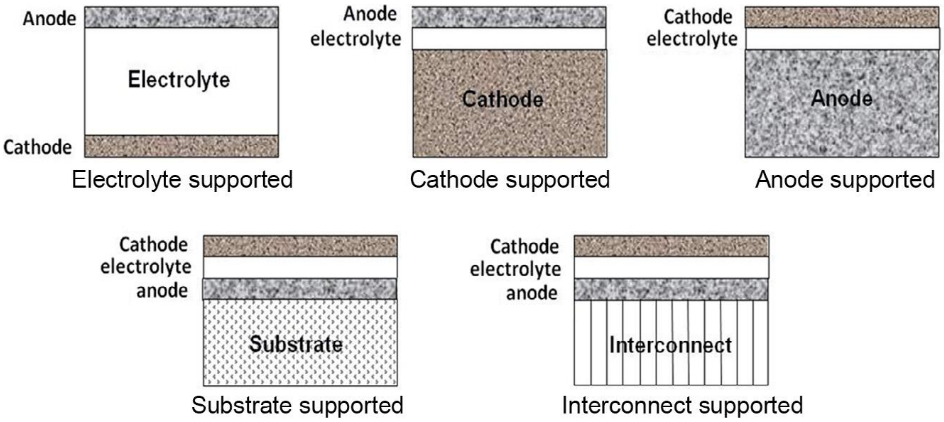

Figure 1-5: Schematic diagrams of various SOFC single cell configurations. Reprinted form Ref. [10] with permission from Elsevier.

1.3.3 Hydrocarbon-operated SOFC

Using pure hydrogen in SOFCs leads to zero emission, however, the majority of H_2 is produced from reforming and/or partial oxidation of hydrocarbons. There will be external energy consumed for these processes, leading to a reduced overall energy efficiency [49-51]. Steam reforming is a well-established process for producing hydrogen and/or syngas from methane and other hydrocarbons. The entire process is highly endothermic and is carried out at temperatures above 650°C in the presence of a nickel catalyst [52, 53]. Because of the similar operating temperature and high catalytic activity of nickel catalyst toward electrocatalytic oxidation reactions of hydrocarbons, SOFC with nickel-based anodes are considered for hydrocarbon operation [15, 54].

Direct electrochemical conversion of hydrocarbons does not produce electrical power in the SOFC system [3]. Park et al,. [55] suggested that hydrocarbon-operated SOFC is actually operated on syngas, a mixture of CO and H_2 produced from the reforming of hydrocarbons. This reforming process allows converting the less active hydrocarbon into more active fuel. Figure 1-6 shows three strategies of using hydrocarbon fuels in an SOFC. (1) external reforming, (2) internal reforming, (3) direct hydrocarbon utilisation. For the case of external reforming, an external reformer is required to reform the hydrocarbon into syngas before supplying to SOFC, which will make the system more expensive and complex. Due to the high operating temperatures of SOFC and the presence of Ni catalyst, internal reforming on the anode of SOFC is feasible by adding an additional reforming catalytic layer or incorporate reforming catalyst with the anode material. Furthermore, simple hydrocarbons such as methane can be direct used on the anode without reforming process. Both internal hydrocarbon reforming and direct utilisation of hydrocarbon on the SOFC anode can significantly reduce the fuel processing cost and considerably enhances the overall energy conversion efficiency [15, 56].

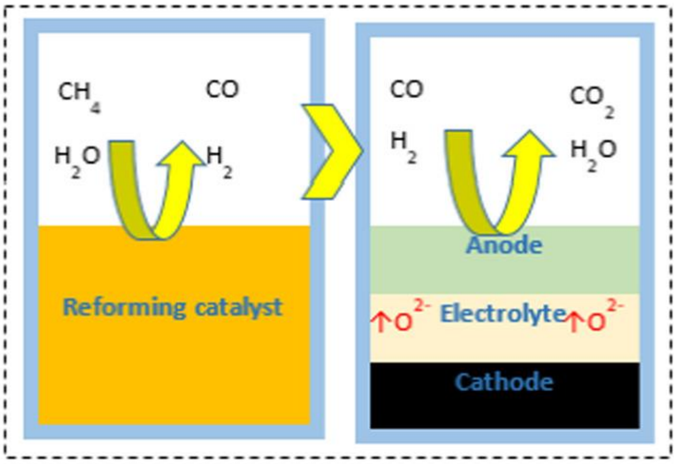

(a) External reforming.

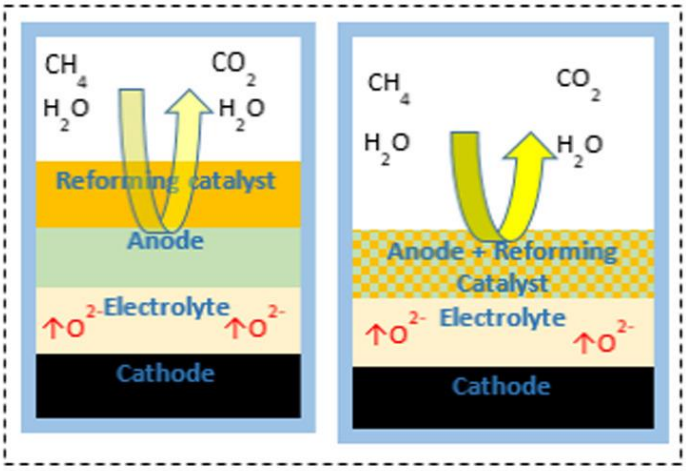

(b) Internal reforming where left is additional reformer layer and right is adding reforming catalyst directly into anode.

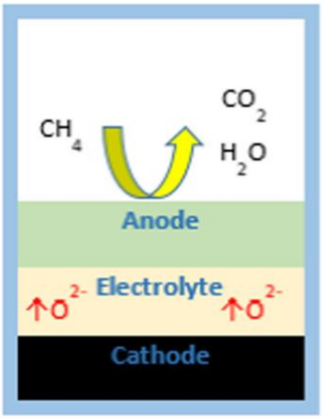

(c) Direct hydrocarbon utilization.

Figure 1-6: Strategies of using hydrocarbon fuels in an SOFC. Reprinted from Ref. [57] with permission from Elsevier.

Typically, there are two types of internal reforming of hydrocarbons that can occur on the SOFC anode, steam reforming and dry reforming. Direct methane-fuelled SOFC is the most widely investigated SOFC with internal reforming of hydrocarbons [13, 58, 59]. The main chemical reactions occurring in an SOFC with internal steam methane reforming (SMR) are shown as Eq.(11) and Eq.(12).

$$CH_4(g) + H_2O(g) \leftrightarrow 3H_2(g) + CO(g) \qquad \Delta H = +206 kJ/mol \tag{11}$$

$$CO\,(g) + H_2O(g) \leftrightarrow H_2(g) + CO_2(g) \qquad \Delta H = -41 kJ/mol \tag{12}$$

In the SMR process, methane is firstly converted to syngas (H_2 and CO) in the presence of steam, shown as Eq.(11). Then, the water gas shift (WGS) reaction, Eq.(12), converts the CO and H_2O into H_2 and CO_2 [58]. Compared with the SMR process, there is no need of steam in the dry methane reforming (DMR) process, which reduces the operation cost and increases the efficiency [49]. Dry reforming of methane is the process that converts CH_4 and CO_2 into syngas. The produced syngas is further oxidised into CO_2 and H_2O [59, 60]. The chemical reactions of DMR are given as Eq.(13). The further reactions are shown in Eq.(14), and Eq.(15).

$$CH_4(g) + CO_2(g) \leftrightarrow 2H_2(g) + 2CO(g) \qquad \Delta H = +247.3\ kJ/mol \tag{13}$$

$$2H_2 + O^{2-} \rightarrow H_2O + 2e^- \tag{14}$$

$$CO + O^{2-} \rightarrow CO_2 + 2e^- \tag{15}$$

Biogas is a renewable energy source that is produced through the anaerobic fermentation process of organic matters such as crops, landfills, wastewater treatment, and livestock waste [60-62]. Typically, biogas consists of methane (55 to 75%), carbon dioxide (25 to 45%), and small amount of nitrogen (0 to 5%). Trace amounts (ppm levels) of hydrogen sulfide, ammonia and hydrogen could also present in biogas depending on the feedstock [2, 63]. Biogas can be a good candidate for methane dry reforming after desulphurisation. Due to the wide availability of biogas, it has been widely investigated as the fuel for SOFCs operated with a DMR process [2, 64-66]. Although biogas is generally considered as a sustainable fuel, biogas produced from livestock waste could has significantly higher greenhouse gas (GHG) emission than other sources, resulting in a higher net emission from the production and utilisation of biogas [67, 68].

1.4 Motivation

Considering the SOFCs with YSZ electrolyte and LSM cathode are mainly operated above 800°C, it is crucial to lower the SOFC operating temperature to reduce the degradation and enable faster start-up. Using electrolyte and cathode materials with high ionic conductivity is necessary to maintain good electrochemical performance of the SOFCs. Using a zirconia-ceria bilayer electrolyte can effectively avoid the reduction of ceria and block the partial electronic conduction within the ceria layer, which provides good electrochemical performance for SOFCs operated at lower temperature. More importantly, the doped ceria acts as a barrier layer that prevents the interaction between the zirconia-based electrolyte and the LSCF cathode during the sintering process and cell operation. Previous work in our group has successfully prepared the anode supported SOFC button cells with scandia ceria-stabilised zirconia (ScCeSZ) electrolyte, Ni/ScCeSZ anode, and LSM cathode, but the operational stability and cell performance at temperatures below 750°C could be further improved by using an LSCF cathode and adding a GDC barrier layer between the electrolyte and cathode.

Due to the mismatch of doped-ceria and stabilised zirconia, many reported fabrication processes of the ceria-zirconia bilayer electrolyte consist of complicated coating procedures such as physical vapour deposition and chemical solution deposition followed by repeated sintering processes [69-72]. Compared to the high cost and time-consuming fabrication process, preparing the bilayer electrolyte by co-tape casting and spin coating is more cost-effective and suitable for large scale SOFC cell fabrication.

Biogas, as a methane-rich fuel, is a sustainable fuel source that can be used for SOFC operation. With the presence of the nickel catalyst in the SOFC anode, internal dry methane reforming can occur at high operating temperatures [2, 61, 62]. However, Ni is also a good catalyst for promoting carbon deposition from methane decomposition and carbon monoxide disproportionation. Hence, carbon accumulation on the SOFC anode would rapidly deteriorate the cell performance by deactivating the catalyst and damaging the anode structure. The presence of CO_2 in biogas offers two key benefits during the operation of biogas-fuelled SOFCs. Firstly, it enables internal dry methane reforming at the anode. Secondly, it reduces the carbon to oxygen (C:O) ratio in the fuel stream. Thermodynamically, a low C:O ratio is unfavoured for carbon deposition, thereby minimising the risk of coking [73]. Furthermore, to ensure stable operation of Ni-based anodes on biogas, incorporating metals [74-78] or metal oxides [49, 79-81] into the Ni-based anode has been extensively studied.

In this research work, Sn, Ag, Cu, and Fe were selected as the dopants to modify the Ni/ScCeSZ anode. Many studies have experimentally showed that Sn-based catalyst can effectively reform organic compound and reducing CO_2 to CO [82-84], which is the desired electrocatalytic property for SOFCs operated with dry methane reforming. Silver catalysts is well known for its good catalytic activity for chemo-selective oxidation, hydrogenation, photo-catalysis, and electro-catalysis [85]. It has also been reported as a good catalyst for CO oxidation with no tendency to carbon deposition [86]. Cu-based catalysts are wide used in chemical industry for water-gas shift reaction, methanol synthesis from CO_2, and CO oxidation [87-89]. Cu has also been reported as a promising electrocatalyst for the electrooxidation of hydrocarbons, which makes it a favourable dopant for Ni-based anodes [56, 90, 91]. The addition of Fe to a catalyst offers redox functionality, improving the carbon resistance of the catalyst [92, 93]. With the presence of CO_2 or H_2O, FeO_x species can be formed during reaction [92], which can further react with the deposited carbon. These key features of Fe make it an attractive dopant for Ni-based anodes operated with hydrocarbon fuels.

1.5 Research aims and objectives

The aim of this work is to fabricate the anode supported planar SOFC with a ScCeSZ-GDC bilayer electrolyte and investigate the effect of doping the Ni/ScCeSZ anode with metal/oxides on anode carbon tolerance. The main objectives of this work can be summarised as follows:

- Develop a water-based slurry for planar SOFC single cell fabrication based on tape casting and spin coating techniques.
- Optimise the fabrication process of the SOFC single cell with Ni/ScCeSZ anode ScCeSZ-GDC bilayer electrolyte, and LSCF cathode.
- Analyse the microstructure of the prepared samples using SEM and elemental distribution using EDS and XRD.
- Evaluate the electrochemical performances (OCV, i-V, EIS, and operational stability) of the prepared SOFC single cells with hydrogen and simulated biogas as fuels.
- Review the carbon-resistant anodes from carbon forming mechanisms to assess the strategies for suppressing carbon accumulation.
- Infiltrate additional catalyst (Sn, Ag, Cu, Fe) into the porous Ni-based anode to modify the cell performance and carbon tolerance, tested under simulated biogas (CH_4, CO_2).
- Evaluate and compare the cell performance of the Sn, Ag, Cu, and Fe-doped cells operated in hydrogen and biogas.
- Investigate the carbon deposition behaviour on the dopant-infiltrated anodes after long-term operation in biogas by Raman spectroscopy, SEM, EDS, and XPS characterisation.

CHAPTER 2: LITERATURE REVIEW

2.1 Fabrication of planar SOFCs via aqueous tape casting

2.1.1 Overview

Typically, the fabrication methods of SOFC planar cells can be classified as particulate approach and deposition approach [10, 45]. Approaches include tape casting, (tape) calendaring, and uniaxial pressing. The prepared ceramic powder is formed into the respective functional cell support layer and then sintered at high temperature. The second approach utilises physical and chemical processes to deposit a layer of cell component onto a substrate, which can entail chemical/physical vapour deposition, electrochemical vapour deposition, pulsed laser deposition, plasma spraying, spin coating, or sol-gel methods [20, 30].

For planar SOFC fabrication, the first step is usually the preparation of a structural support layer, followed by the deposition or printing of other functional layers as thin films. A planar SOFC can be designed as electrode, electrolyte, interconnect, or external substrate supported. Once the supporting substrate is prepared, other components of the cell can be fabricated via the same technique or different techniques. Table 2-1 summarises the benefits and drawbacks of several commonly used planar SOFC fabrication methods. This section reviews the current research state of the tape casting process with water-based slurries.

Table 2-1: Overview of planar SOFC component fabrication methods.

Fabrication method	Benefit	Drawback
Tape casing	- Various tape thicknesses (10 to 3000 µm) - High quality electrolyte - Multi-layer production	- Long slurry preparation time - Slow drying process for water-based tape casting - High crack sensitivity
Uniaxial pressing	- High pellet density - Simple and cost-effective	- Inconsistent pellet thickness - Mainly for support layer fabrication
Screen printing	- Mass production - Minimise cracking problem	- Highly stable and uniformly-distributed ink required
Spin coating	- Simple and low cost - Multilayer production	- Limited sample size - Must carefully prepare slurry for different substrate materials
Chemical vapour deposition	- Able to large-scale produce dense and thin film	- High operating temperature needed
Electrochemical vapour deposition	- Easier to deposit dense films on the porous substrate	- High production cost
Physical vapour deposition	- Commonly used materials can be deposited as different SOFC components	- High production cost - Complex equipment required

2.1.2 Tape casting for ceramic processing

Tape casting is a wet forming method that uses ceramic slurry to fabricate ceramic films. This technique was firstly reported by Howatt et al. [94] for fabricating thin ceramic sheets for capacitors in 1947. The ceramic fabrication process can be described as a machine extruding the prepared ceramic slip onto a moving belt, after which the produced 'green tape' is dried in an oven. This invention was further patented in the US for a high dielectric and high insulation ceramic plates production in 1952 [95]. Since then, this fabrication process has been improved and extensively used for large-scale ceramic manufacturing [96, 97]. This ceramic film fabrication technique has been widely used for planar SOFC production [97-99]. The basic working principle of tape casting for ceramic tapes is shown in Figure 2-1.

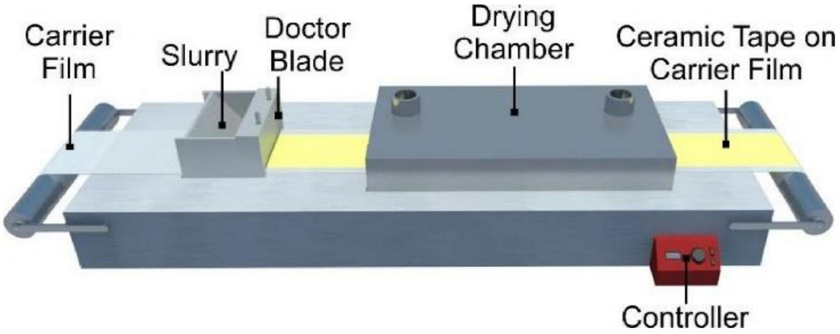

Figure 2-1: Schematic diagram of tape casting equipment. Reprinted from Ref. [97] with permission from Elsevier.

The fabrication process starts with ceramic slurry preparation. Ceramic powder, solvent, dispersant, plasticiser, binder, and de-foamer are added and mixed in the respective ratio and order. The prepared slurry must be a stable suspension of solid and liquid phases to avoid cracks and defects on the prepared tape. The slurry is cast on a carrier film via a doctor blade with adjustable gap. The ceramic tape is dried and then cut before sintering. Dried tapes can be laminated to obtain thicker green tapes. High-temperature sintering promotes organic content removal and ceramic material densification. The entire process of planar SOFC fabrication via tape casting is shown in Figure 2-2. More details will be offered in following sections.

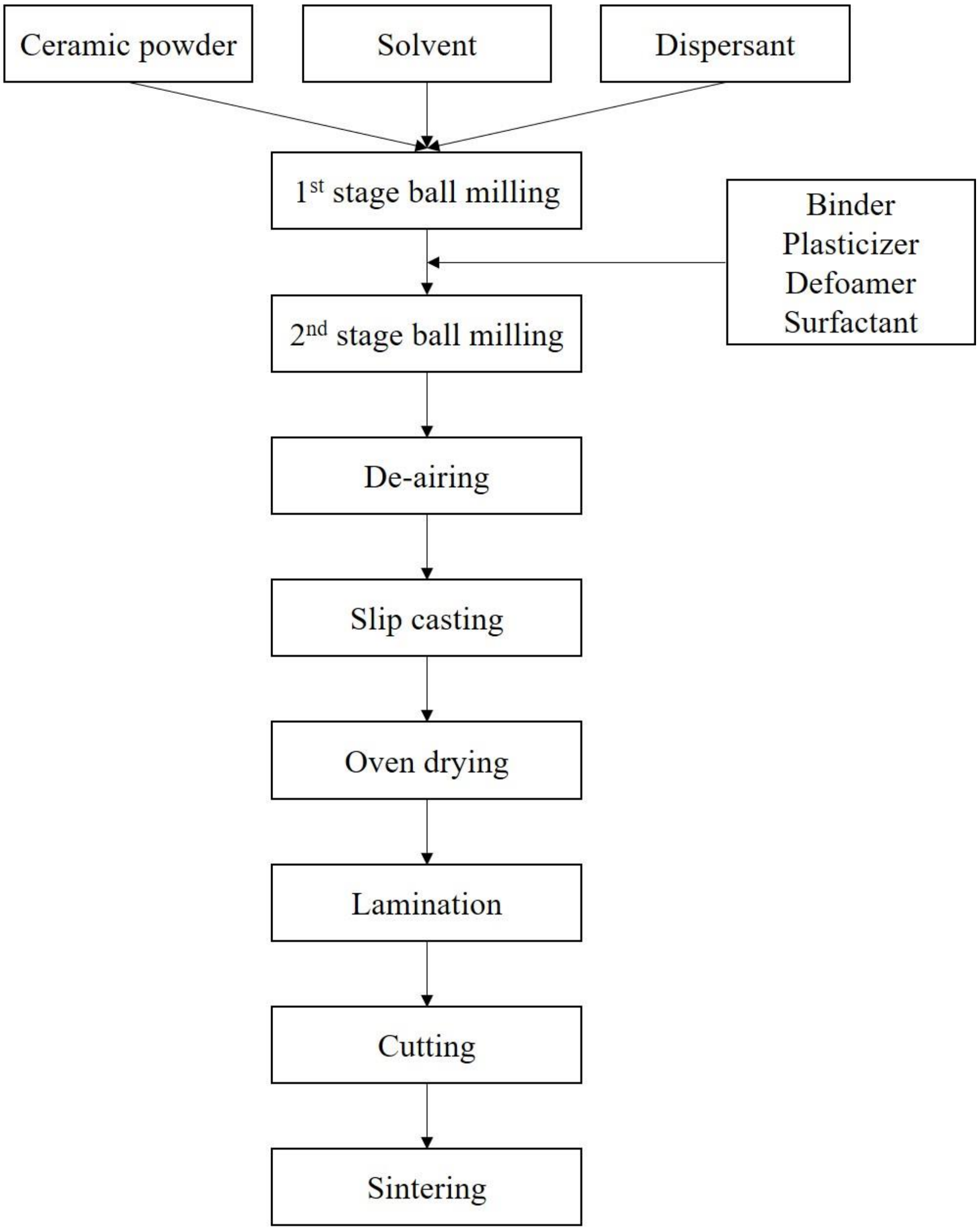

Figure 2-2: General procedure of tape casting ceramic materials.

2.1.3 Slurry development

To obtain a high-quality ceramic tape, the slurry preparation is a key step. The amount of each component in the slurry must be carefully considered to obtain a homogeneous suspension. Organic solvent-based [100-102] and water-based slurries [103-105] are commonly used for tape casting. The use of organic solvents such as ethanol, toluene, and xylene offer a quick mixing and drying process during cell fabrication as they evaporate much quicker than water. Compared to the organic solvent-based slurry, the aqueous phase slurry is more environmentally friendly and cost-effective. More importantly, the wide range of electrostatic force between solid particles in aqueous systems results in improved material dispersion and increased solid loading in a water-based slurry [105].

Nahass et al. [106] reported that the aqueous phase slurries have higher sensitivity for processing than the organic solvent-based slurries, hence an appropriate binder and plasticiser must be used. Producing strong and crack-free green tapes from an organic solvent-based slurry is relatively easier than from an aqueous phase slurry. High quality green tapes can only be obtained from a water-based slurry when all variables are well controlled [107]. Therefore, the investigation on aqueous tape casting has received more attention recently [97, 98, 108].

Due to the difficulties of conducting aqueous tape casting, it is extremely important to control the dispersion, solid loading, and rheology of the water-based slurry [109-111]. Water and organic contents in the slurry should be low to minimise the possibility of defect formation during solvent drying and organic additives burn-out stages. On the other hand, the amount of water must be sufficient to obtain a homogeneous slurry. The amount of dispersant needs to be sufficient to ensure a uniform dispersion of powder in the slurry. In addition, the plasticiser to binder ratio must be adjusted adequately to produce a flexible and high-strength tape [107, 112].

A stable powder dispersion is crucial for reproducing high-quality aqueous slurries. The grinding behaviour and the minimum achievable particle size are strongly influenced by the stability of suspension system. In aqueous systems, the electrostatic repulsive forces caused by particle surface charge are essential for optimal ceramic powder dispersion. This is evaluated by the zeta potential. Measurements of zeta potential versus pH of the slurry are usually carried out to determine the powder dispersion behaviour [113]. Typically, a higher zeta potential (with the same polarity) corresponds to increased electrostatic repulsion among particles in the suspension. Given the correlation between pH value and suspension stability, the zeta potential of a ceramic suspension can be adjusted by adjusting pH value during dispersion [114]. Houivet et al. [115] reported that a good dispersion of all species in the slurry can be achieved when the absolute value of the zeta potential is larger than 20 mV because of the increased electrostatic repulsion. On the contrary, the powder agglomeration and slurry flocculation occur when the zeta potential value is close to zero.

Zeta potential values of different powder systems strongly depend on their preparation method and calcination condition. Figure 2-3 shows the variation of zeta potential with pH value for different powders. It can be seen that both NiO and YSZ exhibit sufficient electrostatic repulsion in either acidic or alkaline media. Nevertheless, the absolute value of LSM zeta potential was above 20 mV when pH > 8. For the case of NiO-YSZ and LSM-carbon pore former mixtures, the pH of slurries needs to be maintained in the range of 9 to 10 so that both components are sufficiently charged [116, 117].

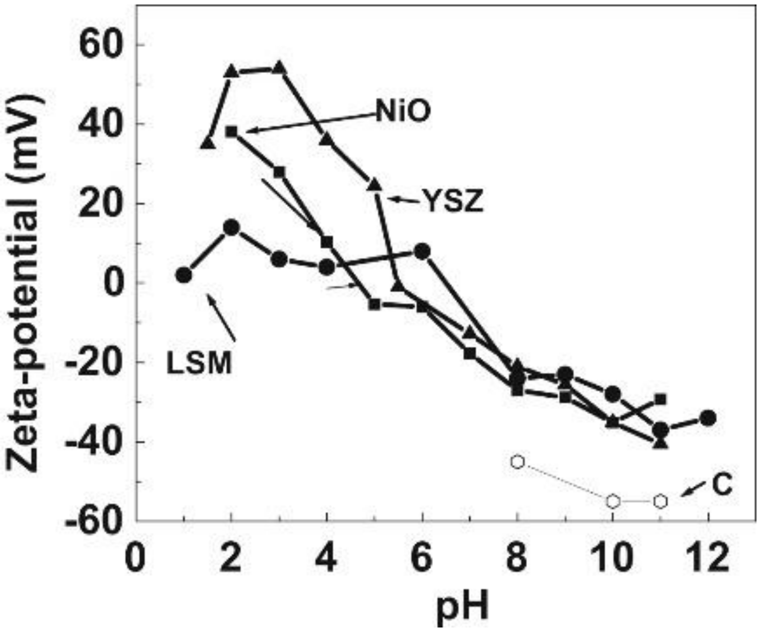

Figure 2-3: Plot of zeta potential vs pH for NiO, YSZ, and LSM powders. Reprinted from Ref. [117] with permission from Springer Nature.

Despite an adequate zeta potential, flocculates are still found in concentrated slurries due to their rheological behaviour, pseudoplasticity, or shear thinning behaviour [115]. The rheological behaviour of the slurry highly depends on type and size of the powder, binder, and other organic additives. The slurry should exhibit pseudoplastic behaviour when it is passing the casting blade, i.e. decrease in viscosity with increase in shear rate. For a pseudoplastic slurry, its viscosity should increase due to the shear forces and then decrease to prevent uncontrolled flow and sedimentation of the ceramic particles. Time dependent flow behaviour, also known as thixotropy, is undesired for high-quality slurry formation, because the flow properties change during tape casting. In this case, mixing and de-airing of the slurry will be difficult [113, 118]. Therefore, pH and rheological behaviour must be carefully monitored and adjusted when developing an aqueous slurry for wet ceramic coating processes, such as tape casting, screen printing and spin coating. A well-optimised aqueous electrode slurry can also maintain good porosity and particle connectivity, resulting in extended TPB length and improved electrode performance [119, 120].

2.1.4 Processing parameters

- Milling and mixing

For most reported aqueous tape casting processes, the slip is prepared through a two-stage milling/mixing [98, 103, 121-123]. The first stage is dispersion milling ceramic powder with solvent and dispersant by using milling machines such as ball mills and vibratory mills. Wear-resistant materials like zirconia or alumina are commonly used as milling media. Agglomerates are broken and dispersants are evenly distributed on the surface of ceramic particles during dispersion milling. More importantly, dispersion milling ensures the ceramic particles stay apart due to steric and/or electrostatic repulsion [107]. In the second stage of mixing, binder and plasticiser are added into the slurry for further mixing. The time of each stage can vary from 2 to 48 hours. The mill rotation speed of the mill should be in the range of 35 to 115% of the critical speed. Critical speed of a ball mill is the point where the centrifugal forces equal gravitational forces at the internal surface of the shell. At this speed, the milling balls will not fall from its position onto the internal shell. The critical speed can be defined by the following Eq.(16) [124]:

$$N_c = 42.3/\sqrt{D} \tag{16}$$

where N_c is the critical rotation speed in rpm, and D is the mill inside diameter in m. After the two-stage milling/mixing, de-airing can be performed by partial vacuum accompanied with gentle stirring or agitation. Air bubbles in the slurry cause defects such as pinholes and cracks in the final green tape, which significantly reduces the tape quality [125].

- Casting and drying

The prepared slurry is normally cast over a substrate by a doctor blade as shown in Figure 2-4. Casting of tape can be achieved by either moving the doctor blade over a fixed support or moving the support under a fixed doctor blade. The first technique is commonly used for laboratory ceramic processing because of the generally limited casting area. The latter can continuously produce ceramic tapes which is suitable for large-scale tape casting. Apart from the slurry preparation, casting parameters such as doctor blade gap height and casting speed can be modified to adjust the tape quality [110, 126, 127].

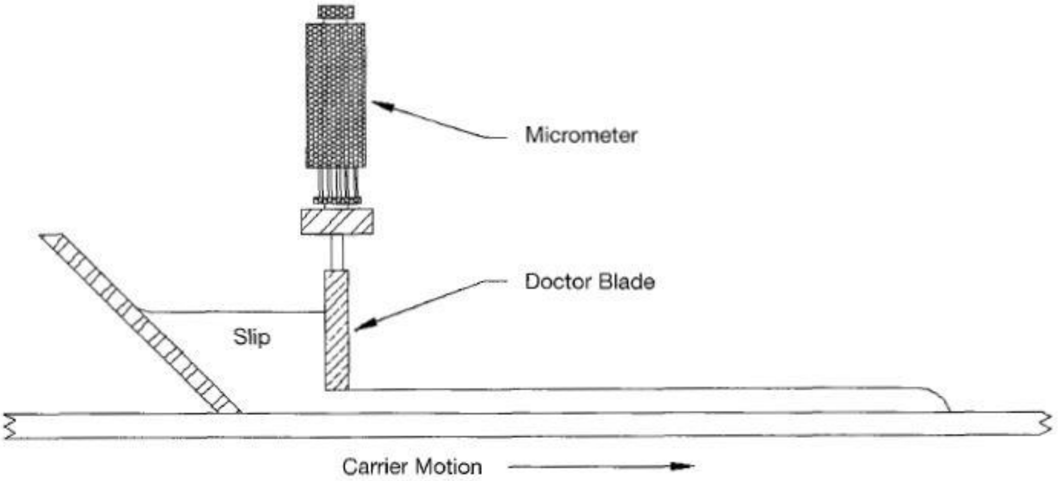

Figure 2-4: Standard doctor blade with one adjustable blade [125].

Drying plays a significant role in the aqueous tape casting process, and significantly influences the quality of the obtained green tape. Because of the low volatility of water, the drying rate of the water-based slurry is inevitably much slower than that of non-aqueous systems [128]. As shown in Figure 2-5, the drying process of the tape is found to have two stages, a constant drying rate stage, followed by a falling drying rate stage [109, 129, 130]. Initially, the drying process is mainly controlled by drying temperature and humidity of the air flow. The mass loss of the tape is linear during this stage. However, the drying kinetics are controlled by the liquid and vapour diffusion in the falling rate period [119, 128]. Typically, only the tape surface is in contact with air, leading to a non-isotropic drying of the slurry. In addition, tape shrinkage takes place in the vertical direction as the thickness reduces. Both non-isotropic drying and shrinkage lead to stress in the tape, which can cause cracking [109].

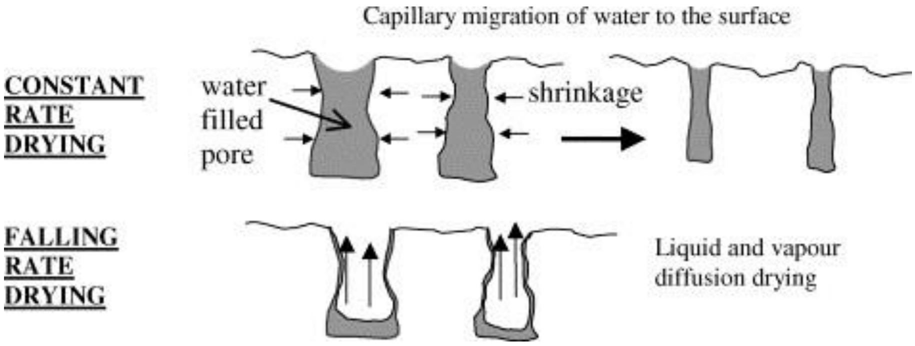

Figure 2-5: Schematic representation of constant rate and falling rate drying steps in aqueous cast tapes. Reprinted from Ref. [109] with permission from Elsevier.

- Sintering

After drying, a flexible tape can be obtained and then cut into the desired sized parts before sintering. Sintering is also known as densification, which reduces the porosity of the ceramic body. The temperature of sintering applied to the ceramic materials is usually 60% to 80% of the material’s melting temperature [131]. Typically, the sintering process of the green tape is divided into two steps, organics burnout and ceramic powder consolidation. Heating rate, sintering temperature and time are the key variables that influence the sintered ceramic properties [97, 105].

Co-sintering a multilayer tape prepared by sequential tape-casting or lamination with several SOFC components is a strategy that greatly reduces the cell fabrication time. The flatness of a sintered planar cell is important, because a flatter cell offers a larger current collection area during cell operation. Apart from warpage, a multilayer tape can suffer delamination during the co-sintering process caused by thermoelastic mismatch between the individual layers [100, 101, 132, 133]. Therefore, all variables must be controlled to ensure high cell flatness and good compatibility of the sintered materials. Many efforts have been made to improve multilayer ceramic tape co-sintering, such as optimising sintering profile [105, 134], applying a sintering load [105, 135, 136], or adding sintering aid [137-139].

Optimising the sintering profile by choosing an appropriate temperature and time for burnout in co-sintering can effectively improve the sintered sample density. The mismatches between electrode (mostly anode) and electrolyte can be alleviated by reducing the heating rate [134]. Applying pressure to the ceramic material during co-sintering is a well-known method to prevent warping [140, 141]. Using a porous sintering load on top of the sample during co-firing not only improves densification, but also ensures the flatness of the obtained sample [105, 135].

SOFCs with zirconia/ceria bilayer electrolytes have been reported to produce high powder density at reduced operating temperature due to the low electronic conductivity of zirconia and high ionic conductivity of ceria. Nevertheless, co-firing of zirconia/ceria bilayer electrolytes is challenging because of the shrinkage mismatch and formation of a solid solution during high-temperature (above 1400°C) sintering [142, 143]. Adding transition metal oxides such as Al_2O_3 [144, 145], Bi_2O_3 [146], CoO [137], CuO [147], and Fe_2O_3 [27, 139] to the electrolyte layers during the manufacturing process was found to promote electrolyte densification at reduced sintering temperatures.

2.1.5 Summary

The reviewed literature suggests that aqueous tape casting is a cost-effective and highly efficient technique for planar SOFC fabrication. Studies indicated that slurry development is the most important step for tape casting ceramic materials, particularly for water-based systems. Powder selection and dispersion, solid loading, and rheology are the key factors to be considered during the slurry preparation stage. A successfully prepared aqueous ceramic slurry for tape casting should exhibit pseudoplastic properties during casting, ensuring a smooth flow without solid sedimentation. Drying and sintering are the two crucial processes that must be carefully handled for multilayer tape casting, as they significantly impact the adhesion, mechanical strength, and flatness of the final sintered multilayer tape. Based on the evidence presented in the literature, aqueous tape casting demonstrates the potential as a viable fabrication method for high-quality planar SOFCs.

2.2 Methane fuelled SOFCs: A review of carbon-resistant anode materials

2.2.1 Overview

Methane has been considered as a promising fuel for SOFCs because of the feasibility of internal reforming at the anode side. Nevertheless, the traditional Ni-based anodes suffer from carbon deposition when hydrocarbon is used as the fuel, potentially leading to irreversible catalyst deactivation and permanent structural damage. Therefore, enhanced anode carbon tolerance is essential for methane-fuelled SOFCs, which can be achieved by suppressing carbon formation or increasing carbon removal rate during the operation. Extensive studies have been carried out to improve both cell performance and carbon resistance. These can be concluded as metal-modified Ni-based anodes, oxide-doped Ni-based anodes, reforming catalyst layered Ni-based anodes, and Ni-free anodes. Recent achievements and approaches to carbon resistant Ni-based anode material development for methane-operated SOFCs are summarised and discussed in this review.

2.2.2 Carbon deposition on Ni-based cermet anode

For a Ni-based anode SOFC with steam methane reforming (SMR) or dry methane reforming (DMR), the formation of carbon species occurs through one of the following reactions:

$$2CO \rightarrow CO_2 + C \tag{17}$$

$$CO + H_2 \rightarrow H_2O + C \tag{18}$$

$$CH_4 \rightarrow C + 2H_2 \tag{19}$$

The first reaction, Eq.(17), is known as Boudouard reaction. Carbon monoxide undergoes disproportionation at lower temperatures (below 700°C) to produce carbon and carbon dioxide [39]. The second carbon forming reaction, Eq.(18), is the reverse ‘water-gas shift’ reaction, which is also favoured at lower temperatures. In this case, carbon monoxide and hydrogen are converted to water vapour and carbon during cell operation. The final reaction Eq.(19) is the methane cracking reaction that normally occurs at a temperature in the range of 700 to 900°C, where methane is directly decomposed into carbon and hydrogen [13, 41].

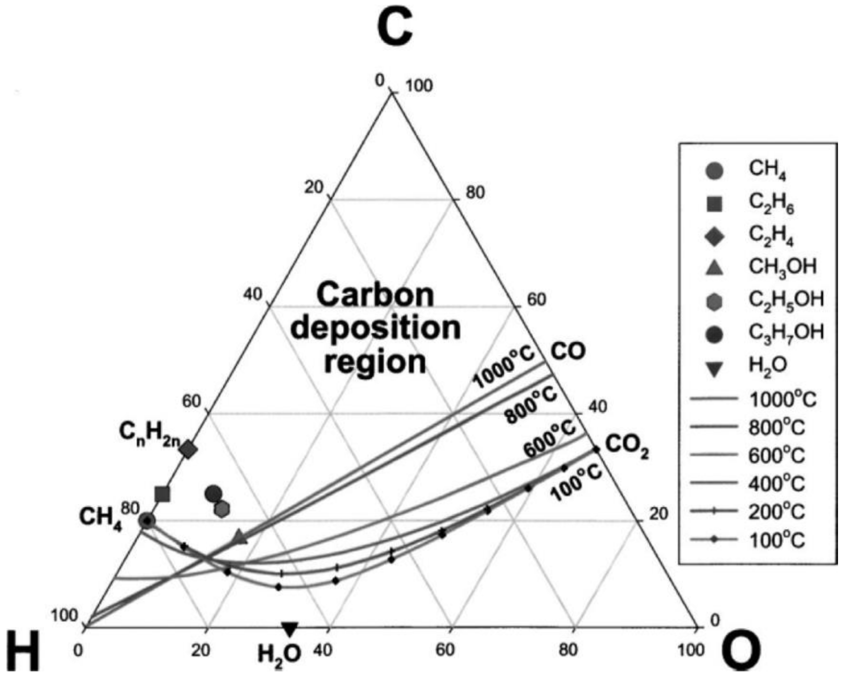

Figure 2-6: Carbon deposition limit lines in the C-H-O phase diagram. Reprinted from Ref. [148] with permission from Electrochemical Society.

Figure 2-6 shows that carbon deposition during hydrocarbon operation is strongly affected by the operating temperature [148] and indicates the region where carbon deposition is favoured at different temperatures for common carbon-containing fuels. The diagram indicates that carbon deposition is thermodynamically favourable at low temperatures, high C:O ratios, and low oxide ion fluxes. From a thermodynamic point of view, carbon deposition can be effectively alleviated by adding O_2 into the anode inlet gas, mainly in the form of water or carbon dioxide, so as not to re-oxidise the Ni catalyst [73]. Furthermore, carbon deposition is affected by the relative rate of the forward and reverse carbon forming reactions, such as Boudouard, reverse 'water-gas-shift', and methane cracking reactions [149].

It is believed that hydrocarbon dissociation produces highly reactive monatomic carbon, C_α. This type of carbon can be easily gasified by reacting with H_2O or CO_2 to form CO, whereas the excessively formed C_α is preferentially polymerised to much less reactive C_β [150, 151]. Although C_β can be partly gasified, it may accumulate on the anode surface and encapsulate or even dissolve into the nickel catalyst particles. Carbon accumulation on the Ni-based cermet anode is suggested to be a result of the imbalance between carbon removal/gasification and carbon formation. Therefore, carbon accumulation on a Ni-based cermet anode occurs when the carbon forming rate is higher than the carbon removal rate [152-154].

The morphology of formed carbon is highly dependent on the thermodynamic conditions and anode materials [155, 156]. Commonly, carbon deposition can be classified as amorphous, filamentous, and graphitic [157]. For an SOFC cell with Ni-based cermet anode, amorphous carbon is more likely to form at lower temperatures and when the catalyst surface area is high, but graphitic carbon is usually found at higher temperature and low catalyst surface area. The formation of carbon filament is often observed in hydrocarbon-operated SOFC anodes, which easily deactivates the Ni catalyst [158, 159].

Takeguchi et al. [160, 161] suggested that carbon deposition on the Ni/YSZ anodes is usually in the form of fibrous carbon. The mechanism of carbon accumulation on a Ni/YSZ cermet has been extensively studied [160-163]. One well-established mechanism of carbon growth on the nickel surface is the diffusion of adsorbed species. For instance, the decomposition of the adsorbed hydrocarbon on the nickel surface could directly lead to the growth of carbon filament [164]. Another carbon accumulation driving force is the concentration gradient across the particles in contact with carbon atoms [162, 163]. Alstrup et al. [163] reported a model that an unstable carbide continuously decomposed into nickel and carbon during the hydrocarbon catalytic reaction. Carbon filament was produced from the decomposition process of carbide, but some surface carbides still remained. Carbon atoms produced from the surface reaction quickly diffuse through the surface carbide, which keeps a constant carbon concentration below the surface. The carbon concentration gradient provides a driving force for carbon atom migration in the catalyst particle, resulting in carbon accumulation.

Due to the wide operating temperature range of SOFCs (550 to 850°C), the anode catalyst microstructure is various and complex. It is difficult to predict which type of carbon will be produced under different thermodynamic conditions [159]. Takeguchi et al. [160, 161] suggested that carbon deposition on the Ni/YSZ anodes is usually in the form of fibrous carbon. He et al. [73] reported whisker carbon deposition on Ni/YSZ pellets after 4 h humidified-methane (~3% water content) operation at temperatures between 500 and 800°C. As shown in Figure 2-7 (b) to (e), carbon nanotubes have formed on the Ni particles at temperatures below 700°C. Moreover, more whisker-like carbon was observed on the anode surface than in the anode centre. This could be explained by the diffusion limitation of methane in the bulk anode. When the temperature was raised to 800°C, deposited carbon seemed to have dissolved into the Ni catalyst, shown in Figure 2-7 (f). Dissolution of deposited carbon into the Ni particles caused serious destruction of the anode, but YSZ particles were still able to maintain their structure after exposure to methane. The results suggested that carbon formed at higher temperatures has stronger bonding to the catalyst, leading to more severe structural damage to the anode.

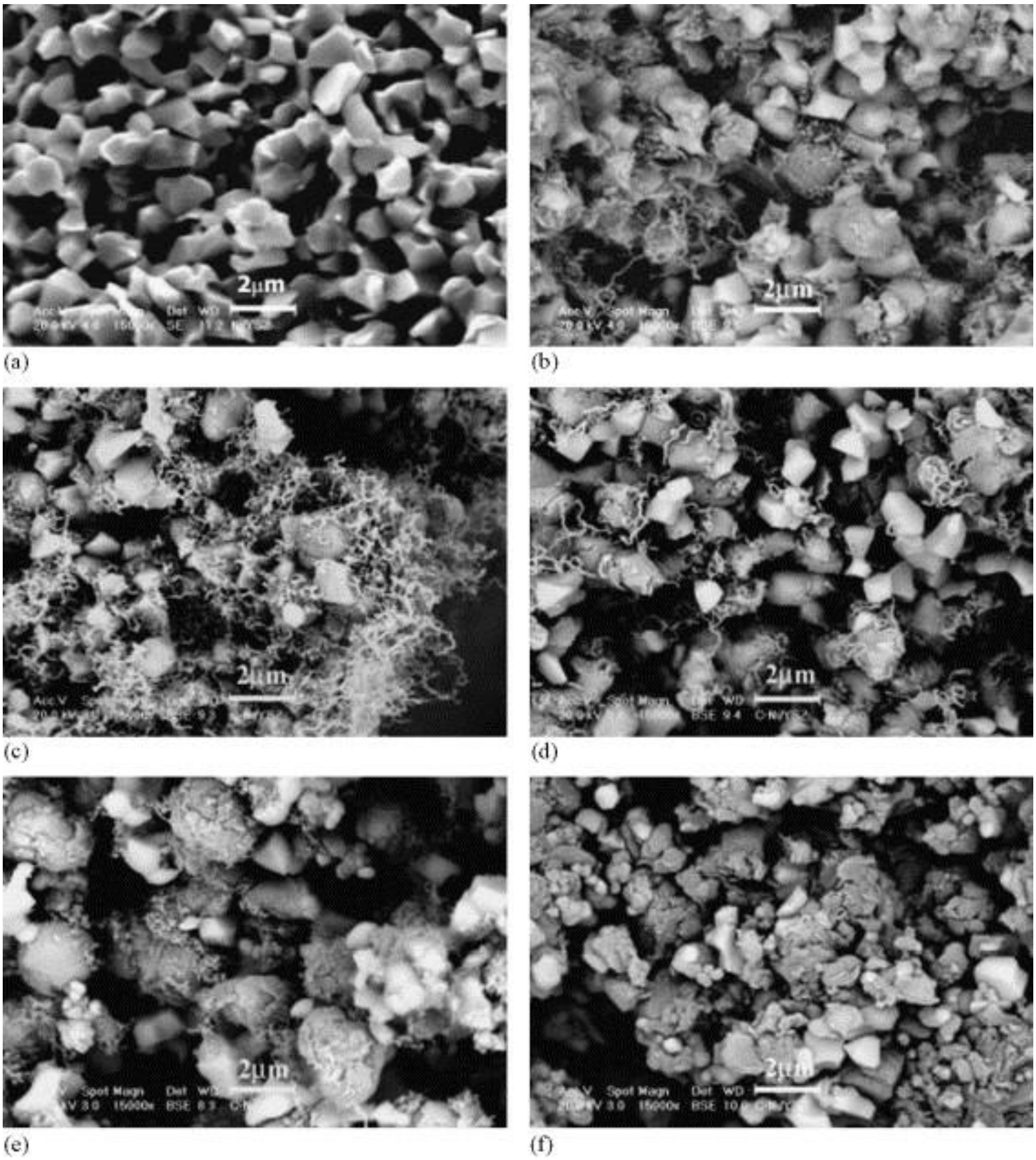

Figure 2-7: SEM images of Ni/YSZ anode (a) as-prepared and tested in humidified methane for 4 hours at (b) 500°C, (c) 600°C, surface, (d) 600°C, (e) 700°C, and (f) 800°C. Reprinted from Ref. [73] with permission from Elsevier.

2.2.3 Carbon tolerant anodes

As mentioned above, Ni-based cermet anodes suffer from carbon deposition under SOFC methane operation. Several strategies have been extensively studied to avoid carbon accumulation on the nickel-based cermet, including (1) the addition of external steam, CO_2, O_2 or H_2 into the fuel gas to lower the C/O ratio, (2) the modification of the Ni-based anode by doping with another metal or oxide to form a surface alloy, (3) the addition of another anode catalyst layer to enhance catalytic activity for methane reforming/oxidation, and (4) the use of Ni-free anode materials that possess low catalytic activity towards carbon forming reactions [13, 149, 165].

It is known that adjusting the fuel composition or substituting an ionic conductor can avoid carbon deposition on the Ni-based anodes. Many efforts have been made to develop suitable fuel compositions for Ni/YSZ/LSM cells with minimal carbon deposition when hydrocarbon fuels are used [166-171]. Supplying the SOFC anode with a certain amount of H_2O, CO_2, O_2 or H_2 was found to improve cell performance and operational stability in hydrocarbon atmosphere. The addition of an oxygen containing gas is the simplest way to mitigate carbon formation thermodynamically, as it decreases the C/O ratio. Steam and carbon dioxide have been added to the methane fuel to create an SMR or DMR environment, respectively [152, 170, 172, 173]. From the thermodynamic point of view, no carbon deposition will occur in a steam methane reforming process when the steam to carbon ratio is greater than 2 [161, 174]. The use of H_2O or CO_2 could alleviate the carbon deposition by promoting carbon removal reactions, however it would be difficult to completely suppress the carbon accumulation on the anode exposed to methane. More importantly, the excessive amount of H_2O or CO_2 in the fuel gas reduces SOFC operating efficiency by diluting the fuel [59, 149].

To achieve high carbon resistance under hydrocarbon operation, the modified SOFC anode must possess two characteristics, speeding up carbon removal and preventing carbon formation. A systematic review of carbon tolerant anode materials for SOFCs to allow the operation with methane and other relevant hydrocarbons is provided in the following.

2.2.4 Metal modified Ni-based anodes

Due to the excellent catalytic activity, mature technology, and low manufacturing cost of Ni-based anodes, metal modified Ni-based anodes with improved carbon resistance have been extensively investigated. The approaches adopted vary from doping noble metals or transition metals with Ni to replacing YSZ by ScCeSZ or ceria [41, 149].

- Modification with noble metals

Gold is the earliest reported precious metal used for improving the carbon tolerance of the Ni-based anodes [165]. The presence of small quantities of Au in the Ni-based cermet results in greatly improved durability, a higher methane conversion rate, and a decreased methane dehydrogenation rate for methane-operated SOFC. Moreover, the formation of graphitic carbon on an Au-doped Ni cermet was prevented under methane-rich operating conditions [175-177]. Proctol et al. [178] suggested that carbon tolerance of Au-doped Ni cermet anodes operated with methane-rich fuel increased with increasing Au loading, but the addition of gold to the anode resulted in a slight reduction of the methane oxidation activity and the selectivity towards methane partial oxidation at lower operating temperatures. Co-doping Mo with the Au-Ni catalyst was found to provide a moderate catalytic activity, but improved the electrocatalytic behaviour and anti-coking properties for the internal SMR reaction [76].

Wang et al. [86] suggested that a silver catalyst on a GDC cermet can provide outstanding catalytic activity towards the CO oxidation reaction. In their study, the prepared Ag/GDC cermet also proved its durability by 50 h stable operation in CO atmosphere at 650°C without carbon deposition. Compared with carbon deposition on a Ni catalyst, carbon formed on Ag/GDC was only present on the surface without dissolution and diffusion into the metal catalyst. Deposited carbon on Ag will not cause structural damage to the anode as with nickel-based anodes [179]. Consequently, modifying the surface of Ni-based anodes with Ag could be a promising approach for the development of carbon-resistant anodes. Ag-doped Ni/YSZ anodes prepared by $AgNO_3$ impregnation [180] and electroless plating [77] showed greatly enhanced carbon resistance and operational stability in dry hydrocarbons at 750°C. On the other hand, silver agglomeration and evaporation at high operating temperatures might affect the cell performance by reducing anode active sites [181]. In order to avoid the blockage of anode active sites, reducing doped-silver particle size and lowering SOFC operating temperature might be feasible solutions.

Nabae et al. [182] found that impregnating Pd-Ni catalysts to an lanthanum strontium chromite/samarium-doped ceria (LSCr-SDC) composite anode can promote methane decomposition to hydrogen and carbon under dry methane operation. Carbon deposition on the CH_4 fed cell was found to be very low under both open- and closed-circuit operating conditions, resulting in a stable operation over more than 12 h. This can be explained by the H_2 produced from CH_4 decomposition being electrochemically oxidised to H_2O during cell operation. Hence, the deposited carbon can be gasified by H_2O and converted to CO and H_2. They also studied the reaction mechanisms of Pd-Ni/LSCr-SDC anodes under dry methane operation. Their results suggested that the reaction taking place over the Pd anode can be described as direct electrochemical oxidation of CH_4, Eq.(20) and Eq.(21) [183].

$$CH_4 + 3O^{2-} \rightarrow CO + 2H_2O + 6e^- \tag{20}$$

$$CH_4 + 4O^{2-} \rightarrow CO_2 + 2H_2O + 8e^- \tag{21}$$

A novel approach of incorporating Pd into different Ni/YSZ anode layers exhibited great improvement in cell performance and durability under butane operation at 600°C. The Pd catalyst was doped into the anode functional layer (AFL) and anode substrate (AS) via sputtering and infiltration, respectively. A Pd-Ni alloy formed at both AFL and AS by combining two doping methods during cell fabrication, which gave higher Pd loading in the anode. More importantly, Pd-sputtered and Pd-infiltrated Ni/YSZ was believed to accelerate electrochemical reactions at the AFL/electrolyte interface and thermochemical reactions at the AS, respectively [184]. Their study demonstrated the potential of using Pd-Ni catalysts for hydrocarbon-fuelled SOFC anodes at low operating temperatures.

A PtNi nano-catalyst supported by alumina has been reported as a highly active and stable catalyst for dry methane reforming [185, 186]. Takeguchi et al. [187] investigated the effect of Pt, Pd, Rh, and Ru addition to Ni/YSZ anodes under steam reforming conditions. In their study, PtNi and RuNi bimetallic catalysts showed improved anode electrochemical activity and reduced gas diffusion resistance. However, the presence of Rh in the anode promoted a higher carbon deposition rate compared to the original Ni/YSZ cermet. In another study, the addition of Rh to a Ni/$Gd_{0.1}Ce_{0.9}O_2$ (Ni/GDC) anode was found to inhibit carbon deposition and give stable performance in sulphur-containing butane [188]. The improved operational stability of the Rh-Ni anode could be explained by the suppression of sulphur poisoning [189]. Another explanation could be the higher catalytic activity of Rh on ceria-based supports towards the water-gas shift reaction, compared with other supports [190].

Ru-Ni has been found to be a suitable catalyst on GDC support for direct hydrocarbon-fuelled intermediate temperature SOFCs (IT-SOFCs) operated in the range of 500 to

750°C. A Ru-doped Ni/GDC anode produced 0.750, 0.716, and 0.648 $W \cdot cm^{-2}$ under dry CH_4, C_2H_6, and C_3H_8 at 600°C, respectively, which is comparable to 0.769 $W \cdot cm^{-2}$ achieved in H_2 operation. Their results also proved that the fuel with higher carbon content was more prone to cause carbon deposition at the same operating conditions [191].

- Modification with transition metals

Using transition metals, such as Co, Fe, Mo, Sn, Cu and Zn, to decorate Ni-based anodes has also been widely investigated. According to comparative studies, introducing a transition metal into the Ni/YSZ anode not only reduces carbon formation, but also reduces the electrochemical catalytic activity towards hydrocarbon oxidation compared to the pure Ni catalyst [13, 192]. Hence, the amount of transition metal added to the Ni-based anode must be carefully considered to maintain sufficient catalytic activity towards the reaction occurring in the hydrocarbon-operated SOFC.

Cobalt is known for its good catalytic activity towards oxidation reactions of carbon-containing fuels. Ni-Co bimetallic catalysts on alumina supports were found to have superior activity for methane decomposition. Although Ni-Co catalysts exhibited remarkable durability in dry methane atmosphere, the growth of non-deactivating carbon was still observed [66]. Djinović et al. [193] reported similar results of carbon nanofiber growth over the Ni-Co catalyst on a CeO_2-ZrO_2 support, however the carbon nanofibers did not deactivate the catalyst. Two conditions were suggested to prevent excessive carbon accumulation; firstly, strong interaction between the Ni-Co particles and ceramic support when the metal loading is lower than 6wt.%. Secondly, high oxygen mobility through a highly defective ceramic phase crystalline lattice which results in effective carbon oxidation during operation.

It was found that iron can reduce carbon deposition on Ni-based anodes under a variety of fuels, including dimethyl ether [194], ethanol [195, 196], methane [197, 198] and propane [199]. Decreased polarisation resistance was observed as a result of the improved electronic conductivity of the anode due to the addition of Fe [195]. Substituting 10wt.% Ni by Fe within the anode materials was found to give the best cell performance under methane operation. It has been suggested that the improved cell performance and stability of Fe-doped anodes could be attributed to a higher activity towards hydrocarbon oxidation and reforming reactions [197-199].

Finnerty et al. [34] found that the addition of 1wt.% of molybdenum to Ni/YSZ anodes significantly reduced carbon deposition in methane fuelled SOFCs. In their follow-up study, the amount of deposited carbon on Ni/YSZ and Mo-Ni/YSZ anodes after 48 h exposure to humidified methane was determined by temperature programmed oxidation (TPO). Carbon accumulation on the Mo-Ni/YSZ anode was only 1/30 of the deposited carbon on the unmodified anode. Moreover, the presence of a small amount of Mo did not affect the electrochemical performance of the Ni-based anodes [175].

Tin has been extensively investigated for suppressing carbon deposition on Ni-based anodes. Sn-Ni cermet anodes were prepared through adding $SnCl_2$ into anode powder during the powder synthesis stage, impregnating $SnCl_2$ solution to the fabricated anode, or applying it directly as a catalytic functional layer on the bulk anode surface [51, 172, 200, 201]. Myung et al. [201] reported a 0.5wt.% Sn-doped Ni/GDC anode showed maximum power densities (P_{max}) of 0.35 W•cm^{-2} and excellent operational stability with 250 h operation in dry methane at 650°C. More importantly, they found that incorporating the Sn catalyst into Ni/GDC anode with an optimised nano-composite structure can greatly improve the cell performance of dry methane-operated SOFC. The maximum power density of a Sn-doped nano-composite Ni/GDC anode increased to 0.93 W•cm^{-2} under the same operating conditions. This can be explained by the extended TPB area of nano-composite structure and more homogeneous distribution of Sn onto a nano-sized NiO/GDC anode powder. The carbon dioxide peak area obtained from TPO results (Figure 2-8) indicates the amount of carbon deposited on Sn-doped cell after 250 h operation was only 9.4% of the deposited carbon on the undoped cell operated for 1.5 h. Kan et al. [51] suggested that the introduction of airflow to the anode side every 100 h can effectively remove the deposited carbon. They reported 300 h stable operation without performance degradation using this technique. It is also worth mentioning that no significant change to Sn loading on the anode surface was reported after such long operation period, suggesting the good stability of the Sn-Ni bimetallic catalyst under wet methane operation. Additionally, anode active sites might be occupied by Sn if an excessive amount of Sn was impregnated into the Ni-based anode, which decreases the cell performance. More severely, the anode was not able to offer enough catalytic activity for carbon gasification, which directly accelerated the degradation rate of an SOFC operated by dry methane [39, 74]. According to many reported studies, 1wt.% of Sn (with respect to Ni) was found to give both improved electrochemical performance and operational stability under direct methane operation [75, 172, 200, 201].

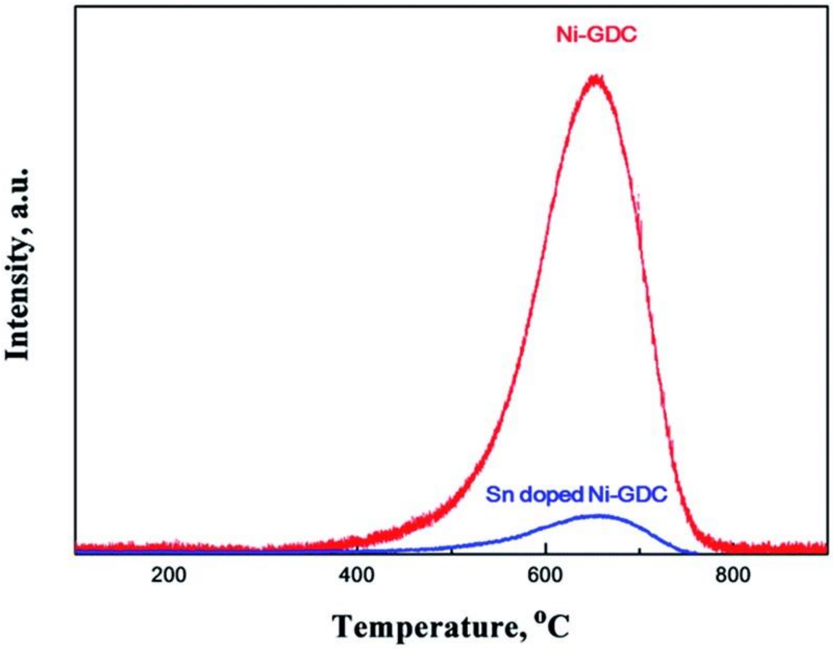

Figure 2-8: TPO results obtained from Ni/GDC and Sn-doped Ni/GDC single cells after long-term stability test in dry methane. Reprinted from Ref. [201] with permission from Royal Society of Chemistry.

Copper is known for its good electronic conductivity and low catalytic activity for C-C bond breaking and carbon forming reactions. Hence, Cu has been considered as an anode catalyst for hydrocarbon-operated SOFCs. Although Cu has attractive properties, it is not as reactive as Ni for hydrocarbon oxidation reactions. Additionally, its relatively low melting point (1085°C) affects the SOFC oxide components sintering [202]. Cu catalytic activity can be enhanced by alloying it with or by adding ceria into the anode [203, 204]. Cu-Ni anodes prepared by impregnation [204, 205], electro/electroless plating [206, 207], or microwave irradiation [208] have been proven to greatly supress carbon deposition under methane operation. Despite the slightly lower P_{max} achieved with Cu-doped anodes compared to Ni-based anodes, the superior operational stability is very attractive for large-scale applications [206]. A carbon resistant anode, NiCu/$BaZr_{0.1}Ce_{0.7}Y_{0.1}Yb_{0.1}O_{3-\delta}$ (BZCYYb), was prepared by metal oxide solution impregnation as reported by Li et al. [209]. No carbon fibres were observed on the NiCu/BZCYYb after 24 h exposure to dry methane at 750°C. More importantly, Figure

2-9 (b) shows the stability results of the prepared cell in wet methane. The cell produced stable voltage output and no performance degradation during 130 h of operation.

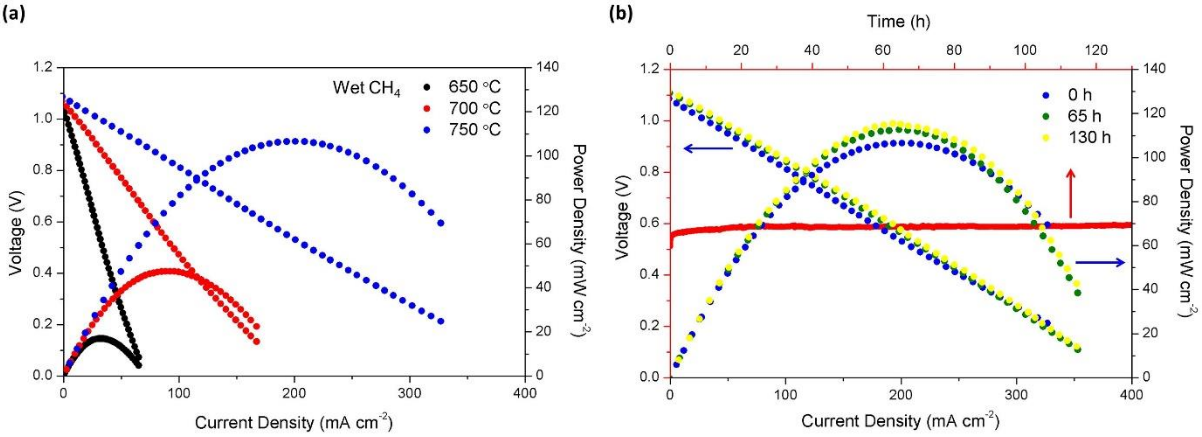

Figure 2-9: Electrochemical performances of NiCu-BZCYYb anode in humidified CH_4: (a) I-V and power curves at various temperatures, (b) stability test at 200 mA•cm^{-2} and I-V and power curves after 65 h and 130 h operation at 750°C. Reprinted from Ref. [209] with permission from Springer Nature.

Recently, Rafique et al. [65] reported a novel Zn-Ni/GDC anode for biogas-operated SOFCs. Figure 2-10 shows the x-ray diffraction (XRD) patterns of the as-prepared and biogas-tested samples. There was no additional phase or carbon peak detected on the sample operated with biogas ($CH_4/H_2/CO_2$) for 48 h, which exhibited extraordinary carbon resistance under dry methane reforming conditions. In their study, Ni and NiO were found to be well dispersed in the anode material as no separate Ni or NiO peaks were observed on the XRD graph, which resulted in improved operational stability with biogas. The prepared Zn-Ni/GDC anode showed peak power densities of 0.400 and 0.548 W•cm^{-2} at 500 and 600°C in biogas, respectively. Moreover, the cell showed extraordinary operational stability at 600°C in biogas by maintaining the power output of 0.55 W•cm^{-2}. Therefore, Zn-modified Ni/GDC could be a very promising anode material for hydrocarbon-operated low temperature SOFCs (≤ 600°C).

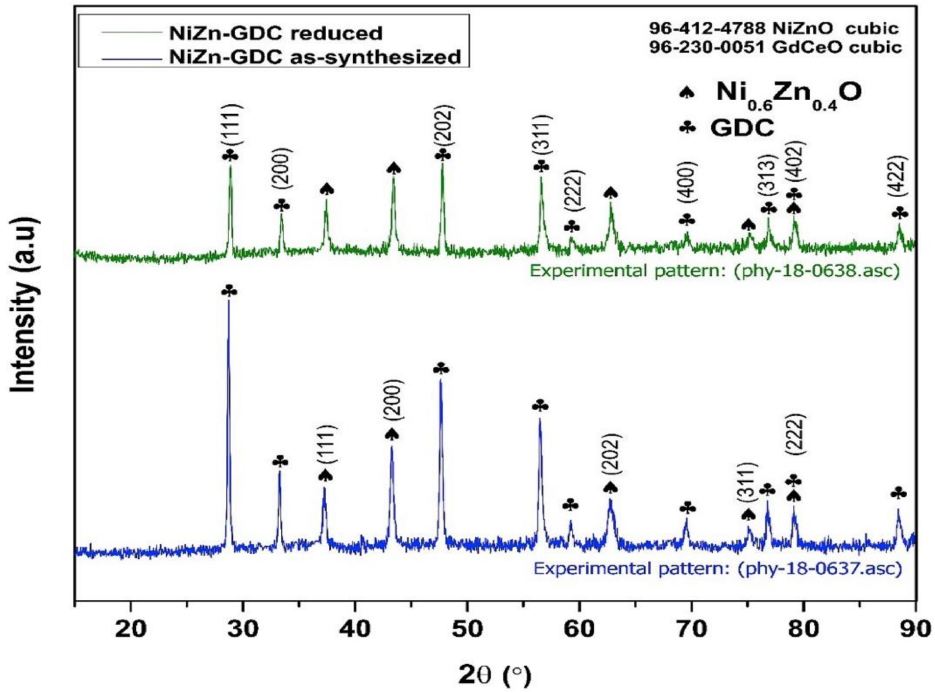

Figure 2-10: XRD patterns of the reduced and as-prepared $Ni_{0.6}Zn_{0.4}/Gd_{0.2}Ce_{0.8}O_{2-\delta}$ composite. Reprinted from Ref. [65] with permission from Elsevier.

Table 2-2 summarises typical metal modified Ni-based anode materials and their electrochemical performances discussed in this section.

Table 2-2: Summary of reported metal modified Ni-based anode materials.

Anode material	**Fuel**	**Temperature (°C)**	**P_{max} ($W•cm^{-2}$)**	**Long-term test (h)**	**Reference**
Au-Ni/YSZ	CH_4/H_2O	850	~ 0.20	60 at 0.5 V	[173]
Au-Ni/YSZ	CH_4/H_2O	850	–	48 at 0.7 V	[175]
Au-Ni/GDC	CH_4/H_2O	850	–	> 100 at 0.5 $A•cm^{-2}$	[177]
	CH_4	850	–	> 100 at 0.5 $A•cm^{-2}$	
Au-Ni/YSZ	CH_4/O_2	700-900	–	–	[178]
Au-Mo/GDC	CH_4/H_2O	800	~ 0.058	140 at 0.057 $A•cm^{-2}$	[76]
Ag-Ni/YSZ	CH_4	750	0.307	100 at 0.6 $A•cm^{-2}$	[180]
Ag-Ni/YSZ	CH_4	750	0.251	24 at 0.2 $A•cm^{-2}$	[77]
	C_2H_6	750	0.379	24 at 0.33 $A•cm^{-2}$	
Ag-Ni/YSZ	CH_4/H_2O	750	~ 0.084	–	[181]
		700	~ 0.058	75	
		650	~ 0.018	–	
Pd-Ni/LSCr-SDC/SDC	CH_4	900	0.42	–	[182]
		800	0.15	12 at 0.5 V	
Pd-Ni/YSZ	n-butane	600	0.486	30 at 0.15 $A•cm^{-2}$	[184]
Pd-Ni/YSZ	CH_4/H_2O	1000	~ 0.32	–	[187]

Pt-Ni/Al_2O_3	CH_4/CO_2	700	–	14	[185]
Pt-Ni/Al_2O_3	CH_4/CO_2	650	–	14	[186]
Pt-Ni/YSZ	CH_4/H_2O	1000	~ 0.32	–	[187]
Rh-Ni/YSZ	CH_4/H_2O	1000	~ 0.25	–	[187]
Rh-Ni/GDC	n-butane/H_2O	600	0.024	24 at 0.038 A•cm^{-2}	[188]
Ru-Ni/YSZ	CH_4/H_2O	1000	~ 0.34	–	[187]
Ru-Ni/GDC	CH_4	600	0.750	> 20 at 0.6 A•cm^{-2}	[191]
	C_2H_6		0.716	–	
	C_3H_8		0.648	–	
Fe-Ni/LSGM	Dimethyl ether	800	1.00	15 at 0.7 V	[194]
		750	0.62	–	
		700	0.47	–	
Fe-Ni/ScCeSZ	Ethanol	850	0.460	–	[195]
		800	0.265	–	
		750	0.165	–	
		700	0.120	48 at 0.7 V	
$Fe_{0.1}Ni_{0.9}$/GDC	CH_4	650	0.34	> 50 at 0.2 A•cm^{-2}	[197]
$Fe_{0.1}Ni_{0.9}$/GDC	CH_4/H_2O	650	1.01	50 at 0.4 A•cm^{-2}	[198]

Fe-Ni/PrBaMn$_2$O$_{5+\delta}$	C_3H_8	700	0.3	–	[199]
Mo-Ni/YSZ	CH_4/H_2O	850	–	48 at 0.7 V	[175]
Sn-Ni/YSZ	CH_4/H_2O	800	0.39	49 at 0.2 A•cm^{-2}	[200]
Sn-Ni/YSZ	CH_4/H_2O	800	1.01	–	[51]
		700	0.68	–	
		650	0.41	137	
Sn-Ni/YSZ	CH_4	740	–	> 5 at 0.6 V	[172]
	isooctane		–	> 15 at 0.5 V	
Sn-Ni/GDC	CH_4	650	0.35	> 250 at 0.5 A•cm^{-2}	[201]
Sn-Ni/GDC (nano-composite)			0.93	> 50 at 1 A•cm^{-2}	
Sn-Ni/SDC	CH_4	700	0.6	–	[74]
		650	0.44	–	
		600	0.27	72 at 0.3 A•cm^{-2}	
Sn-Ni/ScSZ	CH_4/CO_2	750	0.314	–	[75]
Sn-Ni/Al$_2$O$_3$-YSZ	$CH_4/CO_2/H_2S$	850	0.946	48 at 1.25 A•cm^{-2}	[61]
Cu$_{0.7}$Ni$_{0.3}$/CeO$_2$-YSZ	n-butane	700	0.14	–	[204]
Cu-Ni/YSZ	CH_4/H_2O	700	0.24	200 at 0.15 A•cm^{-2}	[206]
Cu-Ni/YSZ	CH_4	750	0.048	180 at 0.4 V	[207]

Cu-Ni/YSZ	CH_4	800	0.049	24 at 0.02 A•cm^{-2}	[208]
Cu-Ni/BZCYYb	CH_4/H_2O	750	0.106	130 at 0.2 A•cm^{-2}	[209]
Zn-Ni/GDC	$CH_4/H_2/CO_2$	500	0.400	–	[65]
		600	0.548	48 at 1.05 A•cm^{-2}	

2.2.5 Oxide modified Ni-based anodes

Considerable work has been conducted on modifying Ni cermet anodes with oxides to inhibit carbon accumulation. Many oxide-modified Ni/YSZ anodes showed good carbon deposition resistance when methane was directly used as fuel [161, 210-213].

Wang et al. [214] found that the addition of a suitable amount of alumina could improve the electrochemical performance of biogas-operated SOFCs. Nevertheless, excessive Al_2O_3 addition showed a negative effect on the cell performance because of its low electronic conductivity and low activity of the anode for methane dry reforming. Recent studies have also shown that incorporating alumina to the Ni/YSZ anode can promote the reaction between NiO and Al_2O_3 to form a $NiAl_2O_4$ spinel structure at the early sintering stage. Formation of $NiAl_2O_4$ in the anode suppressed the grain growth of NiO at high sintering temperature (1400°C), thereby obtaining smaller Ni particles after hydrogen reduction [215, 216].

Ceria is a promising candidate as catalyst for SOFC anodes due to its remarkable oxygen storage capacity. CeO_2 can create oxygen vacancies from the process of reduction of Ce^{4+} to Ce^{3+} under reducing environment and store oxygen under oxidising environment by filling oxygen vacancies. This feature also offers ceria high carbon resistance under methane reforming conditions [217-219]. Hence, the addition of ceria-based materials to Ni cermet anodes has been extensively investigated to modify the anode catalytic activity and reduce the tendency towards carbon deposition [161, 210, 212]. Nakagawa et al. [210] found that CeO_2-doped Ni/YSZ anodes can provide higher catalytic activity towards steam methane reforming reactions than the Ni/YSZ anode at low temperatures as long as the fuel gas contains some hydrogen. Catalytic activity and carbon deposition rate were found to be closely related to the concentration of impregnated ceria (1, 5, and 10wt.%). The carbon formation rate on the 10wt.% CeO_2-doped Ni/YSZ anode was twice as high as on the 1wt.% CeO_2-doped Ni/YSZ anode with steam reforming of methane as the operating condition [161]. Qiao et al. [212] also investigated the effect of different CeO_2 loadings on the cell performance in humidified hydrogen and dry methane. As shown in Table 2-3, the P_{max} obtained by the 3% and 5% ceria-doped Ni/YSZ cells under dry CH_4 operation were significantly higher than the P_{max} obtained with pure Ni/YSZ cells. However, it can be seen that the cell performance in both H_2 and CH_4 fuels decreased with the reduction in Ni content. A further prepared cell with 10wt.% CeO_2 and 25wt.% Ni showed P_{max} of 0.480 $W•cm^{-2}$ and no observable deposited carbon after 5 h operation in dry methane.

Table 2-3: P_{max} and OCVs of cells with different Ni and CeO_2 loading in $H_2/3\%H_2O$ and dry CH_4 at 800°C [212].

Cell name	**Cell-I**	**Cell-II**	**Cell-III**	**Cell-IV**	**Cell-V**
Anode	30% Ni	3% CeO_2-27% Ni	5% CeO_2-25% Ni	10% CeO_2-20% Ni	15% CeO_2-15% Ni
$P_{max}/W•cm^{-2}$ (H_2)	0.209	0.315	0.420	0.219	0.119
$P_{max}/W•cm^{-2}$ (CH_4)	0.057	0.211	0.288	0.069	0.053
OCV/V (H_2)	1.06	1.09	1.09	1.09	1.09
OCV/V (CH_4)	0.87	1.02	1.09	1.09	1.08

Modifying Ni/YSZ anodes with nano-sized doped-ceria such as SDC and GDC has been studied for direct methane SOFCs [220-222]. Chen et al. [220] reported that Ni/YSZ anodes modified with Ti-doped SDC can give better cell performance than the SDC-doped Ni/YSZ anode operated with methane, showing peak power density of 0.444 and 0.420 $W•cm^{-2}$, respectively. Evenly coated nano-sized SDC on the Ni-based anodes was found to suppress carbon deposition by preventing CH_4 approaching Ni particles and enhance the anode catalytic activity towards methane oxidation by improving the oxygen storage capacity. The results were in good agreement with the results reported by Wang et al. [221] and Zhu et al. [223]

Apart from ceria, other rare and alkaline earth oxides such as BaO [213, 224, 225], CaO [49, 226], MgO [80, 81], SrO [49, 226], and La_2O_3 [227] have been used for improving anode carbon resistance under hydrocarbon operation. An anode with nanostructured BaO-Ni interfaces has been reported by Yang et al. [225], providing excellent electrochemical performance and stability under propane, carbon monoxide, and gasified carbon operation compared to conventional Ni/YSZ anodes. According to synchrotron-based X-ray and microstructure analyses, nano-sized BaO islands were formed via vapour deposition of BaO into Ni/YSZ. Nanostructured BaO-Ni interfaces were found to effectively promote water adsorption and water-mediated carbon removal reactions. Figure 2-11 shows the carbon removal process on the anode with BaO-Ni interfaces when propane is used as fuel. Water is firstly captured by the BaO and then split into OH and H (D1). The dissociated OH would react with the carbon produced from hydrocarbon dehydrogenation and CO disproportionation (D2) to form COH. Finally, CO and H species formed by COH dissociation are oxidised at the triple-phase boundaries.

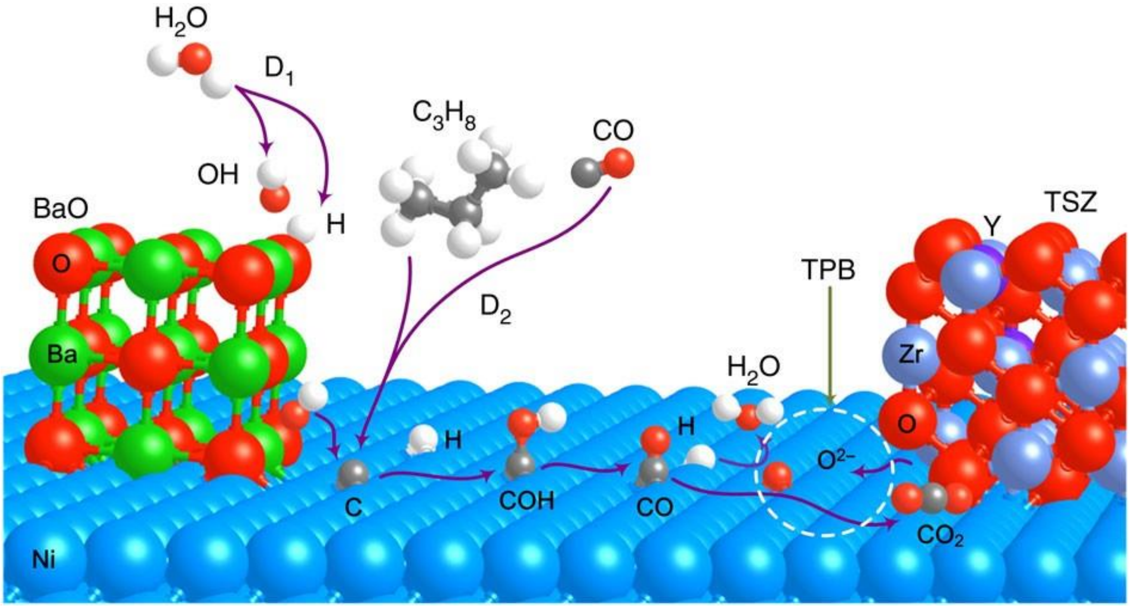

Figure 2-11: Proposed mechanism for water-mediated carbon removal on the anode with BaO/Ni interfaces. Reprinted from Ref. [225] with permission from Springer Nature.

Previous studies suggested that impregnating CaO into Ni-based anodes can suppress carbon deposition in both dry and steam methane reforming conditions, but slightly lower maximum power densities were observed for CaO-doped Ni-based anodes than for purely Ni-based anodes [161, 226]. A comparative study of the performance of Ni/SDC modified with different oxide additives under methane steam reforming conditions has been conducted by Qu et al. [49]. In their work, a CaO-Ni/SDC anode delivered higher power density than the Ni/SDC anodes in humidified methane in the temperature range of 500 to 700°C. The modified anode material was prepared by directly mixing anode powders and CaO. The significant improvement in electrochemical performance of CaO-modified anodes could be attributed to the even distribution of CaO nanoparticles and their high electrical conductivity. Figure 2-12 (a) shows the CO_2 intensity measured from TPO characterisation. According to the CO_2 peak area, it is clear that CaO, BaO, and La_2O_3-modified Ni/SDC anodes had less overall carbon deposition than the other anodes. Coke formation rates of the tested anodes were calculated from the area under the peak, which are shown in Figure 2-12 (b). Reduced coke formation rates further confirmed the suppressed carbon accumulation by adding CaO, BaO, or La_2O_3 to Ni-based anodes. A significant increase of coke formation for the MgO-modified Ni/SDC anode (6 times higher than Ni/SDC) can be seen after the 30 min exposure to methane. According to the XRD results, this was caused by the unreduced $Ni_{0.938}Mg_{0.062}O$ phase at the anode.

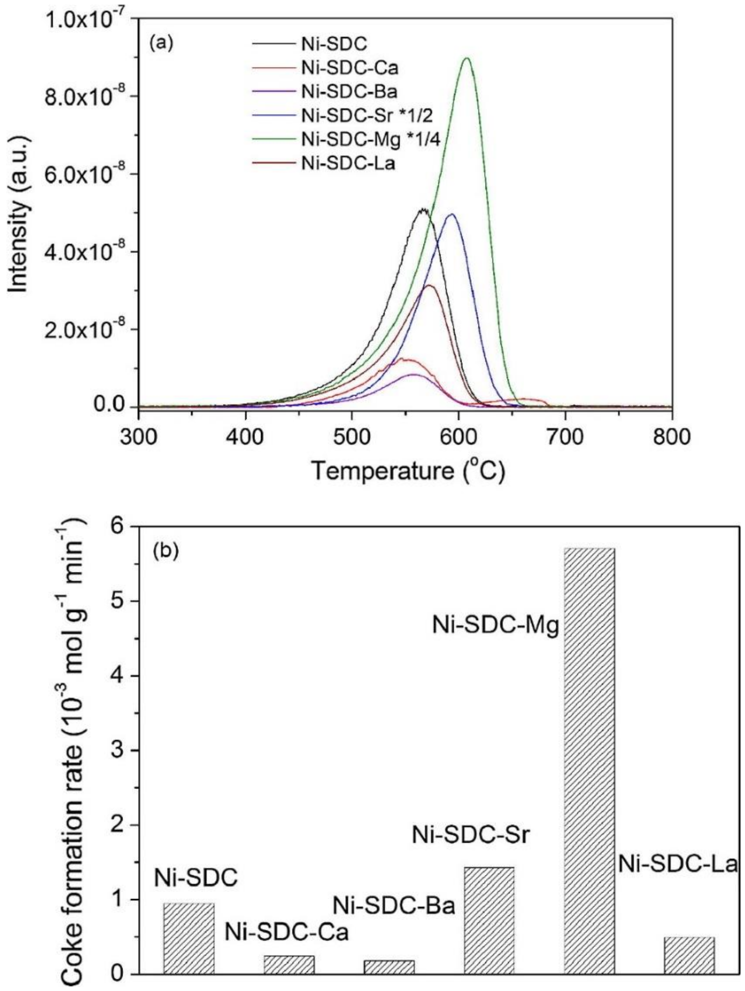

Figure 2-12: TPO results and coke formation rate obtained from different anodes after 30 min methane exposure at 650°C. Reprinted from Ref. [49] with permission from Elsevier.

MgO has been reported as a promoter for Ni-based catalysts to prevent Ni agglomeration during NiO reduction [228]. Impregnating 2.5wt.% MgO (with respect to Ni) into the Ni/SDC anode was found to produce an excellent power density of 0.714 W•cm^{-2} and stable operation over 330 h in humidified methane at 800°C [80]. The addition of MgO to a Ni cermet anode has a similar mechanism as explained in Figure 2-11, which promotes the adsorption and dissociation of H_2O on the surface of MgO nano-plates. More importantly, the MgO-decorated Ni/SDC anodes were found to have significantly enhanced carbon resistance in SMR operating conditions [80, 81]. Lanthanum oxide was found to prevent Ni coarsening and promote uniform distribution of the anode materials in humidified methane, resulting in a higher maximum power density and lower polarisation resistance than Ni/SDC at 600°C [227].

A metal-supported SOFC with $NiMn_2O_4$-modified Ni/GDC anode exhibited exceptional performance in wet hydrogen and methane fuels. The obtained maximum power densities of the modified anode at 600, 650, and 700°C were very similar, regardless of the fuel used. $NiMn_2O_4$ in the modified anode was firstly reduced to Ni and MnO by hydrogen. During this process, fine MnO particles (~ 100 nm) were formed on the surface of the Ni particles, which increased the anode porosity and resistance to Ni agglomeration. Carbon resistance of this modified anode was proven by a stable 100-hour durability test under humidified CH_4 operation [229].

Table 2-4 summarises the oxide modified Ni-based anode materials and their performances under methane and/or other hydrocarbon fuels discussed in this section.

Table 2-4: Summary of reported oxide modified Ni-based anode materials.

Anode material	Fuel	Temperature (°C)	P_{max} (W•cm^{-2})	Long-term test (h)	Ref
Al_2O_3-Ni/YSZ	CH_4/CO_2	850	0.571	–	[214]
		800	0.478	–	
		750	0.350	130 at 0.2 A•cm^{-2}	
		700	0.247	–	
10% CeO_2-25% Ni/YSZ	CH_4	800	0.48	5 at 0.5 A•cm^{-2}	[212]
SCT-Ni/YSZ	CH_4/H_2O	700	0.444	> 85 at 0.5 V	[220]
GDC-Ni/YSZ	CH_4	800	–	–	[221]
SDC-Ni/SDC (SDC coated Ni)	CH_4/H_2O	600	0.353	50 at 0.5 V	[223]
BaO-Ni-Cu/GDC	CH_4	750	0.284	> 200 at 0.6 V	[224]
BaO-Ni/YSZ	C_3H_8	750	~ 0.88	> 100 at 0.5 A•cm^{-2}	[225]
	CO/H_2O		~ 0.70	> 100 at 0.5 A•cm^{-2}	
	gasified C		~ 0.65		
BaO-Ni/SDC	CH_4/H_2O	600	0.307	–	[49]
CaO-Ni/SDC	CH_4	700	0.036	24 (closed circuit)	[226]
CaO-Ni/SDC	CH_4/H_2O	700	1.051	70 at 0.3 A•cm^{-2}	[49]
		650	0.704		

MgO-Ni/SDC	CH_4/H_2O	800	0.714	> 330 at 0.8 V	[80]
MgO-Ni-Cu/SDC	CH_4/H_2O	700	0.670	100 at 0.3 A•cm^{-2}	[81]
La_2O_3-Ni/SDC	CH_4/H_2O	600	0.550	8 at 0.44 A•cm^{-2}	[227]
MnO-Ni/GDC	CH_4/H_2O	700	1.208	–	[229]
		650	0.869	100 at 0.4 A•cm^{-2}	
		600	0.517	–	

2.2.6 Anode catalyst layer addition

Compared with the addition of metal/metal oxides into the anode bulk material, applying an additional anode catalyst layer on the outer surface of the Ni-based anode has been reported for SOFCs operated with methane, butane [230-235], and ethanol [236, 237]. The additional catalyst layer provides high activity for reforming carbon-containing fuels and excellent carbon resistance to the anode during operation. It is worth mentioning that the anode current is collected from the side of the anode when a catalyst layer is applied, which is shown in Figure 2-13 [231].

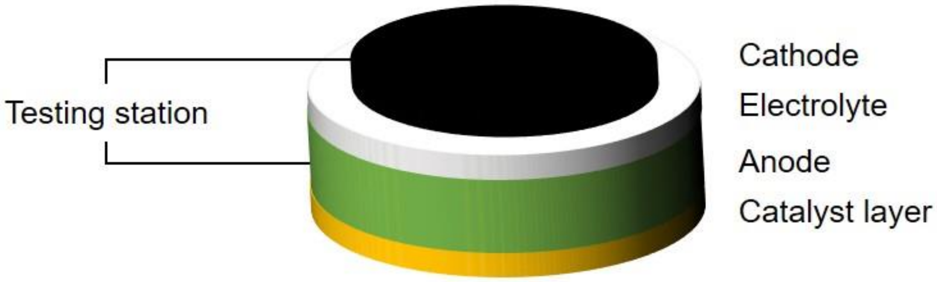

Figure 2-13: Schematic diagram of an SOFC with a catalyst layer on the outer anode surface.

The presence of a Ru-CeO_2 catalyst layer in low-temperature solid oxide fuel cells (LT-SOFCs) exhibited high performance and stable coke-free operation under propane and iso-octane fuels within the operating temperature range of 500 to 600°C [231, 232, 238]. Zhan and Barnett [231] suggested that the avoided carbon deposition could be explained by the good catalytic activity of the Ru catalyst for iso-octane reforming. The Ru-CeO_2 catalyst layer promoted the partial oxidation reaction of octane, producing hydrogen for the cell operation. Moreover, the presence of a catalyst layer effectively reduced the amount of hydrocarbon reacted at the Ni/SDC bulk anode, thereby suppressing carbon accumulation. In their following study, the Ru-ceria catalyst layer was also found to improve the efficiency of propane partial oxidation at 500°C [238].

Ye et al. [236] reported a Ni/YSZ anode with a screen printed Cu-CeO_2 catalyst layer, showing an enhanced cell performance under ethanol operation. Cell performance was found to be strongly affected by the mass ratio of Cu and CeO_2 in the catalyst layer. The catalyst layer with a Cu to CeO_2 mass ratio of 1:3 produced the highest power density of 0.566 W•cm^{-2} at 800°C among all prepared samples, but the cell stability was considerably lower than for the catalyst layer with a 1:2 Cu to CeO_2 mass ratio. Figure 2-14 shows the interface of catalyst layer and bulk anode after 80 h operation in ethanol steam presenting delamination of the catalyst layer and supported anode in Figure 2-14 (b). The delamination could be attributed to the different TECs between CeO_2 and ZnO_2. On the other hand, the catalyst layer with 1:2 Cu to CeO_2 ratio showed a stable operation without performance degradation and no delamination at the same operating conditions. Therefore, the composition of a Cu-CeO_2 catalyst layer must be carefully considered in order to minimise the contact resistance and maximise adherence between different layers [236].

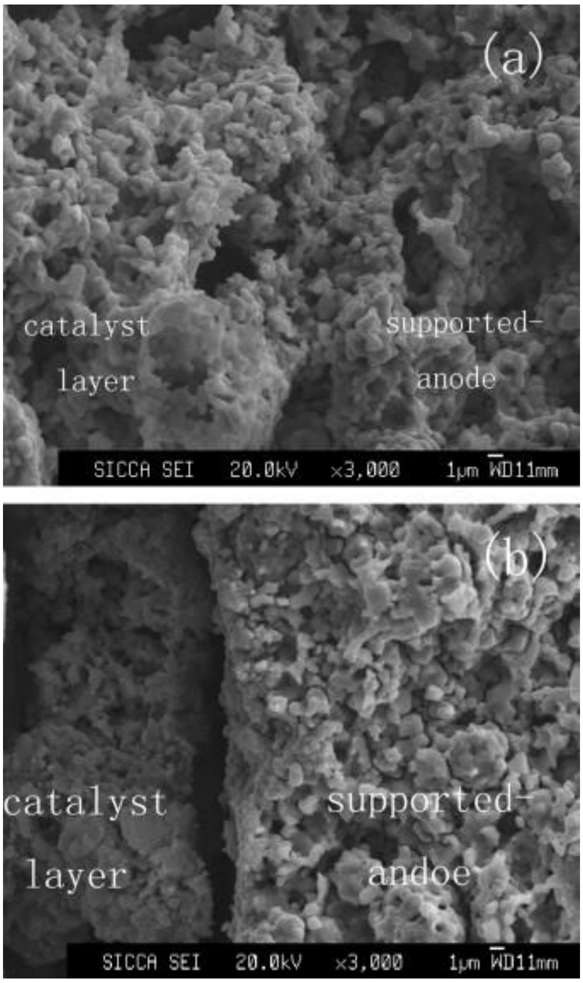

Figure 2-14: SEM images of the interface between the catalyst layer and the bulk anode of cell with 1:2 Cu to CeO_2 ratio (a) and cell with 1:3 Cu to CeO_2 ratio (b) after 80 h operation in ethanol steam. Reprinted from Ref. [236] with permission from Elsevier.

Cu-containing catalyst layers on the Ni/SDC anode have been found to mitigate carbon deposition for direct methane operated SOFCs. Jin et al. [233] reported a Ni/SDC anode with a $Cu_{1.3}Mn_{1.7}O_4$ (CMO)/SDC internal reforming layer showing excellent electrochemical performance in humidified methane between 600 and 700°C. Their results showed the cell could effectively convert CH_4 into CO and H_2 at the printed catalyst layer, thereby the reaction mechanism of prepared anode was similar to H_2 oxidation at the Ni/YSZ anode.

Similar to directly modifying a Ni cermet anode with MnO or Fe, applying a layer of Ni-MnO or Ni-Fe composite catalyst on the Ni-based anode surface showed improved electrochemical performance and carbon resistance in wet CH_4 atmosphere [239, 240]. According to the analysis via Raman spectroscopy, the carbon deposited on the Ni-MnO/Ni/YSZ anode was found to have a lower degree of graphitisation than a Ni/YSZ anode, being more reactive and removable under SMR conditions [239].

Hua et al. [235] achieved a maximum power density of 0.91 $W \cdot cm^{-2}$ and up to 100 h stable operation at 700°C using CH_4-CO_2 as the fuel with a $Ni_{0.8}Co_{0.2}/La_{0.2}Ce_{0.8}O_{1.9}$ (NiCo/LDC) catalyst-coated Ni/BZCYYb anode. Figure 2-15 shows the CO_2 conversion and CO selectivity differences of Ni/BZCYYb and NiCo/LDC catalysts under dry methane reforming conditions at different temperatures. Obviously, CO_2 conversion for both catalysts increased with the increase of temperature. The NiCo/LDC catalyst could provide a 96.9% CO_2 conversion at 700°C, which was about twice as higher as for the Ni/BZCYYb catalyst (48.3%). CO selectivity for NiCo/LDC and Ni/BZCYYb at 700°C was 97.6% and 64.9%, respectively. Therefore, the excellent catalytic activity of NiCo/LDC towards dry reforming reactions ensured significantly improved cell performance in a CH_4-CO_2 atmosphere.

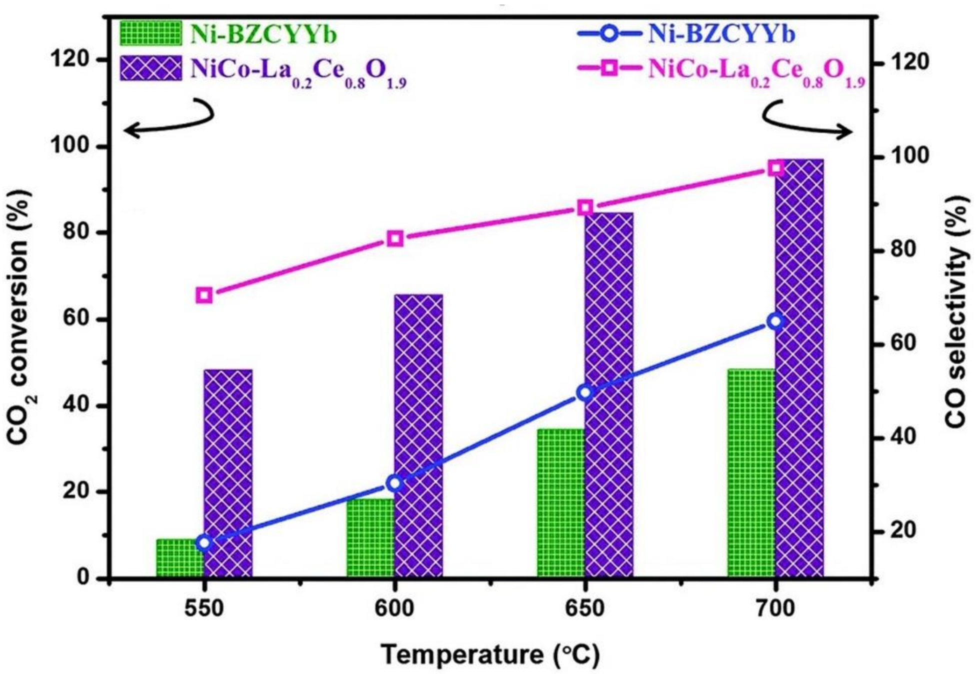

Figure 2-15: CO_2 conversion and CO selectivity comparisons between Ni/BZCYYb and NiCo/LDC catalysts in dry methane reforming conditions in the temperature range of 550 to 700°C. Reprinted from Ref. [235] with permission from Royal Society of Chemistry.

Recently, a comparative study conducted by Hołówko et al. [78] investigated the effect of nano-crystalline materials, undoped and A-doped ceria (A = Mn, Fe, Co, Ni, Cu), on direct biogas-fuelled Ni/YSZ anodes. Figure 2-16 shows a comparison of the produced current density from each prepared cell during a 90-h stability test at 750°C. The cells with $Ce_{0.8}Ni_{0.2}O_{2-\delta}$ and $Ce_{0.8}Co_{0.2}O_{2-\delta}$ catalyst layers provided slightly lower current densities than the other cells during operation, whereas obvious performance degradation/fluctuation was observed from the other cells over time. Enhanced operational stability of $Ce_{0.8}Ni_{0.2}O_{2-\delta}$ and $Ce_{0.8}Co_{0.2}O_{2-\delta}$ layered cells could be attributed to the higher carbon removal rate than carbon accumulation rate during biogas operation.

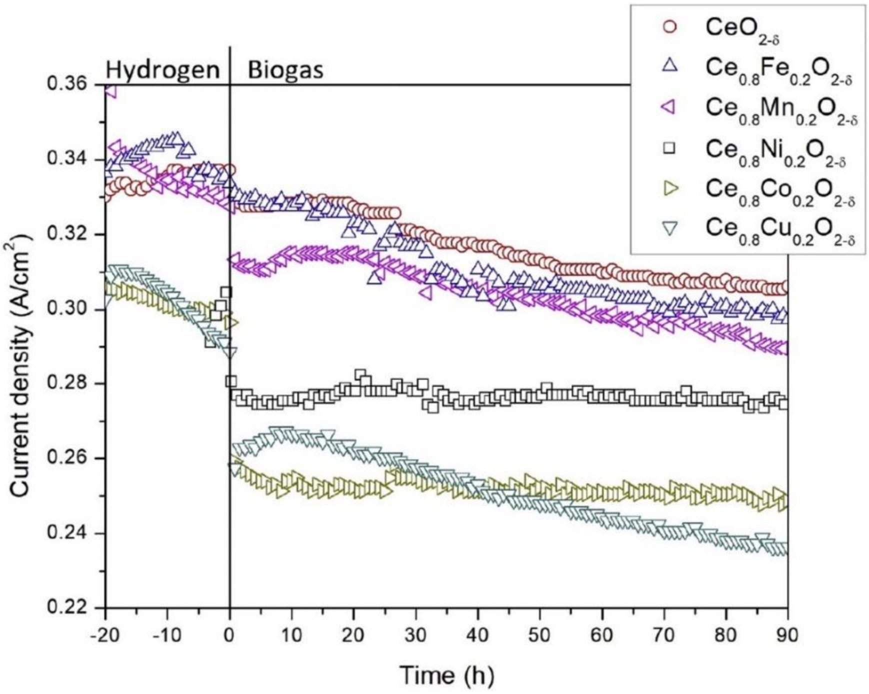

Figure 2-16: Current densities of the cells with undoped and A-doped ceria (A = Mn, Fe, Co, Ni, Cu) catalyst layers during 90-h test with static voltage of 0.65V. Reprinted from Ref. [78] with permission from Elsevier.

Many studies proved that applying a Ni/GDC catalytic layer on the traditional Ni-based anode surface can effectively enhance the cell performance and durability in both dry and wet methane atmosphere [79, 241]. Lee et al. [79] reported a novel Ni/GDC catalytic layer for the Ni/GDC anode operated with dry CH_4. Contrary to directly painting a layer of Ni/GDC catalyst on the anode surface, the NiO in this catalyst layer was covered with GDC nanoparticles (Figure 2-17). The catalyst exhibited high activity toward CO oxidation, which suppressed the carbon formation caused by the Boudouard reaction at low temperatures. The prepared cell achieved a P_{max} of 1.42 W•cm^{-2} at 610°C and over 1000 hours stable operation at a current density of 1.2 A•cm^{-2}. Compared with the GDC infiltration [242] and conventional Ni/GDC [241] catalyst layer, this core-shell structure Ni/GDC catalyst is very promising for improving the electrochemical performance and carbon resistance of LT-SOFCs operated in CH_4.

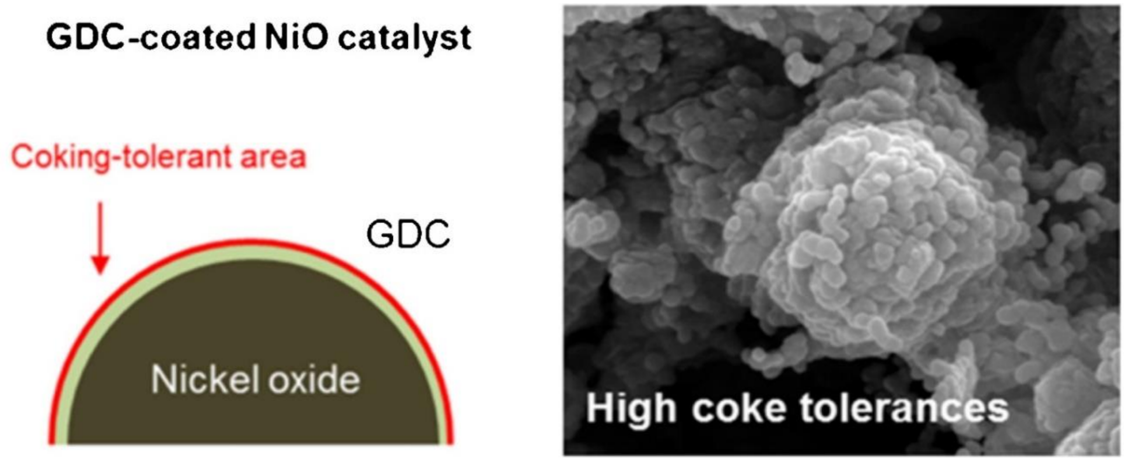

Figure 2-17: High carbon tolerance nickel oxide catalyst covered with nano-sized GDC. Reprinted from Ref. [79] with permission from Elsevier.

Table 2-5 presents typical carbon resistant Ni-containing anodes applied with various catalyst layer.

Table 2-5: Summary of the reported carbon resistant anodes with catalyst layer.

Anode material	**Fuel**	**Temperature (°C)**	**P_{max} ($W \cdot cm^{-2}$)**	**Long-term test (h)**	**Ref**
Ru/CeO_2-Ni/YSZ	iso-octane/CO_2/air	770	0.6	50 at 0.6 $A \cdot cm^{-2}$	[230]
Ru/CeO_2-Ni/SDC	iso-octane/air	590	0.6	50 at 0.8 $A \cdot cm^{-2}$	[231]
Ru/CeO_2-Ni/SDC	iso-octane/air/H_2O/CO_2	600	0.654	–	[232]
Ru/CeO_2-Ni/SDC	C_3H_8/air	500	0.395	–	[238]
		450	0.280	–	
Cu/CeO_2-Ni/YSZ	Ethanol/H_2O	800	0.566	80 at 0.6 V	[236]
Ni/$Ce_{0.8}Zr_{0.2}O_2$-Ni/YSZ	Ethanol/H_2O	700	0.536	–	[237]
		650	0.334	–	
		600	0.162	–	
Ni/$CeO_{2-\delta}$-Ni/YSZ	CH_4/CO_2	750	0.181	90 at 0.65 V	[78]
$Cu_{1.3}Mn_{1.7}O_4$/SDC- Ni/SDC	CH_4/H_2O	700	0.375	–	[233]
		650	0.304	> 80 at 0.6 $A \cdot cm^{-2}$	
		600	0.172	–	
Ni/MnO-Ni/YSZ	CH_4/H_2O	800	–	24 at 0.2 $A \cdot cm^{-2}$	[239]
$La_{0.7}Sr_{0.3}Fe_{0.8}Ni_{0.2}O_{3-\delta}$-Ni/YSZ	CH_4/H_2O	800	0.421	> 100 at 0.335 $A \cdot cm^{-2}$	[240]
	CH_4/air		0.356	> 120 at 0.335 $A \cdot cm^{-2}$	

$Ni_{0.5}Cu_{0.5}Fe_2O_4$/BZCYYb-Ni/YSZ	CH_4/H_2O	800	–	24 at 0.2 A•cm^{-2}	[234]
$Co_{0.2}Ni_{0.8}$/LDC-Ni/BZCYYb	CH_4/CO_2	700	0.91	100 at 1 A•cm^{-2}	[235]
Co/$CeO_{2-\delta}$-Ni/YSZ	CH_4/CO_2	750	0.164	90 at 0.65 V	[78]
Ni/GDC-Ni/GDC	CH_4	610	1.42	> 1000 at 1.2 A•cm^{-2}	[79]
Ni/GDC-Ni/YSZ	CH_4/CO_2	750	0.271	45 at 0.2 A•cm^{-2}	[241]
Sn-Ni/GDC-Ni/GDC	CH_4	650	0.52	> 220 at 0.6 A•cm^{-2}	[243]
Sb-Ni/GDC-Ni/GDC	CH_4	650	0.55	> 230 at 0.6 A•cm^{-2}	[243]

2.2.7 Ni-free anodes

Another solution to prevent carbon deposition on the anode is to replace the Ni with a new catalyst that does not promote carbon forming reactions. Ni-free anode materials have been extensively studied for direct hydrocarbon-fuelled SOFCs, including (1) metal-based cermets such as Au [244] and Cu [40, 56], (2) perovskite-structured materials such as $La_{0.75}Sr_{0.25}Cr_{0.5}Mn_{0.5}O_3$ (LSCM) [245, 246], doped $SrTiO_3$ [247, 248], and BZCYYb [249].

Cu is a metal with good electronic conductivity and inactive to carbon forming reactions under hydrocarbons, which has been considered as a promising candidate to replace Ni. However, poor thermal stability and low electrochemical catalytic activity are the main issues for SOFC with Cu-based anodes [40, 41]. As the melting point of Cu and CuO are 1085°C and 1326°C, respectively, the sintering temperature of Cu-based anodes must be lower than the conventional Ni-based anodes (above 1300°C). At such temperatures, the densification process of the anode could be negatively affected [123, 250]. Therefore, it is not possible to prepare Cu cermet anodes through the same methods as Ni cermet anodes. Typically, Cu is incorporated into the densified ceramic support by impregnating a nitrate salt solution, followed by calcination to form the oxide [15, 56, 251]. Many researchers have found that the addition of ceria into Cu-based anodes can improve the cell performance when carbon-containing fuels are used [56, 91, 244, 252]. Cimenti et al. [203] suggested that adding zirconia into Cu/ceria resulted in better power output and stability in ethanol.

In order to provide sufficient catalytic activity for fuel oxidation, introducing another metal such as Co, Ru, and Fe into the Cu cermet anode has been investigated [203, 204, 253]. Dispersing a small amount of Ru (< 0.5%) into the Cu cermet was found to increase the cell performance and delay the anode deactivation by carbon accumulation in ethanol at 800°C [203]. The Co-Cu bimetallic catalyst on ceria was found to deliver significantly increased cell performance and no carbon accumulation in both CH_4 and n-butane, especially at higher operating temperatures [204, 254]. Kaur and Basu [253] reported a Cu-Fe/CeO_2-YSZ anode stably operated for 46 h in dry methane at 800°C. Figure 2-18 shows that cell ohmic resistance slightly increased after operation. Similar studies suggested that the increased ohmic resistance could be attributed to the sintering of Cu particles at high operating temperature [91, 255].

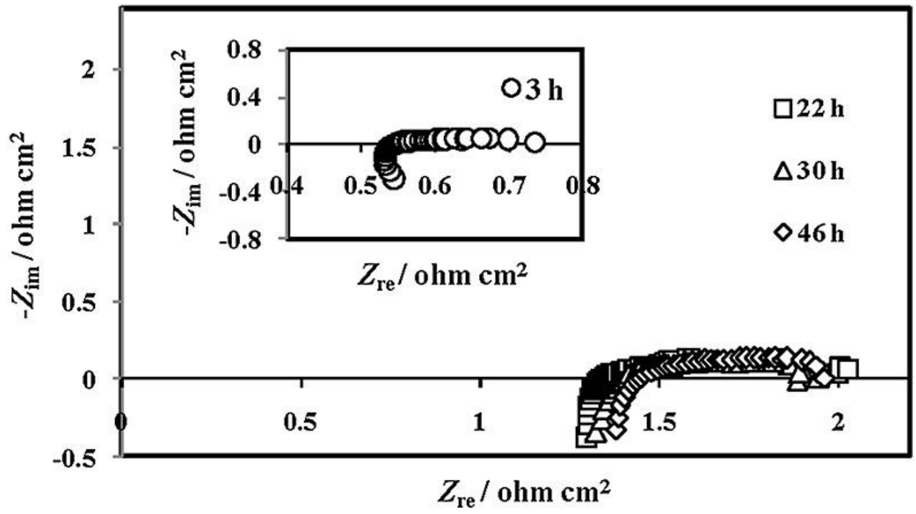

Figure 2-18: Electrochemical impedance spectra for Cu-Fe/CeO_2-YSZ anode-based SOFC as a function of time in dry CH_4 at 800°C. Reprinted from Ref. [253] with permission from John Wiley and Sons.

Perovskite oxides have a basic structure of ABO_3. Great efforts have been made to develop new anode materials by substituting or doping the A or B with another metallic element [256]. Perovskite oxides typically have weak catalytic activity for the carbon forming reaction and superior redox stability. Perovskite oxides have been used as Ni-free anode materials for hydrocarbon-fuelled SOFCs [245, 248, 257-259]. Tao et al. [245] reported that a LSCM anode material exhibited high catalytic activity towards methane oxidation, whereas it showed low electronic conductivity in reducing atmosphere. $SrTiO_3$ was found to be a good electronic conductor and possess high chemical stability and sulphur tolerance. Doped $SrTiO_3$ can give higher ionic conductivity, resulting in better cell performance under hydrocarbons [248, 258]. Although these perovskite-structured materials showed good performance with various hydrocarbon fuels, the main barrier of using perovskite oxides for the SOFC anode could be the complicated preparation process and relatively low conductivity compared with the cermet anode [41].

Table 2-6 shows some reported Ni-free anodes with enhanced carbon tolerance and their performances.

Table 2-6: Summary of the reported carbon resistant Ni-free anode materials.

Anode material	**Fuel**	**Temperature (°C)**	**P_{max} (W•cm^{-2})**	**Long-term test (h)**	**Ref**
Au/CeO_2-SDC	n-butane	650	0.05	–	[244]
Cu/CeO_2-SDC	n-butane	650	0.05	–	[244]
Cu/YSZ	n-butane	700	0.04	–	[56]
Cu/CeO_2-YSZ	CH_4	700	0.09	–	[56]
	n-butane		0.12	70 at 0.15 A•cm^{-2}	
Cu/$Zr_{0.35}Ce_{0.65}O_2$	Ethanol	800	0.385	10 (stopped)	[203]
Cu/GDC-GDC	CH_4	650	0.1	450 at 0.05 A•cm^{-2}	[260]
$Cu_{0.5}Co_{0.5}$/CeO_2-YSZ	n-butane	800	0.36	–	[204]
		700	0.14		
Cu-Co/CeO_2	CH_4	850	0.446	–	[254]
Cu-Fe/CeO_2-YSZ	CH_4	800	0.09	46 at 0.6 V	[253]
Cu-Ru/$Zr_{0.35}Ce_{0.65}O_2$	Ethanol	800	0.345	> 22	[203]
LSCM	CH_4/H_2O	950	0.3	–	[245]
$La_4Sr_8Ti_{11}Mn_{0.5}Ga_{0.5}O_{37.5}$	CH_4/H_2O	950	0.35	–	[247]
$Sr_{0.8}La_{0.2}TiO_3$	$CH_4/C_2H_6/C_3H_8$	800	0.55	> 80	[248]
BZCYYb	CH_4/H_2O	750	–	24 at 1.02 V (OCV)	[249]

Co-Fe/$PrBaMn_2O_{5+\delta}$	C_3H_8	850	1.32	–	[261]
	CH_4	700	–	> 500 at 0.2 A•cm^{-2}	
		850	0.57	–	
$PrBaMn_{1.5}Fe_{0.5}O_{5+\delta}$	CH_4/H_2O	850	0.34	–	[262]
		800	0.17	–	
		750	–	100 at 0.5 A•cm^{-2}	

2.2.8 Summary

In this chapter, the literature covering principles of carbon deposition on the Ni/YSZ anode, and its mitigation were discussed. Carbon deposition on the Ni-based anode occurs when the carbon formation rate is higher than the carbon gasification rate during the hydrocarbon fuel operation. Carbon nanowires are preferentially formed at lower temperatures, whereas dissolution of the deposited carbon takes place at higher temperatures. Carbon accumulation can result in rapid cell performance degradation and severe structural damage of the anode matrix, but carbon accumulation on the hydrocarbon-fuelled SOFC Ni cermet is inevitable. Therefore, great efforts have been made to develop new anode materials to mitigate carbon deposition.

Doping Ni catalysts with other metals (such as Au, Ru, Ag, Fe, Sn, and Zn) or metal oxides (such as CaO, BaO, and MgO) was found to be the most effective way to improve anode carbon tolerance and maximise power density. Typically, the dopant can be easily incorporated with the anode materials during cell fabrication by impregnating the dopant precursor into the bulk anode, followed by calcination of the sample. These doped anodes showed excellent cell performance and stability with methane and related hydrocarbon fuels.

Painting an additional catalyst layer on the outer anode surface was found to greatly increase the hydrocarbon reforming efficiency on the catalyst layer. The use of a reforming catalyst layer not only enhanced cell performance, but also suppressed carbon deposition by reducing the amount of hydrocarbon reacting at the Ni-based bulk anode. Material incompatibility could happen if different materials were used for bulk anode and catalyst layer, thereby the composition of the reforming catalyst layer must be carefully considered to ensure cell integrity during operation.

Ni-free anode materials such as Cu-based cermets and perovskite oxides showed good carbon resistance under hydrocarbon operation, but they still have some issues that need to be solved. Cu-based anodes typically require lower sintering temperatures than the other ceramic cell component. Furthermore, to provide sufficient catalytic activity for hydrocarbon operation, incorporating additional metallic catalyst with the copper is necessary. Many perovskite oxides have proven their potential to be used as anode materials for hydrocarbon-operated SOFCs due to superior redox stability and low activity to carbon formation. Nevertheless, complex material preparation and relatively low electrochemical activity are the main barriers for their commercial-scale applications.

Currently, the reported anode materials have been tested in laboratory-scale single cells with good performance, but the application in industrial-scale SOFC units remains a challenge. In order to be competitive in the industrial-scale SOFCs, further studies on SOFC stacks will be necessary.

CHAPTER 3: MATERIALS AND METHODOLOGY

3.1 Materials

The SOFC single cells used in this work were fabricated in-house from commercial materials using laboratory-scale equipment. All experimental materials used in this thesis are listed in Table 3-1.

Table 3-1: Materials used in the experiments.

Material	Purpose	Supplier
10Sc1CeSZ (d_{50}=0.6±0.1 μm)	SOFC electrolyte material	DAIICHI KIGENSO KAGAKU KOGYO
GDC-10 (d_{50}=0.1-0.4 μm)	Buffer layer between LSCF and 10Sc1CeSZ	Fuel Cell Materials
NiO (d_{50}=1 μm)	SOFC anode material	Hart Materials
$La_{0.6}Sr_{0.4}Cr_{0.2}Fe_{0.8}O_3$ (d_{50}=0.9 μm)	SOFC cathode material	Praxair
Tapioca starch	Pore former for anode	Rose
Ink vehicle	Cathode ink vehicle	Fuel Cell Materials
Dispex Ultra FA 4404	Anode slurry dispersant	BASF
Poly(vinyl alcohol), 87-90% hydrolysed (PVA)	Anode slurry binder	Sigma-Aldrich
Poly(ethylene glycol), average Mn 400 (PEG 400)	Anode slurry plasticiser	Sigma-Aldrich
Antifoam 204	Anode slurry defoamer	Sigma-Aldrich
Glycerol bidistilled, 99.5%	Anode slurry moisturiser	VWR^{TM}
DS001	Electrolyte slurry dispersant	Polymer innovations, Inc.
DF002	Electrolyte slurry defoamer	Polymer innovations, Inc.
PL005	Electrolyte slurry plasticiser	Polymer innovations, Inc.

WB4101	Electrolyte slurry binder	Polymer innovations, Inc.
$SnCl_2\cdot 2H_2O$	Anode dopant	Fisher Scientific
$AgNO_3$, 99.85%	Anode dopant	Acros Organics
$Cu(NO_3)_2\cdot 3H_2O$, 99%	Anode dopant	Acros Organics
$Fe(NO_3)_3\cdot 9H_2O$, 99.95%	Anode dopant	Sigma-Aldrich
Silver Conductive Paint	Current collector	Structure Probe, Inc.
DM-SIP-3063S (Ag paste)	Current collector & sealant	Dycotec Materials
Silver Conductive Paste	Current collector & sealant	Sigma-Aldrich
DAD-87 conductive adhesive	Current collector & sealant	Shanghai Research Institute of Synthetic Resins
Silver wire	Current collector	WIRES
Ceramabond 552	Sealing material	AREMCO
Silicone-Coated Polyester Film Roll	Tape casting substrate	Preservation Equipment Ltd
Hydrogen	Fuel gas	BOC
Methane	Fuel gas	BOC
Carbon dioxide	Fuel gas	BOC
Nitrogen	Fuel gas	BOC
Compressed air	Oxidant	BOC

3.2 Fabrication of anode-supported SOFC button cell with ScCeSZ-GDC bilayer electrolyte

Figure 3-1 shows the detailed preparation process of the anode-supported NiO/ScCeSZ single cells with ScCeSZ-GDC bilayer electrolyte and LSCF cathode.

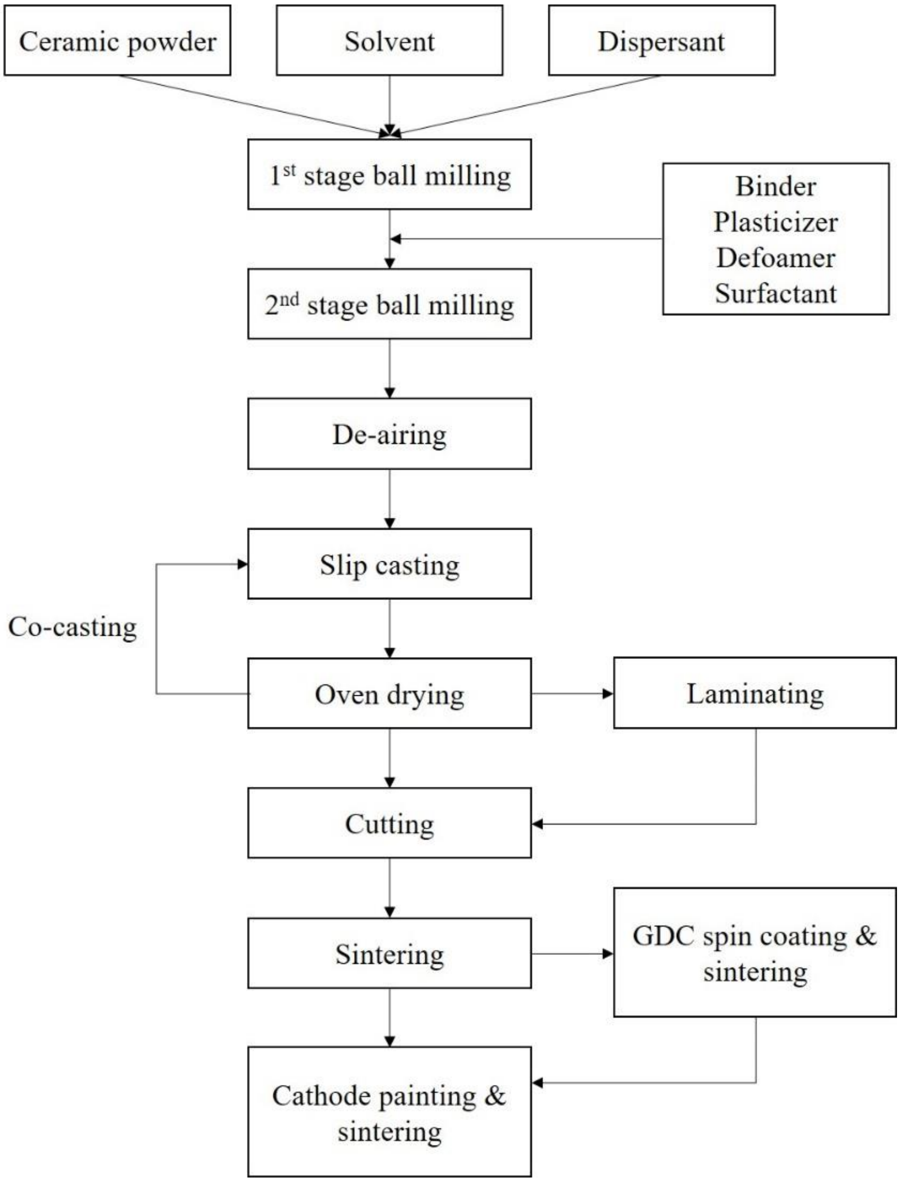

Figure 3-1: Process flow diagram of full cell fabrication.

To prepare the ScCeSZ-GDC bilayer electrolyte SOFC button cells, sequential tape casting is the first step to fabricate NiO/ScCeSZ half-cells without cathode layers. To laminate the ScCeSZ electrolyte layer with the GDC barrier layer, three different types of techniques were used, sequential casting, laminating, and spin coating, which will be explained in the following. Environmentally friendly and low-cost water-based slurries for tape casting and spin coating were successfully developed with the composition shown in Table 3-2 and Table 3-3. There are two types of anode slurries, anode functional layer (AFL) and anode substrate (AS). AS slurry is more viscous than AFL slurry due to the addition of pore former (tapioca starch) and less DI water. Another key difference between AS and AFL slurries is the resulted porosity of sintered layer, with the AS being more porous.

Table 3-2: Slurry compositions for ScCeSZ electrolyte and GDC barrier layer (50g batch).

Material	DI water	DS001	PL005	WB4101	DF002	Powder
Amount (g)	14	1	0.5	9.4	0.3	25

Table 3-3: Slurry compositions for NiO/ScCeSZ anode functional layer and anode substrate (100g batch).

Anode slurry	AFL	AS
DI water (g)	34.5	30.125
BASF Dispex Ultra (g)	1	1
NiO (g)	35.75	35.75
ScCeSZ (g)	19.25	19.25
Starch (g)	0	1.375
PVA (g)	4.5	6
PEG 400 (g)	2.5	3
Glycerol (g)	2	3
Antifoam 204 (g)	0.5	0.5

3.2.1 Tape casting

Fabrication of SOFC single cells mainly consists of three steps, NiO/ScCeSZ half-cell manufacturing, GDC barrier layer preparation, and $La_{0.6}Sr_{0.4}Cr_{0.2}Fe_{0.8}O_3$ (LSCF) cathode application. Slurries were prepared by ball milling materials in polyethylene bottles filled with around 30 vol% mixed size zirconia balls. It is noted that the ScCeSZ powder used for anode substrate slurry was calcined at 900°C in air to improve the compatibility of electrolyte and anode during co-firing. 2.5wt.% of tapioca starch (with respect to anode ceramic powders) was added to the anode substrate slurry to provide higher anode porosity after cell sintering.

Two-stage milling was used for slurry preparation, which follows the details shown in Table 3-4. Once materials were evenly mixed, the slurry was filtered and then transferred to another sample bottle. A de-airing process was carried out in a vacuum desiccator to remove air bubbles. De-aired slurry was cast on a silicone-coated polyester film with the order of ScCeSZ electrolyte, anode functional layer (AFL), and anode substrate (AS). The slurry casting thickness for each layer was 30, 150, and 2000 µm, respectively. Aqueous tape casting was carried out on a tape casting machine with a film applicator (MSK-AFA-III, MTI Corporation) shown in Figure 3-2 (a). Figure 3-2 (b) shows a thick and defect-free AS layer on a bi-layer tape composed of AFL and ScCeSZ electrolyte after casting. This observation indicates a stable ceramic dispersion and the success of the de-airing process.

Table 3-4: Ball milling details for slurry preparation.

Slurry type	**GDC & ScCeSZ**	**AFL & AS**
Dispersion milling	150 rpm for 24 h	150 rpm for 24 h
Binder & Plasticiser milling	150 rpm for 4 h	75 rpm for 24 h

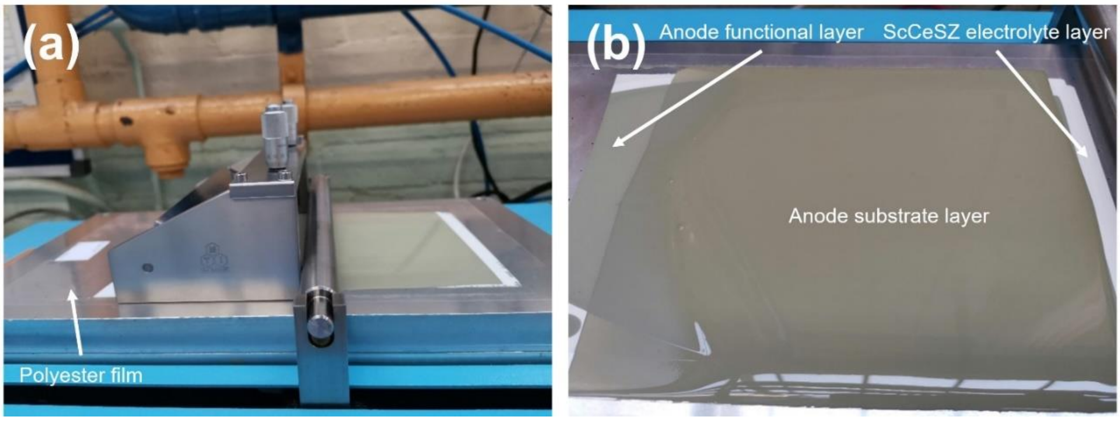

Figure 3-2: (a) Tape casting machine and film applicator used for sequential casting, (b) thick AS layer on a bi-layer green tape (AFL + ScCeSZ electrolyte) after casting.

As mentioned in Chapter 2.1, sequential tape casting incorporated with co-sintering is a widely accepted method to reduce the cell fabrication cost by minimising the fabrication steps of planar SOFC cells [99, 263, 264]. Multilayer green tape can be prepared by using this technique without further lamination or hot pressing. For a full cycle of sequential tape casting, the casting and drying process is repeated for several times to produce a uniformly distributed and stable multilayer structure. In this research thesis, the ScCeSZ electrolyte layer was the first layer cast on a polyester film with a casting gap of 30 µm. After drying at 60°C for 10 min, the AFL slurry was sequentially cast on the electrolyte green tape with a casting gap of 150 µm, followed by drying at 60°C for 15 min. Finally, the thick AS slurry, containing pore former, was cast on the bi-layer tape with a casting gap of 2000 µm. To prevent tape cracking, the thick tape was dried in air at 35°C for 24 h before shaping. The dried green tape was cut into circular disks with a diameter of 3.5 cm before co-sintering. After co-sintering, the obtained half cells have a diameter of 3 cm. For the ScCeSZ electrolyte, sufficient sintered density and ionic conductivity could be achieved above 1350°C [265-267]. In this work, all prepared half-cells were co-sintered at 1400°C for 4 h in air atmosphere. 10 Pa of sintering load was applied on the half-cell surface to ensure the cell flatness. The sintering profile of multilayer tapes is shown as Figure 3-3.

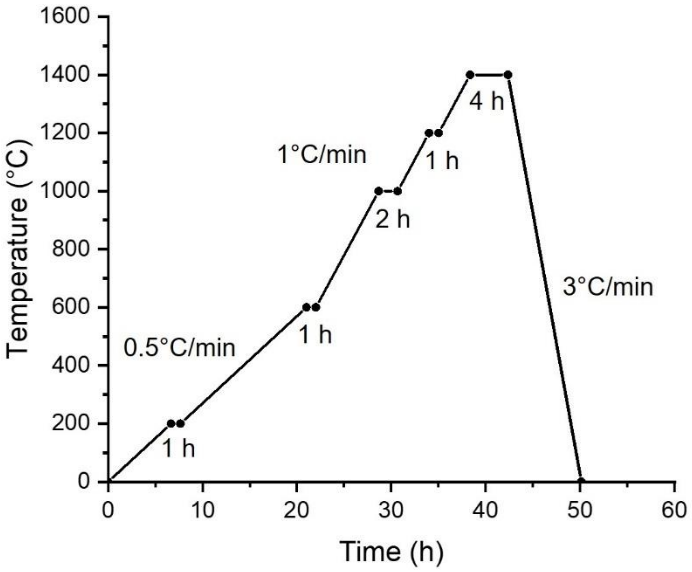

Figure 3-3: NiO/ScCeSZ half-cell sintering profile.

3.2.2 Lamination of multilayer tapes with hot press

In this work, the GDC, ScCeSZ, and AFL tri-layer tape was firstly prepared by sequential casting. To obtain a well laminated green tape without defects, the AS tape was cast separately on a polyester film. After drying, the tri-layer tape and AS tape were laminated using a hot press machine as shown in Figure 3-4. Tapes were cut into the same size before lamination to ensure consistent pressure was applied. Well-laminated multilayer tape was achieved at 80°C for 10 min with a pressure of 25 to 30 MPa. Prior to co-sintering, the multilayer tape was cut into circular half-cells with diameter of 3.5 cm.

Figure 3-4: Hot press machine for multiple tape lamination.

3.2.3 Spin coating

To prevent the chemical reaction between zirconium and strontium, a thin barrier layer of GDC was spin-coated on the ScCeSZ electrolyte of a sintered NiO/ScCeSZ half-cell. An ideal barrier layer should be thin and pore-free to effectively block the Sr cation migration LSCF cathode to ScCeSZ electrolyte via the diffusion of gaseous species [70, 268-271]. For the GDC films prepared by spin coating technique, the GDC films are typically sintered at a slightly lower temperature than the zirconia-based electrolyte to ensure no interdiffusion of Zr and Ce between the electrolyte and barrier layer [269]. However, a low sintering temperature usually produces porous GDC barrier layers, which would negatively influence the blocking effect of Sr cation migration. Plonczak et al. [272] reported that dense and pore-free GDC films can be obtained by performing multiple spin coating rounds. This is attributed to the filled open porosity in the GDC film by additional deposition rounds. Hence, this strategy was deployed in this work to reduce the porosity of GDC films prepared via spin coating.

As show in Figure 3-5, a vacuum-free spin coater (Ossila) with a circular sample holder was used for thin GDC layer preparation. The diameter of the customised sample holder was 3 cm, which was the same as the diameter of sintered half cells. The used GDC coating liquid had the composition shown in Table 3-2. The prepared Ni/ScCeSZ half-cell was placed in a sample holder with the ScCeSZ electrolyte side up. 150 µL GDC slurry was dropped onto the centre of the sample and spin-coated at 2500 rpm for 20s. The GDC layer was dried at 60°C for 10 min. The half-cell was coated three times and then sintered at 1200°C for 4 h with the sintering profile shown in Figure 3-6.

Figure 3-5: Vacuum-free spin coater used for thin GDC film fabrication.

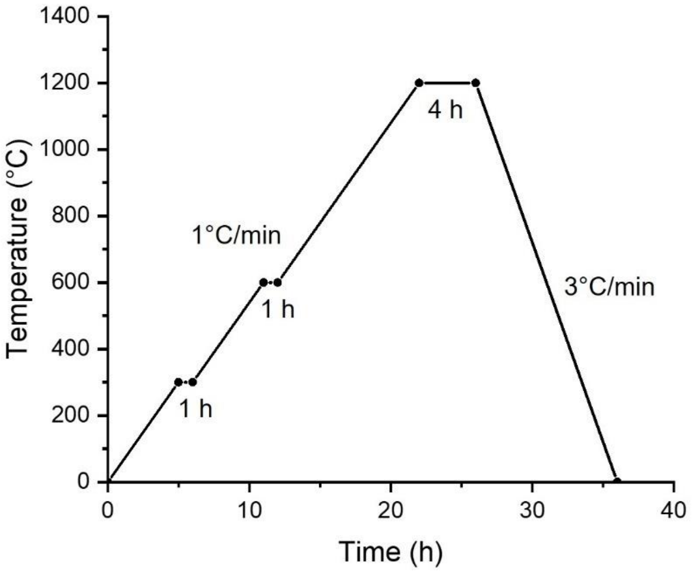

Figure 3-6: GDC layer sintering profile.

3.2.4 Cathode painting

The cathode ink was prepared by three-roll milling by evenly mixing ink vehicle and cathode powder for 30 min. A layer of GDC/LSCF (50:50) ink was first painted on the sintered GDC surface, followed by pure LSCF ink. The solid loading of both GDC/LSCF and pure LSCF cathode inks were 72.5wt.%. The prepared cathode inks were brush painted and then dried in air. Leng et al. [273] suggested that 975°C is an appropriate sintering temperature for LSCF cathodes, because the sintered cathode possesses higher porosity and significantly reduced polarisation resistance compared with cathodes sintered at higher temperatures. In this work, the cathode material was sintered at 975°C for 4 h. The sintering profile for the LSCF cathode is shown in Figure 3-7.

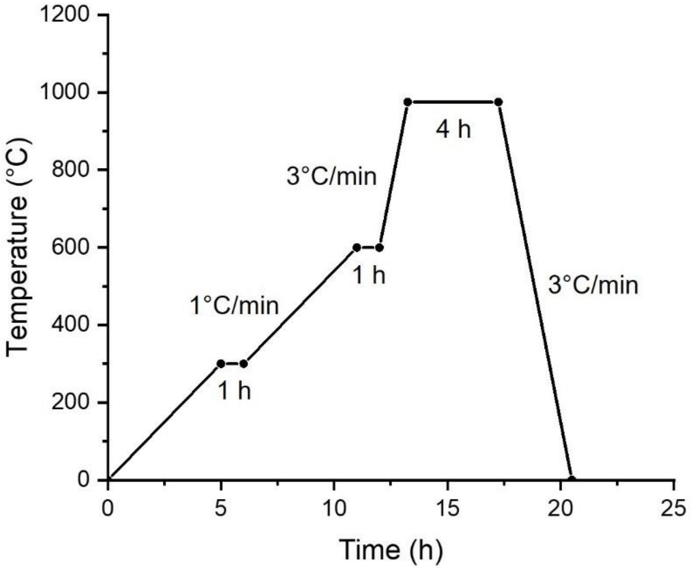

Figure 3-7: LSCF cathode sintering profile.

3.2.5 Single cell structure

Figure 3-8 shows the details of the cell components in a fabricated single cell, including material and thickness for each layer.

Cell component	Material used	Thickness
LSCF layer	LSCF powder, ink vehicle	15 µm
LSCF/GDC layer	LSCF/GDC powder (50:50wt%), ink vehicle	15 µm
GDC barrier layer	GDC powder, deionised water, DS001, WB4101, PL005, DF002	5 to 15 µm
ScCeSZ electrolyte layer	ScCeSZ powder, deionised water, DS001, WB4101, PL005, DF002	8 µm
Anode functional layer	NiO/ScCeSZ powder (65:35wt%), deionised water, Dispex Ultra FA 4404, Glycerol, PVA, PEG 400, Antifoam 204	30 µm
Anode substrate	NiO/ScCeSZ powder (65:35wt%), tapioca starch, deionised water, Dispex Ultra FA 4404, Glycerol, PVA, PEG 400, Antifoam 204,	650 µm

Figure 3-8: Details of each component in the fabricated SOFC single cells.

3.3 Anode material modification

As the prepared cell will be operated in dry methane reforming conditions, additional catalyst in the Ni-based anode is needed to enhance the efficacy of hydrocarbon reforming or carbon removal reactions. Therefore, anode material modification was carried out after the preparation of SOFC fuel cells. Sn-based catalysts have demonstrated excellent catalytic activity towards reforming organic compound and converting CO_2 to CO [82-84]. Silver, recognised for its robust catalytic activity in electro-catalysis process and CO oxidation [85]. Notably, no tendency of carbon deposition was found on the Ag catalyst during CO oxidation [86]. Cu has been used as the catalyst for water-gas shift reaction, CO oxidation, and electrooxidation of hydrocarbons, which exhibited low catalytic activity for C-C bond breaking and carbon forming reactions [87-91]. Introducing Fe into the catalyst offers redox capabilities, potentially accelerate the rate of carbon removal reactions. Under dry methane reforming conditions, FeO_x species can be formed during cell operation due to the presence of CO_2, further improving the carbon resistance of the Ni-based anode [92, 93].

Sn, Ag, Cu or Fe catalyst was introduced into the porous anode support by infiltrating with the precursor listed in Table 3-5. The precursor material was firstly dissolved in a mixture of ethanol and de-ionised water (50:50 vol%) and then ultrasonicated for 30 min. Dopant precursor was applied to the anode surface using a pipette and then dried at ambient temperature. After drying, the doped cells were calcined at different temperatures in air for 3 hours with a heating rate of 3°C/min to form metal oxides [180, 274-276]. Precursors used for each dopant and their calcination temperatures are shown in Table 3-5.

Table 3-5: Dopant precursors and their calcination temperatures [180, 274-276].

	Sn	**Ag**	**Cu**	**Fe**
Precursor	$SnCl_2 \bullet 2H_2O$	$AgNO_3$	$Cu(NO_3)_2 \bullet 3H_2O$	$Fe(NO_3)_3 \bullet 9H_2O$
Calcination temperature (°C)	600	500	400	400

After calcination, dopant precursors were thermally decomposed into SnO_2, Ag, CuO, and Fe_2O_3. The reactions occurring in the calcination process are shown in Table 3-6. During the hydrogen reduction process, SnO_2, CuO, and Fe_2O_3 were further reduced to Sn, Cu, and Fe, respectively.

Table 3-6: Thermal decomposition reactions of dopant precursors during calcination.

Dopant precursor	**Reaction**	**Ref**
$\mathbf{SnCl_2 \cdot 2H_2O}$	$4SnCl_2 \bullet 2H_2O(s) \rightarrow Sn_4(OH)_6Cl_2(s) + 6HCl(g)\uparrow + 2H_2O(g)\uparrow$ $Sn_4(OH)_6Cl_2(s) \rightarrow 3Sn(l) + SnOCl_2(s) + 3H_2(g)\uparrow + 2.5O_2(g)\uparrow$ $SnOCl_2(s) + 0.5O_2(g) \rightarrow SnO_2(s) + Cl_2(g)\uparrow$	[64, 274]
$\mathbf{AgNO_3}$	$2AgNO_3(s) \rightarrow 2Ag(s) + NO_3(g)\uparrow + NO(g)\uparrow + 1.5O_2(g)\uparrow$	[77, 277]
$\mathbf{Cu(NO_3)_2 \cdot 3H_2O}$	$4Cu(NO_3)_2 \bullet 3H_2O(s) \rightarrow Cu(NO_3)_2 \bullet 3Cu(OH)_2(s) + 6NO_2(g)\uparrow + 1.5O_2(g)\uparrow + 9H_2O(g)\uparrow$ $Cu(NO_3)_2 \bullet 3Cu(OH)_2(s) \rightarrow 4CuO(s) + 2NO_2(g)\uparrow + 3H_2O(g)\uparrow + 0.5O_2(g)\uparrow$	[275, 278]
$\mathbf{Fe(NO_3)_3 \cdot 9H_2O}$	$Fe(NO_3)_3 \bullet 9H_2O(s) \rightarrow Fe(NO_3)_3 \bullet 2H_2O(s) + 7H_2O(g)\uparrow$ $2Fe(NO_3)_3 \bullet 2H_2O(s) \rightarrow Fe_2O_3(s) \bullet 3H_2O + 6NO_2(g)\uparrow + H_2O(g)\uparrow$ $Fe_2O_3(s) \bullet 3H_2O \rightarrow Fe_2O_3(s) + 3H_2O(g)\uparrow$	[279, 280]

3.4 SOFC single Cell testing

3.4.1 Testing rig set-up

Prepared full cells were tested in a horizontal furnace (Vecstar) with an alumina cell holder. Silver wires were attached by silver paste on the surface of anode and cathode for current collection. After that, the single cell was sealed onto the alumina cell holder using silver paste, as shown in Figure 3-9 (c). After curing the silver paste at 100°C for 12 h in ambient air, the furnace was heated up with a heating rate of 3°C•min^{-1} to achieve 800°C for H_2 reduction. Once the furnace reached 800°C, the single cells were reduced in a gas mixture of 10 mL•min^{-1} H_2 and 20 mL•min^{-1} N_2 for 14 h. NiO was reduced to Ni by hydrogen during this process, which ensured the catalytic activity of the anode for further testing. The prepared single cells were further tested at 800, 750, and 700°C to compare the effect of operating temperature on the cell performance. The addition of N_2 into the fuel mixture reduced the partial pressure of hydrogen and prevented the formation of additional water vapour on the anode site, leading to slightly increased OCV values [281]. The details of gas flow on the anode side under hydrogen and simulated biogas fuels are shown in Table 3-7. Once all electrochemical measurements had been completed, the single cells were cooled to room temperature with 20 mL•min^{-1} N_2 supply at the anode side to prevent Ni oxidation while cooling down the furnace.

Table 3-7: Anode side gas flowrate under hydrogen and simulated biogas testing.

Gas flow (mL•min^{-1}) / Testing mode	H_2	N_2	CH_4	CO_2
Hydrogen	45	15	0	0
Simulated biogas	0	15	30	15

The testing rig set-up is shown as Figure 3-9. Fuel (hydrogen or simulated biogas) was supplied to the centre of the anode through a custom-made alumina cell holder. Exhaust gas left the testing tube through the exhaust pipes between cell holder and fuel inlet tube. Ceramabond 552 was used at the end of alumina testing tube to ensure gas-tightness during SOFC operation. Ambient air was used as oxidant at the cathode side during cell operation. Voltage and current produced from the cell operation were measured via silver wires. A type-K thermocouple was placed near the cell to measure the real-time cell operating temperature. Electrochemical characterisations of the tested cells were conducted using Solartron 1470E and 1455 FRA analysers (Solartron Analytical).

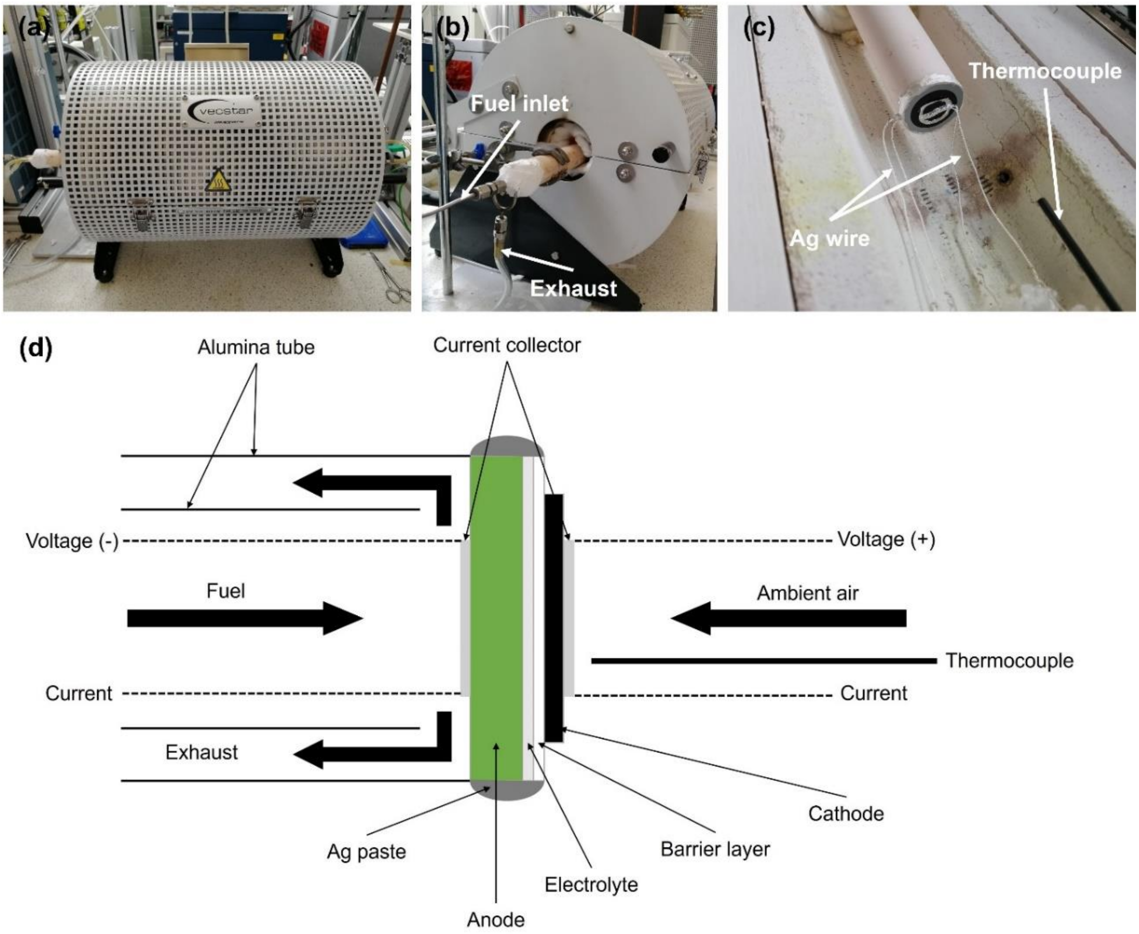

Figure 3-9: Horizontal furnace setup used for cell testing.

3.4.2 Selection of sealant

During the SOFC single cell testing, silver paste was not only used as current collector on both electrodes, but also as sealing material for mounting the cell on the cell holder in the horizontal furnace. Three conductive Ag pastes from different suppliers were used in the experiment. Figure 3-10 (a) shows the cell sealed by Ag conductive paste (Sigma-Aldrich) and then cured at 120°C, indicating many cracks across the surface of the Ag paste. This Ag paste cannot properly seal the Ag wires onto the cell or cell on the testing tube due to its weak binding property and low mechanical strength. Figure 3-10 (b) illustrates the cell attached to a testing tube with DM-SIP-3063S (Dycotec) after 800°C operation for 1 hour. Although the cell and silver wires were firmly attached, silver migration was still observed on the GDC surface. This phenomenon is attributed to Ag melting at high operating temperatures > 700°C, resulting in Ag migration and cell short-circuiting. Among all Ag pastes used, DAD-87 was found to be the most appropriate sealant for cell testing without silver melting and gas leaking issues at the SOFC operating temperatures (700-800°C).

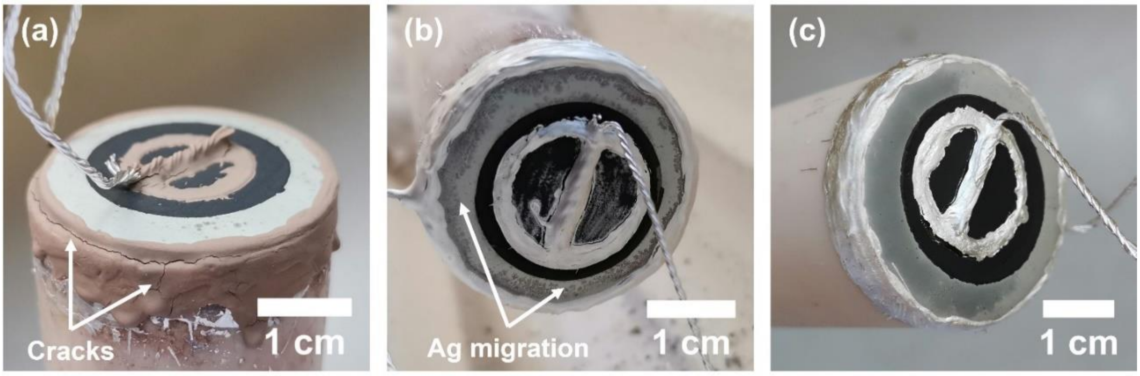

Figure 3-10: Sealing performances of different Ag pastes on testing tube, (a) Sigma-Aldrich, (b) DM-SIP-3063S, and (c) DAD-87.

3.5 Electrochemical characterisation

The electrochemical performance of the prepared single cells was characterised via OCV, polarisation curve, galvanostatic testing, and electrochemical impedance spectra (EIS). Once the testing rig heated to 800°C, OCV of the cell was measured at the initial stage to monitor gas-tightness and reduction status of NiO at the anode side. The polarisation curve is the plot of voltage output of the cell versus current density loading. This curve was obtained by measuring the current density with a potentiostat. The current density values were collected from OCV to 0.4 V with a voltage step size of 25 mV. Galvanostatic testing was performed on the prepared SOFC single cells to determine the operational stability under hydrogen and simulated biogas operations overtime. In this research thesis, the EIS measurement of the single cell with the effective cell area of 1.68 cm^2 was performed at 0.5 V, 0.7 V, and OCV. The frequency range of the alternative current (AC) impedance measurements ranged from 10^5 Hz to 0.01 Hz with a signal amplitude of 10 mV. Details of all methodologies will be discussed in this section.

3.5.1 Open circuit voltage (OCV)

The electrochemical characterisation of an SOFC single cell typically begins with an OCV measurement. For an SOFC operated with hydrogen as fuel, the potential of the cell at open circuit condition can be determined as follows:

$$E = E^0 + \frac{RT}{2F} ln\left(\frac{p_{H_2} * p_{O_2}{}^{\frac{1}{2}}}{p_{H_2O}}\right) \tag{22}$$

where p_{H_2}, $p_{O_2}{}^{\frac{1}{2}}$, and p_{H_2O} are the partial pressure of H_2, O_2, and H_2O at the electrolyte-electrode interface. R, T, F are the gas constant (8.135 J•K^{-1}•mol^{-1}), temperature (K), and Faraday's constant (96485 C•mol^{-1}), respectively. E^0 is the standard cell potential under standard conditions (25°C and 101.325 kPa), defined by the following equation:

$$E^0 = \frac{-\Delta G^0}{2F} = \frac{T\Delta S^0 - \Delta H^0}{2F} \tag{23}$$

where ΔG^0 is the Gibbs free energy change of the cell reaction under the standard condition, which is equal to -237.2 kJ•mol^{-1} at 25°C. T is the temperature (K), ΔS^0 is the entropy change of the cell reaction under standard condition (-163.11 J•mol^{-1}•K for liquid water formation and -44.33 J•mol^{-1}•K for gaseous water formation), and ΔH^0 is the enthalpy change of the cell reaction under standard conditions (-285.838 kJ•mol^{-1} for liquid water formation and -241.827 kJ•mol^{-1} for gaseous water formation) [282]. The OCV of an H_2/O_2 fuel cell operated at different temperatures can be directly calculated using Eq.(23). Table 3-8 shows the calculated Gibbs free energy and standard cell potential at different temperatures. It is very clear that the increase in temperature has a negative impact on the cell potential for a H_2/O_2 fuel cell.

Table 3-8: Gibbs free energy of the cell reaction and standard cell potential at different temperatures.

Temperature (K)	**ΔG^0 (kJ•mol^{-1})**	**E^0 (V)**
298	237.2	1.229
973	198.7	1.030
1023	196.5	1.018
1073	194.3	1.007

3.5.2 Polarisation curve

The polarisation curve is the plot of operating voltage over the operating current density for a fuel cell, which is obtained by controlling cell voltage and cell current by a potentiostat/galvanostat during fuel cell operation. During the measuring process, the response of the current can be determined by slowly stepping the voltage up or down on the potentiostat. The power density can be determined from the polarisation curve by multiplying the cell voltage and current density [3, 7, 10]. As shown in Figure 3-11, the polarisation curve demonstrates the voltage losses relative to the ideal cell voltage. The actual open circuit voltage of a fuel cell will be lower than the theoretical value due to gas crossover through gas leaks and internal leak currents. There are three main contributions of voltage losses during fuel cell operation:

- Activation losses are caused by the activation energy required to drive the electrochemical reactions at the electrode-electrolyte interfaces.
- Ohmic losses are caused by the ionic resistance in the electrolyte and electrodes, electronic resistance in electrodes, current collector, and interconnect, as well as contact resistances.
- Concentration losses are attributed to the mass transfer resistances of reactants and reacting products in the electrodes.

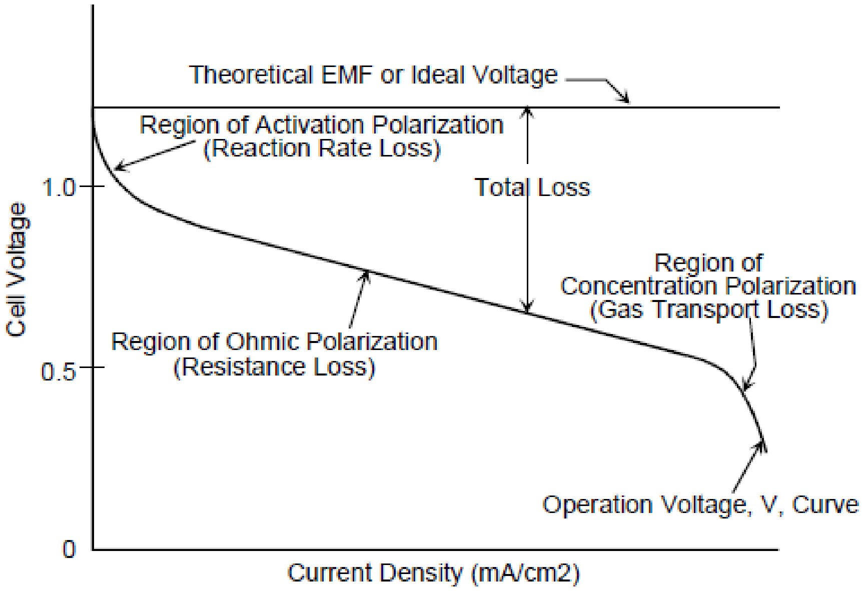

Figure 3-11: A typical polarisation curve for fuel cell [283].

3.5.3 Electrochemical impedance spectroscopy (EIS)

EIS is a sensitive tool that can in-situ characterise the processes that occur in a fuel cell. EIS measurements can help identify the reaction kinetic, ohmic, ionic, contact and diffusion resistances, as well as the species transport limitations in the fuel cell system. This method uses a small sinusoidal perturbation potential to the fuel cell current across a range of frequencies, f, with the resulting AC signal being collected by the frequency response analyser. The obtained AC signal will have a phase shift between AC current and voltage signal, indicating effective capacitances and inductances attributed to the various process occurring in the cell [9, 284]. The impedance measurement can be taken over the frequency ranging from 10^{-4} to 10^{6} Hz, enabling the study of SOFC loss processes with various time constants [285]. The general expression of impedance can be described as the complex ratio of potential and current contributions:

$$Z = \frac{V(t)}{I(t)} \tag{24}$$

Z represents the impedance of the circuit, in units of Ohms (Ω). Different from the resistance of a DC circuit, the impedance of an AC circuits is related to the frequency of the applied signal. As the measurements of impedance were made by applying a sinusoidal voltage, the responses in potential and current can be given as Eq.(25) and Eq.(26), respectively.

$$V(t) = V_0 * cos(\omega t) \tag{25}$$

$$I(t) = I_0 * cos(\omega t + \varphi) \tag{26}$$

where V_0 is the voltage magnitude and ω is the angular frequency ($\omega = 2\pi f$). φ is the phase shift in the unit of degrees (°). Therefore, the expression of impedance can be described as follows:

$$Z = \frac{V_0 * cos(\omega t)}{I_0 * cos(\omega t + \varphi)} = Z_0 \frac{cos(\omega t)}{cos(\omega t + \varphi)} \tag{27}$$

According to Euler's formula shown in Eq.(28), it is possible to express the impedance as Eq.(29):

$$exp^{j\varphi} = \cos\varphi + j * \sin\ \varphi \tag{28}$$

$$Z = \frac{V_0 * exp^{j\omega t}}{I_0 * exp^{(j\omega t - j\varphi)}} = Z_0 * exp^{j\varphi} = Z_0 * (\cos\varphi + j * \sin\varphi) \tag{29}$$

where j is the imaginary unit, $j = \sqrt{-1}$. The real part of impedance, Z_{real}, is described as $Z_0 \cos\varphi$ and the imaginary par of impedance, $Z_{imaginary}$, is described as $Z_0 * j * \sin\varphi$. Figure 3-12 is a typical Nyquist plot for an electrode-supported SOFC with a thin electrolyte. The real part and imaginary part of impedance data are plotted on x-axis and y-axis, respectively. There are two intersection points on the Z_{real} axis. For an electrode-supported SOFC, the left intersection point is the value of ohmic resistance (R_{ohm}), which is mainly contributed by the ionic resistance of electrolyte, electronic resistance of electrodes and current collector. The second intersection point is the sum of ohmic resistance, R_{ohm}, and electrode polarisation resistance, R_p. The electrode polarisation resistance is attributed to the activation and concentration losses of SOFC anode and cathode [3, 9, 286]. Typically, the predominant contribution of the overall impedance comes from electrode processes, with an insignificant contribution from the thin electrolyte. In an SOFC single cell, these electrode processes consist of charge transfer at the electrode/electrolyte interface (also known as activation polarisation) and gas diffusion in the porous electrodes (referred to as concentration polarisation). As shown in Figure 3-12, two semicircles were identified in this example. For the anode-supported button cell used in this work, the high-frequency semicircle is related to the contribution from the anode, specifically the charge transfer at the anode/electrolyte interface. Conversely, the semicircle in the low-frequency domain represents the contribution from the cathode, mainly oxygen diffusion within the cathode. However, there can be some overlapped contributions (such as gas conversion in the anode) on the Nyquist plot [287].

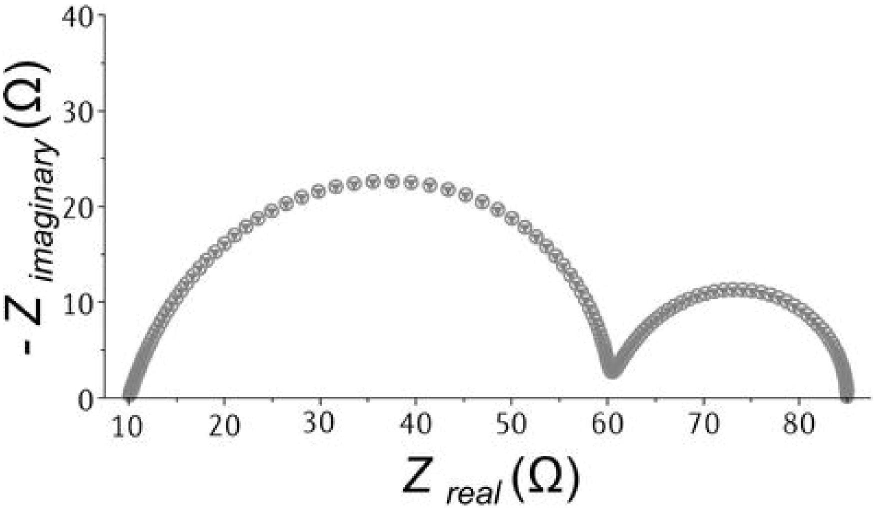

Figure 3-12: Sample of a Nyquist plot [286].

3.5.4 Distribution of relaxation times (DRT)

The DRT method is a well-established technique for complex fuel cell impedance spectra analysis, which can deconvolute the measured impedance spectra into several individual processes [288-290]. This technique has also been extensively used to investigate the degradation behaviour of SOFC single cells and stacks [291-295]. In this work, the measured EIS data were processed by using the MATLAB Toolbox DRTTOOLS [296]. The EIS data was deconvoluted by applying a DRT function that based on Tikhonov regularisation with a regularisation parameter of 0.001. Figure 3-13 shows the detailed setup of DRTTOOLS for the collected EIS data in the present work. Prior to the DRT analysis, the residual of the real and imaginary parts of the obtained EIS data were checked by the Kramers-Kronig validity test with the Lin-KK Tool (Karlsruhe Institute of Technology). If the residuals of EIS data used in this work were below 1%, they suggested a relatively stable system and high-quality impedance spectra measurements.

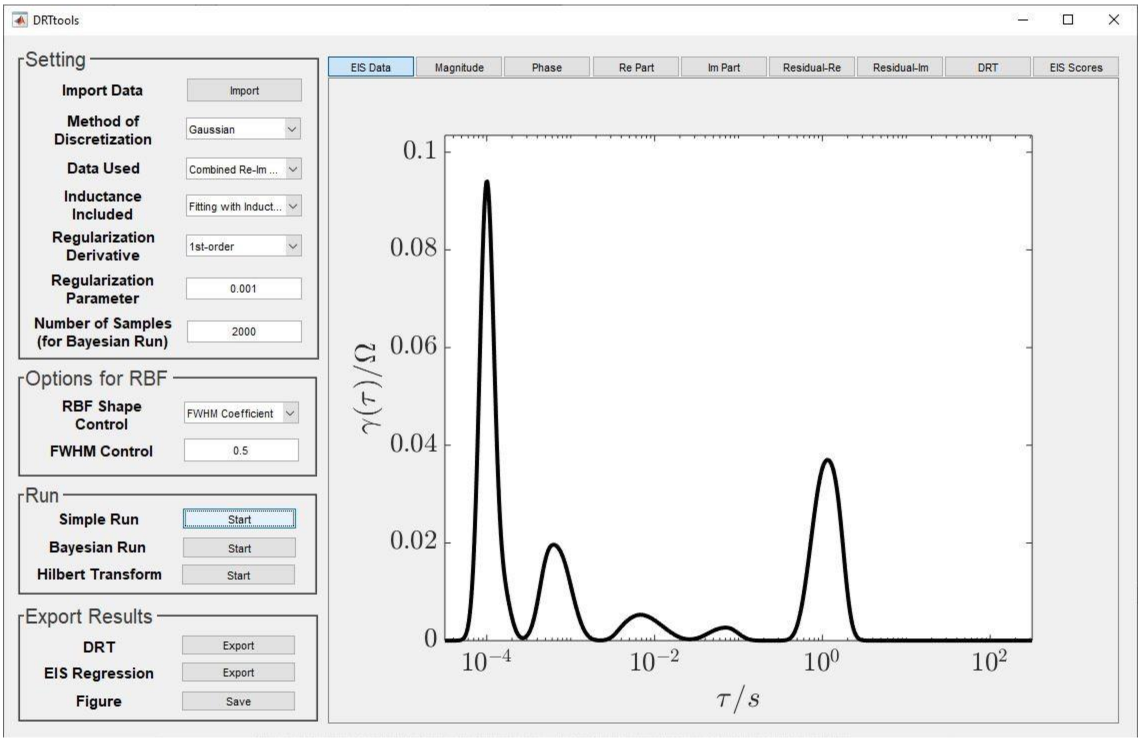

Method of Discretization	Gaussian
Data Used	Combined Re-Im ...
Inductance Included	Fitting with Induct...
Regularization Derivative	1st-order
Regularization Parameter	0.001
Number of Samples (for Bayesian Run)	2000
RBF Shape Control	FWHM Coefficient
FWHM Control	0.5

Figure 3-13: DRTTOOLS in MATLAB, developed by Wan et al. [296].

3.6 Physical characterisation

3.6.1 Scanning electron microscopy (SEM)

SEM can produce high-resolution images of the specimen surface with its structural detail. The prepared specimen is placed in a vacuum chamber of the equipment. The electron source produced from the electron gun is condensed and demagnified by two lenses to a focused spot on the surface of the sample. The sample is scanned by the incident electron beam and the electrons emitted from the sample surface are collected and amplified to produce a video signal [297]. In this work, microstructure analysis of the cells was performed by using tabletop microscopes Hitachi TM3030 Plus, Jeol JSM-6060, and Philips XL30 FEG ESEM with a voltage of 15 to 30 kV. SEM was conducted on the prepared SOFC single cells before and after cell testing to obtain the surface morphology of electrodes and cross-sections. Moreover, both back-scattered electrons (BSE) and secondary electrons (SE) were used for sample analysis.

3.6.2 Energy-dispersive X-ray spectroscopy (EDS)

X-ray fluorescence is generated from the atoms when the sample surface is scanned by the SEM electron beam. The EDS system collects and plots the X-ray signal as energy peaks. Because of the unique atomic structure, each element on the sample surface can be identified by its energy distribution peak. Data produced from the EDS system is used to generate a surface elemental map, obtain elemental quantification, and the spectrum of X-rays collected at each energy level on the specimen surface [9]. EDS (Quantax, Bruker) analysis was carried out by using an energy dispersive X-ray spectrometer attached with the tabletop microscope. Elemental mapping, line-scan, and quantification results were collected from the EDS analysis.

3.6.3 X-ray diffraction (XRD)

X-ray diffraction is a common technique to determine the crystal structure of a material, which produces an average pattern across the area measured. When X-rays impinge on a sample in a given angle, θ, the crystal planes in the material allows diffraction to occur. Radiation is reflected at the upper surface and from the crystal planes below and so forth. Bragg's law, Eq.(30), describes the diffraction [298].

$$2dsin\theta = n\lambda \qquad (30)$$

where d is the interplane spacing, θ is the angle between the sample surface and incident X-rays, n is the diffraction order, and λ is the given wavelength of the incident X-rays. In this thesis, XRD was used to identify the phase change on the prepared GDC and ScCeSZ films after sintering. Diffraction patterns were collected by using Cu Kα radiation within the scan range of $15° \leq 2\theta \leq 80°$ and a scan rate of 1.2°/min on an X-ray diffractometry (Bucker D8 diffractometer).

3.6.4 X-ray photoelectron spectroscopy (XPS)

XPS is a powerful characterisation technique for identifying the elemental composition of a material. It is an extremely surface-sensitive technique operated under ultra-high vacuum condition, it provides detailed chemical information of the sample surface [298]. In this work, XPS was used for determining the elemental composition and carbon deposition on the anode surface after 120 h of biogas exposure. XPS analysis was performed on a Thermo Fisher Scientific NEXSA spectrometer at HarwellXPS. The prepared samples were analysed in a high vacuum system with a monochromatised Al Kα source with the photon energy of 1486.6 eV. Charge neutralisation of the characterised sample was obtained by using both low energy electrons and argon ions. After measurement, sample charging was corrected by using the C 1s peak at 284.8 eV as the reference. The obtained XPS data were fitted and quantified for Ni, C, Sn, Ag, Cu, and Fe by using CasaXPS software.

3.6.5 Raman spectroscopy

Raman spectroscopy is a fast and non-destructive characterisation technique that uses the vibration in molecules and crystals to identify a material. Due to the shallow penetration depth (around 1 μm) of Raman spectroscopy, it is suitable for thin film analysis. A monochromatic laser light with a known wavelength illuminates the sample. Part of the radiation interacts with the sample and is scattered. Raman spectrometer collects the light either directly backscattered or scattered at 90° to the incident beam [298]. In this study, Raman spectroscopy was used for determining the type of deposited carbon on the biogas tested SOFC anode surface. Raman spectra were collected on a Renishaw InVia Raman microscope with a 532 nm laser. Samples were characterised under 50 magnifications and 5% laser power.

3.6.6 Thermogravimetric analysis (TGA)

Thermo-gravimetric analysis records the change of sample weight loss as a function of time and temperature. The main purpose of performing TGA is to determine the suitable organic removal temperature for NiO/ScCeSZ half-cell sintering. TGA was conducted on the TG209F1 (NETZSCH) equipment under an airflow of 50 mL•min^{-1} from 25 to 900°C at a rate of 5/10°C•min^{-1}.

3.6.7 Rheological characterisation

Rheology is the study of the behaviour of liquid or gas flow. The rheological properties of the prepared aqueous slurries were characterised by a Discovery HR-1 Hybrid Rheometer (TA Instruments) at 25°C. A parallel plate with diameter of 40 mm was used to perform the measurements. The de-aired slurry was added to the shear plate and then pre-sheared at 5 s^{-1} for 60 s, followed by resting for 60 s. Viscosity curves were measured by increasing the shear rate logarithmically in 120 s from 5 to 500 s^{-1}.

CHAPTER 4: OPTIMISATION OF SCCESZ-GDC BI-LAYER ELECTROLYTE SOFC SINGLE CELL FABRICATION

4.1 Overview

In this work, anode supported NiO/ScCeSZ single cells with ScCeSZ-GDC bi-layer electrolyte were fabricated via wet ceramic coating techniques including tape casting, spin coating, and ink painting. The fabricated cells were characterised by SEM and EDS analyses to ensure the ScCeSZ-GDC bi-layer electrolyte was dense. The sintering process of half-cells was optimised by adjusting heating rate, sintering temperature, and the use of a sintering load to reduce the cell warpage.

4.2 Water-based slurry development for tape casting

Slurry preparation is one of the most important steps for solid oxide cell (SOC) half-cell fabrication, as it influences both the cell manufacturing, as well as the electrochemical performance [105, 111]. Compositions of ScCeSZ and GDC electrolyte slurries were successfully developed with the ingredients shown in Table 3-2. Anode slurries were carefully developed to achieve high quality anode-supported single cells. The cells had two anode layers, a dense anode functional layer (AFL) and a porous anode substrate (AS). The addition of tapioca starch in the AS slurry not only increased the porosity of the anode, but also increased the viscosity, which was beneficial for thick ceramic film casting. Anode slurries with different NiO:ScCeSZ mass ratios were prepared, 60:40 (AFL1, AS1, and AS2) and 65:35 (AFL2, AS3, and AS4). For the anode slurries with the 60:40 ratio, all tapes cracked after drying at various temperatures. However, AFL2 and AS4 with the 65:35 ratio was found to provide a more flexible and smoother thick anode tape on either PET film or multilayer tapes after optimising the amount of binder (PVA), plasticiser (PEG 400), and moisturiser (glycerol) in the slurries. Table 4-1 shows the compositions of different water-based slurry for anode functional layer and anode substrate.

Table 4-1: Slurry composition for anode functional layer and anode substrate (100g batch).

	Anode functional layer		**Anode substrate**			
Sample ID **Material (g)**	AFL1	AFL2	AS1	AS2	AS3	AS4
DI water	35.4	34.5	31.325	30.125	31.325	30.125
BASF Dispex Ultra	1	1	1	1	1	1
NiO	33	35.75	33	33	35.75	35.75
ScCeSZ	22	19.25	22	22	19.25	19.25
Starch	0	0	1.375	1.375	1.375	1.375
PVA	3.6	4.5	4.8	6	4.8	6
PEG 400	2.5	2.5	3	3	3	3
Glycerol	2	2	3	3	3	3
Antifoam 204	0.5	0.5	0.5	0.5	0.5	0.5
Result	Cracked	✓	Cracked	Cracked	Cracked	✓

4.3 Rheological properties of the developed slurries

Figure 4-1 shows the plot of viscosity versus shear rate and shear stress versus shear rate for the slurries developed. Both AFL and AS slurries showed typical pseudoplastic behaviour in which viscosity decreases with an increase of shear rate. Pseudoplastic behaviour is preferable for slip casting thick layers, because the slurry flows smoothly with the decreasing viscosity during the doctor blade's displacement. Once stress is applied on the slurry by the doctor blade, the shear rate decreases and then the slurry viscosity increases. Higher viscosity can prevent ceramic particle sedimentation and maintain a homogeneous distribution of organic additives during the drying process [105]. Compared with the anode slurries, the viscosity of GDC and ScCeSZ slurries show fluctuation when the shear rate is between 10 and 50 s^{-1}, indicating that the slurry is less likely to be as stable as the developed anode slurries during casting. Due to the thickness of electrolyte layers (5 to 10 μm), the drying duration of the electrolyte layers (10 minutes) is much shorter than that of the anode layers (0.5 to 24 hours). Therefore, particle settling, or inhomogeneous drying is negligible for GDC and ScCeSZ slurries.

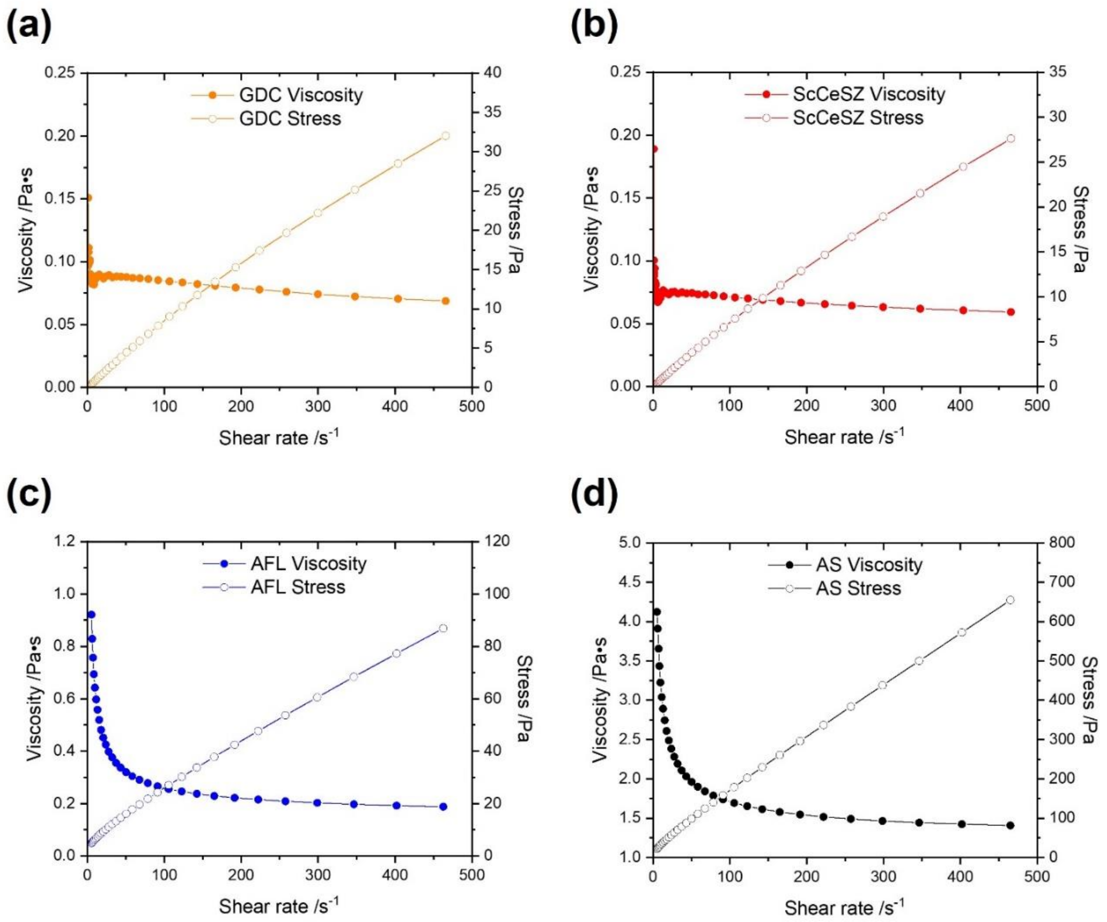

Figure 4-1: Rheological behaviour of the developed (a) GDC, (b) ScCeSZ, (c) AFL, and (d) AS slurries.

4.4 Drying temperature optimisation for the multilayer tape

The drying temperature is a crucial factor that affects the quality of the multilayer tape. For the thin electrolyte and anode functional layers, the drying process is relatively simple as the casted slurry can be dried in 10 to 15 minutes at 60°C showing no defects as results. Nevertheless, the drying kinetics of the thick anode substrate is more complicated, consisting of two stages with a constant drying rate (stage 1) and a falling drying rate (stage 2) [109, 130]. The constant drying rate at stage 1 is mainly controlled by the drying temperature for a thick casting layer. The mass loss of the wet tape is constant at stage 1, whereas the drying kinetics are then controlled by the diffusion of liquid and vapour at stage 2. In this study, drying temperature and time are the key variables investigated. To find the suitable drying temperature for the thick anode substrate, three different drying temperatures were used, 40, 35, and 30°C. Table 4-2 and Figure 4-2 show the resulting quality of the thick anode substrate tape at different temperatures.

Table 4-2: Drying temperature and time for the thick anode substrate tape.

Drying temperature (°C)	**40**	**35**	**30**
Drying time (h)	12 to 15	20 to 24	45 to 50
Result	Cracked	√	Cracked

Figure 4-2 (a), (b), and (c) show the green tapes dried at 40°C for 15 h, 35°C for 24 h, and 30°C for 48 h, respectively. The green tape that dried at higher temperature had a long crack in the centre of the tape. Under a high drying temperature, the water evaporation rate on the tape surface is faster than in the middle, leading to uneven shrinkage of the tape in the vertical direction. The tape shown in Figure 4-2 (c) dried at 30°C for 48 h. It showed minor cracks and pinholes across the surface, as can be observed. As the prepared slurry is a suspension system, a slow drying rate could result in the sedimentation of solid contents whilst drying, leading to further structural failure on the dried green tape. The optimum drying rate for the anode substrate slurry was then achieved at 35°C for 24 h. Figure 4-2 (b) indicates the obtained green tape had a smooth surface without defects. Subsequent experiments confirmed the reproducibility of these results when maintaining the specified drying temperature and duration.

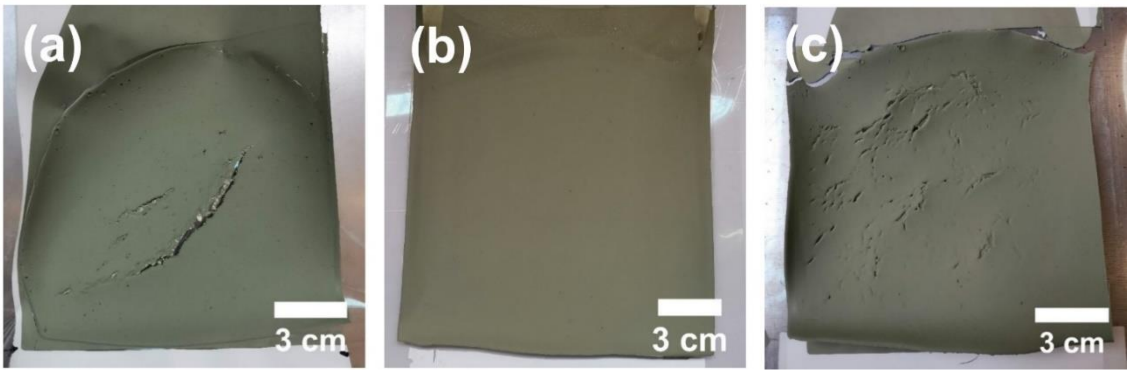

Figure 4-2: Appearance of the sequential cast multilayer tapes with (a) 40°C drying for 15 h, (b) 35°C drying for 24 h, and (c) 30°C drying for 48 h.

4.5 Optimisation of ScCeSZ-GDC bi-layer electrolyte preparation

4.5.1 Sequential casting of GDC and ScCeSZ layer

In this work, sequential casting of GDC and ScCeSZ was the first approach in fabricating bi-layer electrolyte single cells. The GDC film was the first layer casted on the PET film followed by ScCeSZ, AFL, and AS. The half-cells were obtained after co-sintering at 1400°C. Both GDC and ScCeSZ layers were found to easily delaminate from the sintered half-cell when the casting thickness of the GDC film was larger than that of the ScCeSZ film. To minimise the electrolyte resistance, the electrolyte thickness should be fabricated as low as possible. However, the minimum casting height for doctor blade was limited at 20 µm, hence, a GDC film with 20 µm casting thickness was chosen to match the ScCeSZ film with a 30 µm casting thickness.

The SOFC single cells prepared via this approach has a structure shown in Figure 3-8. Figure 4-3 (a) to (c) exhibit the co-sintered GDC layer on the prepared half-cells. Some defects and grainy surface can be seen on the sample surface. More severely, the GDC layer on some areas of the cell can be removed by tweezers. This could be attributed to the different shrinkage behaviour of GDC and ScCeSZ during the co-sintering stage [299, 300]. To further investigate the electrolyte of the prepared single cells, SEM was performed on the GDC surface and half-cell cross-section.

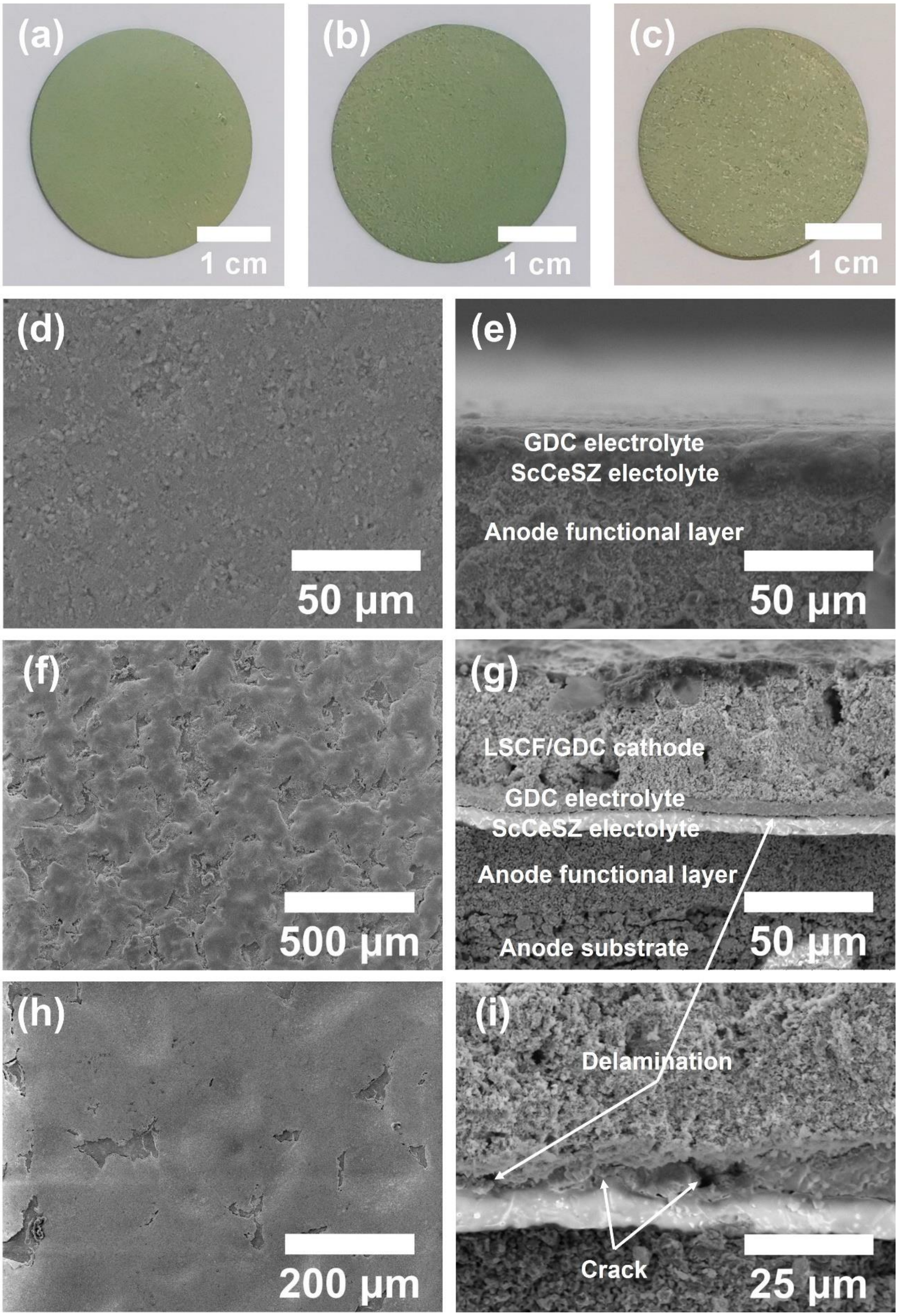

Figure 4-3: (a, b, c) co-sintered GDC layer on the half-cells, (d) surface morphology of GDC film before sintering, (e) cross-section of the pre-sintering green tape, (f, h) microstructure of the 1400°C sintered GDC surface on half-cell and (g, i) cross-section of the ScCeSZ-GDC bi-layer electrolyte full cell prepared by sequential casting.

As shown in Figure 4-3 (f) and (h), cracks developed in the GDC layer after co-sintering at 1400°C. Additionally, cross-sectional images presented in Figure 4-3 (g) and (i) show clear gaps between these two layers, further confirming the lack of adhesion between them. However, no crack and/or deamination was observed from the pre-sintering GDC surface and cross-section of the pre-sintering multilayer tape shown in Figure 4-3 (d) and (e). This suggests that the delamination occurring between the GDC layer and the ScCeSZ layer during sintering process. Such defects in the ScCeSZ-GDC bi-layer electrolyte will have negatively impact on the adhesion of adjacent electrolyte layers and cell mechanical strength. Moreover, the ionic conductivity of the bi-layer electrolyte can be reduced, resulting in impaired performance of the cell [301]. For the GDC and ScCeSZ powders used in this research thesis, the thermal expansion coefficients were measured by dilatometer, showing 13.84×10^{-6} and 10.88×10^{-6} K^{-1} within the temperature range of 298K and 1073K, respectively [302]. Therefore, the shrinkage of the GDC layer during co-sintering is higher than that of the ScCeSZ layer, leading to shear stress between two layers.

As cracks were identified on the GDC side of the sintered half-cells, EDS characterisation was performed to provide insights into the chemical composition of the GDC layer surface on the sintered half-cells. The EDS analysis results shown in Figure 4-4 further confirm the failure of the ScCeSZ-GDC bi-layer electrolyte fabrication due to the presence of Zr on the surface of the sintered GDC layer. The detected Zr on the GDC side of the sintered half-cell could be attributed to the large holes on the GDC layer and the diffusion of Zr from ScCeSZ layer. The appearance of large holds on the sintered GDC layer was due to greater shrinkage of GDC layer compared to the ScCeSZ layer during co-sintering. The formation of (Zr, Ce)O_2-based solid solutions and inter-diffusion between ZrO_2 and CeO_2 can occur during co-sintering process above 1200°C [303, 304]. Detailed interfacial analysis of all prepared samples is provided in Chapter 4.5.6 to give more insights into the interaction between GDC and ScCeSZ layers. Due to defects on the GDC layer and the delamination issue with the adjacent ScCeSZ layer, the GDC layer prepared by sequential casting on the ScCeSZ layer was not dense enough. This prevented it from effectively blocking the chemical reaction between zirconia and strontium during LSCF sintering.

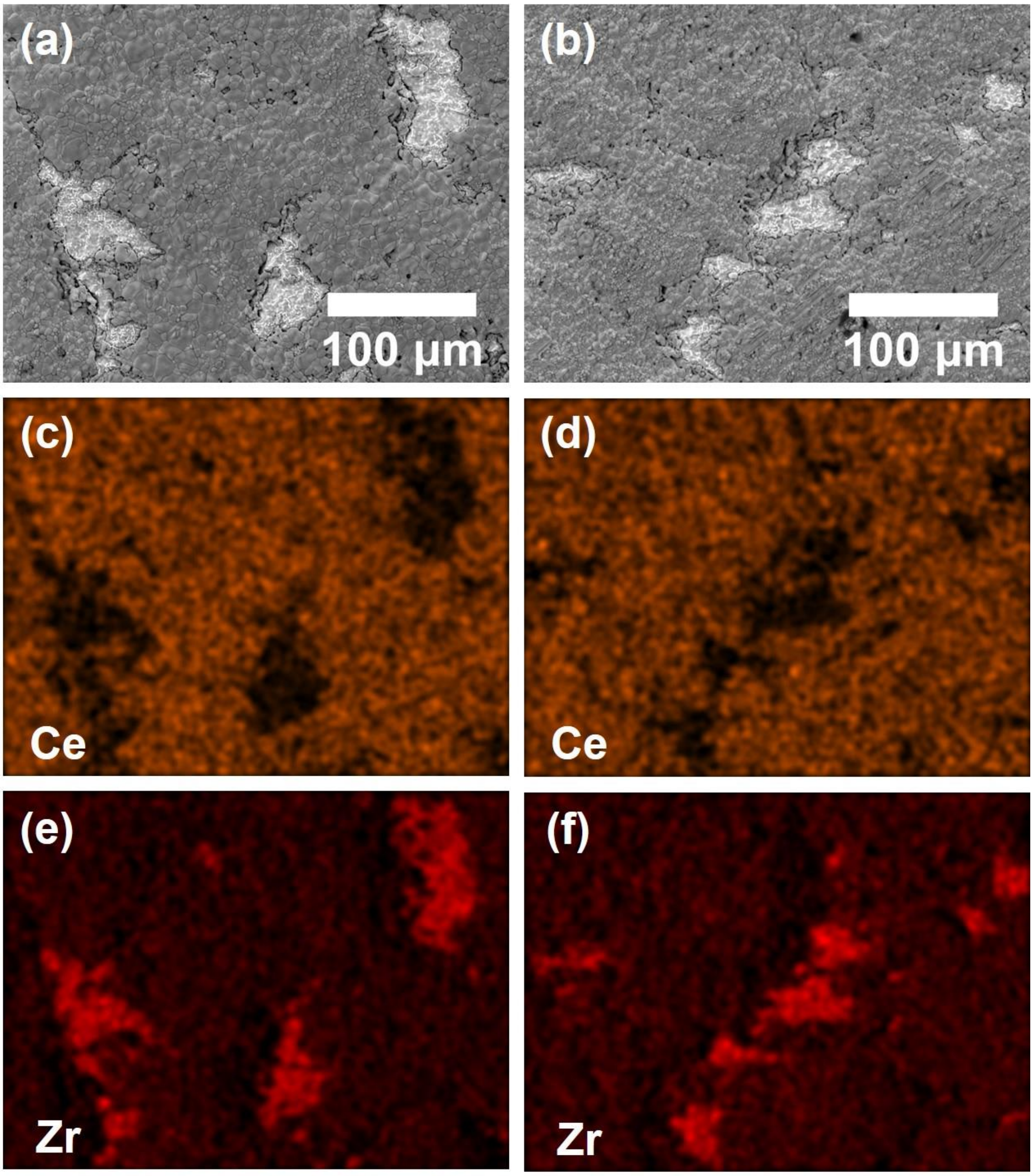

Figure 4-4: (a, b) surface of the GDC layer prepared by sequential casting and co-sintering, (c, d) Ce and (e, f) Zr surface EDS elemental mapping images.

4.5.2 Lamination of multiple tapes

Due to the poor adhesion property of the sequential cast samples, a lamination technique was used in the following to fabricate single cells [139, 305-307]. The lamination temperature reported for most tapes with PVA binder was chosen to be around its glass transition temperature (75 to 85°C) [308]. To investigate the effect of laminating temperature on the resulted tape quality, 60, 70, and 80°C were used. However, the applied pressure varied from 4 to 650 MPa [132, 139, 305, 307, 309]. Prior to tape lamination, the prepared tapes were cut into the size of 3.9 x 3.9 cm^2 which was large enough to obtain a circular button cell with the diameter of 3.5 cm. The operating temperature and pressure of hot pressing were optimised to achieve a good multilayer tape. The parameters and results of tape lamination are summarised in Table 4-3.

Table 4-3: Parameters and results of the tape lamination approach for bi-layer electrolyte cell fabrication.

No.	Temperature (°C)	Pressure (MPa)	Observed Results
1	60	20	Damaged tape
2	70	10	Poor lamination
3		20	Poor lamination
4		30	Poor lamination on the edge
5	80	10	Poor lamination
6		20	Poor lamination
7		25	Good lamination
8		30	Good lamination
9		50	Good lamination but reduced thickness
10		100	Damaged tape

According to the obtained results, a lamination temperature of 80°C (in the range of PVA binder glass transition temperature) and pressure of 25 to 30 MPa were found to be the suitable working conditions for achieving good lamination. Figure 4-5 (a) and (b) show the laminated square tape and pre-sintering button cell, respectively. The green tape was found to be smooth and well laminated without structural damage before sintering.

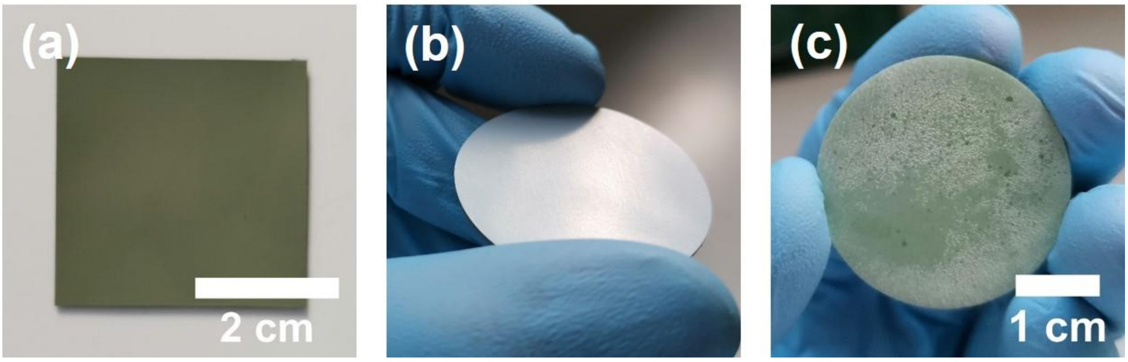

Figure 4-5: (a) laminated 4-layer green tape, (b) pre-sintering half-cell, and (c) sintered half-cell.

Although tape lamination can strongly attach multiple tapes together, delamination between GDC and ScCeSZ layers was not effectively avoided after co-sintering at the temperature range from 1300 to 1400°C. As shown in Figure 4-5 (c), a part of the GDC film peeled off from the ScCeSZ electrolyte, indicating poor adhesion between the GDC and the ScCeSZ layers after sintering. According to the SEM image in Figure 4-6 (a), cracks and large holes can be found on the post-sintering GDC layer. This suggests that there was more shrinkage in the GDC layer than in the ScCeSZ layer during the sintering process. To gain more insights of the element distribution on the GDC surface, EDS elemental mapping was performed. Figure 4-6 (b) to (d) suggest that Zr appeared on the surface of the GDC layer due to large pores created after co-sintering. Therefore, laminating tapes still cannot ensure good adhesion of ScCeSZ-GDC bi-layer electrolyte in the multilayer tape. Further adjustments to the half-cell fabrication process are necessary.

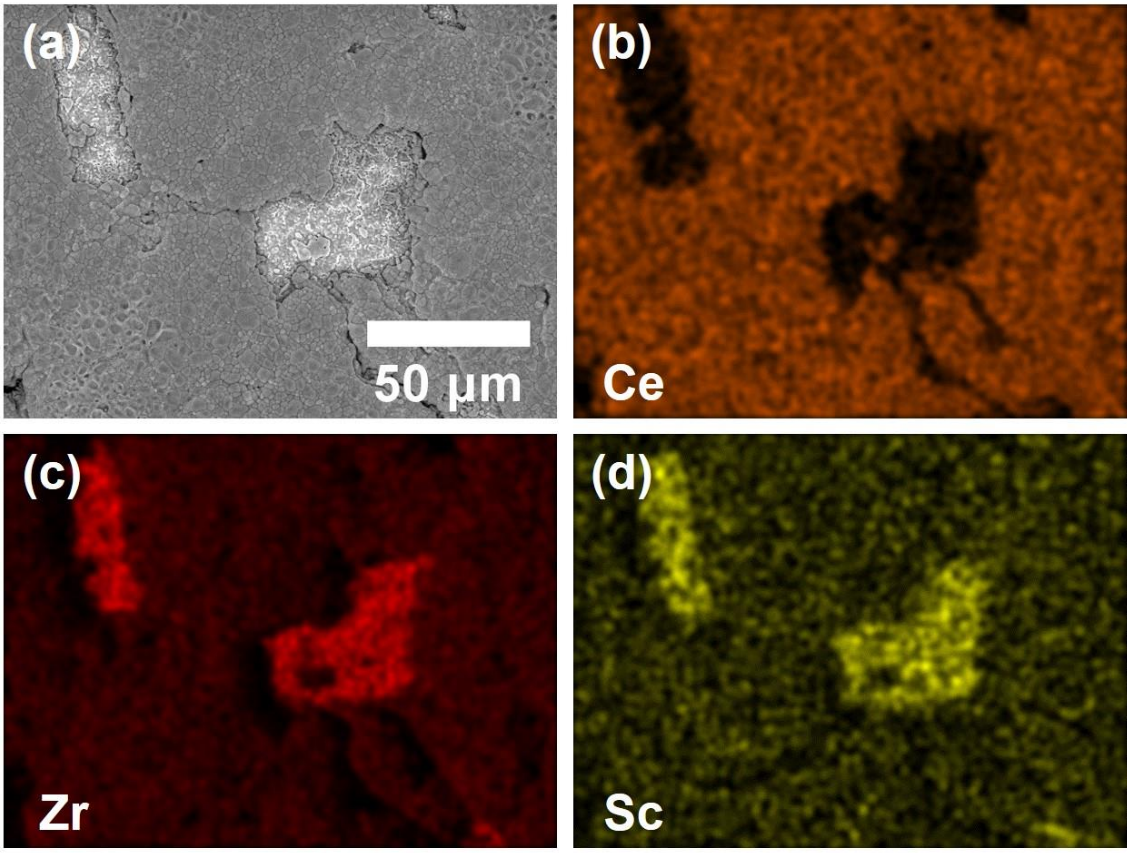

Figure 4-6: (a) surface of the GDC layer prepared by lamination and co-sintering, (b) Ce, (c) Zr, and (d) Sc surface EDS elemental mapping images.

4.5.3 Addition of Fe_2O_3 as sintering aid

Interaction between the GDC and ScCeSZ layers after co-sintering at 1400°C was observed in Figure 4-14 (a) and (b), highlighting the need to reduce the co-sintering temperature to prevent this negative effect during the fabrication process of the ScCeSZ-GDC bi-layer electrolyte. However, densification of GDC typically occurs above 1400°C. Achieving a dense GDC film is important for ensuring the gas tightness of the GDC layer and the function of blocking Sr diffusion from the LSCF cathode [310]. Transition metal oxides such as Bi_2O_3, CoO, CuO, Fe_2O_3, and MnO, have been reported as sintering aids to decrease the sintering temperature of both zirconia-and ceria-based SOFC electrolyte materials. Adding a small amount of sintering aid (0.5 to 2 mol%) to the electrolyte materials can promote the densification of electrolyte materials at a reduced temperature

(1200 to 1300°C). This reduced sintering temperature is attributed to the formation of a transient liquid phase during sintering process, leading to improved grain boundary conductivity [27, 146, 311, 312].

Among the various studied sintering aids, Fe_2O_3 is a cost-efficient option that has exhibited significant improvement in grain boundary conductivity during GDC and/or YSZ electrolyte sintering [27, 139]. Many studies suggested the addition of 1 mol% of Fe_2O_3 to the GDC and/or YSZ can achieve a dense zirconia/ceria bi-layer electrolyte within the sintering temperature range of 1250 to 1300°C. The presence of Fe_2O_3 reduces interfacial void defects, enabling improvement of conductivity and adhesion of two electrolyte layers [138, 139, 311, 313].

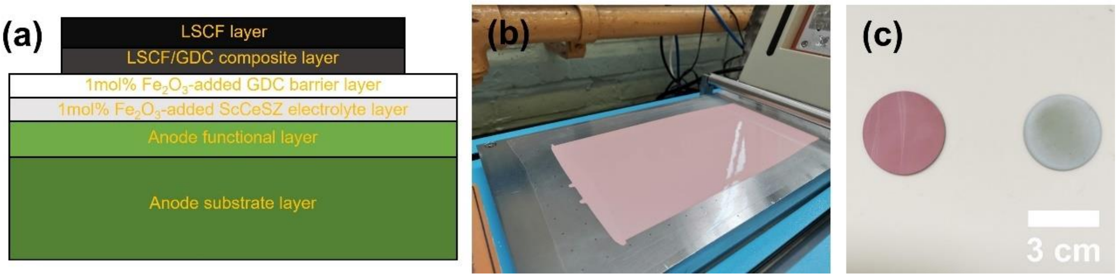

Figure 4-7: (a) structure of the prepared cell with 1 mol% Fe_2O_3 sintering aid in the electrolyte layers (b) tape casting of the 1 mol% Fe_2O_3-added GDC electrolyte, (c) half-cell before and after co-sintering.

In this work, 1 mol% of Fe_2O_3 was mixed with the electrolyte powders (GDC and ScCeSZ) in ethanol solvent for 24 h to achieve a homogeneous distribution. The mixture was then dried and sieved. The resulting electrolyte powders were used for aqueous tape casting, and the half-cells were co-sintered at 1250 and 1300°C. Figure 4-7 (b) shows the tape casting process of the 1 mol% Fe_2O_3-added GDC film and half-cells before and after sintering. The addition of iron oxide caused an obvious colour change in the electrolyte film from white to pink. Compared to the pre-sintering cell, the electrolyte was predominantly white with some small light brown dots. Once the half-cells were prepared, SEM analysis was performed on the GDC surface to determine the material compatibility.

As shown in Figure 4-8, layer exfoliation was still observed on the bi-layer electrolyte sintered at 1250 and 1300°C, indicating the mismatched shrinkage behaviour of the ScCeSZ and GDC layers during sintering. This could be explained by that the GDC layer experienced higher shrinkage than the ScCeSZ layer during the co-sintering process. Figure 4-8 (b) and (d) show a clear comparison of the GDC layers sintered at different temperatures. The increase in sintering temperature resulted in a slight improvement of the obtained GDC layer with larger gain size and fewer surface pores but did not prevent layer exfoliation.

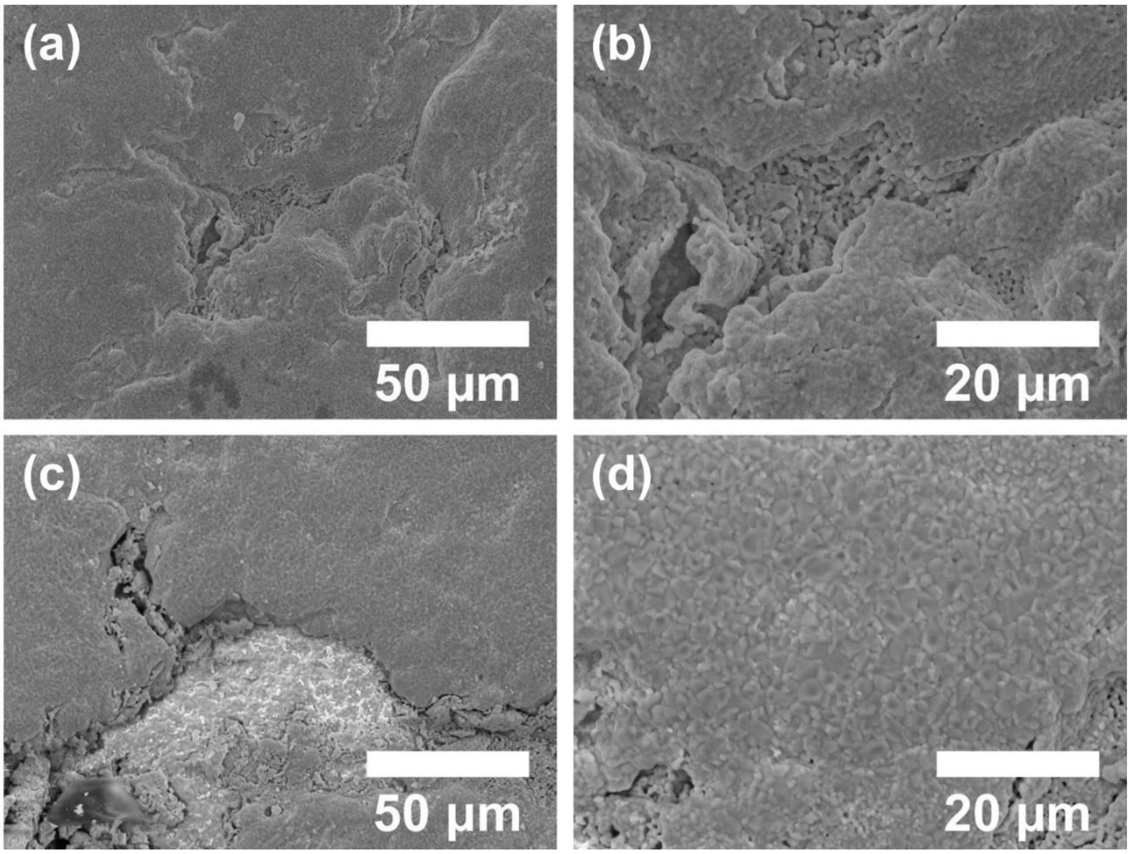

Figure 4-8: (a, b) Microstructure of the 1250°C sintered GDC surface, (c, d) Microstructure of the 1300°C sintered GDC surface of the ScCeSZ-GDC bi-layer electrolyte with the addition of 1 mol% Fe_2O_3 to the electrolyte material.

Figure 4-9 (a) and (b) show the cross-section images (taken at different regions) of the prepared full cells with ScCeSZ-GDC bi-layer electrolyte co-sintered at 1300°C. Delamination of the GDC and ScCeSZ in some regions were still present. Notably, severe delamination with a gap over 20 μm was identified between the ScCeSZ and AFL layers, which would cause a significant increase in cell resistance during SOFC operation. Hence, adding 1 mol% of Fe_2O_3 to the ScCeSZ and GDC layers as sintering aid can be concluded as an unsuccessful approach for the fabrication of bi-layer electrolyte SOFC cells.

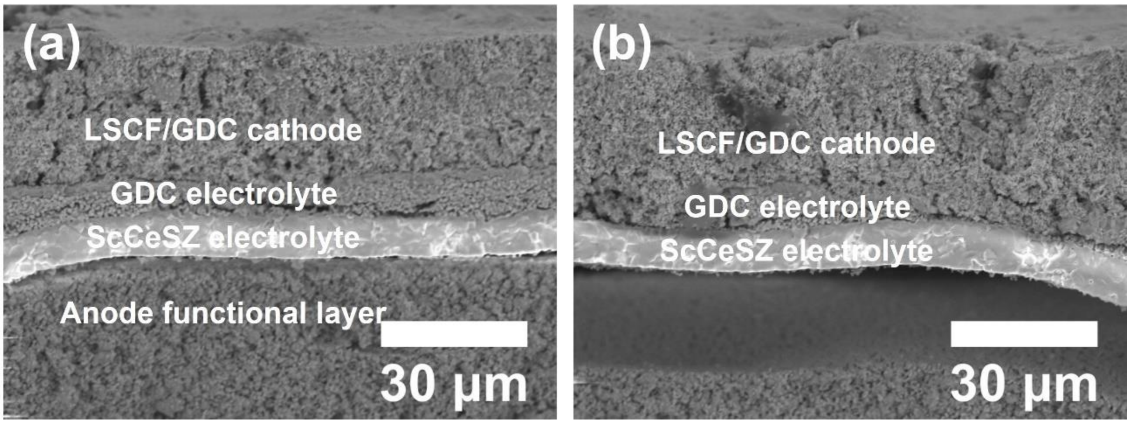

Figure 4-9: (a, b) Cross-section of the 1300°C-sintered ScCeSZ-GDC bi-layer electrolyte full cell with the addition of 1 mol% Fe_2O_3 to the electrolyte material.

4.5.4 Addition of a GDC/ScCeSZ composite layer

Composite layer consisting of both electrode and electrolyte materials have been widely investigated to provide both electronic and ionic conductivity, such as the LSM-YSZ SOFC cathode [314, 315]. The use of a composite layer can also alleviate the incompatibility issues of different materials during the high-temperature sintering process. Since the three fabrication approaches discussed above were not able to consistently produce the bi-layer electrolyte without delamination, using a composite layer between GDC and ScCeSZ layers was considered. This would result in a 'graded' transition from one layer to the other, considerably reducing shear stress between the layers. Figure

4-10 (a) shows the structure of the single cell with a GDC/ScCeSZ composite layer between GDC and ScCeSZ layers. The slurry for the composite layer was prepared using the same procedures as for the electrolyte slurry with 50wt.% of GDC and 50wt.% ScCeSZ powders. Prior to the ScCeSZ layer casting, the composite layer was cast onto the dried GDC tape, which added several microns to the overall electrolyte thickness. As shown in Figure 4-10 (b), the surface of the GDC layer was much smoother than in the cells prepared by the previous approaches.

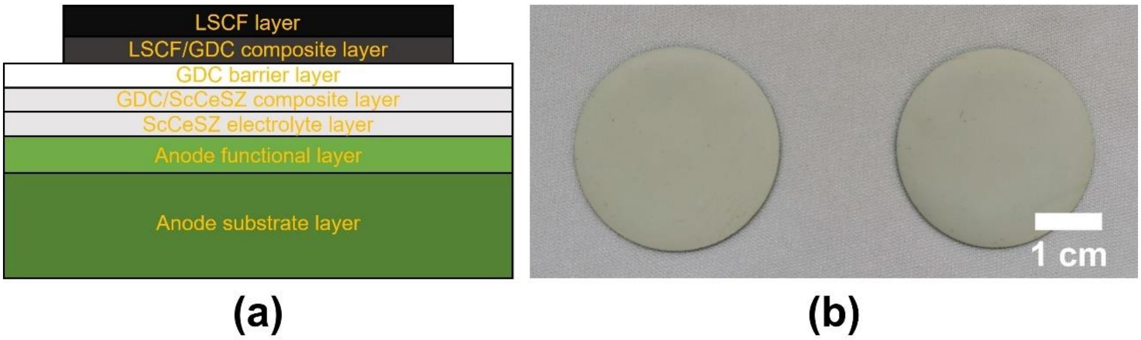

Figure 4-10: (a) single cell structure and (b) sintered GDC layer of the sequential cast cell with a composite layer.

When performing SEM analysis on the half-cell with a composite layer, the GDC surface was found to be smoother and denser compared with the GDC layers on other sequential cast cells. EDS surface quantification results (Table 4-4) further confirms that no Sc or Zr was found on the prepared GDC surface. Hence, the GDC layer prepared using this method had the potential to prevent chemical reaction between Zr and Sr during cathode sintering.

Table 4-4: EDS elemental quantification for GDC surface.

Element	**Normal Concentration (wt.%)**	**Atomic concentration (at.%)**
Cerium	74.22 ± 0.62	33.05 ± 0.87
Oxygen	16.20 ± 0.53	63.15 ± 0.92
Gadolinium	9.58 ± 0.36	3.80 ± 0.18

As shown in Figure 4-11 (a) to (c), the majority of the GDC surface was dense, but a few small pores were present, which could be attributed to the air bubbles remaining in the slurry after de-airing. Because of the limitation of in-house fabrication equipment, it would be difficult to completely remove all air bubbles from the slurry before casting. To obtain an air-bubble free slurry, slow agitation or rotation could be used during or/and after the de-airing process [316, 317]. According to Figure 4-11 (d)-(f), the presence of a composite layer greatly improves the adhesion of the electrolyte layers, especially for GDC and composite layer. Nevertheless, some small gaps were still identified at the interface between composite and ScCeSZ layers shown as Figure 4-11 (d) and (f), which could result in increased ohmic resistance during SOFC operation.

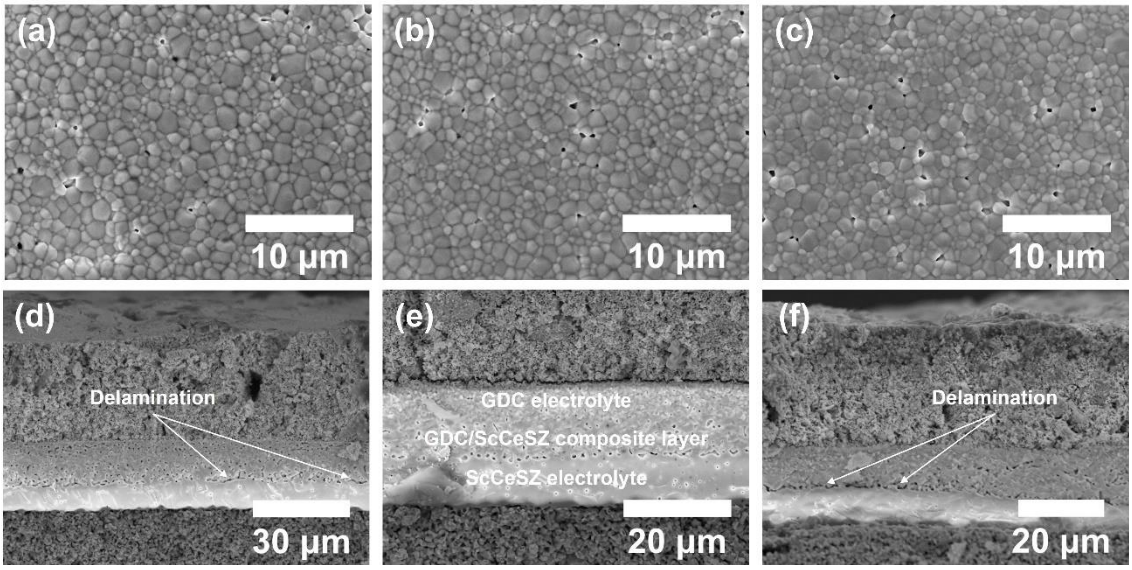

Figure 4-11: (a)-(c) microstructure of the GDC surface and cross-section of the sequential cast cells with a composite layer.

4.5.5 Spin coating the GDC layer

The ohmic resistance of an SOFC increases with the increasing electrolyte thickness, hence, reducing the thickness of the GDC layer is crucial to minimise the cell ohmic resistance. Based on the results from sequential casting, the minimum thickness of a sintered GDC layer obtained by our laboratory-scale doctor blade was 5.5 to 6.0 µm with a minimum casting height of 10 µm. Due to the accuracy limitation of the doctor blade setup, it would be challenging to further reduce the casting thickness of the slurry.

Amongst wet ceramic processing techniques, spin coating is a cost-effective thin film deposition technique that can prepare ceramic coatings under 5 µm [310, 318-320]. Many reported spin-coated ceramic films were prepared with organic solvents such as ethyl cellulose, terpineol, polyvinyl alcohol [310, 319, 321]. Compared with organic solvents, de-ionised water is a more environmentally friendly and low-cost solvent. In this work, the GDC thin film was successfully prepared by using a water based GDC suspension developed for tape casting. The SOFC single cells prepared via this approach has a structure shown in Figure 3-8. The thickness of the GDC film was controlled by the number of coating cycles. One to four cycles of coating were performed on the NiO/ScCeSZ half-cells to determine the optimal coating layers. One-step sintering was used for the spin-coated GDC film, which can greatly simplify the densification process [322, 323]. Figure 4-12 shows a comparison of surface morphology and thickness of the prepared GDC films with different numbers of coating cycles. The 3-cycle coated GDC film had much less defects and cracks than other samples. Therefore, three coating cycles were used for all GDC film preparations in this work.

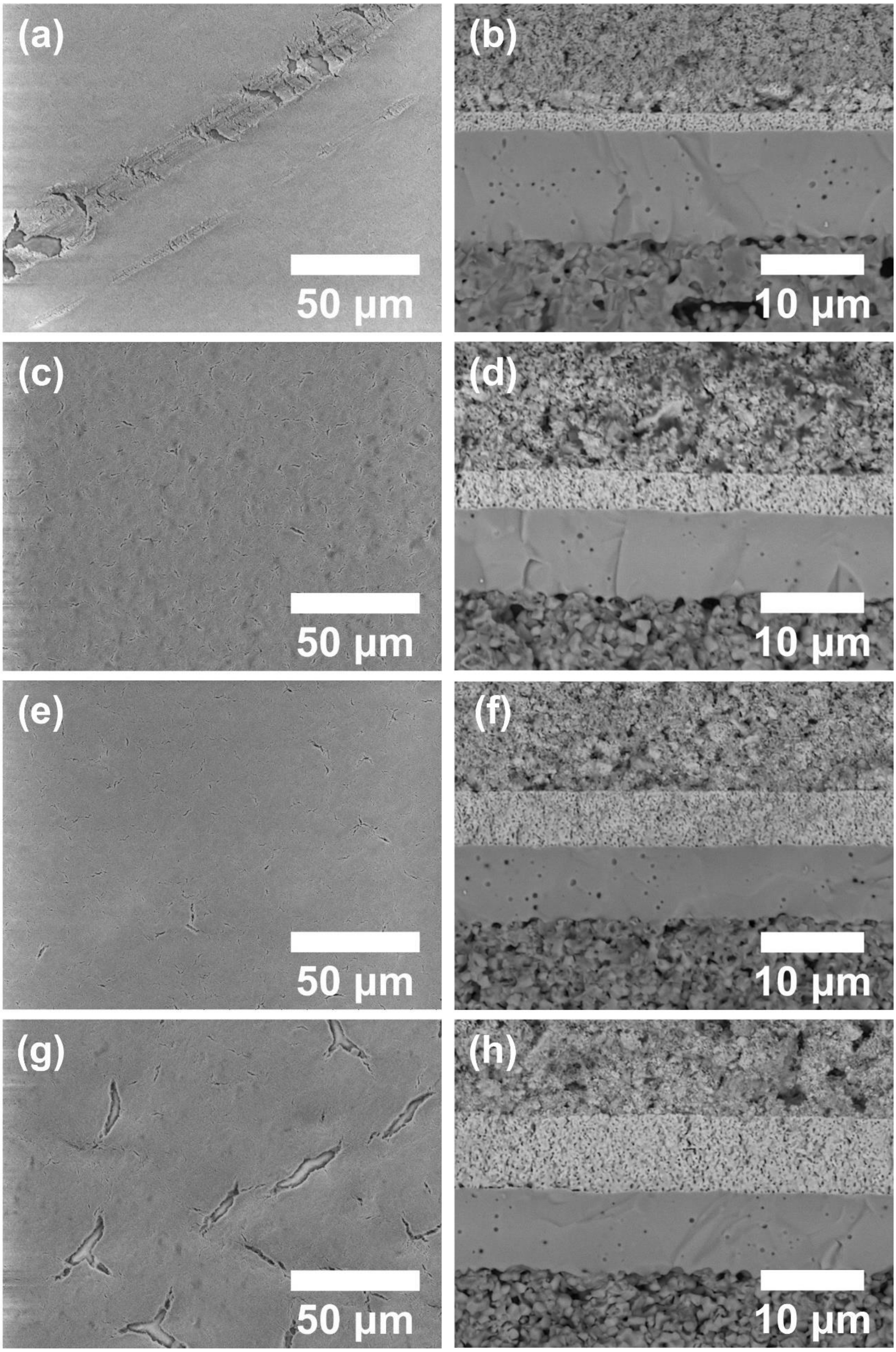

Figure 4-12: Surface morphologies and cross-section images of the GDC films prepared by spin coating for (a, b) 1 cycle, (c, d) 2 cycles, (e, f) 3 cycles, and (g, h) 4 cycles.

Solid loading of the coating slurry is another important factor that affects the prepared film quality. To investigate the effect of solid loading on the prepared GDC film quality, coating slurries with 40, 45, 50, and 55wt.% GDC content were prepared via ball milling. The microstructure images of the sintered GDC surface with different solid loading slurries are shown in Figure 4-13.

The GDC film prepared by the slurry with 40wt.% GDC showed the most porous structure amongst all four samples, as shown in Figure 4-13 (a) and (b). The overall thickness of the deposited GDC films increased with the increase of solid loading. After three coating cycles, the thicknesses of sintered GDC layers were around 3.2, 4, 5.3, and 7.8 µm for 40, 45, 50, and 55wt.% GDC slurry, respectively. The pore volume of GDC films was found to decrease with the increasing solid loading from 40 to 50wt.%. However, large cracks were identified on the GDC surface when the 55wt.% slurry is used. This could be attributed to the insufficient binder for holding the ceramic particles in the suspension, resulting in uneven distribution of GDC powder on the ScCeSZ electrolyte surface [319, 324]. Therefore, spin coating the slurry with 50wt.% GDC content for three cycles was found to give the best thin GDC film in the prepared half-cells.

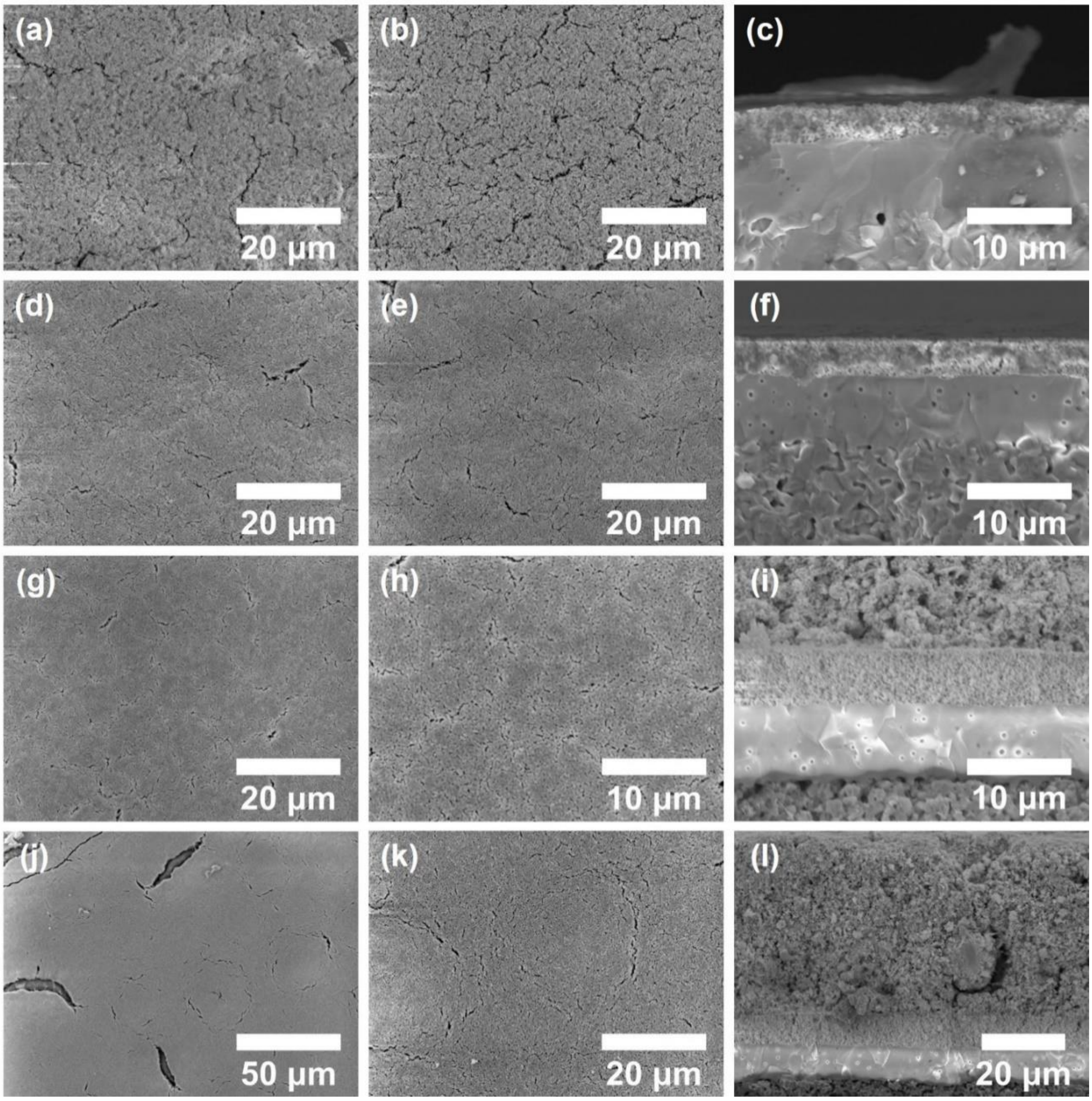

Figure 4-13: Three cycles spin-coated GDC film on ScCeSZ electrolyte with different solid loading, (a)-(c) 40wt.%, (d)-(f) 45wt.%, (g)-(i) 50wt.%, and (j)-(l) 55wt.%.

4.5.6 Comparison of the bi-layer electrolyte prepared by different methods

According to the preparation techniques, the type of GDC film prepared in this work can be classified as sequential cast (Cell I), composite (Cell II), and spin-coated cells (Cell III). Tsoga et al. [303, 304] suggested that ZrO_2- and CeO_2-based materials react and diffuse into each other during the sintering process above 1200°C, leading to the formation of $(Zr, Ce)O_2$-based solid solutions. It is known that $(Zr, Ce)O_2$-based solutions have low ionic conductivity, which can negatively affect the operation of SOFCs [325, 326]. Figure 4-14 shows a comparison of EDS elemental mapping and line-scan results for Cell I, Cell II, and Cell III. According to the elemental maps of cross sections, Zr diffusion is found on GDC boundaries for both Cell I and Cell II. This could be explained by diffusion of Zr and replacement of Ce at 1400°C sintering. A 2 µm interlayer consisting of $(Zr, Ce)O_2$-based solution is identified between GDC and ScCeSZ layers on Cell I. The line-scan results of Cell I and Cell II confirm the presence of this interlayer between the GDC and ScCeSZ interface given by the shift of Zr peaks at the GDC and ScCeSZ layer boundaries. Nevertheless, Zr diffusion was successfully avoided for Cell III because of the lower sintering temperature (1200°C) of the spin-coated GDC layer.

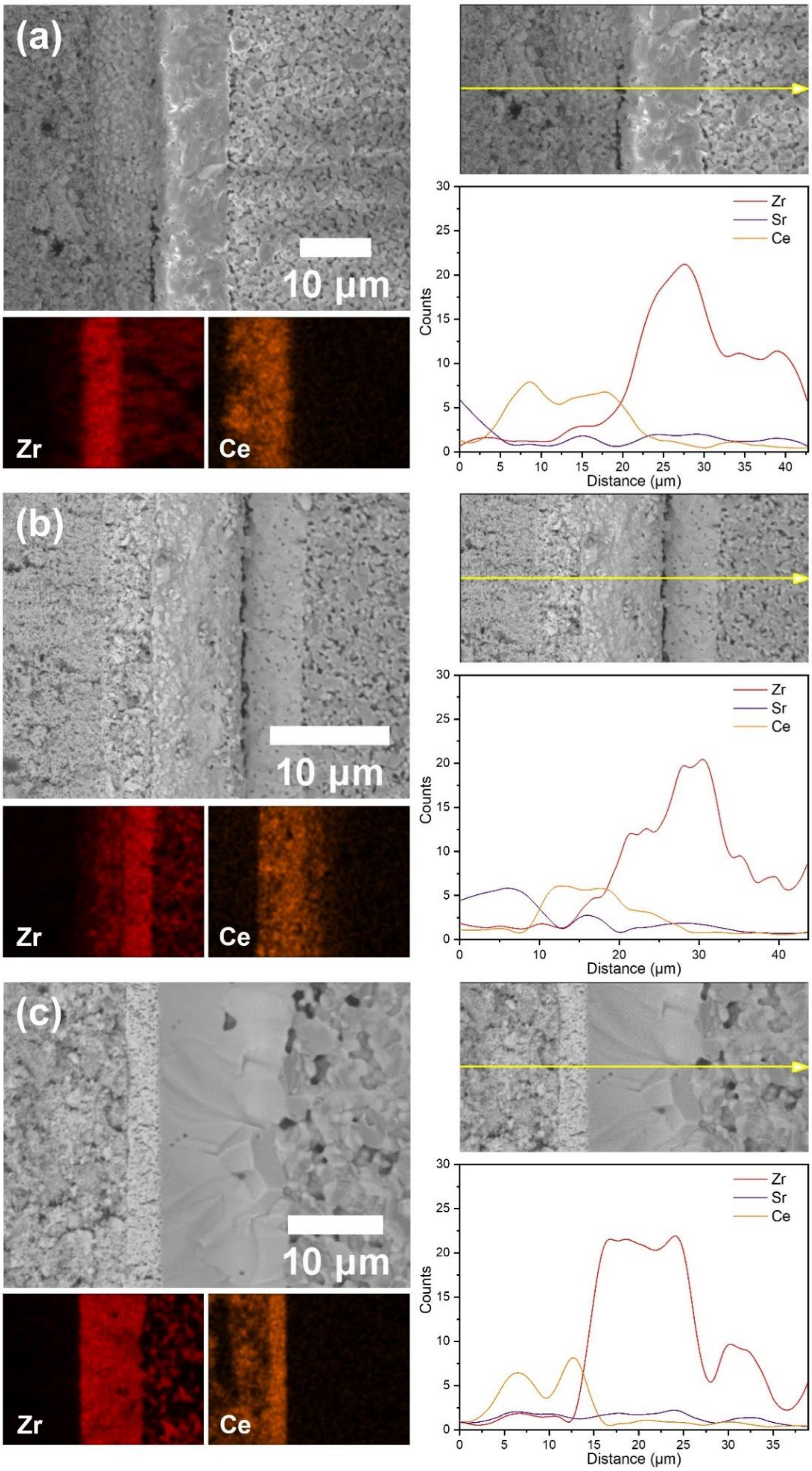

Figure 4-14: EDS mapping and line-scan results for (a) Cell I, (b) Cell II, and (c) Cell III.

4.6 Physical characterisation of the prepared cells

4.6.1 Anode

The prepared NiO/ScCeSZ anode was characterised by SEM and EDS analyses to determine the morphology and distribution of NiO and ScCeSZ on the anode surface. An estimation of porosity of the anode before and after hydrogen reduction was obtained by using the ImageJ software, following the technique reported in [327, 328]. Figure 4-15 shows the uniform distribution of Ni, Zr, and Sc elements on the pre-tested anode surface, which indicates that NiO and ScCeSZ were well dispersed during the slurry mixing stage.

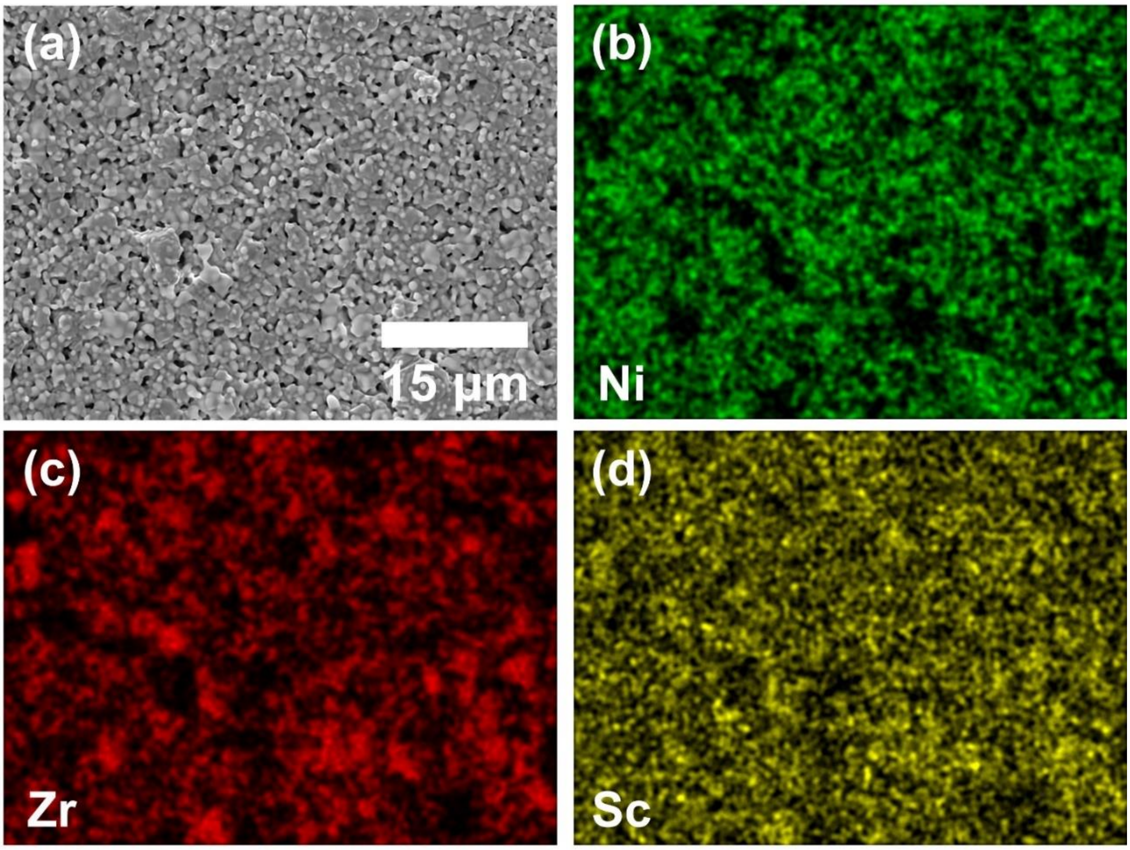

Figure 4-15: EDS elemental mapping results of the pre-tested NiO/ScCeSZ anode surface.

The surface morphologies of the pre-tested and H_2-reduced (24 h) AS and AFL were obtained by SEM analysis, which is shown in Figure 4-16. Due to the addition of 2.5wt.% pore former (in respect of the ceramic powder weight) in the AS slurry, the porosity of the pre-tested AS (4.54 ± 0.33%) was slightly higher than that of the AFL (8.51 ± 0.31%). After hydrogen reduction, the anode porosity was considerably increased up to 34.00 ± 1.00% and 24.55 ± 0.83% in the AS and AFL, respectively. A highly porous anode substrate is beneficial for the fuel gas to flow and then reach the triple-phase boundaries thus reacting with O^{2-} in the anode functional layer during SOFC operation.

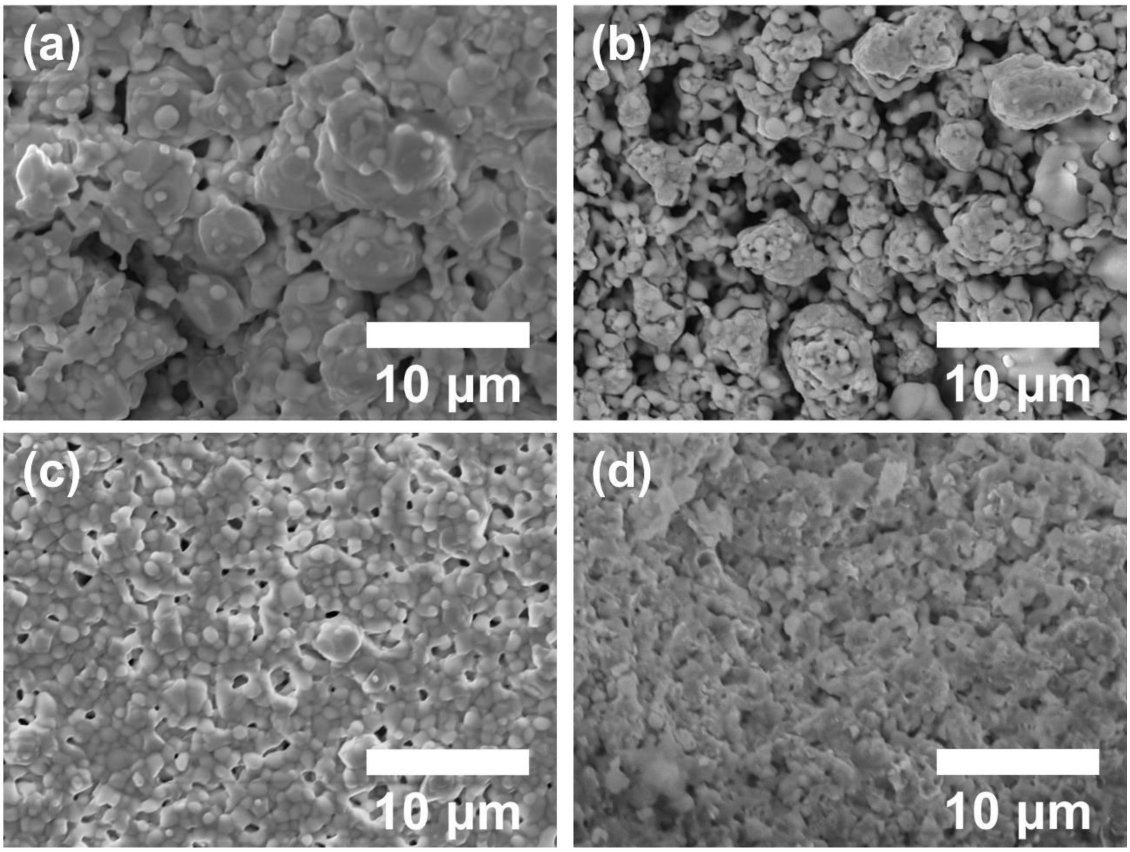

Figure 4-16: Anode surface of the prepared cell (a) pre-test AS, (b) H2-reduced AS, (c) pre-test AFL, (d) H2-reduced AFL.

4.6.2 Electrolyte

The surface morphology of the successfully prepared ScCeSZ electrolyte was characterised by SEM. As shown in Figure 4-17, the ScCeSZ electrolyte layer prepared by co-sintering was dense, with a grain size of 4.63 ± 0.17 µm. The ScCeSZ grain size on the electrolyte layer was around five times larger than on the hydrogen reduced anode surface (0.99 ± 0.16 µm). The difference between ScCeSZ grain size in anode and electrolyte layers could be explained by the uniformly distributed NiO and ScCeSZ particles, which suppressed the grain growth [329].

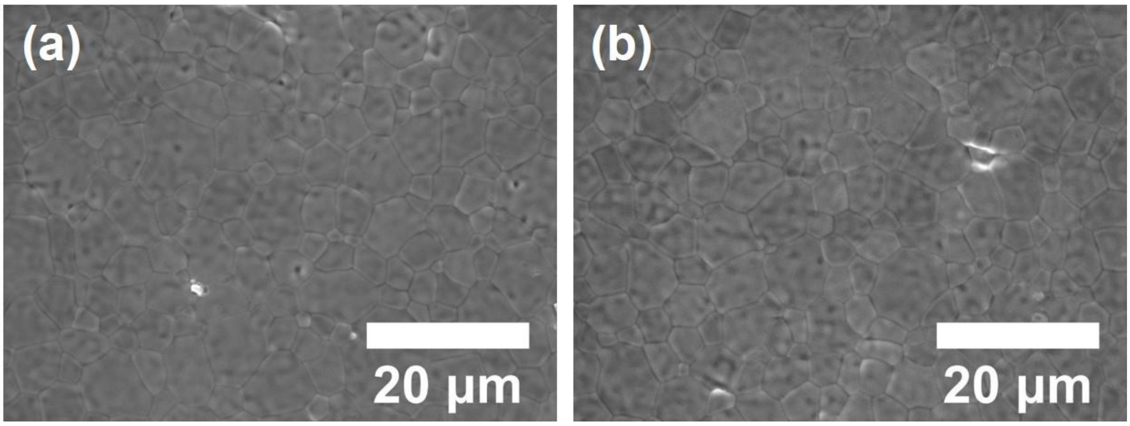

Figure 4-17: (a, b) surface morphology of the ScCeSZ electrolyte prepared by co-sintering at 1400°C.

Figure 4-18 shows the XRD pattern of the ScCeSZ electrolyte surface of a 1400°C co-sintered half-cell, indicating that the ScCeSZ was fully crystallised. However, a small peak of NiO is identified from the plot, which could be attributed to the contamination from the in-house fabricated sintering aid.

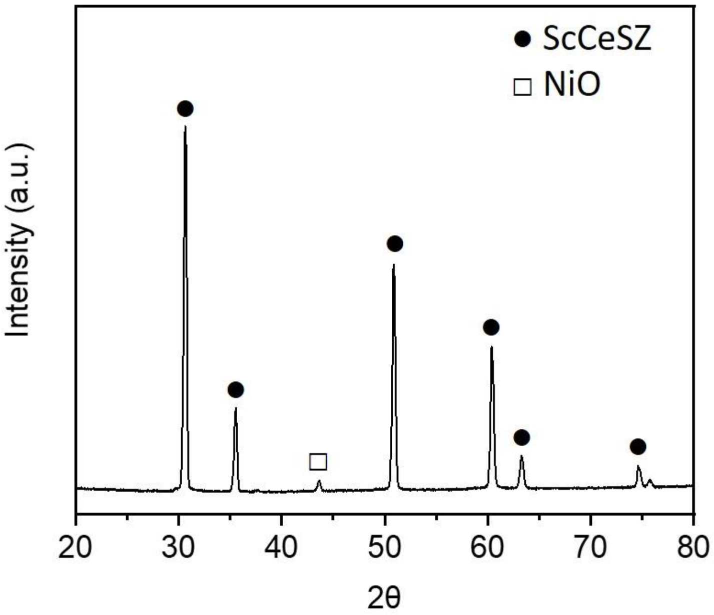

Figure 4-18: XRD scan of the ScCeSZ surface of the 1400°C co-sintered half-cell.

XRD analysis was performed for each type of sample to investigate the purity of the sintered GDC layer. Figure 4-19 shows the XRD pattern for the GDC film prepared by different techniques. It can be clearly seen that GDC interacted with the other materials (ZrO_2 or NiO) during the co-sintering stage for both Cell I and Cell II. ZrO_2-CeO_2 and ZrO_2-$CeO_{1.5}$ solid solutions were found on the XRD pattern of GDC films of Cell I and Cell II. These solid solutions have low electrical conductivity, which will lead to significant performance reduction [304]. Nevertheless, the GDC layer prepared by spin coating was fully crystallised without any secondary phase based on its XRD plot. The peaks identified in the GDC film sintered at 1200°C were found to be in the same agreement with previous work [330].

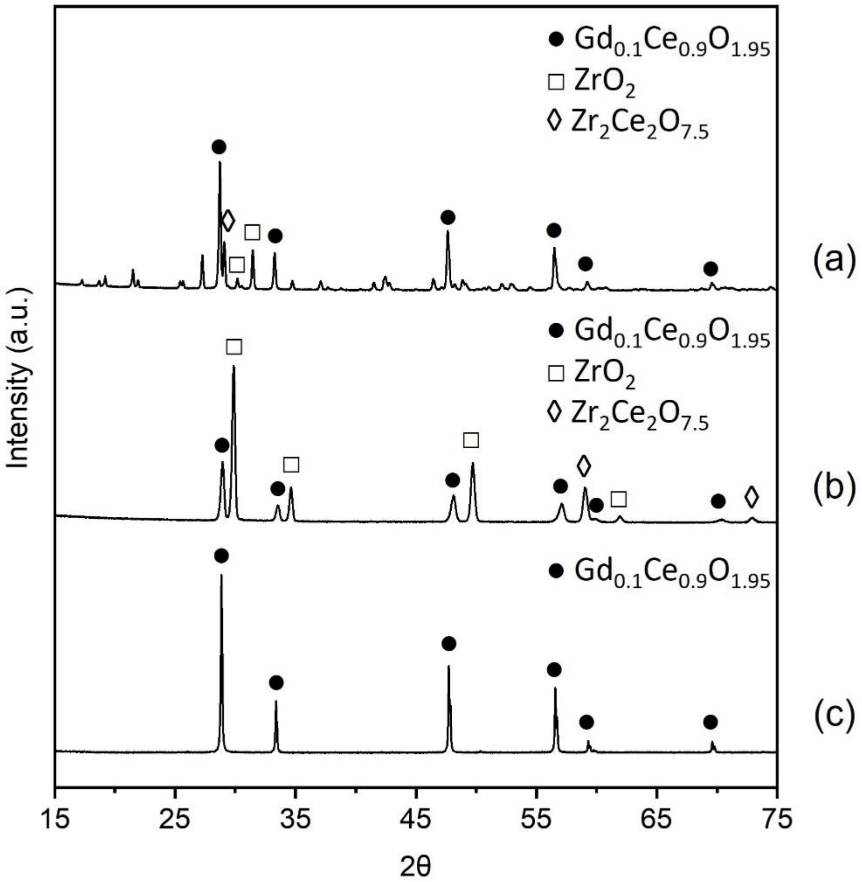

Figure 4-19: XRD scan of the GDC surface of the cells: (a) Cell I: sequential cast cell, (b) Cell II: composite cell, and (c) Cell III: spin-coated cell.

4.6.3 Cathode

LSCF/GDC (50:50) and LSCF were used as cathode functional layer and current collecting layer, respectively. Bi-layer cathodes were brush painted on the surface of the sintered GDC layer and then sintered at 975°C. Figure 4-20 (a) indicates that the sintered LSCF had a diameter of 2 cm. According to the obtained SEM images of the LSCF cathode surface Figure 4-20 (b) and cross-section Figure 4-20 (c), the cathode layer was highly porous and evenly adhered onto the GDC layer with the overall thickness of around 30 µm. The characterisation of cathode is focused on the interaction between LSCF and ScCeSZ during the SOFC operation, which is provided in Chapter 5.4.

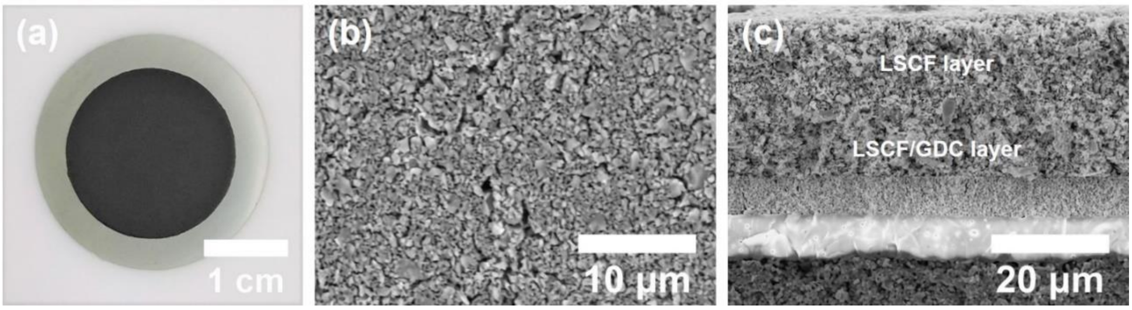

Figure 4-20: (a) prepared LSCF cathode on SOFC full cell, (b) microstructure of the LSCF cathode surface and (c) cross-section image of the LSCF cathode.

4.7 Sintering process optimisation

Co-sintering is a technique employed to densify multilayer ceramic tapes fabricated by tape casting. This method enables a significantly reduced cell fabrication duration. Due to the use of different materials in anode and electrolyte layers, the sintering shrinkage or sintering strain rate can vary during the co-sintering process [105]. Warpage and/or distortion are common issues for co-sintering of multilayer ceramic tapes, which are affected by factors like heating rate, sintering strain rate mismatch amongst the different layers, layer thickness ratio, and viscosity ratio [135, 331]. Applying a small amount of pressure to the sample has been found to be an effective method for improving the flatness of the sintered ceramic [140, 141, 332]. Therefore, the heating profile design and applied sintering load were herein investigated to achieve highly dense and flat half-cells.

TGA analysis was firstly performed on the multilayer tape for determining the organic burn-off temperature. Figure 4-21 indicates that the sample presented a 22wt.% loss during the TGA measurement. At the beginning, 2.2wt.% loss in the temperature range of 25 to 130°C was attributed to water evaporation. The largest change of 13.9wt.% was observed between 200 and 365°C. Since the boiling points of the organic additives used (PVA, PEG 400, and glycerol) were below 300°C, this temperature range is considered as the major organic burn-off stage. After that, the remaining 4.54wt.% of organic contents were completely removed before 560°C. To prevent any structural failure of the sintered half-cells, 300 and 600°C were chosen as the two dwelling temperatures for organic additive removal. Several studies found that a slow heating rate in the co-sintering process is very important to ensure the flatness of the cell and density of the electrolyte [134, 333, 334]. Hence, the heating rate was maintained at 1°C/min throughout the sintering stage, with 1 hour of dwelling steps at the critical temperatures of 300 and 600°C.

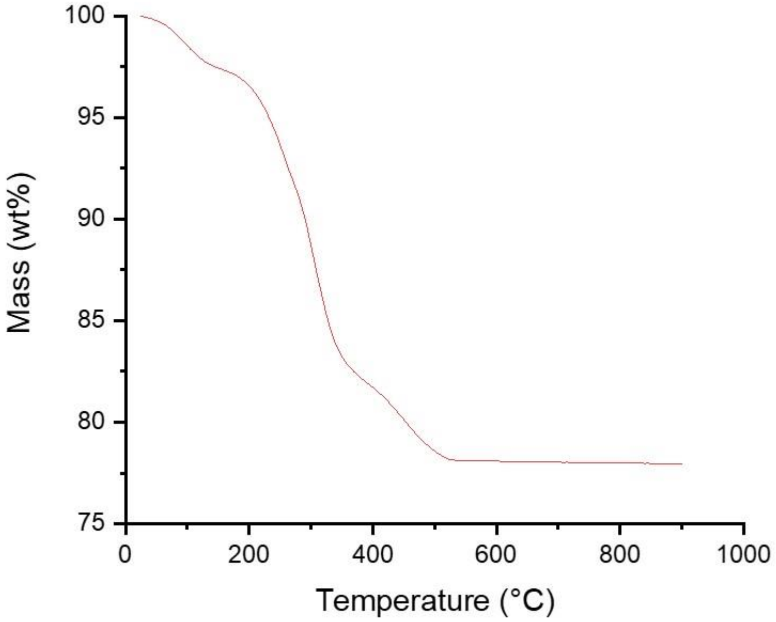

Figure 4-21: TGA plot of the multilayer tape in the temperature range of 25 to 900°C.

The optimal sintering load for the multilayer tape was investigated by comparing the flatness and electrolyte surface of the co-sintered half-cells. A porous YSZ substrate was used as sintering load for half-cell co-sintering. The porous structure ensured organic contents removal while applying external pressure onto the half-cell during the sintering process.

Table 4-5 shows the effect of applying different amounts of sintering load to the half-cells. Although increasing sintering load can improve the flatness of the half-cell, the samples with sintering loads above 10 Pa were found to crack. Therefore, an applied pressure of 10 Pa was used during co-sintering for our in-house fabricated half-cells.

Table 4-5: Comparison of the co-sintered half-cells with different sintering load.

Sintering load (Pa)	Obtained half-cell appearance
0	
5	
10	
15	
20	

4.8 Summary

In summary, the study successfully developed an optimised process for the fabrication of NiO/ScCeSZ anode-supported half-cells using aqueous tape casting and co-sintering techniques. The key process parameters, including aqueous slurry composition, drying temperature, heating rate, and sintering load, were optimised to achieve dense and flat half-cells. A thin GDC barrier layer with the thickness of 5 µm was prepared by spin coating and then sintered at 1200°C. Compared to Cell I and Cell II, Cell III showed a uniformly deposited GDC layer without delamination. More importantly, no formation of (Zr, Ce)O_2-based solid solutions was found on the ScCeSZ and GDC layer boundaries for Cell III due to the reduced temperature of sintering. The flatness of the cell was ensured by applying a 10 Pa sintering load via a porous YSZ substrate on top of the multilayer tape during sintering. These findings could contribute to the development of high-performance planar SOFCs and provide guidance for the optimisation of similar SOFC single cell fabrication processes.

CHAPTER 5: SOFC SINGLE CELL TESTING ON HYDROGEN OPERATION AND POST-TEST CHARACTERISATIONS

5.1 Overview

The electrochemical performance of Cell I, Cell II, and Cell III with 8.0 to 9.0 µm ScCeSZ electrolytes was evaluated with hydrogen as fuel operating in the temperature range of 800 to 700°C. The main difference between different cells used for electrochemical characterisation was the fabrication approach of the GDC layer. Table 5-1 shows the fabrication approaches used for different cells prepared in this work. To evaluate the effect of GDC layer thickness on the electrochemical performance, three samples of each cell with different GDC layer thickness (from high to low) were prepared.

Table 5-1: GDC layer fabrication approaches on different cells.

Cell I	Sequential casting on the ScCeSZ layer
Cell II	Sequential casting on the GDC/ScCeSZ composite layer
Cell III	Spin coating on the sintered ScCeSZ layer

Polarisation characterisation, EIS, and operational stability analysis were performed besides SOFC single cell operation. Microstructure and surface elemental distribution of the post-tested cells were characterised by SEM and EDS, respectively.

5.2 Electrochemical characterisation

5.2.1 Cell I: sequential cast cells

Three cells labelled as Cell I-A, Cell I-B, and Cell I-C were prepared. The casting thickness of the GDC layer for each cell was 30, 20, and 10 µm, respectively. The sintered GDC layer thicknesses of the prepared single cells are shown in Table 5-2. According to the cell fabrication results of the GDC layer prepared by tape casting, a casting thickness change of 10 µm resulted in approximately 2.6 µm change in the sintered thickness. Nevertheless, the sintered GDC layer thickness only changed linearly with the casting thickness when this was above 20 µm due to the 10 µm limitation of minimal unit on the doctor blade.

Table 5-2: Thickness of the GDC layers on Cell I samples.

Cell type	**GDC layer thickness (µm)**	
	Casting	Sintered
Cell I-A	30	8.8
Cell I-B	20	6.2
Cell I-C	10	5.2

Figure 5-1 (a), (c), and (e) show the i-V curves of Cell I-A, Cell I-B, and Cell I-C, respectively, operated with hydrogen as fuel at temperature of 800°C, 750°C, and 700°C. The open-circuit voltages (OCVs) of the cells were 0.90, 0.92, and 0.93 V, respectively. However, the OCV values for Cell I were around 18% lower than the theoretical OCV values (e.g., 1.10 V). After conducting several identical cell tests on Cell I, the lower OCV values could be explained by the potential loss inside the electrolyte at zero current. The potential loss in Cell I could be mainly attributed to the gas crossover through the thin ScCeSZ-GDC bilayer electrolyte due to the delamination between ScCeSZ and GDC layers, alongside with the formation of pinholes in these two layers during co-sintering (shown in Figure 4-3 and Figure 4-4). If delamination and pinholes exist in the electrolyte, gas crossover through the electrolyte could occur. This would result in reduced partial pressure for both hydrogen and oxygen. According to Nernst equation shown in Eq.(22), in a hydrogen-oxygen fuel cell, a drop in partial pressure of hydrogen and oxygen will lead to a decreased OCV. Cell I-A showed maximum power densities of 0.09, 0.05, and 0.03 W•cm^{-2} at each operating temperature, respectively, which were substantially lower than those for Cell I-B and Cell I-C.

After analysing the ohmic resistance (R_{ohm}) and overall electrode polarisation resistance (R_p) of the three samples, it was found that Cell I-A had a R_{ohm} value around twice as high as the R_{ohm} values of Cell I-B and Cell I-C. Additionally, the R_p values of Cell I-A were also found to be ten times higher than the R_p values of Cell I-B and Cell I-C at all operating temperatures. As Cell I-A had the thickest GDC layer, the increase in R_{ohm} of Cell I-A could be attributed to the more severe delamination that occurred at the interface of GDC and ScCeSZ layers. This delamination not only reduced the ionic conductivity of the bi-layer electrolyte but also reduce the length of TPB at the electrolyte/electrode interface [335]. Consequently, Cell I-A showed the highest polarisation resistance and the lowest power output among all samples. When the thickness of the GDC layer was reduced from 8.8 µm in Cell I-A to 6.2 µm in Cell I-B, the SOFC power output increased more than four times. Cell I-B exhibited the highest power output among all three prepared cells, with peak power densities (P_{max}) of 0.416, 0.298, and 0.184 W•cm^{-2} at 800°C, 750°C, and 700°C, respectively. However, the power output of Cell I-C did not increase with the decreasing thickness of GDC layer to 5.5 µm, showing ~10% decrement in P_{max} compared to Cell I-B. As R_p for Cell I-B and Cell I-C were similar, the reduced cell performance of Cell I-C can be attributed to the larger R_{ohm} that caused by defects (cracks and layer delamination) in the ScCeSZ-GDC bilayer electrolyte.

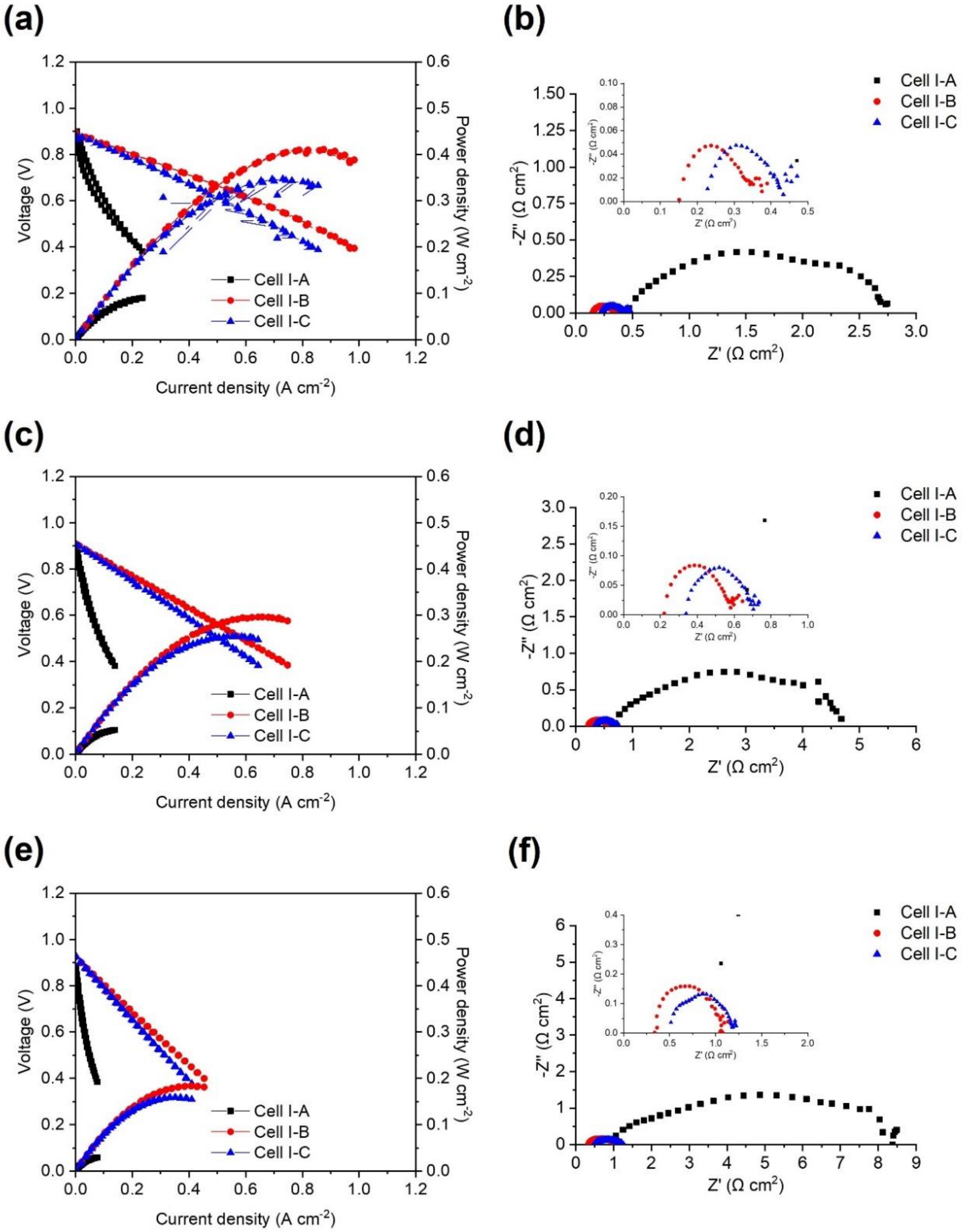

Figure 5-1: i-V curves and Nyquist plots of Cell I-A, Cell I-B, and Cell I-C operated with hydrogen at (a, b) 800°C, (c, d) 750°C, and (e, f) 700°C (the insets in b, d, f represent a magnified view for the presented Nyquist plots).

Figure 5-2 shows the plots of OCV, P_{max}, R_{ohm}, and R_p versus GDC layer thickness for three Cell I samples at different operating temperatures. Figure 5-3 (a) shows the cross-section of Cell I-A after cell testing at various temperatures. Like Cell I-B and Cell I-C, delamination between GDC and ScCeSZ layers can be identified. Distinctively, the GDC layer in the Cell I-A was found to be cracked after cell testing. This finding explained the lowest OCV of Cell I-A among all tested samples even if it has the thickest GDC layer. If the cracks were formed before or during cell testing, it could further compromise the adhesion between GDC and ScCeSZ layers and reduced the TPB length at the interface of LSCF cathode and GDC layer. Consequently, the R_{ohm}, and R_p of the Cell I-A were higher than the other tested Cell I samples. It can be concluded that the thickness and quality of the GDC layer play a critical role in the performance of the bi-layer electrolyte SOFCs. Despite reducing the GDC layer thickness can improve the SOFC performance in terms of the improved power output and reduced cell resistance, care must be taken to avoid the formation of cracks and or delamination in the bi-layer electrolyte.

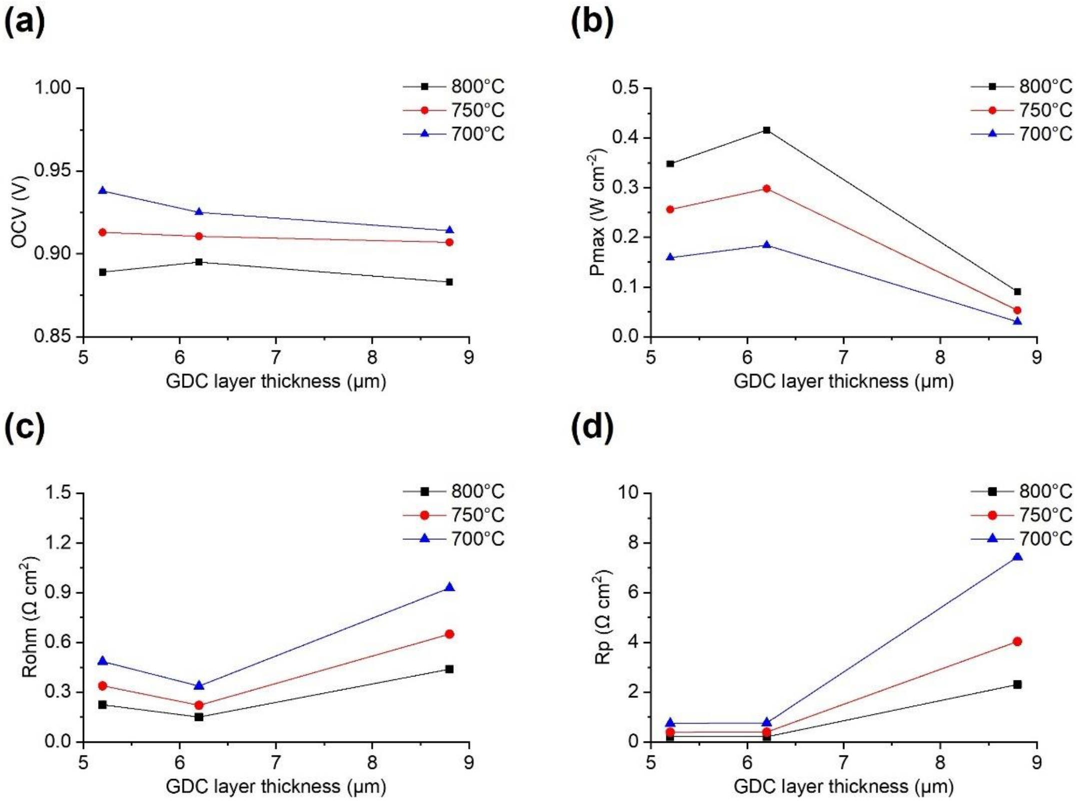

Figure 5-2: Plots of (a) OCV, (b) P_{max}, (c) R_{ohm}, and (d) R_p vs GDC layer thickness for Cell I at different temperatures.

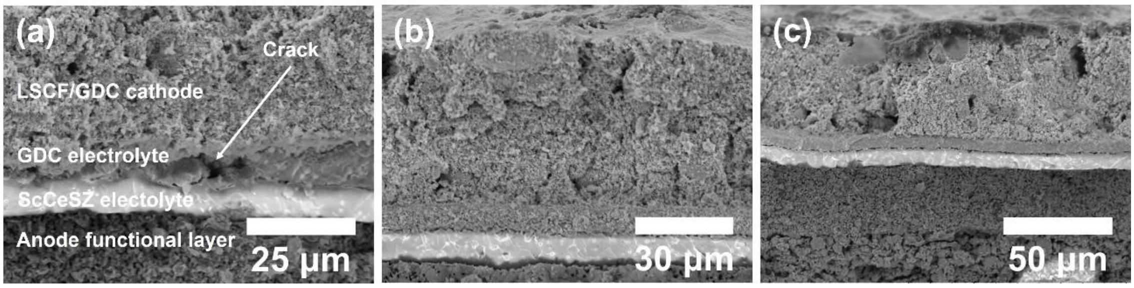

Figure 5-3: Cross-section of the (a) Cell I-A, (b) Cell I-B, and (c) Cell I-C after hydrogen operation at 800°C, 750°C, and 700°C.

5.2.2 Cell II: composite cells

The use of a composite gradient layer has been extensively studied to promote the adhesion between electrode and electrolyte layers during the co-sintering process [336-338]. Coddet et al. [72] reported that a YSZ/GDC gradient barrier layer could effectively provide a smooth transition between the YSZ and the GDC layers. The gradient layer not only prevented the delamination between different layers in an SOFC single cell prepared by co-deposition, but also improved the electrochemical performance with hydrogen operation. Similar to Cell I, the fabrication approach for Cell II was to reduce the thickness of the ScCeSZ, composite, and GDC layers to minimise the contribution of R_{ohm} to SOFC resistance. Table 5-3 shows the thickness details of the GDC and the composite layers for the successfully prepared samples.

Table 5-3: Thickness of the GDC, composite, and ScCeSZ layers on Cell II samples.

Cell type	**GDC layer thickness (μm)**		**Composite layer thickness (μm)**	
	Casting	Sintered	Casting	Sintered
Cell II-A	30	8.7	30	8.5
Cell II-B	20	6.6	20	6.5
Cell II-C	10	5.2	10	5.3

According to the cross-section SEM images of Cell II in Figure 4-11, the presence of the composite layer greatly improved the adhesion between the ScCeSZ and GDC layers. It is worth mentioning that no increased number of defects was observed on the tri-layer electrolyte even after reducing the thickness of GDC and composite layers. As shown in Figure 5-4 (a), (c), and (e), both Cell II-B and Cell II-C showed around 50% increment in P_{max} compared to Cell II-A at all operating temperatures.

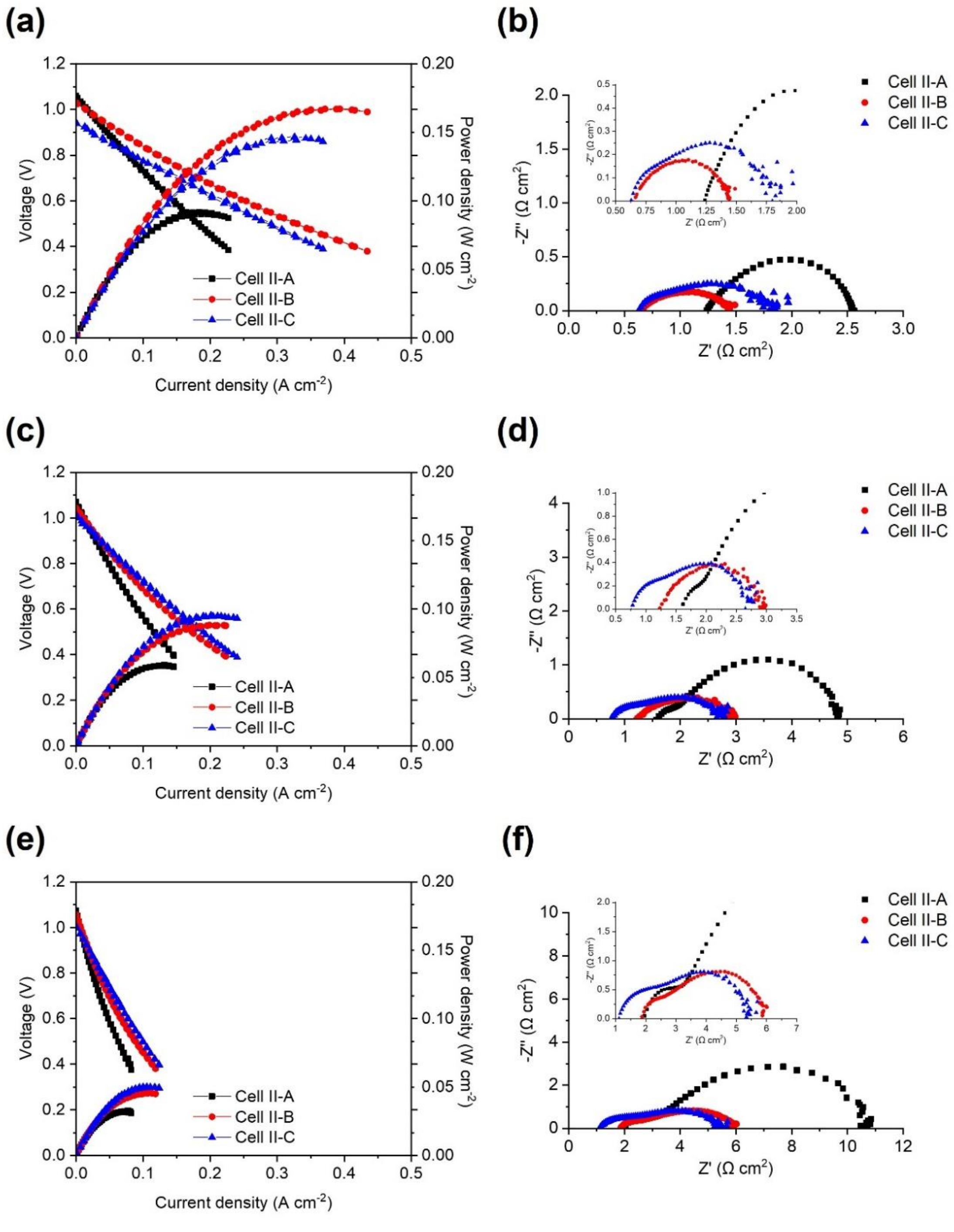

Figure 5-4: i-V curves and Nyquist plots of Cell II-A, Cell II-B, and Cell II-C operated with hydrogen at (a, b) 800°C, (c, d) 750°C, and (e, f) 700°C (the insets in b, d, f represent a magnified view for the presented Nyquist plots).

Figure 5-5 shows the plots of OCV, P_{max}, R_{ohm}, and R_p versus GDC layer thickness for all tested Cell II samples at different operating temperatures. It is observed that Cell II-C showed the minimum R_{ohm} of 0.63, 0.76, 1.11 Ω•cm^2 amongst all three cells at 800°C, 750°C, and 700°C, respectively. As shown in Figure 5-6, no obvious cracks in electrolyte layers of Cell II can be identified. This implies that Cell II has much a denser electrolyte compared to Cell I. The OCV and R_p of Cell II decrease with decreasing thickness of GDC layers. Similar findings have been also reported on the anode-supported SOFC with GDC [339] and YSZ-GDC [340] electrolytes. Part and Barnett [340] suggested a possible explanation is gas leakage caused by the thinner electrolyte, allowing oxygen leakage into the anode side. This will produce additional steam on the anode side and therefore decrease the OCV and R_p values [222, 341].

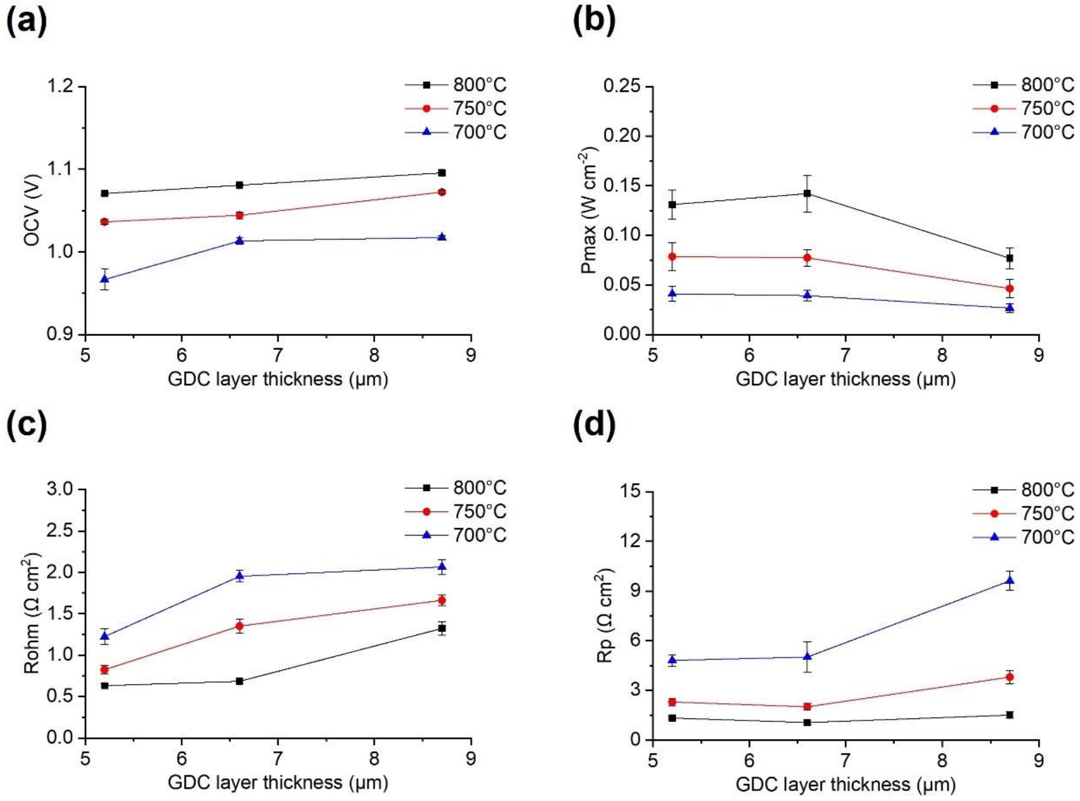

Figure 5-5: Plots of (a) OCV, (b) P_{max}, (c) R_{ohm}, and (d) R_p vs GDC layer thickness for Cell II at different temperatures.

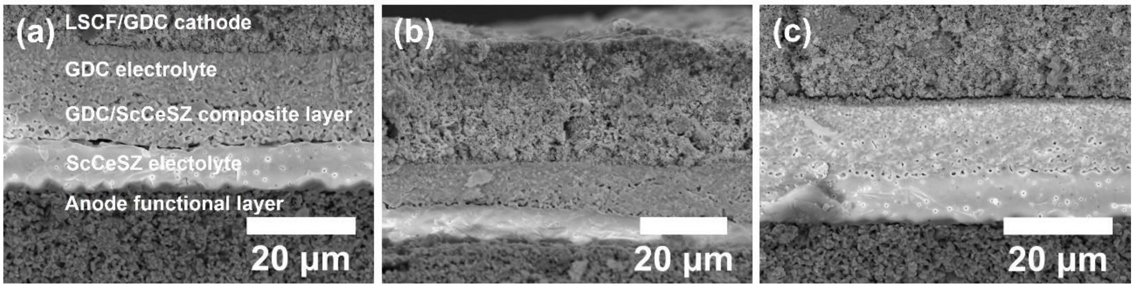

Figure 5-6: Cross-section of the (a) Cell II-A, (b) Cell II-B, and (c) Cell II-C after hydrogen operation at 800°C, 750°C, and 700°C.

5.2.3 Cell III: spin-coated cells

Electrochemical performances of the single cells with GDC films prepared by spin coating are compared based on the number of coating cycles and solid loading. Samples of Cell III with two or three spin coating cycles were prepared for SOFC single cell testing. Table 5-4 shows the details of thickness of four prepared cells with different coating cycles, which was determined from Figure 4-12 (d) and (f). Each coating cycle can give around 1.7 μm additional thickness to the GDC layer.

Table 5-4: Number of spin coating cycle and thickness for the GDC films on Cell III samples.

Cell type	GDC solid loading	Spin coating cycle	GDC film thickness (μm)
Cell III-A	50wt.%	2	3.9
Cell III-B	50wt.%	2	3.7
Cell III-C	50wt.%	3	5.3
Cell III-D	50wt.%	3	5.4

The impact of GDC loading on the thickness of GDC films was investigated using four slurries, with GDC loadings of 40wt.%, 45wt.%, 50wt.%, and 55wt.%. Three cycles of spin coating were deployed to every slurry on the prepared half cells. Table 5-5 shows thickness measurements of the prepared GDC films with different solid loading, which was derived from Figure 4-13 (c), (f), (i), (l). The results indicate that as the GDC loading in the coating slurry increases, the thickness of the resulting GDC film also increases.

Table 5-5: Effect of GDC loading on the thickness of GDC films with three coating cycles.

Cell type	GDC solid loading	Spin coating cycle	GDC film thickness (μm)
Cell III-40	40wt.%	3	3.2
Cell III-45	45wt.%	3	4
Cell III-50	50wt.%	3	5.4
Cell III-55	55wt.%	3	7.8

In Figure 5-7 (a), (b), and (c), it is observed that Cell III-C and Cell III-D have thicker GDC layers, showed slightly higher OCV and power output than Cell III-A and Cell III-B. This implies denser GDC films were achieved by three spin coating cycles. More importantly, Cell III-C and Cell III-D showed consistent and repeatable power output at all operating temperatures. The P_{max} for the successfully prepared Cell III-C and Cell III-D were around 1.10, 1.00, and 0.80 $W \cdot cm^{-2}$ at 800°C, 750°C, and 700°C, respectively.

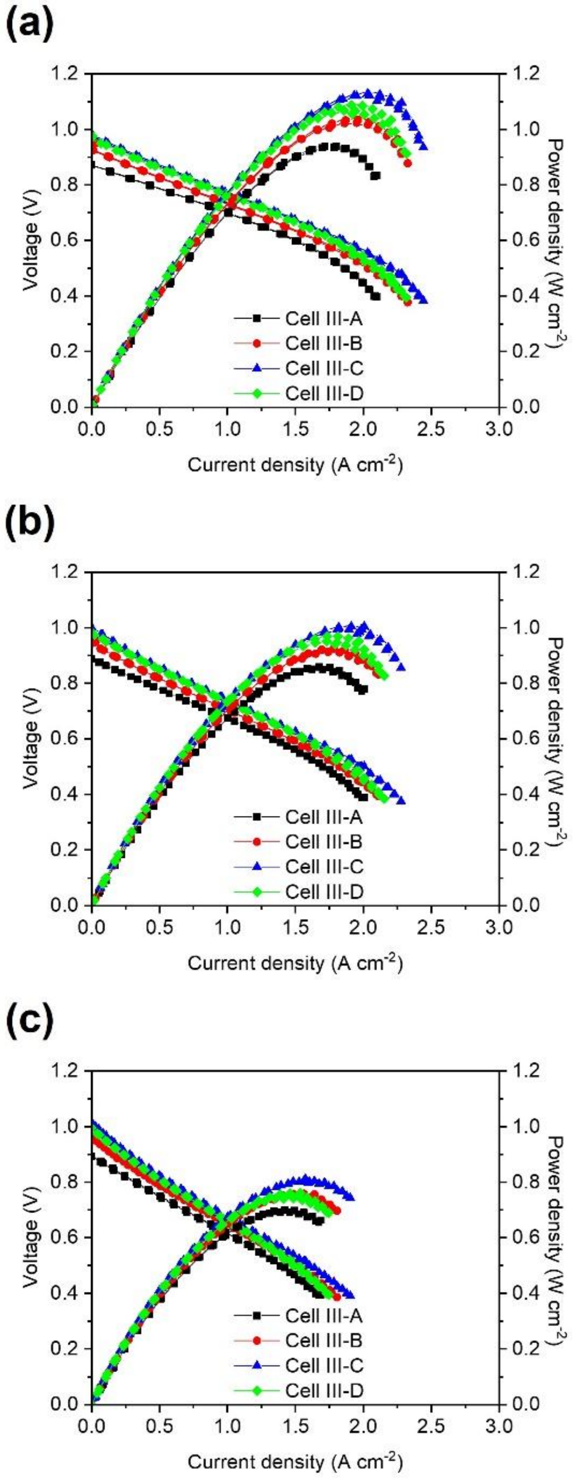

Figure 5-7: i-V curves of Cell III-A, Cell III-B, Cell III-C, and Cell III-D operated with hydrogen at (a) 800°C, (b) 750°C, and (c) 700°C.

Figure 5-8 (a), (c), and (d) show the impedance spectra measured from four Cell III samples operated with hydrogen at 800°C, 750°C, and 700°C, respectively. DRT analysis was performed to the obtained impedance data to gain more understanding on the electrode processes during cell operation [289]. Figure 5-8 (b), (d), and (e) show the corresponding DRT plots for four Cell III samples operated at different temperatures. Five peaks can be identified from the DRT plots, suggesting five individual electrode processes during cell operation. Based on previous studies on the anode-supported SOFCs, these five peaks can be explained as follows [289, 291, 294, 342, 343]:

- P1 (4-20 kHz): Ionic transport and gas diffusion within the anode functional layer.
- P2 (0.4-4 kHz): Charge transfer process at TPBs within the anode functional layer.
- P3 (10-400 Hz): Chemical surface exchange of O_2 and bulk diffusion of O^{2-} within the cathode.
- P4 (1-10 Hz): Gas diffusion in the pores of anode substrate and overlapped gas conversion.
- P5 (0.1-1 Hz): Gas diffusion in the cathode at low oxygen partial pressure.

To quantify and analyse the contribution of each process to the overall cell polarisations, the measured impedance spectra were fitted by a DRT-based equivalent circuit model (ECM) shown in Figure 5-8 (g). The DRT-based ECM includes a resistor, Rs, that is connected in series with five parallel resistor-constant phase elements (R-CPEs). Rs represents the R_{ohm} of the cell, which was determined as the first intersection of the Nyquist plot with the real values axis. Five parallel-connected R-CPE elements, R1-CPE1, R2-CPE2, R3-CPE3, R4-CPE4, and R5-CPE5 represent five distinct processes, P1, P2, P3, P4, and P5, respectively.

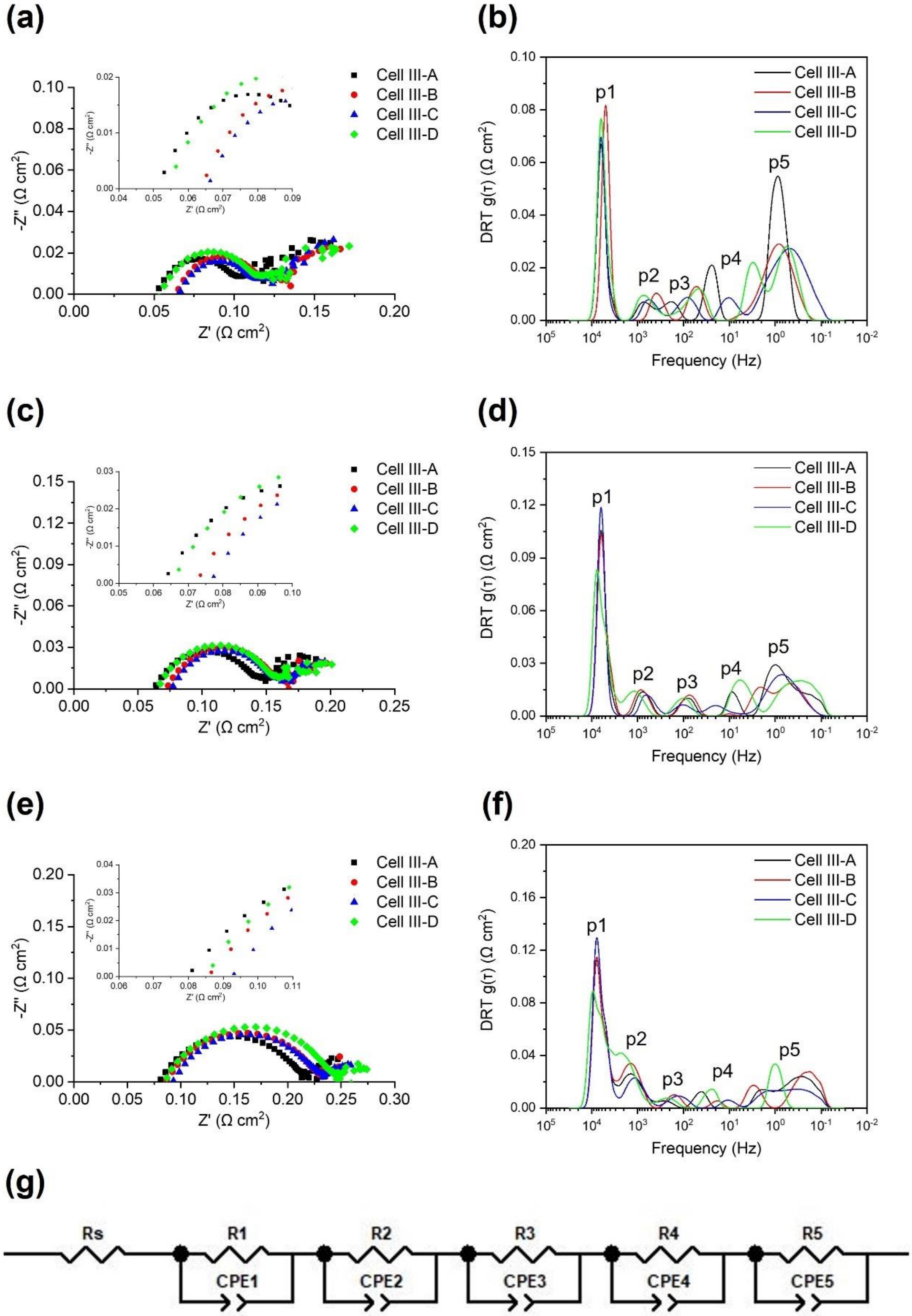

Figure 5-8: Nyquist plots and corresponding DRT plots of Cell III-A, Cell III-B, Cell III-C, and Cell III-D operated with hydrogen at (a, b) 800°C, (c, d) 750°C, and (e, f) 700°C, (g) DRT-based equivalent circuit model used for impedance data simulation in ZView (the insets in a, c, e represents a magnified view for the presented Nyquist plots).

The fitting of the measured impedance data was carried out with the commercial software ZView. Line plots in Figure 5-9 (a), (b), and (c) show the ECM-fitted impedance spectra for the prepared four Cell III samples operated with hydrogen at 800°C, 750°C, and 700°C, respectively. Aided by the DRT analysis and ECM-fitting in ZView, the resistance of each electrode and overall polarisation resistance can be obtained. The deconvoluted resistance and CPE values obtained by using the ECM shown in Figure 5-8 (g) and values shown in Appendix Table 5, Appendix Table 6, and Appendix Table 7. The EIS results confirmed that the variations in R_{ohm} and R_p of Cell III samples at the same operating temperature are relatively small, which may be attributed to the slight difference in the GDC layer thickness. By comparing the microstructure of the prepared GDC films and the resulted power output of the Cell III samples, it was concluded that three cycles of GDC spin coating were necessary to give consistent and high electrochemical performances for Cell III on hydrogen fuel operation.

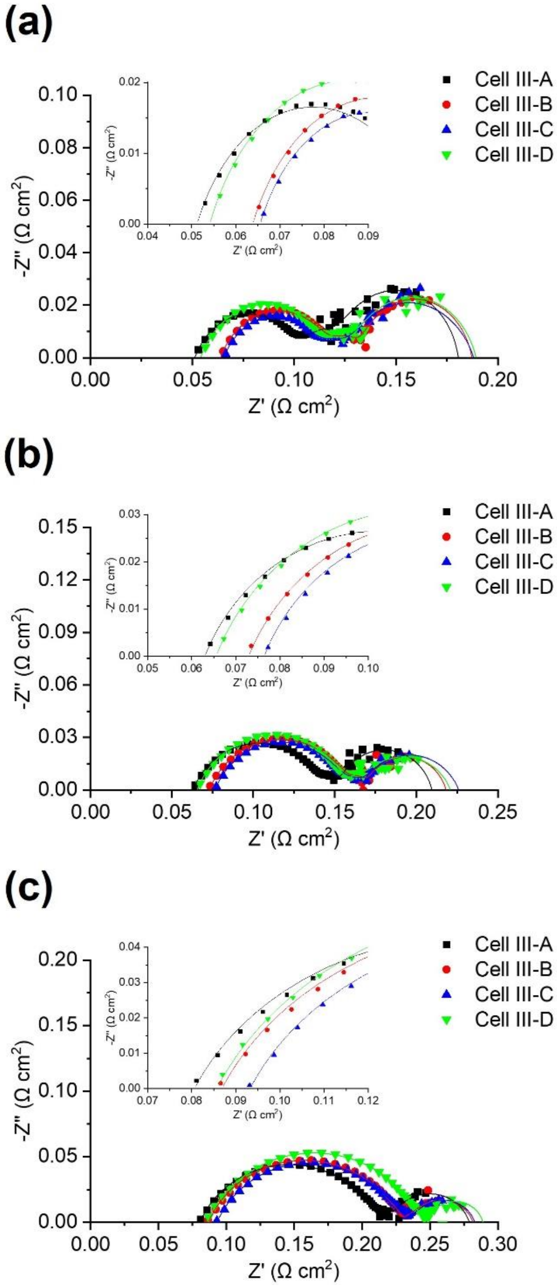

Figure 5-9: Nyquist plots (scatter plots: measured EIS data, line plots: ECM-fitted data) of Cell III-A, Cell III-B, Cell III-C, and Cell III-D operated with hydrogen at (b) 800°C, (c) 750°C, and (d) 700°C (the insets in a, b, and c represents a magnified view for the presented Nyquist plots).

The performance of the cell with three-cycle 40, 45, 50, 55wt.% GDC films was assessed on NiO/ScCeSZ anode-supported half cells with the same configuration as Cell III. According to Figure 5-10 (a), Cell III-50 outperformed the other cells, achieving a P_{max} of 1.0 W•cm^{-2} at 750°C. The cells with 40 and 45wt.% GDC films exhibited closely aligned P_{max} of 0.91 and 0.86 W•cm^{-2}, respectively. However, Cell III-55 produced the lowest P_{max} of 0.80 W•cm^{-2} among the tested samples. This could be attributed to its thick GDC layer (7.8 µm) and cracks across the GDC layer as shown in Figure 4-13 (j), (k), (l).

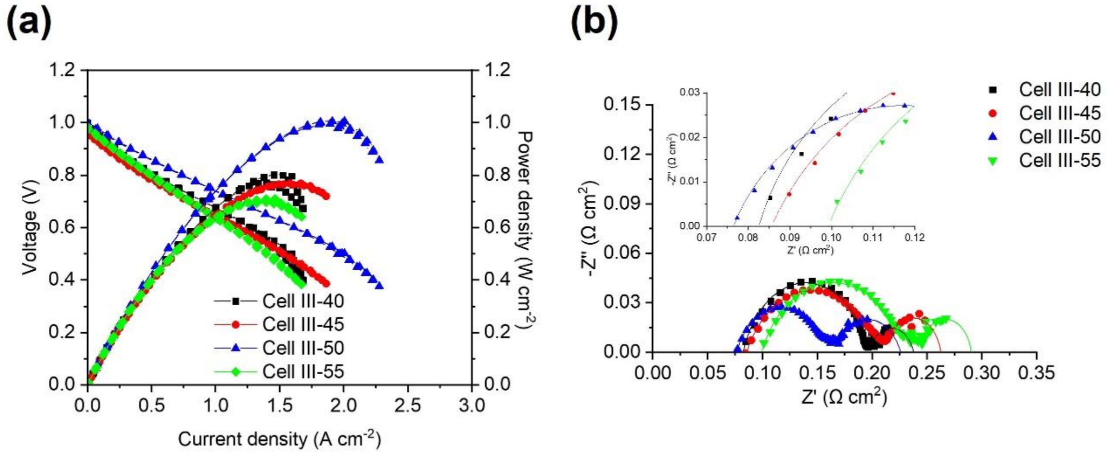

Figure 5-10: (a) i-V curves and (b) Nyquist plots (scatter plots: measured EIS data, line plots: ECM-fitted data) of Cell III with 40-55wt.% GDC films operated with hydrogen at 750°C (the inset in b represents a magnified view for the presented Nyquist plots).

As shown in Table 5-5, the thickness of the GDC film increased with the increase of GDC solid content in the coating liquid. Although 40 and 45wt.% GDC films provided larger thickness of 3.2 and 4 µm, respectively, no significant change in R_{ohm} of the cells was observed from the Nyquist plots shown in Figure 5-10 (b). Cell III-55 exhibited the highest R_{ohm} among all samples because of its thickest GDC film. For the overall polarisation resistance, R_p, a large drop in R_p for the 50wt.% GDC cell was observed. The difference between four Nyquist plots at the low frequency range (0.1 to 100 Hz) is relatively minor, suggesting the invariant gas diffusion processes in the electrodes. Hence, the drop in R_p for the cell with a 50wt.% GDC film can be related to the substantially lowered contribution in the frequency range of 10^2 to 10^4 Hz [344]. The increased high-frequency contributions for the cells with 40, 45, and 55wt.% GDC films are considered to be due to the more porous structure of GDC film (as shown in Figure 4-13) which may worsen the interconnectivity between cathode and GDC layers and then negatively affect the charge transfer at the interface of cathode and GDC layers [319].

Figure 5-11 show the comparison of OCV, P_{max}, R_{ohm}, and R_p across all tested Cell III samples with a 50wt.% GDC loading, subjected to 2 or 3 coating cycles at various temperatures. Notably, both OCV and P_{max} increase with an increasing number of coating cycles. This indicates that a denser GDC layer and better electrochemical performance of the single cell can be achieve with 3 cycles of spin coating.

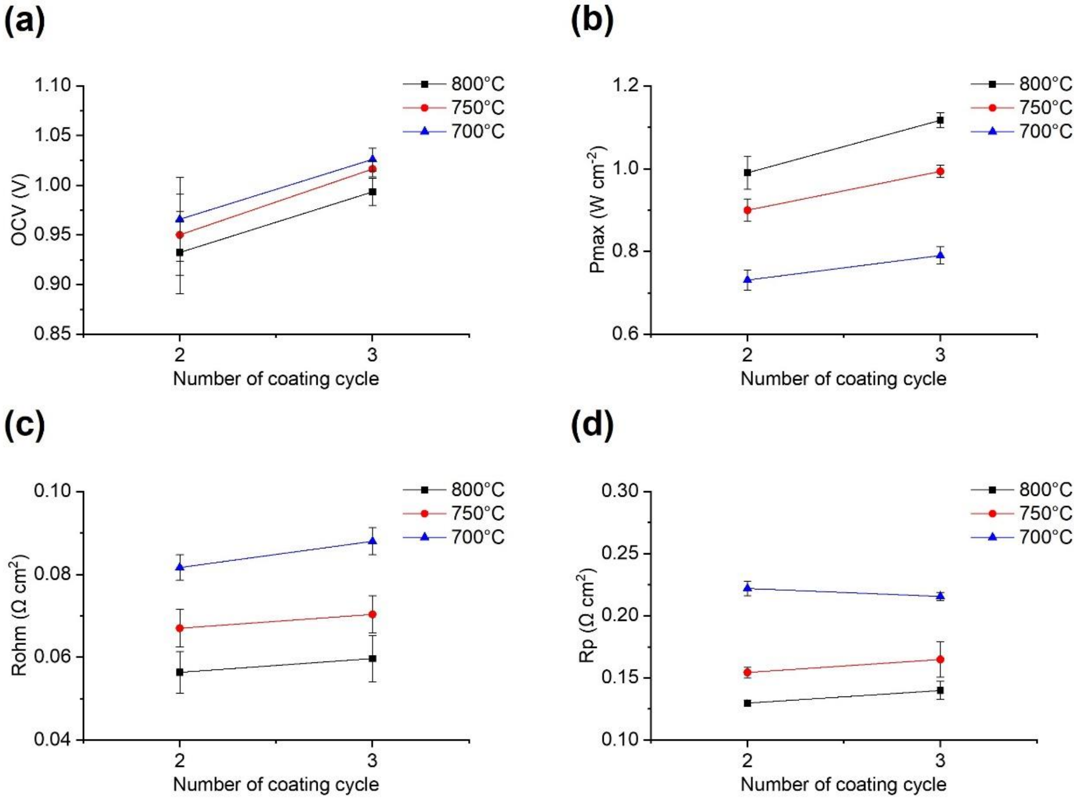

Figure 5-11: Plots of (a) OCV, (b) P_{max}, (c) R_{ohm}, and (d) R_p vs number of coating cycle for Cell III with 50wt.% GDC films at different temperatures.

5.3 Electrochemical performance comparison of the fabricated cells

When studying the effect of fabrication techniques on the electrochemical performance of the prepared single cells, Cell I was found to have low OCVs (~ 0.92 V) at all operating temperatures. After adding a GDC/ScCeSZ composite layer between the GDC and ScCeSZ layers, the OCVs of Cell II increased to ~1.07 V, indicating the improved layer lamination and good electrolyte layer adhesion. Nevertheless, Cell II had the lowest power output and the highest resistance (both ohmic and electrode) amongst all other single cells. This can be attributed to the increased overall electrolyte thickness and the formation of highly resistive (Zr, Ce)O_2-based solid solutions at the interface of GDC and ScCeSZ layers. According to the polarisation curves shown in Figure 5-12 (a)-(c), the slopes (ASR) of Cell II's curve are substantially higher than Cell I's and Cell III's, particularly in the voltage range of 0.5-1.0 V, confirming the high ohmic polarisation of Cell II. The main contribution of ohmic polarisation is the resistance of O^{2-} transport through the electrolyte [10]. In the case of Cell II, a highly resistive electrolyte reduced not only ionic conduction through the electrolyte but also the availability of O^{2-} for electrochemical reactions at the electrode/electrolyte surface [335, 345]. Therefore, even though the electrodes used in three types of cells were identical, the structural change and fabrication approach of the electrolyte were the predominant factors responsible for the significantly lower performance of Cell II.

Figure 5-12 (e) shows that the R_{ohm} of Cell III was around 1/3 and 1/20 of the R_{ohm} of Cell I and Cell II, respectively. This can be explained by the fact that a well-laminated structure, a smaller overall electrolyte thickness, and a higher ionic conductivity are critical properties for the bi-layer electrolyte to minimise the R_{ohm}. Cell I had a thin bi-layer electrolyte with cracks and pores on the GDC layers and delamination between the GDC and ScCeSZ layers after co-sintering, whereas for Cell II, the presence of the

GDC/ScCeSZ composite layer effectively alleviated the delamination issue, but greatly increased the overall thickness of the electrolyte. Furthermore, (Zr, Ce)O_2-based resistive interlayers caused by the interdiffusion of Zr and Ce during co-sintering at 1400°C were found at the interface of GDC and ScCeSZ layers for both Cell I and Cell II, as shown in Figure 4-14 (a) and (b). This resistive layer will substantially reduce the ion conducting performance of the electrolyte during SOFC operation. Cell III, with a spin-coated GDC layer, maintained a thin overall electrolyte thickness and prevented the formation of resistive interlayer, demonstrating the best electrochemical performance among three types of cells. It is also worth mentioning that significant variation in the electrode polarisations between Cell I, Cell II and Cell III was observed in Figure 5-12 (f). Activation polarisation is associated with the electrochemical reactions involved at the electrodes, including hydrogen oxidation at the anode side and oxygen reduction at the cathode side. Since the fabrication process of electrode layers was identical, activation losses caused by the difference in electrolyte/electrode interface between cells could be considered as the main contribution to the increase of R_p.

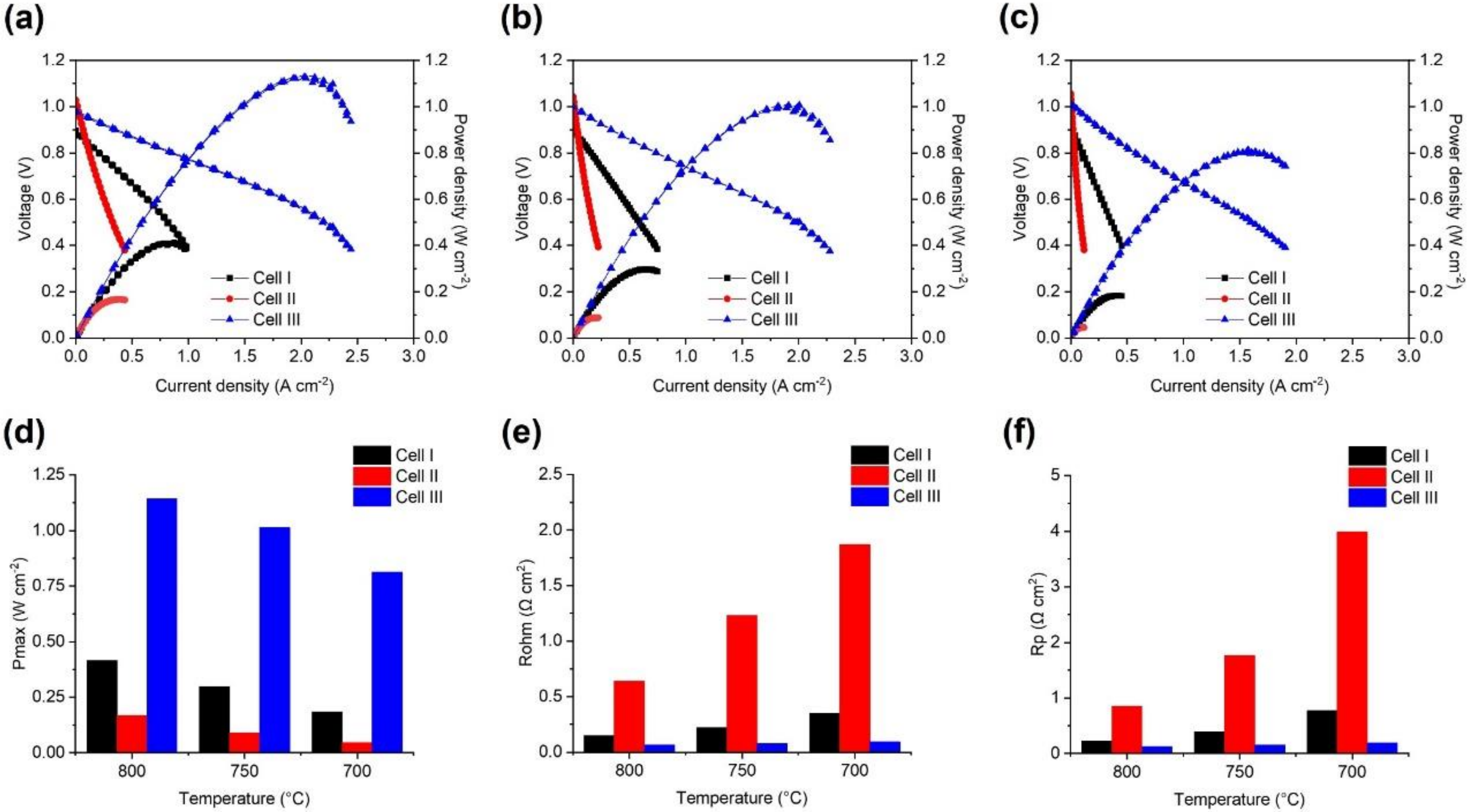

Figure 5-12: (a)-(c) i-V curves of the prepared cells with hydrogen operation and comparison between (d) P_{max}, (e) R_{ohm}, and (f) R_p of the prepared cells at 800°C, 750°C, and 700°C.

5.4 Degradation analysis of the prepared cells

Several operational stability tests were performed on Cell III with a three-cycle coated GDC film to investigate the degradation behaviour under different current loads. Two long-term tests were conducted at 750°C with a current load of 0.2 A•cm^{-2} (Cell III-200) and 1.0 A•cm^{-2} (Cell III-1000) over 1200 h and 500 h, respectively.

Prior to the operational stability test, Cell III-200 was reduced in hydrogen for 12 h until OCV reached 1.0 V, followed by initial electrochemical measurements such as OCV, EIS, and i-V characterisations. After the initial measurements, Cell III-200 was operated in galvanostatic mode with an applied current density of 0.2 A•cm^{-2} at 750°C for 1200 h during the long-term test. Figure 5-13 (a) illustrates the change in cell voltage under the galvanostatic 0.2 A•cm^{-2} current density as a function of operating time. Rapid performance degradation with a 0.074 V (8.23% in respect to the starting voltage) voltage drop in the first 300 h of operation was identified. Afterwards, the cell voltage linearly dropped for the following 900 h of operation with a greatly reduced degradation rate of 0.028 V/kh or 3.16%/kh. Compared to the state-of-art cell performance degradation rate of 0.5 to 1%/kh for planar ASCs operated at similar temperatures [346-348], the degradation rate of Cell III-200 at the stable stage was more than doubled. Therefore, the primary objective of the degradation analysis in this study was to analyse factors that caused rapid degradation of cell performance at different stages and to provide potential solutions to prevent it.

After conducting the Kramers-Kronig validity test using the Lin-KK Tool, the residual for real (Z') and imaginary part (Z'') of the measured impedance data at 0 h over frequency can be plotted as shown in Figure 5-13 (b). Most of the relative errors of real and imaginary part of the impedances are below the acceptable threshold of 0.5% [289]. Thus, DRT analysis can be performed to the measured impedance data of Cell III-200 to study the degradation behaviour of each electrode process as a function of operating time.

Figure 5-13 (c) shows the obtained DRT plots of Cell III-200 at different operating time, with five identified peaks. The AFL-related processes P1 and P2 continuously increased with the operating time, which was caused by the change of anode structure due to Ni coarsening [292, 293]. Ni coarsening within the anode functional layer decreased the TPB length at the anode/electrolyte interface, thus leading to cell performance degradation by restricting electrochemical reaction and charge transfer [349-351]. On the other hand, P3 and P4 peaks slightly increased at the first 240 h and then remained stable until 715 h of operation. P3 is a process related to oxygen surface exchange and O^{2-} diffusion in the LSCF cathode, while P4 mainly represents the gas diffusion in the porous anode substrate. Notably, no obvious variation of P5 was observed from the DRT plots, suggesting a relatively stable gas diffusion process in the porous cathode.

Values of the time constant and resistance for each electrode process can be derived from the DRT analysis for quantitative interpretation and investigation on degradation behaviour of various electrode processes [293, 352]. Using the DRT-based equivalent circuit model (ECM) shown in the insect of Figure 5-13 (d), the measured impedance data of Cell III-200 at various time were fitted with ZView. The data obtained from the ECM fit aligns closely with the measured impedance data, as shown in Figure 5-13 (d).

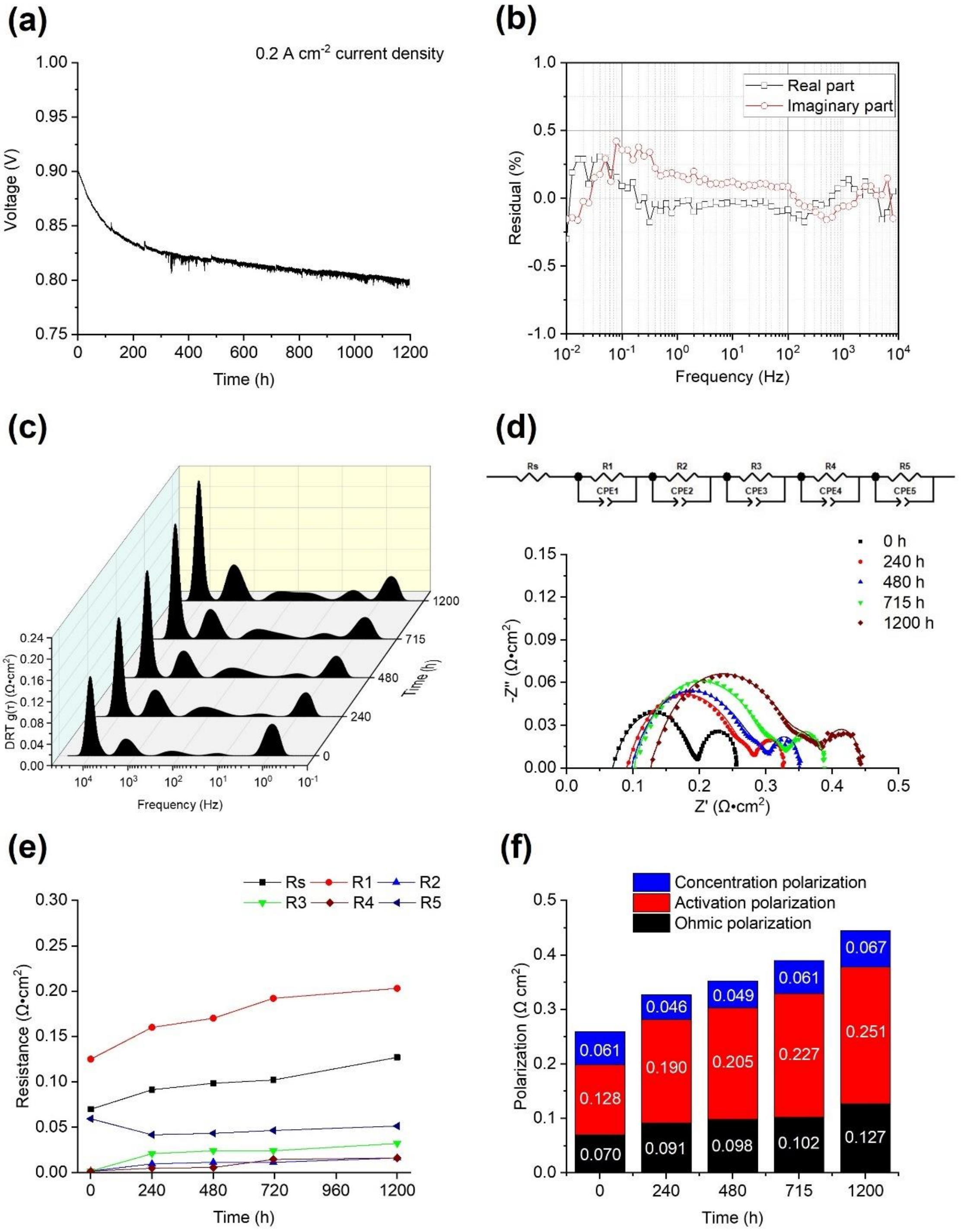

Figure 5-13: (a) voltage output of Cell III-200 during stability test with 0.2 A•cm^{-2} applied current at 750°C, (b) plot of Kramers-Kronig residuals for the real (Z') and imaginary part (Z'') of the measured impedance data, (c) DRT plots of the measured impedance data, (d) Nyquist plots (scatter plots: measured EIS data, line plots: ECM-fitted data) of Cell III-200 (the inset represents the DRT-based equivalent circuit model used for impedance data fitting), (e) evolution of the each ECM-fitted resistance during the long-term operation, (f) contribution of different polarisations at different operating time.

Aided by DRT analysis and ECM fitting, the impedance of Cell III-200 can be separated into ohmic resistance and five polarisation resistances. The evolution of each resistance over long-term operation can be plotted as Figure 5-13 (e). As Rs represents the ohmic resistance of the cell, an obvious increase of R_{ohm} was observed after 240 h and 1200 h of operation compared to their previous measurements. The sealing material (Ag paste) for SOFC button cell testing was found to be slightly damaged after cooling down the testing furnace, leading to the reoxidation of Ni on the edges of the button cell, as shown in Figure 5-14 (a). As the current collector on the anode side was contacted with the sealing material, the presence of NiO on the anode side could also reduce the electronic conductivity, negatively impacting on the current collecting during cell operation. Figure 5-14 (b) presents a cross-section image of Cell III-200, demonstrating a cracked GDC/ScCeSZ bi-layer electrolyte after 1200 h of operation. At least three slope values can be observed from the voltage evolution curve shown in Figure 5-13 (a) in the first 300 h of operation, but EIS measurements and SEM characterisations were only performed after an electrochemical measurement cycle and the end of cell operation, respectively. Thus, insufficient information of impedance spectra information and cell microstructure can be provided to associate the difference in degradation rate with the specific post-test findings. However, it is speculated that sealing degradation and the formation of the $SrZrO_3$ resistive compound at the GDC/ScCeSZ interface occurred at the beginning of operational stability test (before 240 h), thus causing rapid cell performance degradation and a substantial increase in R_{ohm} at the starting stage of cell operation.

As shown in Figure 5-13 (e), R1, R2, R3, represented as the activation polarisation of the Cell III-200, showed an obvious increment during the cell operation, which are in good agreement with the DRT analysis. Ni depletion in the anode functional layer and Ni coarsening can drastically decrease the active TPB length of the SOFC anode, resulting in the deteriorated anodic ionic transport and gas diffusion processes, as well as the negatively affected charge transfer reactions in the anode functional layer. R3, the polarisation resistance caused by oxygen surface exchange and ionic diffusion in the SOFC cathode, showed a significant increase from 0.0016 $\Omega \bullet cm^2$ at the beginning to 0.0208 $\Omega \bullet cm^2$ at 240 h of operation. The sealing degradation and/or the structural damage of GDC/ScCeSZ bi-layer electrolyte that occurred amidst the first 240 h of operation were responsible for the growth of R3. In the following 960 h of operation, R3 only increased from 0.0208 $\Omega \bullet cm^2$ to 0.0320 $\Omega \bullet cm^2$, suggesting a slow deterioration of cathode microstructure during long-term operation [293].

R4 & R5 are responsible for the concentration polarisation of Cell III-200, representing gas diffusion in both electrodes and anode gas conversion. Leonide et al. suggested the polarisation contribution from gas diffusion in the LSCF cathode (P5) is negligible when air is used as oxidant for SOFC [289]. Hence, the change of concentration polarisation can be attributed to gas diffusion and gas conversion in the anode substrate. As P4 is associated with gas diffusion and gas conversion in the anode substrate, the change of P4 over time could be mainly affected by porosity, sealing, and TPB density [292]. When compared to the continuously increasing activation polarisation shown in Figure 5-13 (f), the concentration polarisation of Cell III-200 initially reduced from 0.061 to 0.046 $\Omega \bullet cm^2$ during the initial 240 h of operation and finally increased to 0.067 $\Omega \bullet cm^2$ after 1200 h of operation. Since the cell was initially reduced in hydrogen for 12 h under OCV condition, the high concentration polarisation at the start of the operation can be attributed to the incomplete reduction of part of NiO in the anode. Without full reduction of NiO in the anode, the gas diffusion in the anode can be restricted during cell operation, resulting in a high concentration polarisation [292]. Further increase in concentration polarisation could be explained by the hindered anode gas diffusion due to the microstructural change of anode from Ni coarsening and Ni reoxidation [353]. Compared to the smooth nickel particles with a diameter of around 1.0 µm in the as-reduced anode surface shown in Figure 5-14 (c), it is evident that larger and more porous nickel agglomerates with a diameter ranging from 2.0 to 4.0 µm were found on the post-test anode surface, as shown in Figure 5-14 (d). Such evidence confirmed the Ni coarsening and Ni reoxidation in the anode over long-term operation.

Figure 5-14 (b) shows a cross-section image of Cell III-200 after the long-term stability test, demonstrating the cracked ScCeSZ-GDC bi-layer electrolyte. This can be considered as the main contribution to the increase in R_{ohm} during cell operation. Since the anode current collector was contacted with the sealing material, the damaged sealing material shown in Figure 5-14 (a) could also have increased the cell R_{ohm} by negatively affecting the current collection during SOFC operation. It is known that zirconia-based materials can maintain good microstructural stability during SOFC operation at high temperature [336, 353-355]. Hence, redox of Ni contents is the major cause of anode microstructural change. Compared to the smooth nickel particles on the as-reduced AS shown in Figure 5-14 (c), larger and porous nickel agglomerates with sizes of 2 to 4 µm were found on the post-test AS surface shown in Figure 5-14 (d). The growth of Ni particle size on the anode surface was attributed to Ni coarsening and Ni redox cycling during SOFC operation [353, 355-357]. Additionally, Sr has been found at the interface of the GDC and ScCeSZ layers after the 1200-hour operational stability test, as shown in Figure 5-14 (e). This finding confirms the diffusion of Sr from the LSCF cathode during operation.

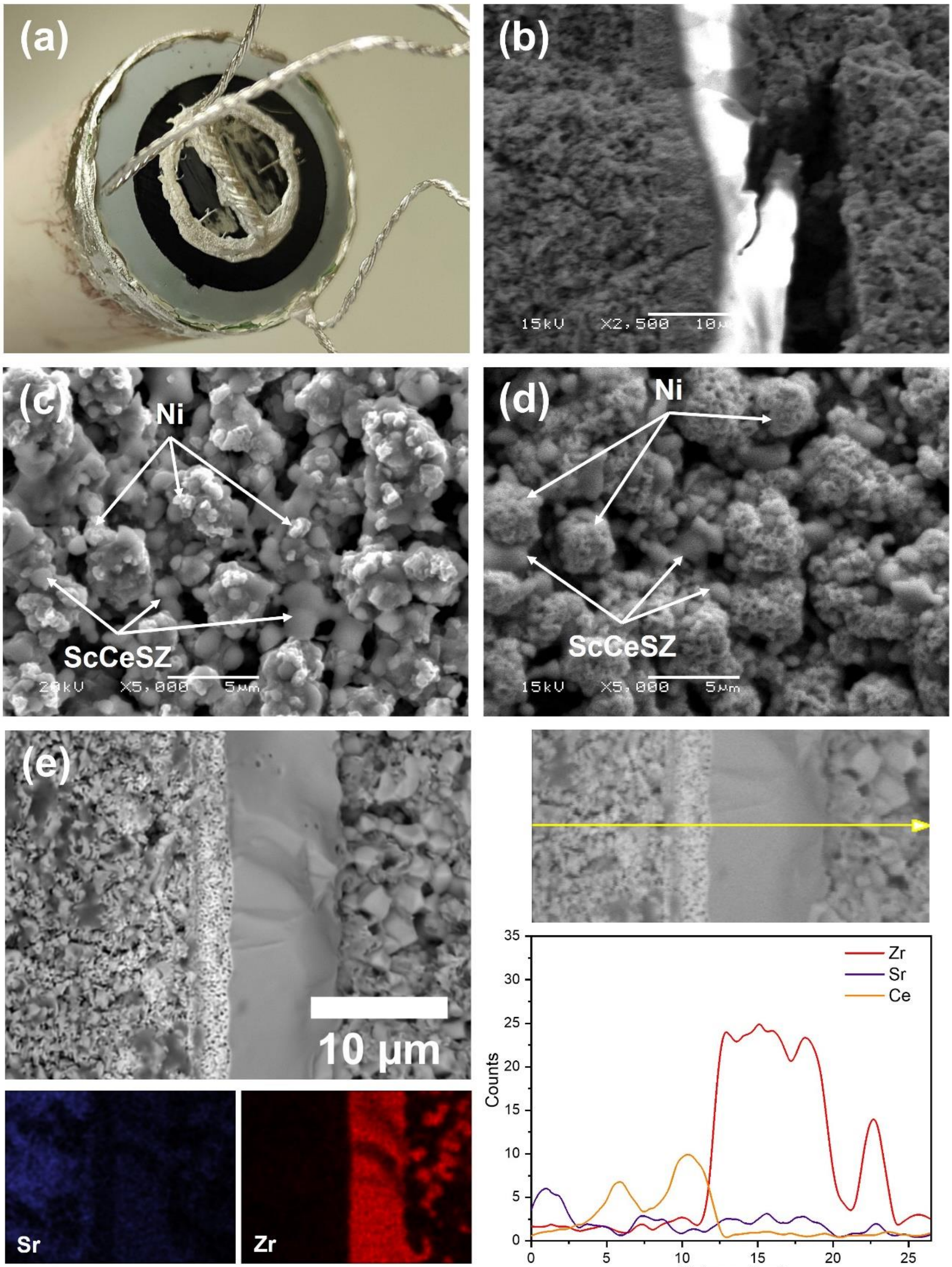

Figure 5-14: (a) cell appearance after 1200 h operation in hydrogen, (b) cross-section with cracked ScCeSZ electrolyte, (c) AS surface after H_2 reduction, (d) AS surface after 1200 h operational stability test in H_2, and (e) cross-section image of post-test Cell III-200 with EDS mapping and line-scan results.

For the Cell III-1000 operated at the applied current density of 1 A•cm^{-2} at 750°C, a voltage degradation rate of 0.098 V/kh was observed in Figure 5-15 (a) during 500-h operation. By comparing the degradation rate of Cell III-200 and Cell III-1000, the degradation rate of the SOFC single cell increased with increasing current density. This is in good agreement with the degradation results reported by Hagen et al. at 750°C [358]. Compared with the 6.76% degradation in voltage output, the P_{max} of Cell III-1000 decreased by 16.04% after 500 h of operational stability test. The polarisation curves in Figure 5-15 (b) can be divided into three regions, activation polarisation dominated region (0 to 0.5 A•cm^{-2}); ohmic polarisation dominated region (0.5 to 1.5 A•cm^{-2}); and concentration polarisation dominated region (> 1.5 A•cm^{-2}). The i-V slope in the activation polarisation dominated region increased with operating time, but no significant changes can be observed in the other i-V curve regions. Barfod et al. [349] reported that the high-frequency and low-frequency parts of the Nyquist plot were related to activation and concentration polarisation, respectively. Figure 5-15 (c) shows the ECM-fitted Nyquist plots of the cell measured at 0.7 V after 0, 100, 200, 300, 400, and 500 h of operation, which were obtained by performing ECM simulation in ZView software based on the measured impedance data. According to the determined five processes identified from DRT analysis, the contribution of polarisation of the cell can be determined and plotted as shown in Figure 5-15 (d). The activation polarisation (first semi-circle) of the cell increased as a function of time, but ohmic polarisation only slightly changed after 400 h of operation. The increase in the contribution of ohmic and activation polarisation were around 22.4% and 31.2%, respectively. Nevertheless, the change in concentration polarisation was negligible.

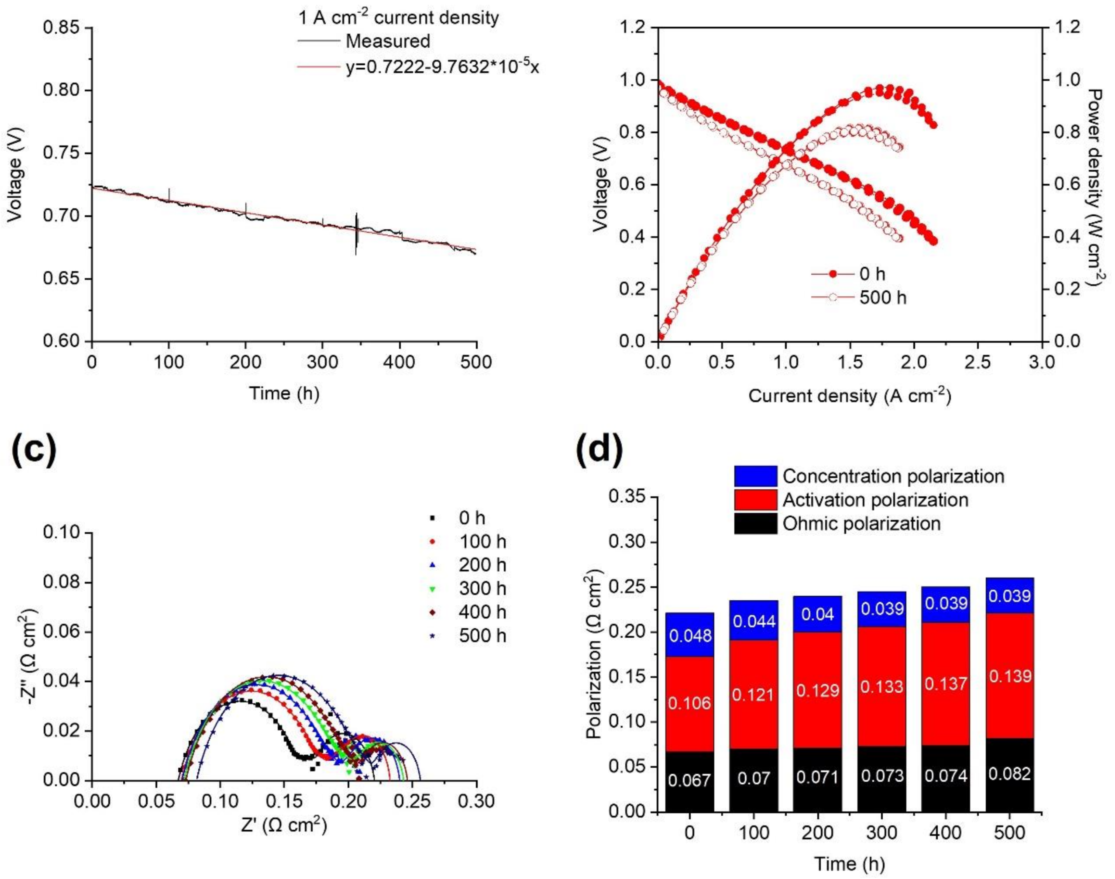

Figure 5-15: (a) voltage output of Cell III-1000 during stability test with 1 A•cm^{-2} applied current at 750°C, (b) i-V curves before and after stability test, (c) Nyquist plots (scatter plots: measured EIS data, line plots: ECM-fitted data), and (d) contribution of different polarisation elements of the cell at different operating times.

Figure 5-16 (a) and (b) show the Ni/ScCeSZ anode surface morphology of Cell III-1000 after the 500-hour stability test with hydrogen as fuel, where significant nickel grain growth and porosity reduction were observed. The size of Ni grains on the Cell III-1000 anode surface was in the range of 3.0 to 7.0 µm, which was slightly greater than the Ni agglomerates on the anode surface of Cell III-200. This finding suggests that the growth rate of Ni particles is higher at high current density. Figure 5-16 (c) shows the elemental distribution of Sr throughout the cross section of the post-tested Cell III-1000. A sharp increase of Sr concentration can be identified at the interface of GDC and ScCeSZ layers, indicating the diffusion of Sr from the LSCF cathode to the ScCeSZ electrolyte. Formation of a $SrZrO_3$ insulating layer between the zirconia-based electrolyte and ceria-based barrier layer was found after LSC/LSCF cathode sintering when the barrier layer is porous [270, 359-361]. To achieve a fully densified GDC layer, the sintering temperature should be around 1500°C [27, 362]. As the GDC layer prepared in this work was sintered at 1200°C, it was more porous than the 1400°C sintered ScCeSZ layer. Khan et al. [363] have reported that an SOFC with a 2.4 µm porous GDC layer showed more $SrZrO_3$ formation at the GDC/ScCeSZ interface compared to an SOFC with a 3.4 µm dense GDC layer after long-term testing. Lu et al. [364] also suggested that the porous doped-ceria would give relatively weak prevention of Sr diffusion towards zirconia electrolyte during both cathode sintering and cell operation. The diffusion of Sr through the GDC layer not only promotes the formation of a highly resistive $SrZrO_3$ layer but also reduces catalytic activity of the cathode for the oxygen reduction reaction [293, 365]. Therefore, the performance degradation of Cell III-1000 during SOFC operation could be mainly attributed to the increase in activation polarisation caused by the Ni coarsening in the anode incorporated with the Sr migration in the cathode [366-368].

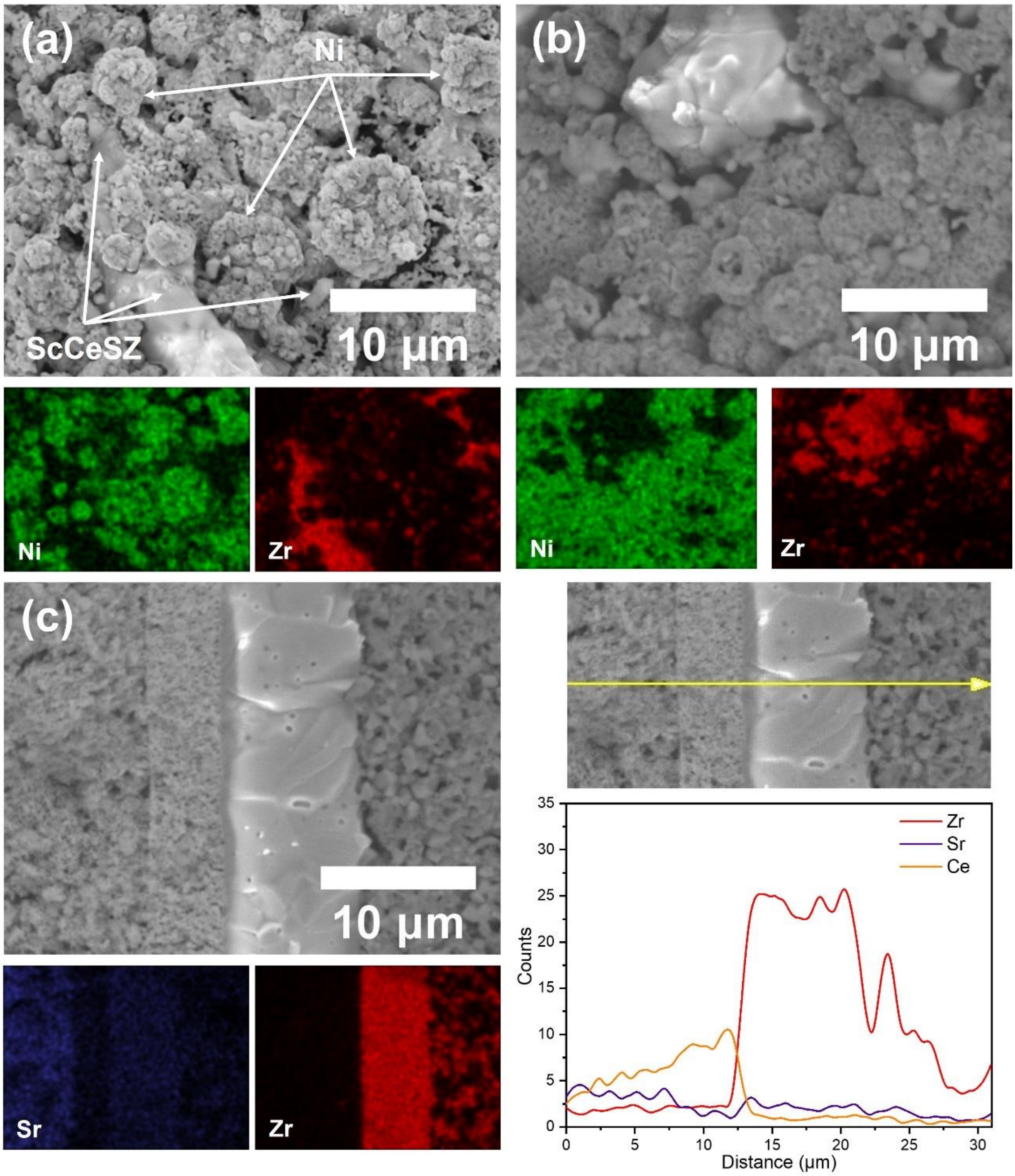

Figure 5-16: (a, b) Anode surface morphology with EDS mapping results, (c) cross-section image with EDS mapping and line-scan results for Cell III-1000 after 500 h operation in hydrogen.

Ni coarsening has been considered as one of the most dominant causes for the performance degradation in both Cell III-200 and Cell III-1000, resulting in decreased Ni catalytic activity, degraded surface area, poor connectivity of the Ni network, and reduced gas diffusivity [366, 369]. According to the obtained results, it was noticed that both Ni growth rate on the anode surface and voltage degradation rate increased with the applied current load. Mogensen et al. [370, 371] reported that Ni migration away from the anode active layer is more severe at high current density (0.5 to 1.0 $A \cdot cm^{-2}$) than at low current density (< 0.25 $A \cdot cm^{-2}$). Additionally, the humidity level at the anode side is an important factor that affects cell performance degradation for the horizontal testing rig. Despite the fact that the SOFC test rig is connected to a bubbler after the fuel exhaust for trapping generated water during cell operation, water accumulation at anode triple phase boundaries (TPBs) could still occur. At high current density operating conditions, the production rate of steam from anode TPB is also high [350, 358]. This can negatively affect the diffusion of H_2 to the anode TPBs, especially in the anode substrate [372, 373]. The horizontal set-up of the testing rig may promote the condensation of water vapour at the exhaust end of the alumina tube that was placed outside of the furnace, thus resulting in an increased humidity atmosphere at the anode side and decreased gas exhausting efficiency during SOFC operation. Holzer et al. [374] reported the accelerated growth rate of nickel grains on the Ni/GDC anode in humid environment in comparison to a dry environment. In a humidified reducing environment, volatile $Ni(OH)_2$ can be formed with low formation energy, which can enhance the diffusivity of Ni in the anode and thus accelerate Ni coarsening [375-377]. As a result, TPB length would be reduced and eventually lead to cell performance degradation [367, 369, 375, 378-380].

5.5 Summary

The electrochemical performance of each type of prepared cells was evaluated and compared for three types of cells. Cell III, with a spin-coated GDC thin barrier layer on the ScCeSZ electrolyte, exhibited outstanding electrochemical performance with hydrogen operation in terms of great power density, low ohmic and electrode resistance, and good operational stability at different applied current loads for over 500 h. An equivalent circuit model with five electrode processes was successfully built by deconvoluting the measured impedance spectra of a 1200 h-operated Cell III via DRT analysis. Aided by this model, the degradation behaviour of Cell III could be thoroughly studied. The main mechanism of cell performance degradation was addressed, which was most likely the Ni coarsening at the anode and migration of Sr from the LSCF cathode to the ScCeSZ electrolyte.

CHAPTER 6: DEVELOPMENT OF A CARBON TOLERANT NI-BASED ANODE

6.1 Overview

This chapter presents the electrochemical characterisation of the SOFC cells prepared with 1wt.% of Sn, Ag, Cu, and Fe-modified anodes operated with simulated biogas as fuel. The simulated biogas consisted of 50% CH_4 and 25% CO_2, and 25% N_2, allowing dry methane reforming at the anode side of cells. The electrochemical performance of the prepared cells was evaluated whilst operating with hydrogen or simulated biogas fuels. For each type of cell in this chapter, two samples prepared by the same process and labelled as Ni1, Ni2, Sn1, Sn2, Ag1, Ag2, Cu1, Cu2, Fe1, and Fe2. The cells were subjected to i-V, EIS, and operational stability tests. Post-mortem analyses such as Raman Spectroscopy and SEM were performed to identify the type of deposited carbon on the anode exposed to a dry methane reforming atmosphere. EDS and XPS characterisations were conducted to investigate the elemental distribution and oxidation states of the prepared anodes, respectively.

6.2 Characterisation of the undoped cells

6.2.1 Electrochemical performance

Figure 6-1 (a) and (b) demonstrate the cell voltage and power densities as a function of current density for two undoped cells Ni1 and Ni2, operated with hydrogen or biogas as fuel at 750°C. The maximum power densities (P_{max}) with hydrogen operation were 0.847 and 0.945 $W{\bullet}cm^{-2}$, respectively. The performance difference between the two cells could be attributed to the inevitable deviation of electrolyte and electrode thicknesses of the in-house SOFC single cell fabrication. However, the power output of Ni1 and Ni2 were drastically lower when the cells were operated with biogas as fuel, with P_{max} values of 0.092 and 0.096 $W{\bullet}cm^{-2}$, respectively. According to the operational stability results of Ni1 and Ni2 with biogas operation shown in Figure 6-1 (c) and (d), both cells ceased operation at around 11 h. This halt in cell operation was caused by the structural damage caused to the cell, as indicated by the inset in Figure 6-1 (c). The damage was a result of carbon deposition occurred on the anode when simulated biogas was fed to the fuel stream. Cracks were identified on the biogas-tested cell surface, as well as damage to the electrodes and current collector.

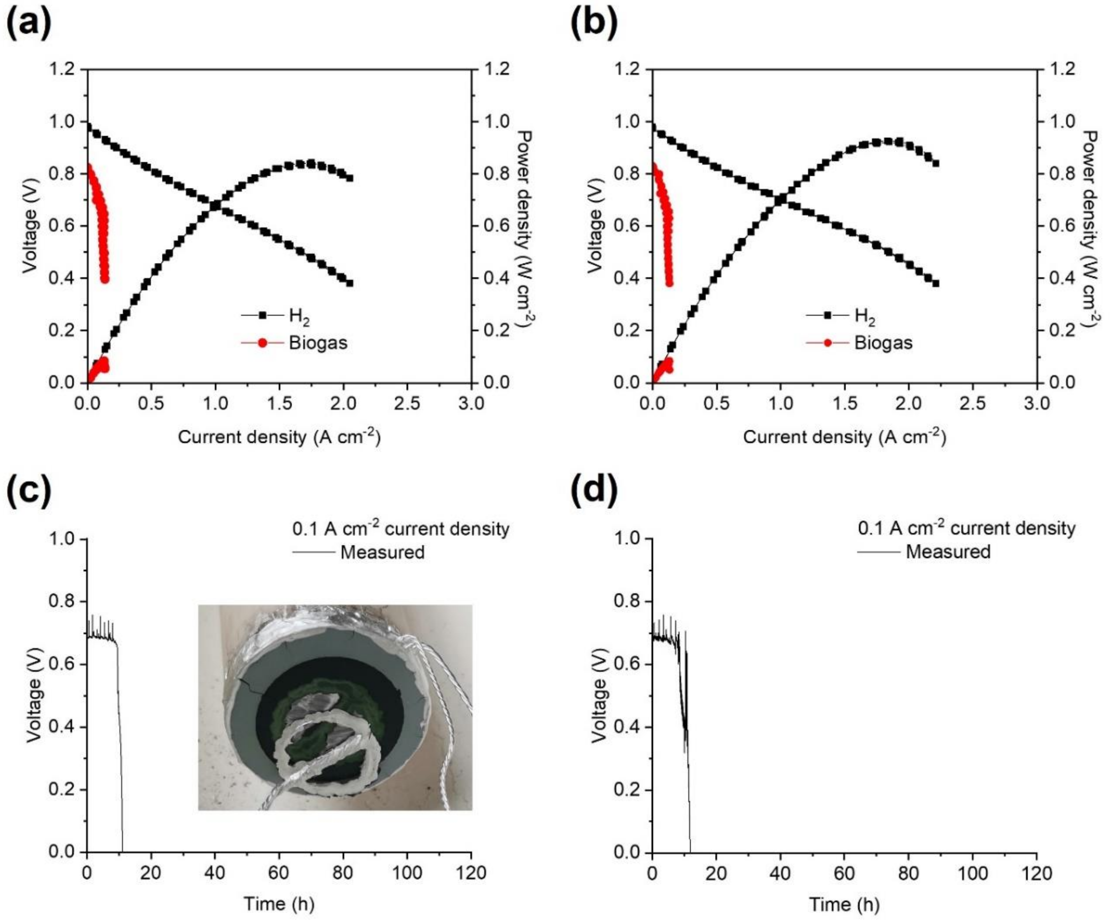

Figure 6-1: i-V curves of (a) Ni1 and (b) Ni2 in hydrogen and simulated biogas at 750°C, voltage output of (c) Ni1 and (d) Ni2 during biogas stability test at 750°C.

Figure 6-2 demonstrates the Nyquist plots for Ni1 and Ni2 operated with different fuels. The R_{ohm} of the two cells were similar, 0.069 and 0.063 Ω•cm^2, respectively, whilst operating with hydrogen as fuel. However, the R_p of Ni1 (0.210 Ω•cm^2) was found to be 0.022 Ω•cm^2 higher than the R_p of Ni2 (0.188 Ω•cm^2), which may be responsible for the lower power output of Ni1. It was also noticed that the first arc of the Nyquist plot for hydrogen-operated Ni1 was larger than that of Ni2, hence, the increase in R_p was caused by higher activation losses during cell operation. By comparing the Nyquist plots of the undoped cells obtained with hydrogen and biogas operations, the cells showed a disproportionately high increase in ohmic and electrode resistances when the fuel was switched from hydrogen to biogas. This suggests poor electrochemical performance of the Ni/ScCeSZ anode in biogas operation. The increased R_{ohm} could be attributed to the reduced anode conductivity caused by carbon deposition on the anode surface, which is consistent with the results reported by Chen et al. [158] in a study of a Ni/YSZ anode SOFC fuelled with simulated syngas (CH_4, CO_2, CO, H_2, and H_2O) at 750°C. Studies have shown that the R_p of the cell increases when switching from hydrogen to carbon-containing fuels [62, 158, 381, 382]. This increase in R_p could be caused by the carbon accumulation at the triple phase boundaries (TPBs), which can restrict electrochemical reactions and fuel gas diffusion to the anode functional layer (AFL).

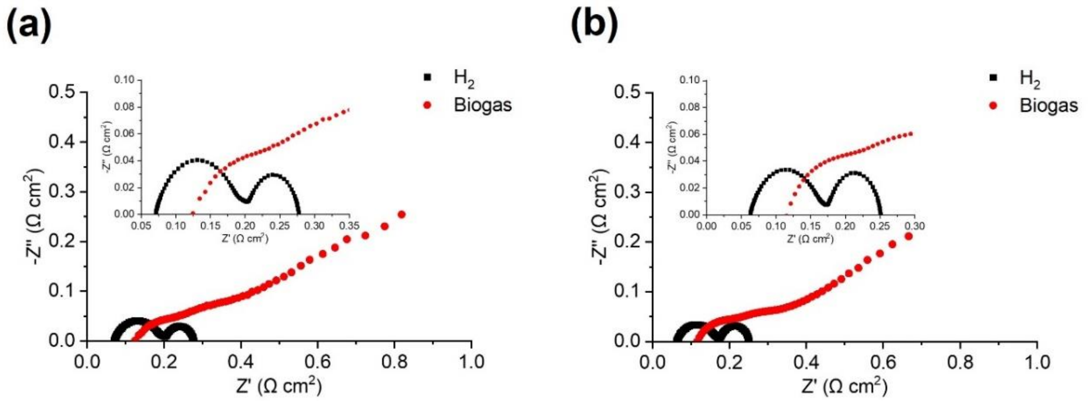

Figure 6-2: Nyquist plots for (a) Ni1 and (b) Ni2 with hydrogen operation (ECM-fitted) and biogas at 750°C.

6.2.2 Post-mortem characterisation

Detection of carbon deposition has been commonly achieved by using Raman spectroscopy [57, 153, 254, 383]. Typically, there are two carbon peaks appeared at around 1350 cm^{-1} and 1580 cm^{-1}, also known as D and G bands. Figure 6-3 demonstrates the Raman spectra obtained from the biogas-tested cells. The strongest vibrational band in the Raman spectra at ~620 cm^{-1} is assigned to the cubic zirconia [384]. Two large peaks at 1090 cm^{-1} and 1485 cm^{-1}, associated with nickel oxide were detected [353, 385]. Since the undoped cell had severe structural damage after biogas operation, the reduced Ni-based anode exposed to ambient air and then re-oxidised to green nickel oxide. There are two possible explanations for the NiO peaks on the Raman spectra of the doped anode surface. One is the electrochemical oxidation of Ni caused by the O^{2-} ions during SOFC operation, the other explanation involves the oxidation of Ni by O_2 due to the damaged sealings on the cell holder. Both D and G bands appeared on the undoped anode surface after biogas operation at ~1360 cm^{-1} and ~1590 cm^{-1}, respectively, with a D/G intensity ratio of 0.75. This finding suggests that the preferred carbon deposition on the undoped cell is graphitic carbon.

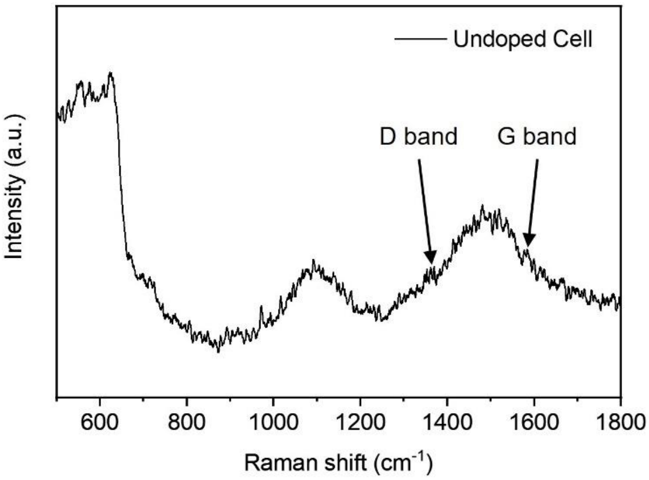

Figure 6-3: Raman spectra of the biogas-tested anode surface of undoped cell.

To investigate the type/morphology of the deposited carbon, SEM was performed to anode surface of the biogas-tested anodes. As Ni1 and Ni2 were completely re-oxidised after the operational stability test in biogas, identifying the deposited carbon was very challenging by SEM. Therefore, a new undoped cell used for identifying carbon deposition was prepared and then operated with biogas as fuel under 0.10 A•cm^{-2} galvanostatic current density for 2 h. Figure *6-4* shows the undoped anode surface after long-term biogas operation. Some carbon fibres can be observed on the Ni particles. The presence of fibrous carbon on the undoped anode surface after biogas operation is in a good agreement of the Raman spectroscopy results.

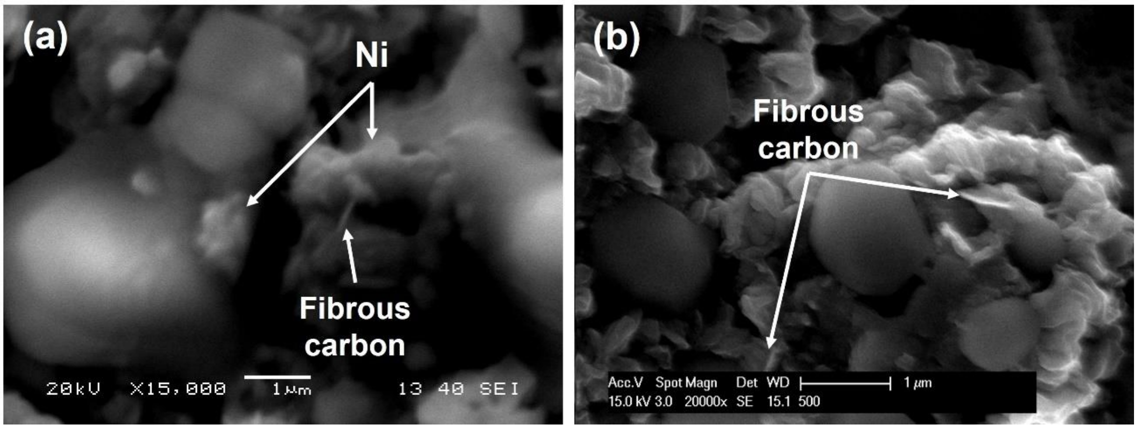

Figure 6-4: SEM images of the anode surface of the undoped cell after biogas operation.

XPS analysis was performed to investigate the surface composition and elemental oxidation states of the biogas-tested anodes. Figure 6-5 (a) and (b) show the XPS spectra for Ni and C the undoped anode surfaces, respectively. The obtained Ni 2p data fitted well with the multiplet-split peaks of NiO at 854.1 and 855.8 eV from Ni $2p_{3/2}$ and a Ni $2p_{1/2}$ peak of NiO at 872.6 eV. The contribution of Ni 2p peaks of Ni metal at 852.6 eV and 870 eV were relatively small. As part of the nickel on the anode surface had been re-oxidised to nickel oxide during the cell testing process, hence, the Ni 2p data of all anodes showed that all samples contained a mixture of NiO (major contribution) and Ni (minor contribution) surface domains [386, 387]. The XPS spectra for C 1s highlighted three main peaks at binding energy of 284.7 eV, 285.8 eV, and 288.5 eV for C-C and C=C bond, C-O-C bond, and O-C=O, respectively. The fitted peaks were highly symmetric and perfectly matched with the sp^3 carbon [388-390].

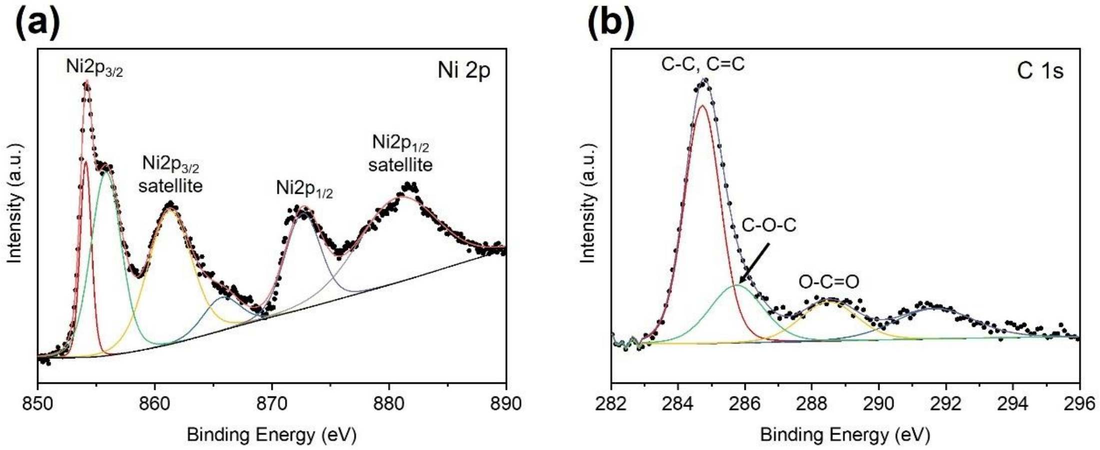

Figure 6-5: XPS spectra for (a) Ni and (b) C of the anode surface of the undoped cell after biogas operation.

6.3 Characterisation of the Sn-doped cell

6.3.1 Electrochemical performance

Figure 6-6 (a) and (b) demonstrate the i-V curves of the Sn1 and Sn2 cells operated with the hydrogen or biogas fuel stream at 750°C. Sn1 exhibited P_{max} values of 0.997 and 0.963 W•cm^{-2} in hydrogen and biogas, respectively. After 120 hours of relatively stable operation with biogas, the P_{max} of Sn1 reduced to 0.810 and 0.786 W•cm^{-2} in hydrogen and biogas, respectively. Compared to Sn1, Sn2 showed slightly lower power output with either hydrogen or biogas as fuels in initial operation, being 0.835 and 0.765 W•cm^{-2}, respectively, but the voltage output degradation rate of Sn2 (0.152 V/kh) was about 47% lower than that of Sn1 (0.286 V/kh) during the biogas operational stability test. After 120 hours of exposure to biogas, the P_{max} of Sn1 and Sn2 decreased by approximately 18.8% and 13.3%, respectively, when the fuel stream was switched to hydrogen. The difference in electrochemical performance between Sn1 and Sn2 could be attributed to the component thickness variations between different batches and heterogeneous distribution of Sn dopant within the porous Ni/ScCeSZ anode.

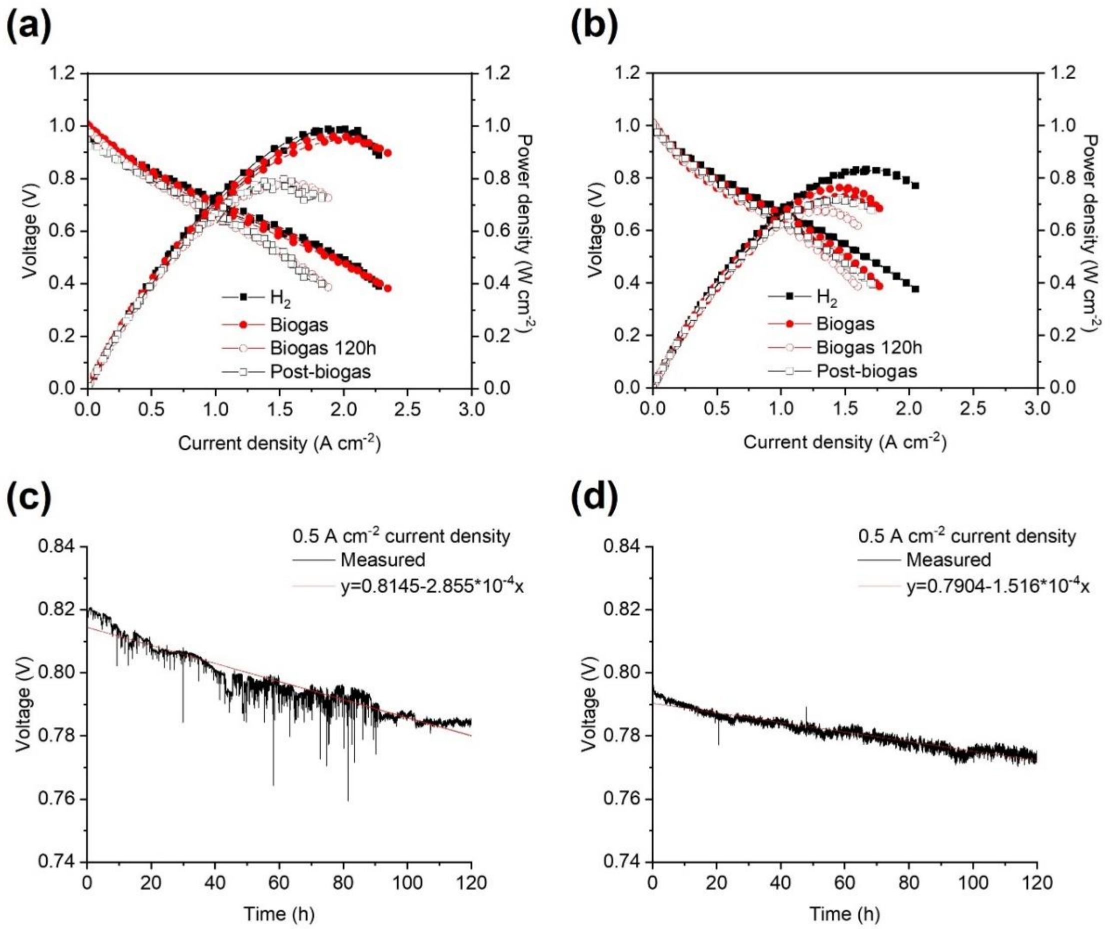

Figure 6-6: i-V curves of (a) Sn1 and (b) Sn2 in hydrogen, simulated biogas, and post-biogas at 750°C, voltage output of (c) Sn1 and (d) Sn2 during biogas stability test at 750°C.

Among all the biogas-tested cells, the Sn-doped cells, Sn1 and Sn2, were the only two samples that demonstrated stable behaviour during the EIS measurement. The residuals of the acquired EIS data from Sn1 and Sn2 were below 1% when subjected to the Kramers-Kronig validity test, thus the EIS data of Sn1 and Sn2 can be thoroughly analysed using the DRT method and ECM fitting. Figure 6-7 (a) and (b) show the ECM-fitted Nyquist plots for Sn1 and Sn2 based on the measured EIS data. Compared to the Sn-doped cells operated with hydrogen fuel, the R_{ohm} and R_p of the biogas-fuelled cells increased by 0.010 and 0.015 Ω•cm^2, respectively. The first arc in the Nyquist plots, in the frequency range of 10 to 10^4 Hz, was found to be the main difference between the EIS results acquired during hydrogen or biogas operation, which is known as activation polarisation. This is in good agreement with the results reported by Arifin et al. [75]. By using the ECM fitting, the impedance data could be deconvoluted to determine the contribution of ohmic, activation and concentration polarisations, as shown in Figure 6-7 (c) and (d). The activation polarisations of the Sn-doped cells in hydrogen increased by 10% after the 120-hour stability test in biogas. Notably, the activation polarisation of Sn1 and Sn2 increased by 27.3% and 7.2%, respectively. In contrast, the change of concentration polarisation for Sn1 and Sn2 were much smaller compared to the activation polarisation, suggesting a relatively stable gas diffusion process in the porous electrodes. Therefore, the increased R_p of the Sn-doped cells was mainly attributed to the increase in activation polarisation. Although optically no obvious carbon deposition was observed from the post-test Sn-doped anode surface shown in Figure 6-9 (a) and (b), carbon deposition could still occur on the anode that is not covered by the Sn dopant during the preparation process. Carbon deposition on the anode, particularly on TPBs, may restrict the charge transfer process of electrochemical reactions and gas diffusion to the AFL, resulting in an increment in activation polarisation [158].

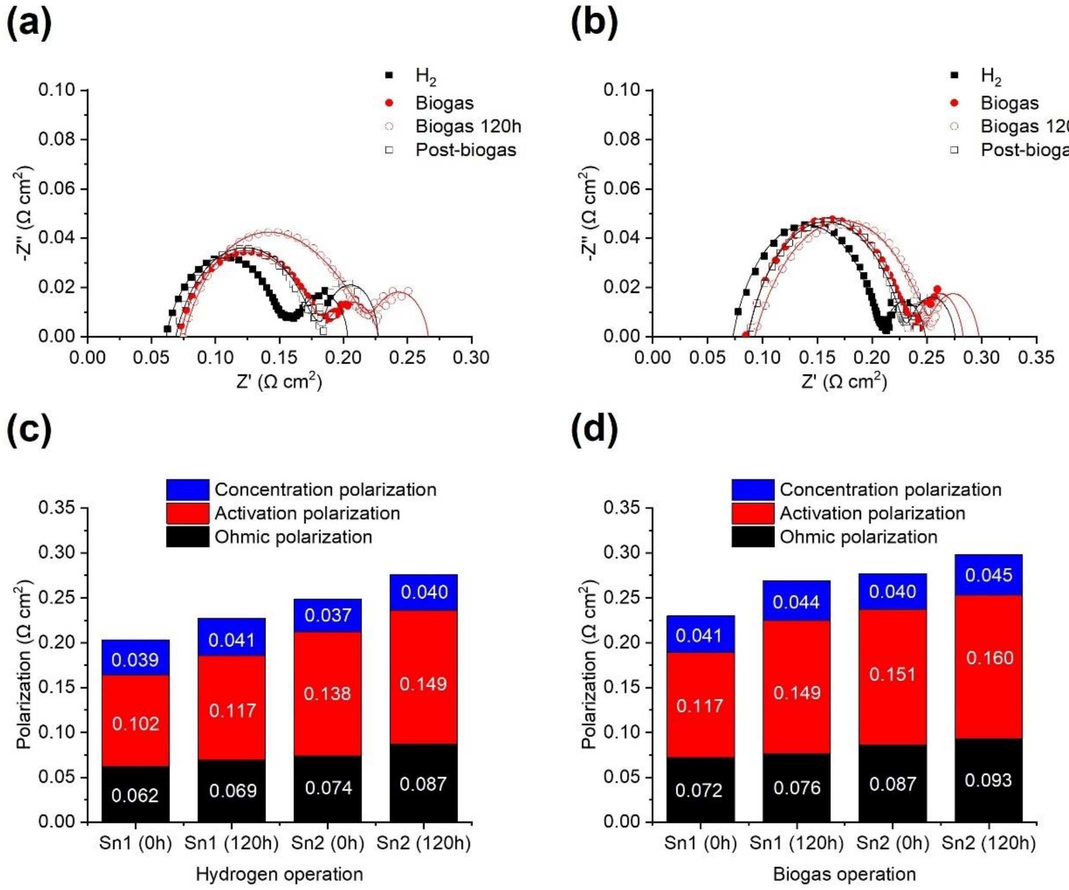

Figure 6-7: Nyquist plots (scatter plots: measured EIS data, line plots: ECM-fitted data) for (a) Sn1 and (b) Sn2 with hydrogen operation (before and after biogas exposure) and biogas at 750°C, contribution of different polarisation for Sn1 and Sn2 with (c) hydrogen and (d) biogas operation.

6.3.2 Post-mortem characterisation

Figure 6-8 shows the Raman spectra of the Sn-doped anode after simulated biogas operation. No observable carbon peaks can be identified due to the presence of broad NiO peak at 1485 cm^{-1}. Therefore, it is necessary to perform SEM to further investigate the carbon deposition on the biogas-tested Sn-doped anode surface.

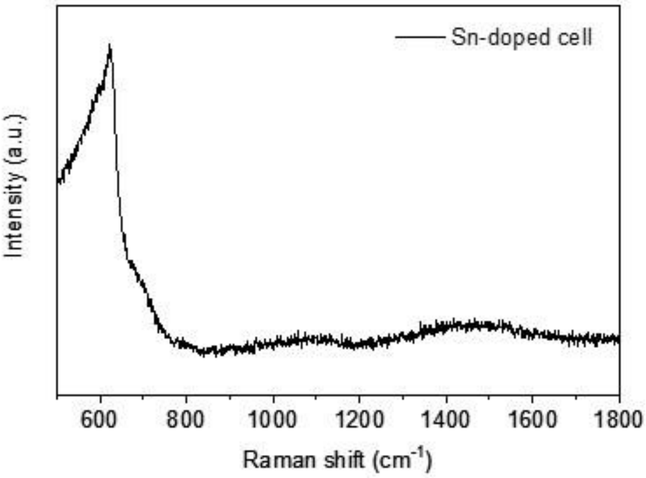

Figure 6-8: Raman spectra of the biogas-tested anode surface of Sn-doped cell.

Figure 6-9 (a) and (b) show the surface of the Sn-doped anodes after biogas operation. No observable carbon can be identified on the Sn-doped anode surface. Compared to the other samples, the size of Ni particles showed no significant growth from the reoxidation process, which was in good agreement with the Raman spectroscopy results.

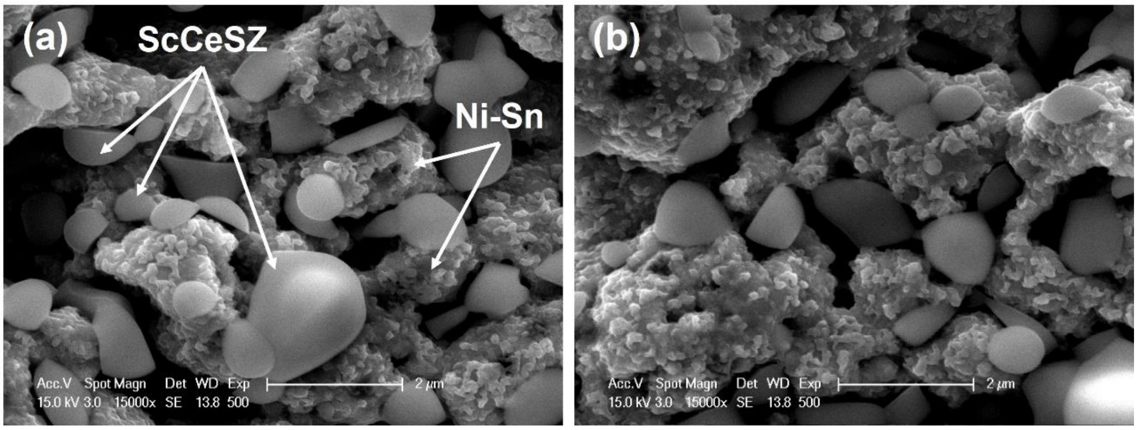

Figure 6-9: SEM images of the anode surface of the Sn-doped cell after biogas operation.

The XPS spectra of Ni of the Sn-doped anode are highly similar with the result of the undoped anode, with contribution from both NiO and Ni. As shown in Figure 6-10 (c), two large peaks that appeared at 486.5 eV and 494.9 eV were from Sn $3d_{5/2}$, Sn $3d_{3/2}$ of SnO_2, respectively [391]. The peak for Sn metal appeared at ~485.2 eV has a much weaker signal than the peaks for SnO_2, indicating mostly oxidised Sn on the anode surface [392].

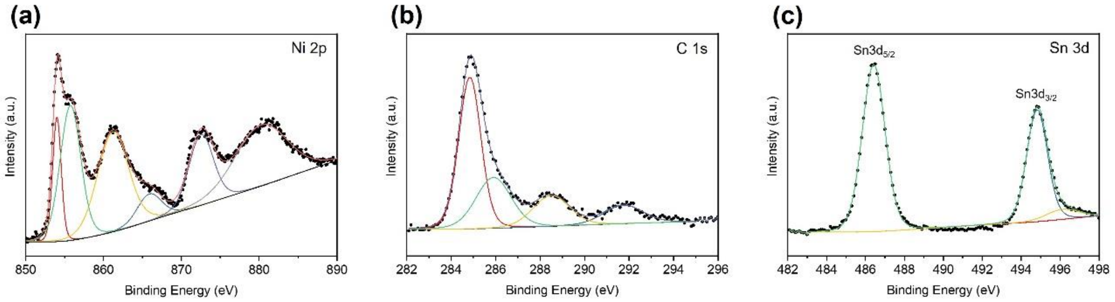

Figure 6-10: XPS spectra for (a) Ni, (b) C, and (c) Sn of the anode surface of the Sn-doped cell after biogas operation.

6.4 Characterisation of the Ag-doped cell

6.4.1 Electrochemical performance

The electrochemical performance of two 1wt.% Ag-doped cells, Ag1 and Ag2, were evaluated, and the results are presented in Figure 6-11. Ag1 exhibited excellent power output in hydrogen as fuel with maximum power density of 0.965 W•cm^{-2} at 750°C, but Ag2 was found to have a lower P_{max} of 0.643 W•cm^{-2} due to sealing material degradation during cell testing. Compared to the undoped Ni/ScCeSZ cells, Ag1 showed a slightly higher P_{max} of 0.135 W•cm^{-2} than the undoped cell with biogas operation. Moreover, the voltage degradation rate of Ag1 upon the biogas fuel stream was 0.461 V/kh during the operational stability test under a 0.10 A•cm^{-2} applied current density, thus demonstrating the enhanced carbon tolerance of the anode due to the addition of a small amount of Ag dopant. Nevertheless, a furnace heating incident occurred at around 92 h, leading to cracking of the cell because of a sudden cooling process. Therefore, Ag1 ceased operation in simulated biogas at around 94 h.

According to Figure 6-12, Ag1 operated on hydrogen as fuel showed R_{ohm} and R_p values of 0.064 and 0.126 Ω•cm^2, respectively, however, the R_{ohm} and R_p for Ag2 were 0.079 and 0.203 Ω•cm^2, respectively. Moreover, the activation and concentration losses for Ag2 were found to be higher than those for Ag1. One possible explanation for the increased losses in Ag2 is the formation of larger Ag particles because of the melting and diffusion of small Ag particles at high operating temperature (750°C). This was confirmed by the EDS results of the Ag-doped anode before and after biogas operation, Figure 6-28 (c) and (d), respectively. The coalescence of these small particles resulted in the formation of larger Ag particles that blocked the Ni catalytic active sites on the anode and hindered gas diffusion channels in the porous anode. Consequently, the blocking of anode active sites and hindrance of anode gas diffusion led to the increase in activation and concentration losses, respectively.

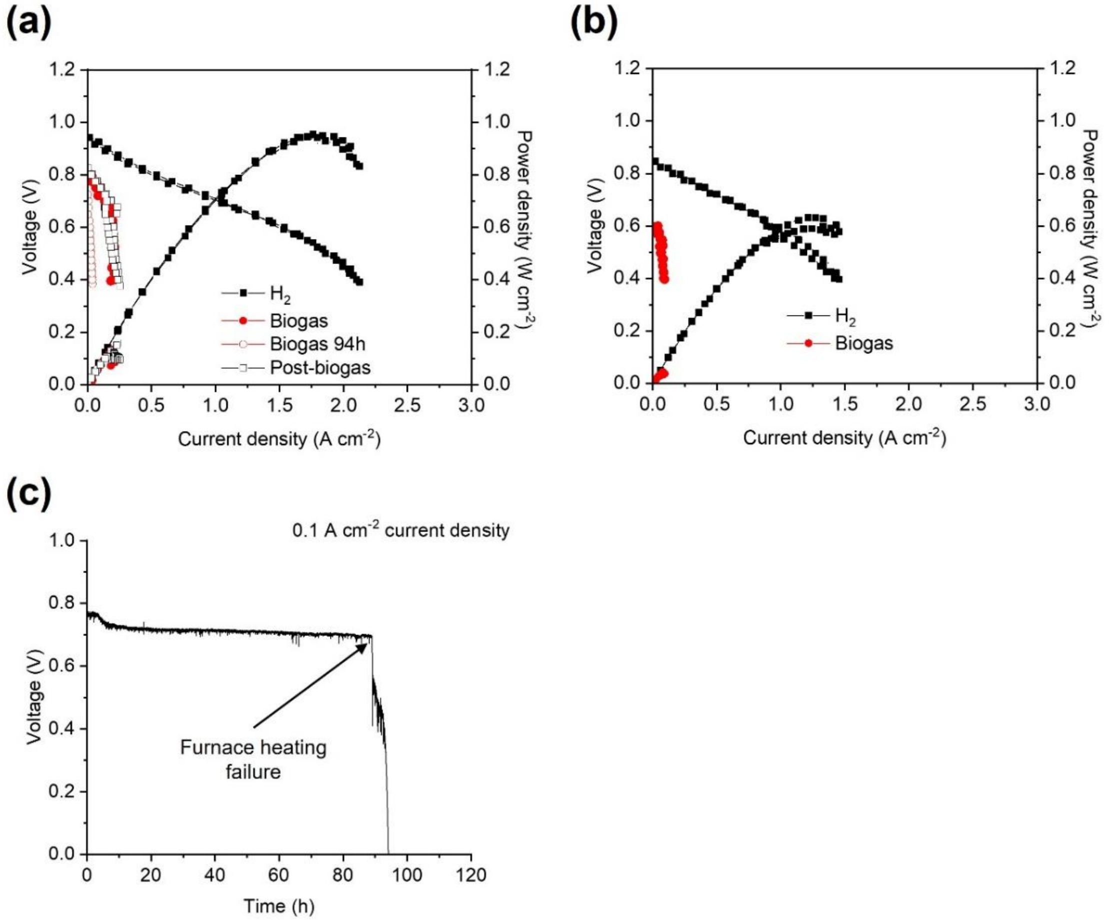

Figure 6-11: i-V curves of (a) Ag1 and (b) Ag2 in hydrogen and simulated biogas at 750°C, (c) voltage output of Ag1 during biogas stability test at 750°C.

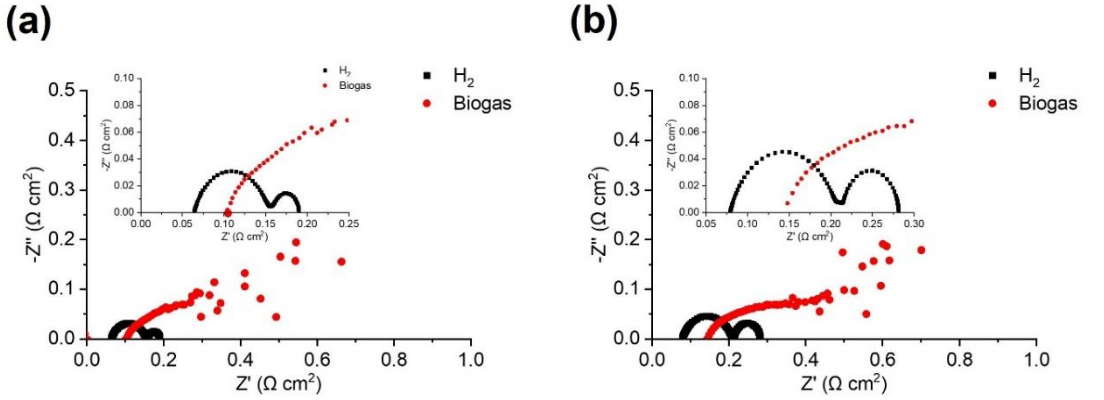

Figure 6-12: Nyquist plots for (a) Ag1 and (b) Ag2 with hydrogen operation (ECM-fitted) and biogas at 750°C.

6.4.2 Post-mortem characterisation

The Raman spectra shown in Figure 6-13 indicates no observable carbon peak due to the presence of broad NiO peak at 1485 cm^{-1}. Hence, it is difficult to detect the type of deposited carbon by using Raman spectroscopy.

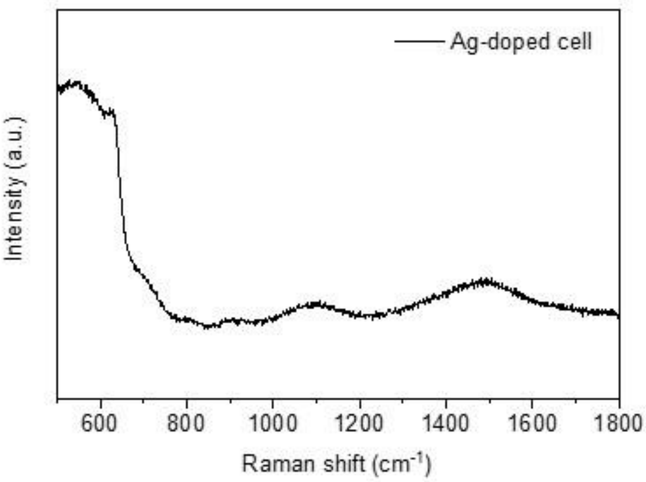

Figure 6-13: Raman spectra of the biogas-tested anode surface of Ag-doped cell.

Similarly, no visible carbon deposition was found on the anode surface of Ag-doped cell, but clearly re-oxidised Ni particles can be observed on both anode surfaces. Some spherical Ag particles with various particle sizes remained on the Ag-doped anode surface after the operational stability test. The primary reason for the improved operational stability of the Ag-doped anodes operated with simulated biogas could be attributed to the suppressed carbon deposition [77].

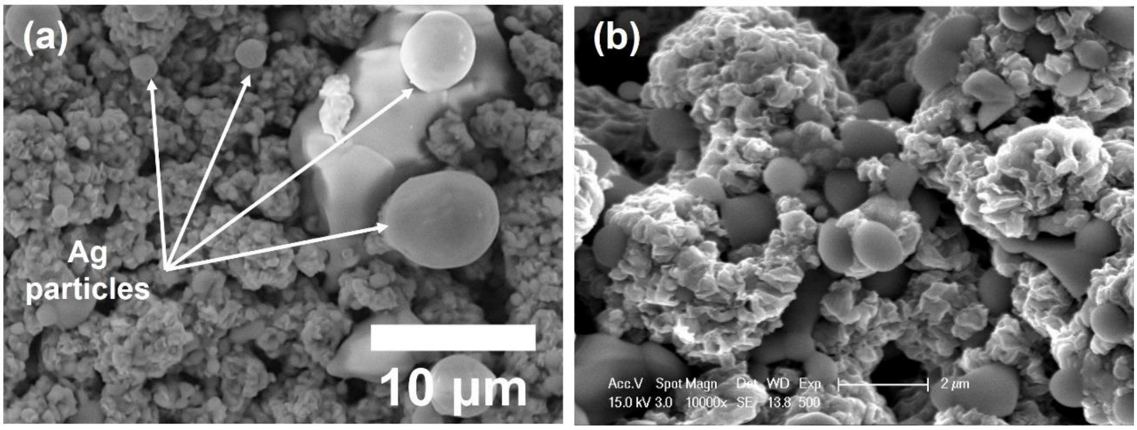

Figure 6-14: SEM images of the anode surface of the Ag-doped cell after biogas operation.

According to Figure 6-15 (b), the carbon deposited on the Ag-doped anode is sp^3 carbon. Figure 6-15 (c) shows the XPS spectra of Ag 3d on the Ag-doped anode after biogas operation. Two peaks at 368.4 eV and 374.4 eV can be observed, which are associated to Ag 3d$_{5/2}$ and Ag 3d$_{3/2}$ of Ag metal, respectively.

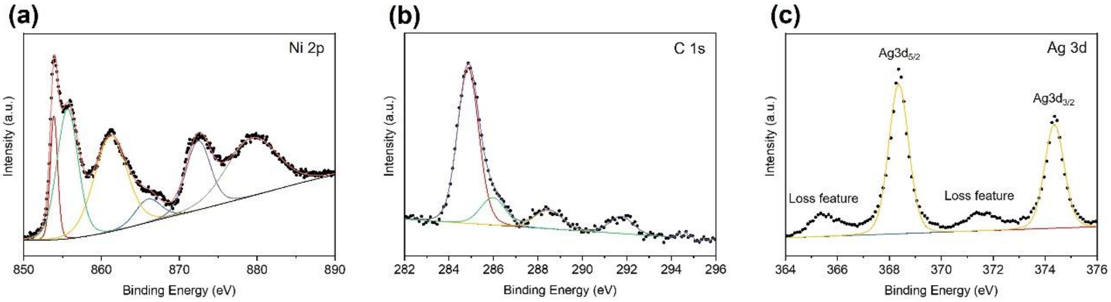

Figure 6-15: XPS spectra for (a) Ni, (b) C, and (c) Ag of the anode surface of the Ag-doped cell after biogas operation.

6.5 Characterisation of the Cu-doped cell

6.5.1 Electrochemical performance

Compared to the undoped cells, the addition of 1wt.% of Cu did not significantly improve the cell power output with either hydrogen or biogas as fuels. As shown in Figure 6-16 (a) and (b), Cu1 and Cu2 exhibited a P_{max} similar to Ni1 and Ni2 in hydrogen or biogas, indicating the unchanged catalytic activity of the Cu-infiltrated anode operated with biogas as fuel. Islam and Hill [208] suggested that the role of copper in the Ni-based cermet anode is to suppress the carbon depositing reactions instead of providing extra catalytic activity towards hydrocarbon oxidations and C–H splitting, as Cu is a poor catalyst for these reactions [206, 207]. Hence, the operational stability of Cu1 and Cu2 in biogas was found to be significantly improved compared to the undoped cells, showing a voltage degradation rate of 0.551 and 0.396 V/kh, respectively. After operating with biogas galvanostatically at 0.10 A•cm^{-2} current density, the P_{max} of Cu1 and Cu2 decreased by approximately 16.7% after switching back to hydrogen.

Figure 6-17 (a) and (b) show the Nyquist plots of Cu1 and Cu2 under different operating conditions. Similar to the Sn and Ag-doped cells, the R_p values of Cu1 and Cu2 when hydrogen served as fuel were slightly lower than the undoped Ni/ScCeSZ anode SOFCs, which could be attributed to the increased connectivity of metal phase in the hydrogen-reduced anode [90, 393]. However, Cu1 and Cu2 exhibited poor electrochemical performance when the fuel was switched from hydrogen to biogas, which also brought a drastic increase in R_{ohm} and R_p. After 120 hours of operation in biogas, the activation polarisation of Cu-doped cells with hydrogen fuel increased by ~0.035 Ω•cm^2. The imaginary part of the impedance plot (-Z'') of the Cu-doped cells also increased by ~0.01 Ω•cm^2. This could be attributed to the migration of Cu in the porous anode at high operating temperature and therefore block the Ni active sites on the anode.

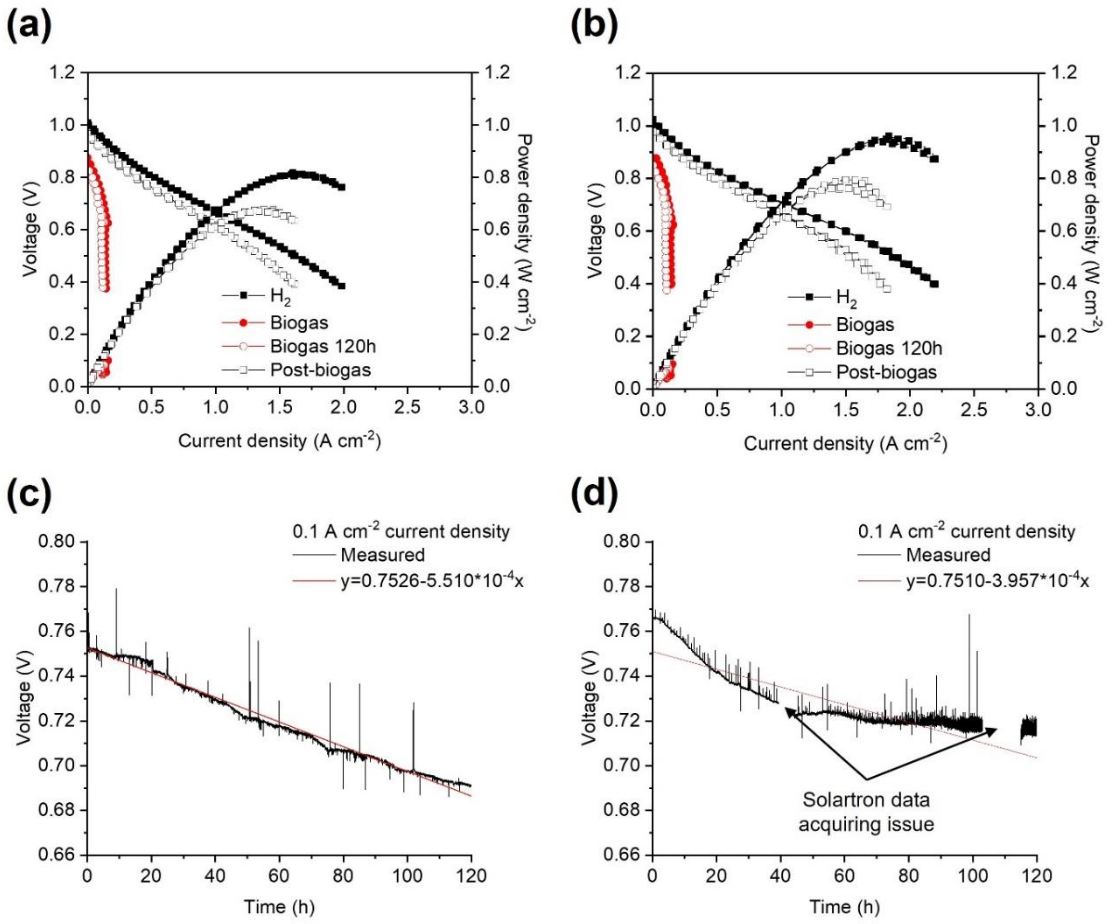

Figure 6-16: i-V curves of (a) Cu1 and (b) Cu2 in hydrogen and simulated biogas at 750°C, voltage output of (c) Cu1 and (d) Cu2 during biogas stability test at 750°C.

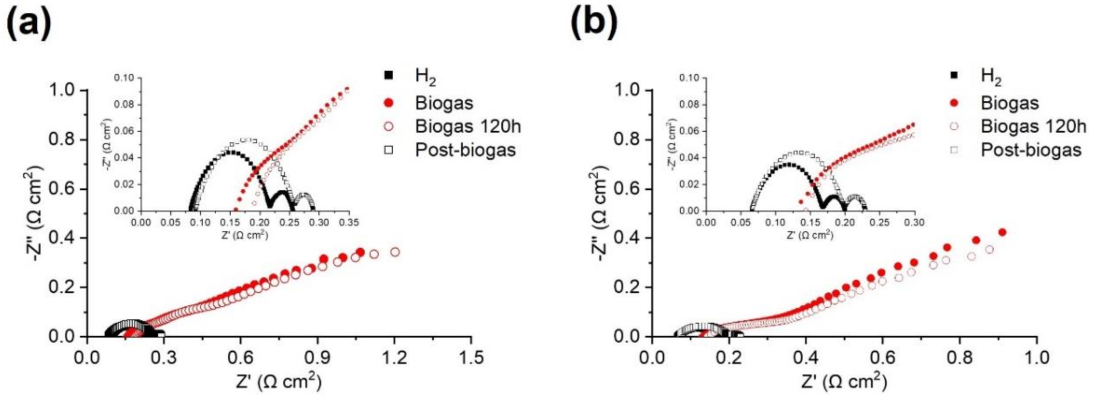

Figure 6-17: Nyquist plots for (a) Cu1 and (b) Cu2 with hydrogen operation (ECM-fitted, before and after biogas exposure) and biogas at 750°C.

6.5.2 Post-mortem characterisation

Figure 6-18 shows that no observable carbon peaks can be identified from the Raman spectra of the Cu-doped anode after biogas operation. Compared to the Sn and Ag-doped anodes, the intensities of the NiO peaks at 1090 cm^{-1} and 1485 cm^{-1} are higher, suggesting a more severely oxidised Ni contents.

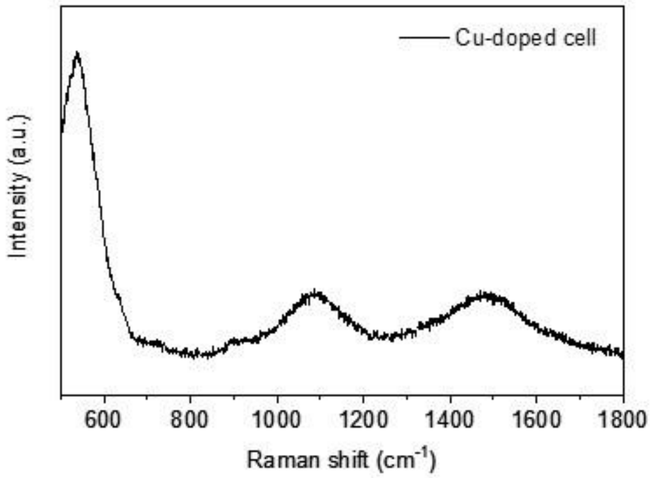

Figure 6-18: Raman spectra of the biogas-tested anode surface of Cu-doped cell.

According to Figure 6-19, part of the Ni on the Cu-doped anode was re-oxidised after biogas operation. It is worth mentioning that no carbon deposition can be found on the post-biogas anode surface, highlighting the successfully suppressed carbon deposition.

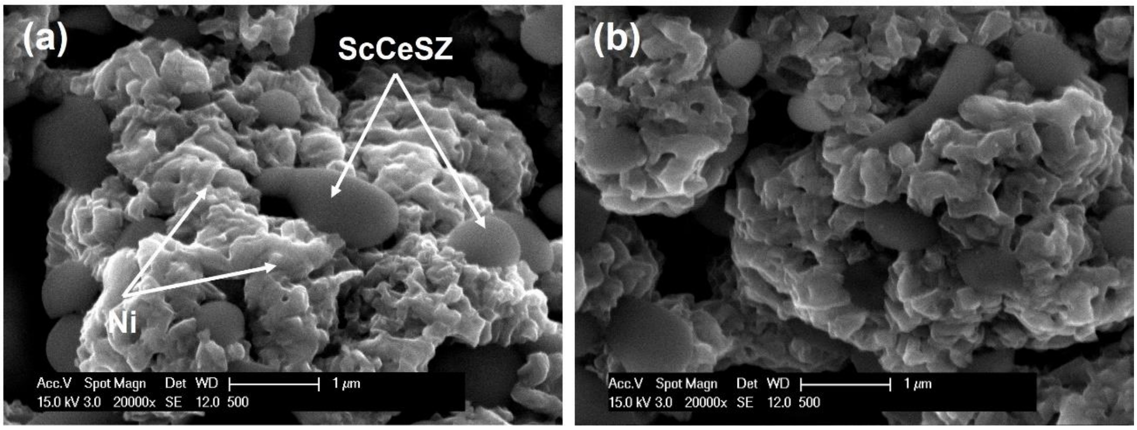

Figure 6-19: SEM images of the anode surface of the Cu-doped cell after biogas operation.

In the Cu 2p XPS spectra shown in Figure 6-20 (c), four large peaks of Cu 2p appeared at 934 eV, 941.9 eV, 954 eV, and 962.1 eV which were from Cu $2p_{3/2}$, Cu^{2+} satellite, Cu $2p_{1/2}$, and Cu^{2+} satellite of CuO, respectively. However, the main peak located at 934 eV could be further deconvoluted into two peaks of Cu metal peak at 932.8 eV and CuO peak at 934.6 eV, suggesting the presence of metallic Cu on the anode surface [394].

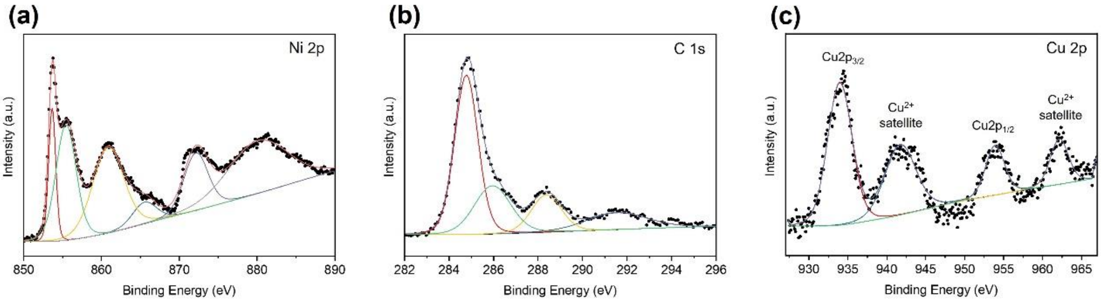

Figure 6-20: XPS spectra for (a) Ni, (b) C, and (c) Cu of the anode surface of the Cu-doped cell after biogas operation.

6.6 Characterisation of the Fe-doped cell

6.6.1 Electrochemical performance

Figure 6-21 (a) and (b) indicate that the infiltration of 1wt.% of Fe into the Ni/ScCeSZ anode largely decreased the power output of the single cell, particularly in the low current density range (0.00 to 0.25 A•cm^{-2}). The P_{max} of Fe1 and Fe2 with hydrogen as fuel were 0.528 and 0.569 W•cm^{-2}, respectively, which were over 40% lower than the undoped cells. Some studies suggested that the Fe to Ni weight ratio in the anode above 1:4 could worsen the catalytic activity of the Ni-based anode during SOFC operation with hydrogen, methane, or ethanol steam [195, 395]. It has been reported that NiFe-ZrO_2 catalyst resulted in severe current collecting issues due to its poor electrical conductivity [395, 396]. Nevertheless, the operational stability of the Fe-doped cells with biogas operation was greatly improved compared to the undoped cells in terms of degradation rate, which was 0.360 V/kh and 0.412 V/kh, respectively.

To investigate the reason for the decreased cell performance shown in Figure 6-21 (a) and (b), EIS of the Fe-infiltrated cells was acquired. It can be seen that the Fe1 and Fe2 cells had the largest increase in R_{ohm} and R_p resistances amongst all prepared cells, around 0.10 and 0.25 Ω•cm^2, respectively. Bohnke et al. [397, 398] reported that 3 mol% Fe_2O_3-substituted yttria-stabilised zirconia (YSZ) or scandia-stabilised zirconia (ScSZ) showed reduced ionic conductivity compared to the unsubstituted YSZ or ScSZ. As Fe dopant will not only retain on the anode surface, part of Fe dopant could also infiltrate into the AFL and ScCeSZ electrolyte. The increase in R_{ohm} could be mainly attributed to the accumulation of Fe_2O_3 on the electrolyte surface caused by infiltration of Fe dopant. The increased R_p could be contributed to the accumulation of Fe dopant on the Ni/ScCeSZ anode surface and presence of NiFe-ZrO_2 catalyst. The presence of excessive Fe dopant on the anode surface could block anode active sites for fuel reduction. As NiFe-ZrO_2 catalyst has been reported with poor electrical conductivity, the appearance of NiFe-ZrO_2 catalyst on the anode surface would negatively affect the current collection during electrochemical characterisation [395, 396]. Both arcs in the Nyquist plots of the Fe-doped cells are larger than for other cells with hydrogen operation, suggesting increased activation and concentration polarisations from the addition of Fe into the anode.

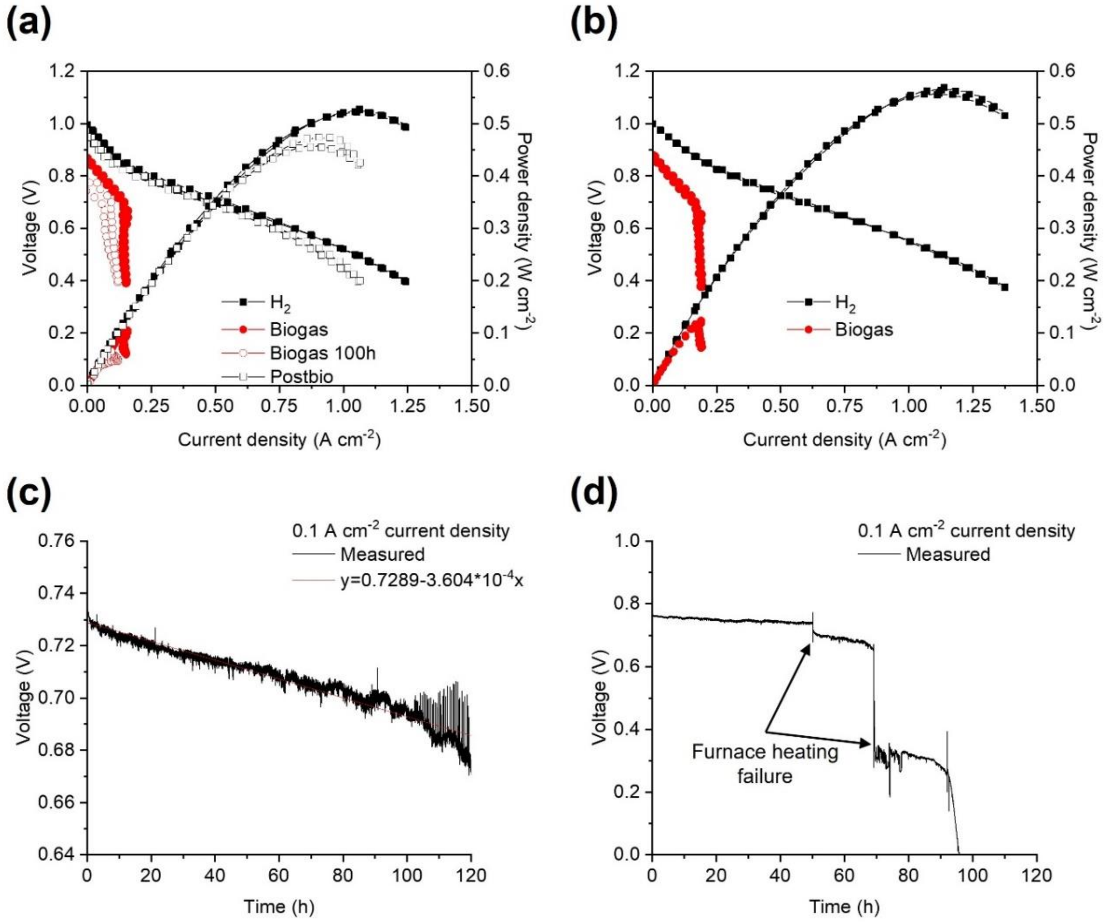

Figure 6-21: i-V curves of (a) Fe1 and (b) Fe2 in hydrogen and simulated biogas at 750°C, voltage output of (c) Fe1 and (d) Fe2 during biogas stability test at 750°C.

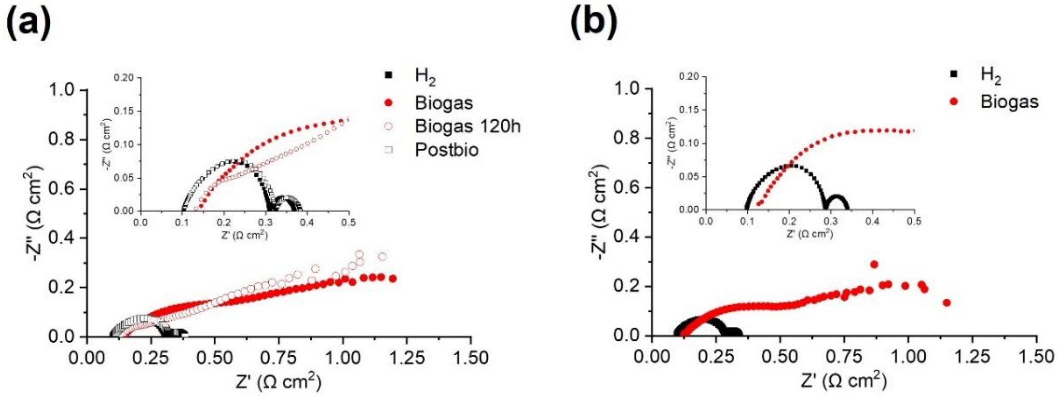

Figure 6-22: Nyquist plots for (a) Fe1 and (b) Fe2 with hydrogen operation (ECM-fitted, before and after biogas exposure) and biogas at 750°C.

6.6.2 Post-mortem characterisation

Similar to the anode of the undoped cell, peaks of D and G bands were also observed on the anode surface of the Fe-doped cell after biogas operation (Figure 6-23), with a D/G intensity ratio of 0.93. This finding indicates a lower graphitisation of the deposited carbon on the Fe-doped anode than the undoped anode. The identified carbon peaks closely match with carbon fibres and graphite [153, 207, 399, 400].

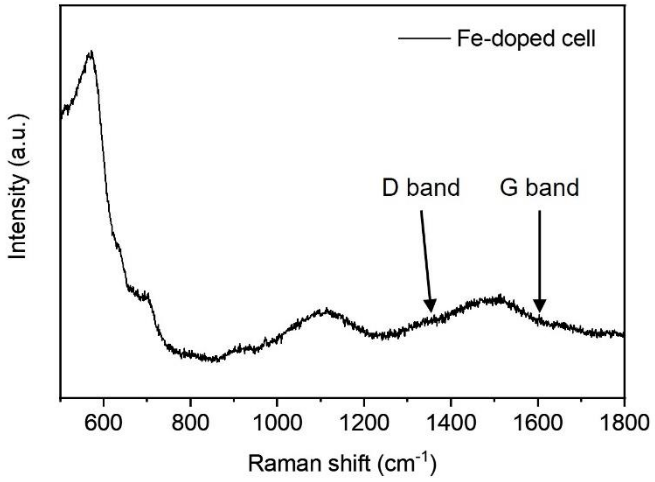

Figure 6-23: Raman spectra of the biogas-tested anode surface of Fe-doped cell.

It is notable that a lot of fibrous or flaky carbon with the length of 0.5 to 1.0 µm was found on the Fe-doped anode surface after 120-hour operation with biogas. The presence of fibrous carbon on the undoped and Fe-doped anode surfaces after biogas operation are consistent with the Raman spectroscopy findings. Li et al. [401] reported a similar morphology of deposited carbon on the Ni-Fe anodes after operating under methane steam reforming conditions at 600°C, particularly at the interface between the anode and the electrolyte. Hence, it can be concluded that infiltrating 1wt.% Fe dopant into the Ni-based anode cannot effectively avoid carbon deposition under dry methane reforming such as the other modified anodes, but the presence of the Fe phase resulted in a reduced formation of graphitic carbon that can dissolve into the Ni catalyst [198, 382].

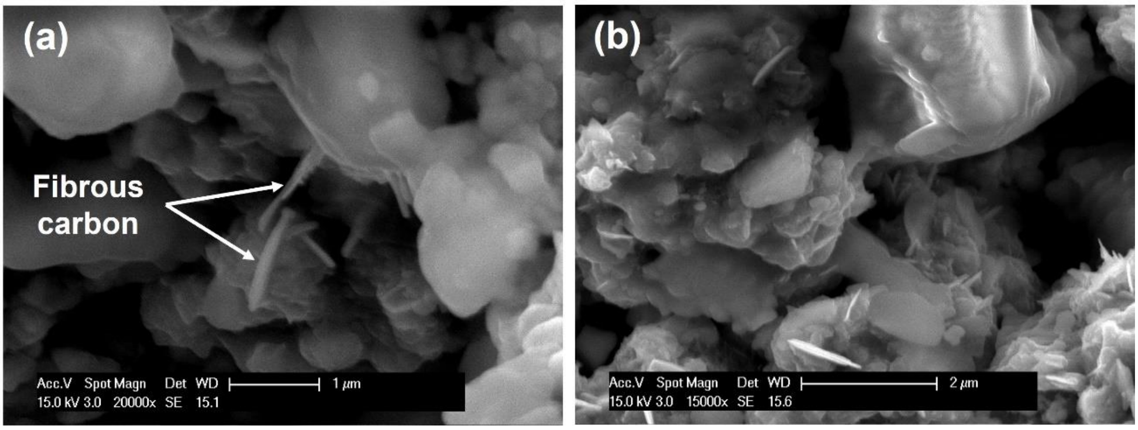

Figure 6-24: SEM images of the anode surface of the Fe-doped cell after biogas operation.

The Fe 2p XPS spectra, shown in Figure 6-25 (c), indicates a small peak at 706.5 eV from metallic Fe. Two peaks appeared at 711.4 eV and 724.9 eV were from Fe $2p_{3/2}$ and Fe $2p_{1/2}$ of Fe_2O_3, respectively [402]. The XPS results show that Ni and Ni^{2+} coexisted with the Fe and Fe^{3+} on the surface of Fe-infiltrated anodes after biogas operation due to the reoxidation of the metallic content.

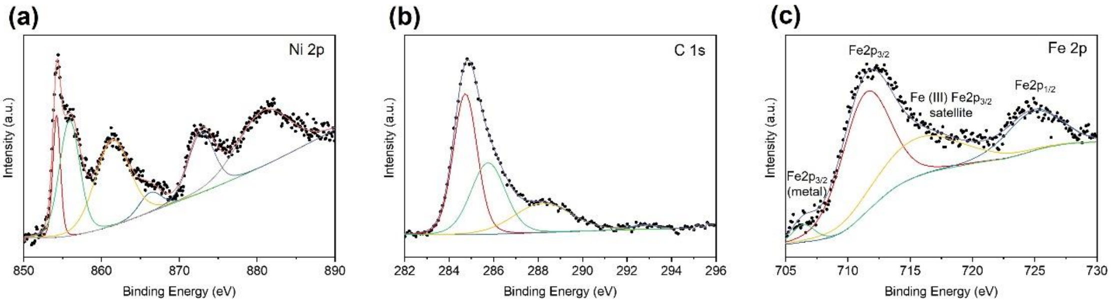

Figure 6-25: XPS spectra for (a) Ni, (b) C, and (c) Fe of the anode surface of the Fe-doped cell after biogas operation.

6.7 Electrochemical performance comparison of the prepared cells with hydrogen and biogas operations

Figure 6-26 (a) and (c) show the i-V curves and Nyquist plots of all hydrogen-tested cells with similar cell configurations, respectively. It is evident that the undoped, Sn, Ag, and Cu-doped Ni/ScCeSZ cells achieved comparable polarisation curves and P_{max} of around 0.97 W•cm^{-2}. The increased power output and slightly lower polarisation resistances of the cells modified with Sn, Ag, and Cu dopants compared to the undoped cell could be attributed to the improved connectivity of the metallic phase in the porous anode [90, 393]. However, the addition of Fe dopant into the porous anode drastically increased both R_{ohm} and R_p of the cell by reducing ionic conductivity and forming a poor electrical conduction Ni-Fe alloy, respectively, leading to around 40% drop in P_{max} at 750°C.

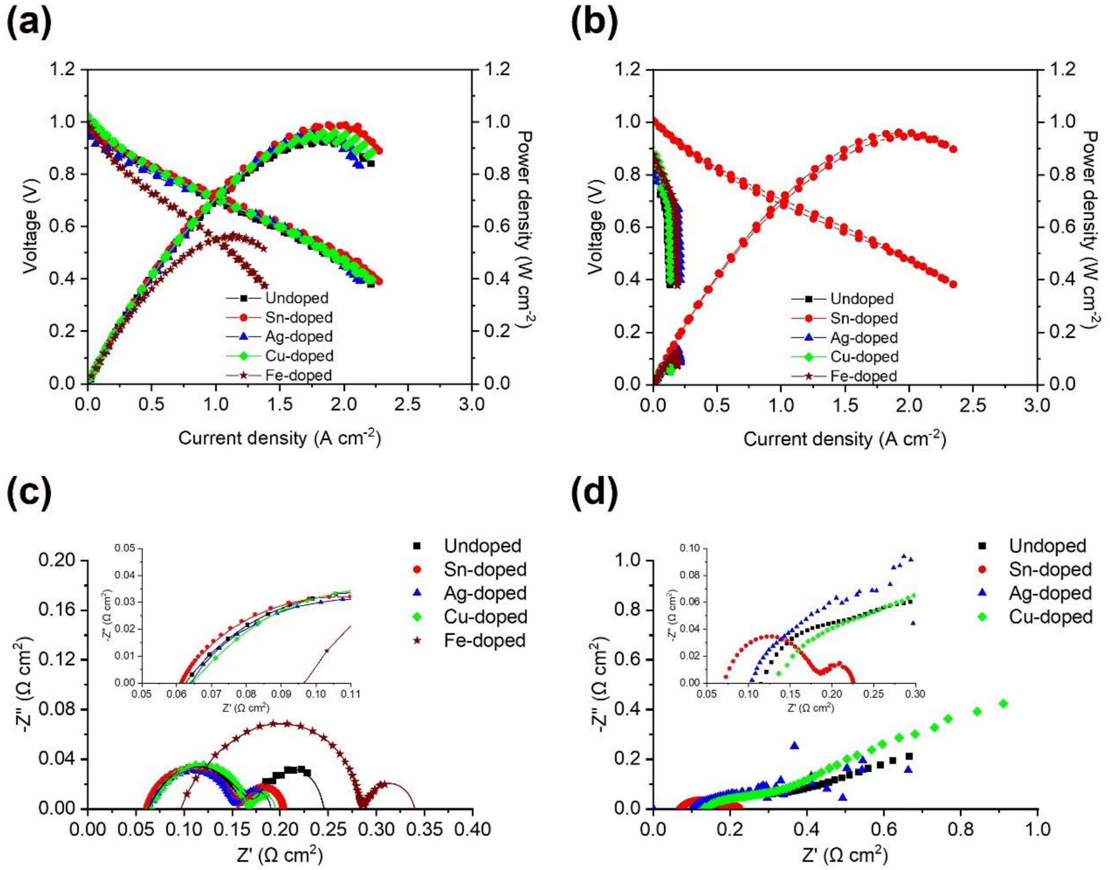

Figure 6-26: i-V plots and Nyquist plots (scatter plots: measured EIS data, line plots: ECM-fitted data) of the prepared single cells operated with hydrogen (a, c) and simulated biogas (b, d) at 750°C.

When the fuel gas switched from hydrogen to simulated biogas, a large difference in polarisation curves between the Sn-doped cell and the other cells was observed, as shown in Figure 6-26 (b). The Sn-doped cell exhibited comparable power output when hydrogen or biogas served as fuels, showing a P_{max} of 0.997 and 0.963 W•cm^{-2} at 750°C, respectively. On the other hand, the other cells produced a significantly lower P_{max} of around 0.10 W•cm^{-2} and significantly increased polarisation resistances on biogas operation, as shown in Figure 6-26 (d), demonstrating the low efficiency of dry methane reforming during simulated biogas operation.

The operational stability of the prepared cells was examined by measuring the cell voltage under the galvanostatic conditions. According to Figure 6-27, the undoped Ni/ScCeSZ cell showed rapid voltage degradation after 9 h of operation with biogas as fuel and then ceased operation at 11 h of exposure. Structural damage of the undoped cell was also identified after cell testing, which was caused by severe carbon deposition during biogas operation. In contrast, all doped cells demonstrated greatly improved stability with biogas as fuel at 750°C compared to the undoped cell.

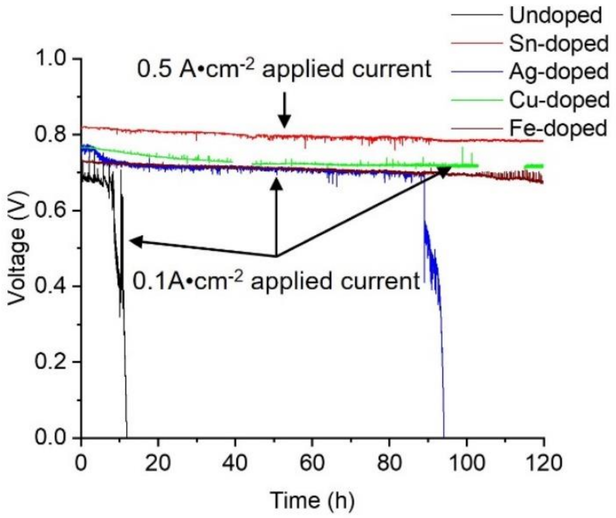

Figure 6-27: Operational stability of the prepared cells with simulated biogas at 750°C.

Among all prepared cells, the Sn-doped cell exhibited the lowest voltage degradation rate of 0.285 V/kh. It is important to note that the Sn-doped cell was operated at a higher current density (0.5 A•cm^{-2}) than the Ag, Cu, and Fe-doped cells (0.1 A•cm^{-2}). It has been reported that the performance degradation rate for SOFCs increases with the increasing current density due to more rapid depletion of fuel and oxidant gases in the cell, as well as more severe Ni coarsening issue [350, 358]. This finding indicates that doping Sn with the Ni/ScCeSZ anode can maintain great operational stability at high current density with simulated biogas as fuel, which is critical for the practical application of the biogas-operated SOFCs. The improved electrochemical performance of the Sn-doped anode in terms of power output and operational stability could be explained by two factors. Firstly, the Sn-Ni catalyst preferentially oxidises C atoms than forming C–C bonds, compared to the monometallic Ni catalyst under internal methane reforming conditions. Secondly, there is a weaker binding of carbon structure on the active sites on the Sn-Ni catalyst than on the Ni catalyst [403, 404]. Finally, the Sn-doped Ni cermet anode tends to absorb more water due to the oxophilic nature of Sn. This enables an easier H_2O dissociation during hydrocarbon operation [405]. Therefore, adding Sn to the Ni-based anode not only promoted the carbon removal reactions but also inhibited the carbon forming reactions under dry methane reforming atmosphere, which is consistent with the reported results on Sn-modified Ni-based anodes [200].

Ag and Cu, as metallic catalysts for hydrocarbon-operated SOFCs, are known for having low catalytic activity for C–C bond formation. In addition, Ag and Cu have lower carbon solubility compared to Ni, which can avoid the structural damage of the anode caused by carbon dissolution during hydrocarbon fuel operation [179, 180, 207, 208]. Therefore, the improved operational stability of the Ag-doped and Cu-doped cells can be mainly attributed to the suppressed carbon forming reactions during biogas operation. The Fe-doped cell exhibited the second lowest voltage degradation rate (0.360 V/kh) among all cells. The improved operational stability of the Fe-dope cell could be attributed to the reduced graphitisation degree of carbon deposited on the anode compared to the undoped cell, which was confirmed by the Raman spectroscopy results shown in Figure 6-3 and Figure 6-23 [395]. As discussed earlier, the decrease in voltage output of the prepared cells can not only be explained by carbon deposition but also the contribution from Ni coarsening and degradation of sealing material at the beginning of operation. The improved operational stability of the 1wt.% metal-infiltrated cells also revealed the enhanced carbon tolerance of the infiltrated cells under dry methane reforming atmosphere.

6.8 Elemental distribution analysis before and after cell testing

EDS element mapping was performed on the modified anode to compare the surface elemental distribution before and after biogas operation, followed by the quantitative analysis of the elements present on the surface. Figure 6-28 shows the EDS elemental maps of the dopant-infiltrated anodes before and after long-term operation with biogas as fuel. For Sn, Ag, and Cu-doped samples, large dopant particles (SnO_2, Ag, CuO) were identified on the anode surface prior to reduction under the hydrogen fuel stream. This could be attributed to the agglomeration of precursor on the anode surface during the infiltration process.

EDS quantification was performed to four spots on every sample. Table 6-1 shows the average concentration of each element on the surface of the prepared anodes before and after the long-term biogas fuelled operation. It can be observed that the surface concentration of Ni increased by around 10wt.% after the operation compared to the pre-operation level. The Ni enrichment on the anode surface could be attributed to the thermally driven nickel migration (also known as Ni coarsening) over the long long-term operation, but the rate of Ni enrichment in the fuel cell mode is typically slower than the electrolysis mode [348, 406]. The ratio of dopant to nickel for Sn, Ag, and Cu before cell testing was 11.220, 40.725, and 10.117wt.%, respectively. Similar surface accumulation of Ag particle was also reported by Wu et al. [180] and Ruiz-Trejo et al. [407] after infiltrating $AgNO_3$ precursor into the porous Ni cermet anode. After 120 hours of operation in biogas, the surface concentration of Sn, Ag, and Cu (with respect to Ni) decreased to 0.710, 7.056, and 2.881wt.%, respectively, suggesting the loss of metal dopant during the cell operation. The depletion of metal dopant content in the anode was consistent with the previously reported results [180, 200, 387]. The depletion of Sn and Ag on the anode surface might be due to the evaporation process caused by their low melting points of 231.9°C and 961.8°C [180, 408, 409]. Additionally, by comparing Figure

6-28 (c) and (d), significant Ag particle size growth was also found after the operational stability test with biogas as fuel, possibly caused by melting and diffusion of small Ag particles at high operating temperature (750°C). For the Cu-doped doped anode, the decreasing Cu content on the anode surface could be attributed to the diffusion of Cu into the Ni lattice during the formation of a Cu-Ni alloy at 750°C [207, 410]. Unlike other dopants, an increase in Fe to Ni ratio was found on the anode surface of the Fe-doped cell after long-term operation with biogas, from 1.314wt.% before test to 2.298wt.% after test. Additionally, enrichment of Ce on the anode surface of the Fe-doped cell was also identified after 120 h of operation in biogas. The increasing surface concentration of Fe and Ce might be caused by thermally-driven Fe diffusion [411, 412] and Ce segregation along the grain boundaries in the anode substrate [413], respectively.

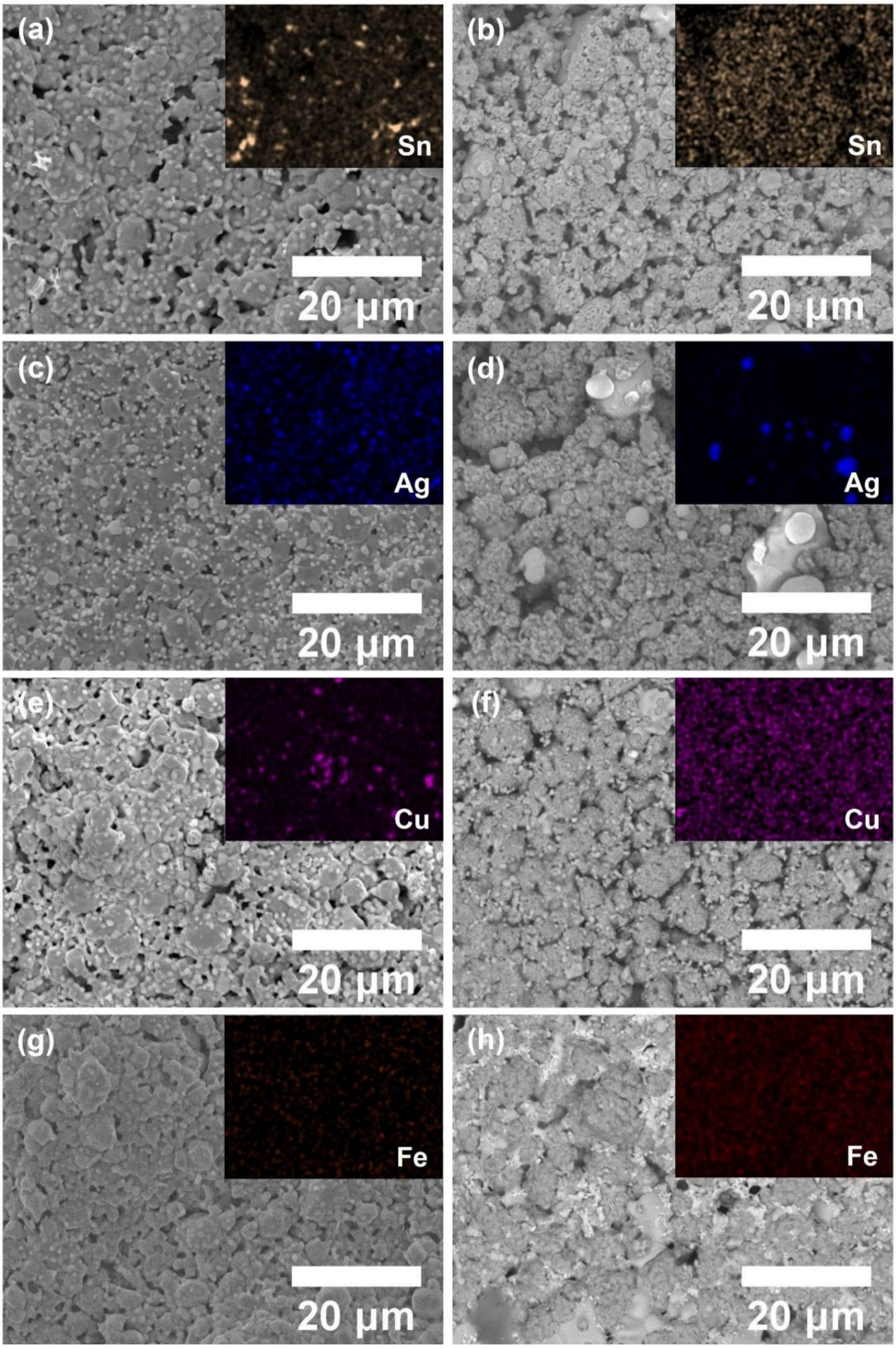

Figure 6-28: EDS mapping results for Sn, Ag, Cu, and Fe-doped cells before (left) and after (right) biogas operation at 750°C.

Table 6-1: Doped-anode surface elemental concentration before and after biogas operation.

Element	**Before biogas operation (wt.%)**				**After biogas operation (wt.%)**			
	Sn	Ag	Cu	Fe	Sn	Ag	Cu	Fe
Ni	44.140	41.958	43.088	47.010	56.682	54.988	55.764	51.602
Zr	24.465	16.950	24.810	24.843	24.757	15.850	17.415	14.975
Sc	2.280	1.670	2.483	2.288	2.374	1.605	1.730	1.505
Ce	0.163	0.163	0.285	0.230	0.740	0.188	0.744	6.797
O	24.000	22.210	24.965	25.013	15.045	21.303	22.768	23.932
Sn	4.953	-	-	-	0.402	-	-	-
Ag	-	17.048	-	-	-	3.965	-	-
Cu	-	-	4.368	-	-	-	1.607	-
Fe	-	-	-	0.618	-	-	-	1.186

6.9 Summary

After evaluating the electrochemical performance of all cells prepared in this work, it can be concluded that the Sn-doped Ni/ScCeSZ anode SOFC exhibited extraordinary power output and good operational stability with biogas operation at 750°C. The P_{max} of Sn-doped cell reached 0.963 $W\bullet cm^{-2}$ with biogas as fuel, which was highly comparable to the P_{max} of 0.997 $W\bullet cm^{-2}$ when hydrogen was the fuel. Although infiltrating Ag, Cu and Fe into the porous anode largely improved the operational stability in biogas, no obvious enhancement to the power output under biogas fuelled operation was found. It is notable that the addition of Fe into the anode decreased P_{max} in hydrogen operation by around 40% due to the substantial increase in R_{ohm} and R_p. This could be caused by the blocked catalytically active sites for hydrogen reduction on the Fe-Ni/ScCeSZ anode. According to the SEM results, no visible carbon deposition was found on the anode surface of the Sn, Ag, and Cu-doped cells, suggesting the suppressed carbon deposition from Sn, Ag, and Cu infiltration. However, fibrous carbon was identified on the undoped and Fe-doped anode surface after operation in biogas. Therefore, carbon deposition and blocked active sites in the anode are the main factors contributing to the performance degradation of the Fe-doped cell operated with biogas. The EDS results indicated a decrease in Sn, Ag, and Cu concentration on the anode surface after operation in biogas. This finding suggests that the electrochemical performance degradation of the Sn, Ag, and Cu-doped cells could be attributed to the loss of metal dopant in the anode. Furthermore, the obtained XPS results confirmed the presence of NiO, SnO_2, CuO and Fe_2O_3 on the post-tested cells with biogas as fuel, suggesting the re-oxidation of the metal during or after cell testing.

CHAPTER 7: CONCLUSION AND FUTURE WORK

7.1 Conclusion

The present research thesis aimed to optimise the fabrication process of high-performance IT-SOFC planar cells and improve the carbon tolerance of the Ni-based anode operated with simulated biogas as fuel. Several key findings were obtained from the study:

i. Separate sintering processes are necessary for the fabrication of a ScCeSZ electrolyte with a GDC barrier layer without the formation of the resistive interlayer consisting of (Zr, Ce)O_2-based solid solutions at the boundary of ScCeSZ and GDC layers.

ii. Thin GDC films can be effectively and precisely fabricated through spin coating with a water-based slurry, but further reduction of GDC layer porosity is needed to thoroughly block the Sr cation migration (diffusion of gaseous species) from LSCF cathode to ScCeSZ electrolyte over long-term SOFC operation.

iii. Through extensive investigation of the degradation behaviour of the anode-supported SOFCs operated with hydrogen as fuel, it was found that Ni coarsening at the anode and Sr diffusion from LSCF cathode to the ScCeSZ electrolyte were the main factors causing the cell performance degradation. These factors led to reduced active sites in the anode and formation of a $SrZrO_3$ resistive compound with the ScCeSZ electrolyte, respectively.

iv. The addition of 1wt.% of Sn, Ag, Cu, or Fe metal dopant into the Ni-based anodes by the infiltration method improved the operational stability of the cells during simulated biogas operation (over 120 h at 750°C), compared to the undoped cell (less than 12 h). The improved stability of Sn, Ag, and Cu-doped cells can be attributed to the suppressed carbon forming reactions during biogas operation. However, formation of fibrous carbon was observed on the Fe-doped anode surface. In the case of Fe-doped anode, the improved operational stability during biogas operation could be attributed to a lower graphitisation degree of carbon compared to the undoped anode after exposure to biogas.

v. The Sn-doped cell showed excellent operational stability in biogas operation and comparable electrochemical performance in terms of power output and resistances compared to those in hydrogen operation. This suggests an enhanced catalytic activity of the Sn-doped anode towards dry methane reforming reactions. The addition of Ag or Cu dopant resulted in lower cell polarisation resistances due to the improved connectivity of metallic phase in the anode, but no significant enhancement in power output was observed. Nevertheless, modifying the Ni/ScCeSZ anode with 1wt.% of Fe showed a negative impact on the cell electrochemical performance with hydrogen operation due to the hindered active sites for fuel reduction on the SOFC anode.

7.2 Future work

From the results and summaries of the previous chapters, the following research questions and tests have deduced that were not explored within the scope of this work:

- Fabricate GDC barrier layer by wet ceramic coating techniques (e.g. spin coating, screen printing, and spray coating) with the use of sintering aids. As the GDC layer needs to be sintered at slightly lower temperature than the ScCeSZ electrolyte, the use of sintering aid in the GDC layer enables better densification of GDC layer at reduced temperature.
- Perform inductively coupled plasma atomic emission spectroscopy (ICP-AES) to acquire the accurate elemental quantification data of the metal-infiltrated samples before and after biogas operation. Since some biogas-tested cells are fragile or damaged, sample preparation is difficult for EDS elemental analysis. By dissolving a small amount of tested anode with nitric acid, the precise elemental

components of the anode can be determined via ICP-AES.

- Explore the effect of Sn concentration within the Ni-based anode on both cell performance and anode carbon resistance under the operation of simulated biogas. EDS analysis indicated obvious Sn enrichment on the anode surface, which could be attributed to the surface-enriched intermetallic phase between Ni and Sn. Notably, Ni_3Sn is recognised as an exceptionally active catalysts for hydrocarbon oxidation, thereby mitigating the coking propensity of the Ni-based anode operated with hydrocarbon. To understand the metal dispersion and active site density of Sn-Ni intermetallic, hydrogen chemisorption and temperature programmed desorption (TPD) characterisations will be pivotal.
- Analyse the elemental distribution at the cross section of the undoped cells after operational stability test in hydrogen and the doped cells after simulated biogas operation by transmission electron microscopy (TEM), aiming to understand the spatial distribution of infiltrated dopant and $SrZrO_3$ interdiffusion layer, respectively.

REFERENCES

[1] P.A. Owusu, S. Asumadu-Sarkodie, A review of renewable energy sources, sustainability issues and climate change mitigation, Cogent Engineering, 3 (2016) 1167990.

[2] S.A. Saadabadi, A. Thallam Thattai, L. Fan, R.E.F. Lindeboom, H. Spanjers, P.V. Aravind, Solid Oxide Fuel Cells fuelled with biogas: Potential and constraints, Renewable Energy, 134 (2019) 194-214.

[3] M. Singh, D. Zappa, E. Comini, Solid oxide fuel cell: Decade of progress, future perspectives and challenges, International Journal of Hydrogen Energy, 46 (2021) 27643-27674.

[4] C.L. Benson, C.L. Magee, On improvement rates for renewable energy technologies: Solar PV, wind turbines, capacitors, and batteries, Renewable Energy, 68 (2014) 745-751.

[5] T.T.D. Tran, A.D. Smith, fEvaluation of renewable energy technologies and their potential for technical integration and cost-effective use within the U.S. energy sector, Renewable and Sustainable Energy Reviews, 80 (2017) 1372-1388.

[6] A. Hussain, S.M. Arif, M. Aslam, Emerging renewable and sustainable energy technologies: State of the art, Renewable and Sustainable Energy Reviews, 71 (2017) 12-28.

[7] A. Kirubakaran, S. Jain, R.K. Nema, A review on fuel cell technologies and power electronic interface, Renewable and Sustainable Energy Reviews, 13 (2009) 2430-2440.

[8] I. EG&G Technical Services, Fuel Cell Hand book, Seventh ed., U.S. Department of Energy, Morgantown, 2004.

[9] C. Spiegel, Designing and Building Fuel Cells, McGraw-Hill, New York, 2007.

[10] K. Kendall, M. Kendall, High-Temperature Solid Oxide Fuel Cells for the 21st Century: Fundamentals, Design and Applications: Second Edition, Elsevier, London, 2015.

[11] M. Ghouse, Fuel Cells and Their Applications, 2012.

[12] R.M. Dell, P.T. Moseley, D.A.J. Rand, Chapter 8 - Hydrogen, Fuel Cells and Fuel Cell Vehicles, in: R.M. Dell, P.T. Moseley, D.A.J. Rand (Eds.) Towards Sustainable Road Transport, Academic Press, Boston, 2014, pp. 260-295.

[13] W. Wang, C. Su, Y. Wu, R. Ran, Z. Shao, Progress in Solid Oxide Fuel Cells with Nickel-Based Anodes Operating on Methane and Related Fuels, Chemical Reviews, 113 (2013) 8104-8151.

[14] F.S. da Silva, T.M. de Souza, Novel materials for solid oxide fuel cell technologies: A literature review, International Journal of Hydrogen Energy, 42 (2017) 26020-26036.

[15] M.D. Gross, J.M. Vohs, R.J. Gorte, Recent progress in SOFC anodes for direct utilization of hydrocarbons, Journal of Materials Chemistry, 17 (2007) 3071-3077.

[16] N.M. Sammes, K. Galloway, M.F. Serincan, T. Suzuki, T. Yamaguchi, M. Awano, W. Colella, Solid Oxide Fuel Cells, in: W.-Y. Chen, J. Seiner, T. Suzuki, M. Lackner (Eds.) Handbook of Climate Change Mitigation, Springer US, New York, NY, 2012, pp. 1703-1727.

[17] J.W. Fergus, Electrolytes for solid oxide fuel cells, Journal of Power Sources, 162 (2006) 30-40.

[18] N. Mahato, A. Banerjee, A. Gupta, S. Omar, K. Balani, Progress in material selection for solid oxide fuel cell technology: A review, Progress in Materials Science, 72 (2015) 141-337.

[19] T. Liu, X. Zhang, X. Wang, J. Yu, L. Li, A review of zirconia-based solid electrolytes, Ionics, 22 (2016) 2249-2262.

[20] Z. Zakaria, Z. Awang Mat, S.H. Abu Hassan, Y. Boon Kar, A review of solid oxide fuel cell component fabrication methods toward lowering temperature, International Journal of Energy Research, 44 (2020) 594-611.

[21] X. Ge, X. Huang, Y. Zhang, Z. Lu, J. Xu, K. Chen, D. Dong, Z. Liu, J. Miao, W. Su, Screen-printed thin YSZ films used as electrolytes for solid oxide fuel cells, Journal of Power Sources, 159 (2006) 1048-1050.

[22] J.T.S. Irvine, J.W.L. Dobson, T. Politova, S. García Martín, A. Shenouda, Co-doping of scandia–zirconia electrolytes for SOFCs, Faraday Discussions, 134 (2007) 41-49.

[23] A.J. Jacobson, Materials for Solid Oxide Fuel Cells, Chemistry of Materials, 22 (2010) 660-674.

[24] 7 - Nanostructured semiconductor composites for solid oxide fuel cells (SOFCs), in: S. Zhuiykov (Ed.) Nanostructured Semiconductor Oxides for the Next Generation of Electronics and Functional Devices, Woodhead Publishing2014, pp. 321-373.

[25] H. Inaba, H. Tagawa, Ceria-based solid electrolytes, Solid State Ionics, 83 (1996) 1-16.

[26] V.V. Kharton, F.M. Figueiredo, L. Navarro, E.N. Naumovich, A.V. Kovalevsky, A.A. Yaremchenko, A.P. Viskup, A. Carneiro, F.M.B. Marques, J.R. Frade, Ceria-based materials for solid oxide fuel cells, Journal of Materials Science, 36 (2001) 1105-1117.

[27] C.J. Fu, Q.L. Liu, S.H. Chan, X.M. Ge, G. Pasciak, Effects of transition metal oxides on the densification of thin-film GDC electrolyte and on the performance of intermediate-temperature SOFC, International Journal of Hydrogen Energy, 35 (2010) 11200-11207.

[28] H.S. Spacil, Electrical device including nickel-containing stabilized zirconia electrode, General Electric Co, 1970.

[29] B. Shri Prakash, S. Senthil Kumar, S.T. Aruna, Properties and development of Ni/YSZ as an anode material in solid oxide fuel cell: A review, Renewable and Sustainable Energy Reviews, 36 (2014) 149-179.

[30] J.W. Fergus, R. Hui, X. Li, D.P. Wilkinson, J. Zhang, Solid Oxide Fuel Cells: Materials Properties and Performance, CRC Press, Boca Raton, 2008.

[31] T. Klemensø, M. Mogensen, Ni–YSZ Solid Oxide Fuel Cell Anode Behavior Upon Redox Cycling Based on Electrical Characterization, Journal of the American Ceramic Society, 90 (2007) 3582-3588.

[32] J.H. Yu, G.W. Park, S. Lee, S.K. Woo, Microstructural effects on the electrical and mechanical properties of Ni–YSZ cermet for SOFC anode, Journal of Power Sources, 163 (2007) 926-932.

[33] K. Thydén, Y.L. Liu, J.B. Bilde-Sørensen, Microstructural characterization of SOFC Ni–YSZ anode composites by low-voltage scanning electron microscopy, Solid State Ionics, 178 (2008) 1984-1989.

[34] C.M. Finnerty, N.J. Coe, R.H. Cunningham, R.M. Ormerod, Carbon formation on and deactivation of nickel-based/zirconia anodes in solid oxide fuel cells running on methane, Catalysis Today, 46 (1998) 137-145.

[35] H. Kurokawa, L. Yang, C.P. Jacobson, L.C. De Jonghe, S.J. Visco, Y-doped $SrTiO_3$ based sulfur tolerant anode for solid oxide fuel cells, Journal of Power Sources, 164 (2007) 510-518.

[36] C. Peng, J. Luo, A.R. Sanger, K.T. Chuang, Sulfur-Tolerant Anode Catalyst for Solid Oxide Fuel Cells Operating on H_2S-Containing Syngas, Chemistry of Materials, 22 (2010) 1032-1037.

[37] T. Klemensø, C. Chung, P. H. Larsen, M. Mogensen, The Mechanism Behind Redox Instability of Anodes in High-Temperature SOFCs, Journal of the Electrochemical Society, 152 (2005) A2186-A2192.

[38] T. Kim, G. Liu, M. Boaro, S.I. Lee, J.M. Vohs, R.J. Gorte, O.H. Al-Madhi, B.O. Dabbousi, A study of carbon formation and prevention in hydrocarbon-fueled SOFC, Journal of Power Sources, 155 (2006) 231-238.

[39] A. Singh, J.M. Hill, Carbon tolerance electrochemical performance and stability of solid oxide fuel cells with Ni/yttria stabilized zirconia anodes impregnated with Sn and operated with methane, Journal of Power Sources, 214 (2012) 185-194.

[40] S. McIntosh, R.J. Gorte, Direct Hydrocarbon Solid Oxide Fuel Cells, Chemical Reviews, 104 (2004) 4845-4866.

[41] K. Wei, X. Wang, R.A. Budiman, J. Kang, B. Lin, F. Zhou, Y. Ling, Progress in Ni-based anode materials for direct hydrocarbon solid oxide fuel cells, Journal of Materials Science, 53 (2018) 8747-8765.

[42] M. Shen, P. Zhang, Progress and challenges of cathode contact layer for solid oxide fuel cell, International Journal of Hydrogen Energy, 45 (2020) 33876-33894.

[43] Z. Shao, S.M. Haile, A high-performance cathode for the next generation of solid-oxide fuel cells, Nature, 431 (2004) 170-173.

[44] V.A.C. Haanappel, A. Mai, J. Mertens, Electrode activation of anode-supported SOFCs with LSM- or LSCF-type cathodes, Solid State Ionics, 177 (2006) 2033-2037.

[45] L.S. Mahmud, A. Muchtar, M.R. Somalu, Challenges in fabricating planar solid oxide fuel cells: A review, Renewable and Sustainable Energy Reviews, 72 (2017) 105-116.

[46] K.S. Howe, G.J. Thompson, K. Kendall, Micro-tubular solid oxide fuel cells and stacks, Journal of Power Sources, 196 (2011) 1677-1686.

[47] M.Z. Khan, A. Iltaf, H.A. Ishfaq, F.N. Khan, W.H. Tanveer, R.-H. Song, M.T. Mehran, M. Saleem, A. Hussain, Z. Masaud, Flat-tubular solid oxide fuel cells and stacks: a review, Journal of Asian Ceramic Societies, 9 (2021) 745-770.

[48] G. Li, Y. Gou, J. Qiao, W. Sun, Z. Wang, K. Sun, Recent progress of tubular solid oxide fuel cell: From materials to applications, Journal of Power Sources, 477 (2020) 228693.

[49] J. Qu, W. Wang, Y. Chen, X. Deng, Z. Shao, Stable direct-methane solid oxide fuel cells with calcium-oxide-modified nickel-based anodes operating at reduced temperatures, Applied Energy, 164 (2016) 563-571.

[50] J.N. Armor, The multiple roles for catalysis in the production of H_2, Applied Catalysis A: General, 176 (1999) 159-176.

[51] H. Kan, H. Lee, Sn-doped Ni/YSZ anode catalysts with enhanced carbon deposition resistance for an intermediate temperature SOFC, Applied Catalysis B: Environmental, 97 (2010) 108-114.

[52] S.H. Clarke, A.L. Dicks, K. Pointon, T.A. Smith, A. Swann, Catalytic aspects of the steam reforming of hydrocarbons in internal reforming fuel cells, Catalysis Today, 38 (1997) 411-423.

[53] R. Reimert, F. Marschner, H.-J. Renner, W. Boll, E. Supp, M. Brejc, W. Liebner, G. Schaub, Gas Production, 2. Processes. In Ullmann's Encyclopedia of Industrial Chemistry, 2011.

[54] S.P. Jiang, S.H. Chan, A review of anode materials development in solid oxide fuel cells, Journal of Materials Science, 39 (2004) 4405-4439.

[55] S. Park, J.M. Vohs, R.J. Gorte, Direct oxidation of hydrocarbons in a solid-oxide fuel cell, Nature, 404 (2000) 265-267.

[56] R.J. Gorte, S. Park, J.M. Vohs, C. Wang, Anodes for Direct Oxidation of Dry Hydrocarbons in a Solid-Oxide Fuel Cell, Advanced Materials, 12 (2000) 1465-1469.

[57] H.A. Shabri, M.H.D. Othman, M.A. Mohamed, T.A. Kurniawan, S.M. Jamil, Recent progress in metal-ceramic anode of solid oxide fuel cell for direct hydrocarbon fuel utilization: A review, Fuel Processing Technology, 212 (2021) 106626.

[58] W. Sangtongkitcharoen, S. Assabumrungrat, V. Pavarajarn, N. Laosiripojana, P. Praserthdam, Comparison of carbon formation boundary in different modes of solid oxide fuel cells fueled by methane, Journal of Power Sources, 142 (2005) 75-80.

[59] R.O.d. Fonseca, A.A.A.d. Silva, M.R.M. Signorelli, R.C. Rabelo-Neto, F.B. Noronha, R.C.C. Simões, L.V. Mattos, Nickel/Doped Ceria Solid Oxide Fuel Cell Anodes for Dry Reforming of Methane, Journal of the Brazilian Chemical Society, 25 (2014) 2356-2363.

[60] Y. Shiratori, T. Ijichi, T. Oshima, K. Sasaki, Internal reforming SOFC running on biogas, International Journal of Hydrogen Energy, 35 (2010) 7905-7912.

[61] B. Hua, M. Li, Y.-F. Sun, Y.-Q. Zhang, N. Yan, J. Chen, J. Li, T. Etsell, P. Sarkar, J.-L. Luo, Biogas to syngas: flexible on-cell micro-reformer and NiSn bimetallic nanoparticle implanted solid oxide fuel cells for efficient energy conversion, Journal of Materials Chemistry A, 4 (2016) 4603-4609.

[62] Y. Shiratori, T. Oshima, K. Sasaki, Feasibility of direct-biogas SOFC, International Journal of Hydrogen Energy, 33 (2008) 6316-6321.

[63] S.E. Evans, J.Z. Staniforth, R.J. Darton, R.M. Ormerod, A nickel doped perovskite catalyst for reforming methane rich biogas with minimal carbon deposition, Green Chemistry, 16 (2014) 4587-4594.

[64] L. Troskialina, A. Dhir, R. Steinberger-Wilckens, Improved Performance and Durability of Anode Supported SOFC Operating on Biogas, ECS Transactions, 68 (2015) 2503-2513.

[65] A. Rafique, R. Raza, A. Ali, M.A. Ahmad, M. Syväjärvi, An efficient carbon resistant composite $Ni_{0.6}Zn_{0.4}O_{2-\delta}$-GDC anode for biogas fuelled solid oxide fuel cell, Journal of Power Sources, 438 (2019) 227042.

[66] D. San-José-Alonso, J. Juan-Juan, M.J. Illán-Gómez, M.C. Román-Martínez, Ni, Co and bimetallic Ni–Co catalysts for the dry reforming of methane, Applied Catalysis A: General, 371 (2009) 54-59.

[67] A.K. Boulamanti, S. Donida Maglio, J. Giuntoli, A. Agostini, Influence of different practices on biogas sustainability, Biomass and Bioenergy, 53 (2013) 149-161.

[68] O. Hijazi, S. Munro, B. Zerhusen, M. Effenberger, Review of life cycle assessment for biogas production in Europe, Renewable and Sustainable Energy Reviews, 54 (2016) 1291-1300.

[69] D. Pergolesi, E. Fabbri, A. D'Epifanio, E. Di Bartolomeo, A. Tebano, S. Sanna, S. Licoccia, G. Balestrino, E. Traversa, High proton conduction in grain-boundary-free yttrium-doped barium zirconate films grown by pulsed laser deposition, Nature Materials, 9 (2010) 846-852.

[70] G. Nurk, M. Vestli, P. Möller, R. Jaaniso, M. Kodu, H. Mändar, T. Romann, R. Kanarbik, E. Lust, Mobility of Sr in Gadolinia Doped Ceria Barrier Layers Prepared Using Spray Pyrolysis, Pulsed Laser Deposition and Magnetron Sputtering Methods, Journal of The Electrochemical Society, 163 (2015) F88-F96.

[71] E.-O. Oh, C.-M. Whang, Y.-R. Lee, S.-Y. Park, D.H. Prasad, K.J. Yoon, J.-W. Son, J.-H. Lee, H.-W. Lee, Extremely Thin Bilayer Electrolyte for Solid Oxide Fuel Cells (SOFCs) Fabricated by Chemical Solution Deposition (CSD), Advanced Materials, 24 (2012) 3373-3377.

[72] P. Coddet, M.-L. Amany, J. Vulliet, A. Caillard, A.-L. Thomann, YSZ/GDC bilayer and gradient barrier layers deposited by reactive magnetron sputtering for solid oxide cells, Surface and Coatings Technology, 357 (2019) 103-113.

[73] H. He, J.M. Hill, Carbon deposition on Ni/YSZ composites exposed to humidified methane, Applied Catalysis A: General, 317 (2007) 284-292.

[74] P. Li, Z. Wang, X. Yao, N. Hou, L. Fan, T. Gan, Y. Zhao, Y. Li, J.W. Schwank, Effect of Sn addition on improving the stability of Ni-$Ce_{0.8}Sm_{0.2}O_{1.9}$ anode material for solid oxide fuel cells fed with dry CH_4, Catalysis Today, 330 (2019) 209-216.

[75] N.A. Arifin, L. Troskialina, A.H. Shamsuddin, R. Steinberger-Wilckens, Effects of Sn doping on the manufacturing, performance and carbon deposition of Ni/ScSZ cells in solid oxide fuel cells, International Journal of Hydrogen Energy, 45 (2020) 27575-27586.

[76] C. Neofytidis, V. Dracopoulos, S.G. Neophytides, D.K. Niakolas, Electrocatalytic performance and carbon tolerance of ternary Au-Mo-Ni/GDC SOFC anodes under CH_4-rich Internal Steam Reforming conditions, Catalysis Today, 310 (2018) 157-165.

[77] X. Wu, Y. Tian, J. Zhang, W. Zuo, X. Kong, J. Wang, K. Sun, X. Zhou, Enhanced electrochemical performance and carbon anti-coking ability of solid oxide fuel cells with silver modified nickel-yttrium stabilized zirconia anode by electroless plating, Journal of Power Sources, 301 (2016) 143-150.

[78] B. Hołówko, P. Błaszczak, M. Chlipała, M. Gazda, S.F. Wang, P. Jasiński, B. Bochentyn, Structural and catalytic properties of ceria layers doped with transition metals for SOFCs fueled by biogas, International Journal of Hydrogen Energy, 45 (2020) 12982-12996.

[79] J.G. Lee, O.S. Jeon, H.J. Hwang, J. Jang, Y. Lee, S.H. Hyun, Y.G. Shul, Durable and High-Performance Direct-Methane Fuel Cells with Coke-Tolerant Ceria-Coated Ni Catalysts at Reduced Temperatures, Electrochimica Acta, 191 (2016) 677-686.

[80] Q. Yang, F. Chai, C. Ma, C. Sun, S. Shi, L. Chen, Enhanced coking tolerance of a MgO-modified Ni cermet anode for hydrocarbon fueled solid oxide fuel cells, Journal of Materials Chemistry A, 4 (2016) 18031-18036.

[81] Y. Xie, N. Shi, X. Hu, M. Liu, Y. Yang, D. Huan, Y. Pan, R. Peng, C. Xia, Novel in-situ MgO nano-layer decorated carbon-tolerant anode for solid oxide fuel cells, International Journal of Hydrogen Energy, 45 (2020) 11791-11801.

[82] R. Burch, L.C. Garla, Platinum-tin reforming catalysts: II. Activity and selectivity in hydrocarbon reactions, Journal of Catalysis, 71 (1981) 360-372.

[83] G.W. Huber, J.W. Shabaker, J.A. Dumesic, Raney Ni-Sn Catalyst for H_2 Production from Biomass-Derived Hydrocarbons, Science, 300 (2003) 2075-2077.

[84] S. Zhao, S. Li, T. Guo, S. Zhang, J. Wang, Y. Wu, Y. Chen, Advances in Sn-Based Catalysts for Electrochemical CO2 Reduction, Nano-Micro Letters, 11 (2019) 62.

[85] C. Wen, A. Yin, W.-L. Dai, Recent advances in silver-based heterogeneous catalysts for green chemistry processes, Applied Catalysis B: Environmental, 160-161 (2014) 730-741.

[86] F.-Y. Wang, S. Cheng, B.-Z. Wan, Porous Ag–CGO cermets as anode materials for IT-SOFC using CO fuel, Fuel Cells Bulletin, 2008 (2008) 12-16.

[87] C. Ratnasamy, J.P. Wagner, Water Gas Shift Catalysis, Catalysis Reviews, 51 (2009) 325-440.

[88] R.V. Gonçalves, R. Wojcieszak, H. Wender, C. Sato B. Dias, L.L.R. Vono, D. Eberhardt, S.R. Teixeira, L.M. Rossi, Easy Access to Metallic Copper Nanoparticles with High Activity and Stability for CO Oxidation, ACS Applied Materials & Interfaces, 7 (2015) 7987-7994.

[89] M.B. Gawande, A. Goswami, F.-X. Felpin, T. Asefa, X. Huang, R. Silva, X. Zou, R. Zboril, R.S. Varma, Cu and Cu-Based Nanoparticles: Synthesis and Applications in Catalysis, Chemical Reviews, 116 (2016) 3722-3811.

[90] S. McIntosh, J.M. Vohs, R.J. Gorte, Role of Hydrocarbon Deposits in the Enhanced Performance of Direct-Oxidation SOFCs, Journal of The Electrochemical Society, 150 (2003) A470.

[91] X.-F. Ye, B. Huang, S.R. Wang, Z.R. Wang, L. Xiong, T.L. Wen, Preparation and performance of a Cu–CeO_2–ScSZ composite anode for SOFCs running on ethanol fuel, Journal of Power Sources, 164 (2007) 203-209.

[92] S.A. Theofanidis, V.V. Galvita, C. Konstantopoulos, H. Poelman, G.B. Marin, Fe-Based Nano-Materials in Catalysis, Materials (Basel), 11 (2018).

[93] A. Casnati, M. Lanzi, G. Cera, Recent Advances in Asymmetric Iron Catalysis, Molecules, 25 (2020).

[94] G.N. Howatt, R.G. Breckenridge, J.M. Brownlow, FABRICATION OF THIN CERAMIC SHEETS FOR CAPACITORS*, Journal of the American Ceramic Society, 30 (1947) 237-242.

[95] G.N. Howatt, Method of producing high dielectric high insulation ceramic plates, Google Patents, 1952.

[96] R.E. Mistler, The principles of tape casting and tape casting applications, in: R.A. Terpstra, P.P.A.C. Pex, A.H. de Vries (Eds.) Ceramic Processing, Springer Netherlands, Dordrecht, 1995, pp. 147-173.

[97] R.K. Nishihora, P.L. Rachadel, M.G.N. Quadri, D. Hotza, Manufacturing porous ceramic materials by tape casting—A review, Journal of the European Ceramic Society, 38 (2018) 988-1001.

[98] J. Zhou, L. Zhang, C. Liu, J. Pu, Q. Liu, C. Zhang, S.H. Chan, Aqueous tape casting technique for the fabrication of $Sc_{0.1}Ce_{0.01}Zr_{0.89}O_{2+\Delta}$ ceramic for electrolyte-

supported solid oxide fuel cell, International Journal of Hydrogen Energy, 44 (2019) 21110-21114.

[99] M. Liu, Y. Liu, Multilayer tape casting of large-scale anode-supported thin-film electrolyte solid oxide fuel cells, International Journal of Hydrogen Energy, 44 (2019) 16976-16982.

[100] H. Moon, S.D. Kim, S.H. Hyun, H.S. Kim, Development of IT-SOFC unit cells with anode-supported thin electrolytes via tape casting and co-firing, International Journal of Hydrogen Energy, 33 (2008) 1758-1768.

[101] H. Moon, S.D. Kim, E.W. Park, S.H. Hyun, H.S. Kim, Characteristics of SOFC single cells with anode active layer via tape casting and co-firing, International Journal of Hydrogen Energy, 33 (2008) 2826-2833.

[102] W. Schafbauer, N. H. Menzler, H. Buchkremer, Tape Casting of Anode Supports for Solid Oxide Fuel Cells at Forschungszentrum Jülich, International Journal of Applied Ceramic Technology, 11 (2014) 125-135.

[103] T. Baquero, J. Escobar, J. Frade, D. Hotza, Aqueous tape casting of micro and nano YSZ for SOFC electrolytes, Ceramics International, 39 (2013) 8279-8285.

[104] J. Zhou, Q. Liu, Q. Sun, S. Hwa Chan, A Low Cost Large-Area Solid Oxide Cells Fabrication Technology based on Aqueous Co-Tape Casting and Co-Sintering, Fuel Cells, 14 (2014) 667-670.

[105] C. Goulart, D. de Souza, Critical analysis of aqueous tape casting, sintering, and characterization of planar Yttria-Stabilized Zirconia electrolytes for SOFC, International Journal of Applied Ceramic Technology, 14 (2017) 413-423.

[106] P. Nahass, W.E. Rhine, R.L. Pober, Comparison of aqueous and nonaqueous slurries for tape-casting, and dimensional stability in green tapes, Ceramic Transactions, 15 pp., 355 (1990).

[107] D. Hotza, P. Greil, Review: aqueous tape casting of ceramic powders, Materials Science and Engineering: A, 202 (1995) 206-217.

[108] S. Lee, K. Lee, Y.-h. Jang, J. Bae, Fabrication of solid oxide fuel cells (SOFCs) by solvent-controlled co-tape casting technique, International Journal of Hydrogen Energy, 42 (2017) 1648-1660.

[109] J. Kiennemann, T. Chartier, C. Pagnoux, J.F. Baumard, M. Huger, J.M. Lamérant, Drying mechanisms and stress development in aqueous alumina tape casting, Journal of the European Ceramic Society, 25 (2005) 1551-1564.

[110] M.a.P. Albano, L.B. Garrido, Influence of the slip composition on the properties of tape-cast alumina substrates, Ceramics International, 31 (2005) 57-66.

[111] S. Nayak, B.P. Singh, L. Besra, T.K. Chongdar, N.M. Gokhale, S. Bhattacharjee, Aqueous Tape Casting Using Organic Binder: A Case Study with YSZ, Journal of the American Ceramic Society, 94 (2011) 3742-3747.

[112] B. Bitterlich, C. Lutz, A. Roosen, Rheological characterization of water-based slurries for the tape casting process, Ceramics International, 28 (2002) 675-683.

[113] S. Ramanathan, M.B. Kakade, Aqueous slurry processing of monolithic films for SOFC – YSZ, LSM and YSZ–NiO systems, International Journal of Hydrogen Energy, 36 (2011) 14956-14962.

[114] S. Sakthivel, V.V. Krishnan, B. Pitchumani, Influence of suspension stability on wet grinding for production of mineral nanoparticles, Particuology, 6 (2008) 120-124.

[115] D. Houivet, J. El Fallah, J.-M. Haussonne, Dispersion and Grinding of Oxide Powders into an Aqueous Slurry, Journal of the American Ceramic Society, 85 (2002) 321-328.

[116] S. Ramanathan, K.P. Krishnakumar, P.K. De, S. Banerjee, Powder dispersion and aqueous tape casting of YSZ-NiO composite, Journal of Materials Science, 39 (2004) 3339-3344.

[117] S. Ramanathan, K.P.K. Kumar, P.K. De, S. Banerjee, Role of dispersion conditions on grindability of yttria stabilized zirconia (YSZ) powders, Bulletin of Materials Science, 28 (2005) 109-114.

[118] K. Nagata, Effect of Functionalities of Binders on Rheological Behavior of Alumina Suspensions and Properties of Green Sheets, Journal of the Ceramic Society of Japan, 101 (1993) 845-849.

[119] J.A. Lewis, Colloidal Processing of Ceramics, Journal of the American Ceramic Society, 83 (2000) 2341-2359.

[120] M.R. Somalu, A. Muchtar, W.R.W. Daud, N.P. Brandon, Screen-printing inks for the fabrication of solid oxide fuel cell films: A review, Renewable and Sustainable Energy Reviews, 75 (2017) 426-439.

[121] L.H. Luo, A.I.Y. Tok, F.Y.C. Boey, Aqueous tape casting of 10mol%-Gd_2O_3-doped CeO_2 nano-particles, Materials Science and Engineering: A, 429 (2006) 266-271.

[122] J. Zhou, Q. Liu, L. Zhang, S.H. Chan, A study of short stack with large area solid oxide fuel cells by aqueous tape casting, International Journal of Hydrogen Energy, 41 (2016) 18203-18206.

[123] D.M. Amaya, D. Estrada, D. Hotza, J.B. Rodrigues Neto, J.A. Escobar, Porous Cu/YSZ anodes processed by aqueous tape casting for IT-SOFC, Journal of the European Ceramic Society, 37 (2017) 5233-5237.

[124] O.A. Paul, Handbook of ball mill and pebble mill operation, Paul O. Abbé Inc., Little Falls, N.J., 1964.

[125] R.E. Mistler, E.R. Twiname, Tape Casting: Theory and Practice, The American Ceramic Society, Westerville, 2000.

[126] M. Jabbari, R. Bulatova, A.I.Y. Tok, C.R.H. Bahl, E. Mitsoulis, J.H. Hattel, Ceramic tape casting: A review of current methods and trends with emphasis on rheological behaviour and flow analysis, Materials Science and Engineering: B, 212 (2016) 39-61.

[127] C.A. Gutiérrez, R. Moreno, Influence of slip preparation and casting conditions on aqueous tape casting of Al2O3, Materials Research Bulletin, 36 (2001) 2059-2072.

[128] B.J. Briscoe, G. Lo Biundo, N. Özkan, Drying kinetics of water-based ceramic suspensions for tape casting, Ceramics International, 24 (1998) 347-357.

[129] M.P. Albano, L.B. Garrido, Aqueous tape casting of yttria stabilized zirconia, Materials Science and Engineering: A, 420 (2006) 171-178.

[130] M.P. Albano, L.B. Garrido, Influence of the aging time of yttria stabilized zirconia slips on the cracking behavior during drying and green properties of cast tapes, Ceramics International, 34 (2008) 1279-1284.

[131] R.W. Rice, Ceramic fabrication technology, CRC Press2002.

[132] H.-G. Park, H. Moon, S.-C. Park, J.-J. Lee, D. Yoon, S.-H. Hyun, D.-H. Kim, Performance improvement of anode-supported electrolytes for planar solid oxide fuel

cells via a tape-casting/lamination/co-firing technique, Journal of Power Sources, 195 (2010) 2463-2469.

[133] J. Malzbender, W. Fischer, R.W. Steinbrech, Studies of residual stresses in planar solid oxide fuel cells, Journal of Power Sources, 182 (2008) 594-598.

[134] C. Jin, Y. Mao, N. Zhang, K. Sun, Fabrication and characterization of Ni-SSZ gradient anodes/SSZ electrolyte for anode-supported SOFCs by tape casting and co-sintering technique, International Journal of Hydrogen Energy, 40 (2015) 8433-8441.

[135] S.-H. Lee, G.L. Messing, M. Awano, Sintering Arches for Cosintering Camber-Free SOFC Multilayers, Journal of the American Ceramic Society, 91 (2008) 421-427.

[136] X.-V. Nguyen, C.-T. Chang, G.-B. Jung, S.-H. Chan, W.C. Huang, K.-J. Hsiao, W.-T. Lee, S.-W. Chang, I.C. Kao, Effect of Sintering Temperature and Applied Load on Anode-Supported Electrodes for SOFC Application, Energies, 9 (2016).

[137] H. Dai, H. Kou, Z. Tao, K. Liu, M. Xue, Q. Zhang, L. Bi, Optimization of sintering temperature for SOFCs by a co-firing method, Ceramics International, 46 (2020) 6987-6990.

[138] Z. Gao, D. Kennouche, S.A. Barnett, Reduced-temperature firing of solid oxide fuel cells with zirconia/ceria bi-layer electrolytes, Journal of Power Sources, 260 (2014) 259-263.

[139] A.S. Mehranjani, D.J. Cumming, D.C. Sinclair, R.H. Rothman, Low-temperature co-sintering for fabrication of zirconia/ceria bi-layer electrolyte via tape casting using a Fe_2O_3 sintering aid, Journal of the European Ceramic Society, 37 (2017) 3981-3993.

[140] R. Weinstein, Process for flattening alumina substrates, U.S. Patent No. 3792139A, US Department of Army, 1974.

[141] R. Raj, Co-fired multilayer ceramic tapes that exhibit constrained sintering, U.S. Patent No. US5102720A, Cornell Research Foundation Inc, 1992.

[142] T. Kawada, H. Yokokawa, M. Dokiya, N. Sakai, T. Horita, J. Van Herle, K. Sasaki, Ceria-Zirconia Composite Electrolyte for Solid Oxide Fuel Cells, Journal of Electroceramics, 1 (1997) 155-164.

[143] X. Zhang, M. Robertson, C. Decès-Petit, Y. Xie, R. Hui, W. Qu, O. Kesler, R. Maric, D. Ghosh, Solid oxide fuel cells with bi-layered electrolyte structure, Journal of Power Sources, 175 (2008) 800-805.

[144] C.X. Guo, J.X. Wang, C.R. He, W.G. Wang, Effect of alumina on the properties of ceria and scandia co-doped zirconia for electrolyte-supported SOFC, Ceramics International, 39 (2013) 9575-9582.

[145] L. Lei, Y. Bai, J. Liu, Ni-based anode-supported Al_2O_3-doped-Y_2O_3-stabilized ZrO_2 thin electrolyte solid oxide fuel cells with Y_2O_3-stabilized ZrO_2 buffer layer, Journal of Power Sources, 248 (2014) 1312-1319.

[146] V. Gil, J. Tartaj, C. Moure, P. Duran, Rapid densification by using Bi_2O_3 as an aid for sintering of gadolinia-doped ceria ceramics, Ceramics International, 33 (2007) 471-475.

[147] C.G.M. Lima, T.H. Santos, J.P.F. Grilo, R.P.S. Dutra, R.M. Nascimento, S. Rajesh, F.C. Fonseca, D.A. Macedo, Synthesis and properties of CuO-doped $Ce_{0.9}Gd_{0.1}O_{2-\delta}$ electrolytes for SOFCs, Ceramics International, 41 (2015) 4161-4168.

[148] K. Sasaki, Y. Teraoka, Equilibria in Fuel Cell Gases: II. The C-H-O Ternary Diagrams, Journal of the Electrochemical Society 150 (2003) A885-A888.

[149] P. Boldrin, E. Ruiz-Trejo, J. Mermelstein, J.M. Bermúdez Menéndez, T. Ramírez Reina, N.P. Brandon, Strategies for Carbon and Sulfur Tolerant Solid Oxide Fuel Cell Materials, Incorporating Lessons from Heterogeneous Catalysis, Chemical Reviews, 116 (2016) 13633-13684.

[150] J.G. McCarty, H. Wise, Hydrogenation of surface carbon on alumina-supported nickel, Journal of Catalysis, 57 (1979) 406-416.

[151] D.L. Trimm, Catalysts for the control of coking during steam reforming, Catalysis Today, 49 (1999) 3-10.

[152] C.-j. Liu, J. Ye, J. Jiang, Y. Pan, Progresses in the Preparation of Coke Resistant Ni-based Catalyst for Steam and CO_2 Reforming of Methane, ChemCatChem, 3 (2011) 529-541.

[153] F. Yu, J. Xiao, Y. Zhang, W. Cai, Y. Xie, N. Yang, J. Liu, M. Liu, New insights into carbon deposition mechanism of nickel/yttrium-stabilized zirconia cermet from methane by in situ investigation, Applied Energy, 256 (2019) 113910.

[154] K. Girona, J. Laurencin, J. Fouletier, F. Lefebvre-Joud, Carbon deposition in CH_4/CO_2 operated SOFC: Simulation and experimentation studies, Journal of Power Sources, 210 (2012) 381-391.

[155] C.H. Bartholomew, Carbon Deposition in Steam Reforming and Methanation, Catalysis Reviews, 24 (1982) 67-112.

[156] C.H. Bartholomew, Mechanisms of catalyst deactivation, Applied Catalysis A: General, 212 (2001) 17-60.

[157] R.T.K. Baker, M.A. Barber, P.S. Harris, F.S. Feates, R.J. Waite, Nucleation and growth of carbon deposits from the nickel catalyzed decomposition of acetylene, Journal of Catalysis, 26 (1972) 51-62.

[158] T. Chen, W.G. Wang, H. Miao, T. Li, C. Xu, Evaluation of carbon deposition behavior on the nickel/yttrium-stabilized zirconia anode-supported fuel cell fueled with simulated syngas, Journal of Power Sources, 196 (2011) 2461-2468.

[159] A. Lanzini, P. Leone, C. Guerra, F. Smeacetto, N.P. Brandon, M. Santarelli, Durability of anode supported Solid Oxides Fuel Cells (SOFC) under direct dry-reforming of methane, Chemical Engineering Journal, 220 (2013) 254-263.

[160] T. Takeguchi, S.-n. Furukawa, M. Inoue, Hydrogen Spillover from NiO to the Large Surface Area CeO_2–ZrO_2 Solid Solutions and Activity of the NiO/CeO_2–ZrO_2 Catalysts for Partial Oxidation of Methane, Journal of Catalysis, 202 (2001) 14-24.

[161] T. Takeguchi, Y. Kani, T. Yano, R. Kikuchi, K. Eguchi, K. Tsujimoto, Y. Uchida, A. Ueno, K. Omoshiki, M. Aizawa, Study on steam reforming of CH_4 and C_2 hydrocarbons and carbon deposition on Ni-YSZ cermets, Journal of Power Sources, 112 (2002) 588-595.

[162] J. Rostrup-Nielsen, D.L. Trimm, Mechanisms of carbon formation on nickel-containing catalysts, Journal of Catalysis, 48 (1977) 155-165.

[163] I. Alstrup, A new model explaining carbon filament growth on nickel, iron, and Ni□Cu alloy catalysts, Journal of Catalysis, 109 (1988) 241-251.

[164] H.E. Grenga, K.R. Lawless, Active Sites for Heterogeneous Catalysis, Journal of Applied Physics, 43 (1972) 1508-1514.

[165] F. Besenbacher, I. Chorkendorff, B.S. Clausen, B. Hammer, A.M. Molenbroek, J.K. Nørskov, I. Stensgaard, Design of a Surface Alloy Catalyst for Steam Reforming, Science, 279 (1998) 1913.

[166] M. Pillai, Y. Lin, H. Zhu, R.J. Kee, S.A. Barnett, Stability and coking of direct-methane solid oxide fuel cells: Effect of CO_2 and air additions, Journal of Power Sources, 195 (2010) 271-279.

[167] T. Papadam, G. Goula, I.V. Yentekakis, Long-term operation stability tests of intermediate and high temperature Ni-based anodes' SOFCs directly fueled with simulated biogas mixtures, International Journal of Hydrogen Energy, 37 (2012) 16680-16685.

[168] C. Guerra, A. Lanzini, P. Leone, M. Santarelli, N.P. Brandon, Optimization of dry reforming of methane over Ni/YSZ anodes for solid oxide fuel cells, Journal of Power Sources, 245 (2014) 154-163.

[169] Z. Lyu, W. Shi, M. Han, Electrochemical characteristics and carbon tolerance of solid oxide fuel cells with direct internal dry reforming of methane, Applied Energy, 228 (2018) 556-567.

[170] H. Sumi, Y.-H. Lee, H. Muroyama, T. Matsui, K. Eguchi, Comparison Between Internal Steam and CO_2 Reforming of Methane for Ni-YSZ and Ni-ScSZ SOFC Anodes, Journal of the Electrochemical Society, 157 (2010) B1118-B1125.

[171] H. Aslannejad, L. Barelli, A. Babaie, S. Bozorgmehri, Effect of air addition to methane on performance stability and coking over NiO–YSZ anodes of SOFC, Applied Energy, 177 (2016) 179-186.

[172] E. Nikolla, J. Schwank, S. Linic, Direct Electrochemical Oxidation of Hydrocarbon Fuels on SOFCs: Improved Carbon Tolerance of Ni Alloy Anodes, Journal of The Electrochemical Society, 156 (2009) B1312-B1316.

[173] I. Gavrielatos, V. Drakopoulos, S.G. Neophytides, Carbon tolerant Ni–Au SOFC electrodes operating under internal steam reforming conditions, Journal of Catalysis, 259 (2008) 75-84.

[174] G.J. Offer, J. Mermelstein, E. Brightman, N.P. Brandon, Thermodynamics and Kinetics of the Interaction of Carbon and Sulfur with Solid Oxide fuel Cell Anodes, Journal of the American Ceramic Society, 92 (2009) 763-780.

[175] C.M. Finnerty, Internal Reforming and Electrochemical Performance Studies of Doped Nickel/Zirconia Anodes in SOFCs Running on Methane, ECS Proceedings Volumes, 1999-19 (1999) 583-592.

[176] N.C. Triantafyllopoulos, S.G. Neophytides, Dissociative adsorption of CH_4 on NiAu/YSZ: The nature of adsorbed carbonaceous species and the inhibition of graphitic C formation, Journal of Catalysis, 239 (2006) 187-199.

[177] D.K. Niakolas, J.P. Ouweltjes, G. Rietveld, V. Dracopoulos, S.G. Neophytides, Au-doped Ni/GDC as a new anode for SOFCs operating under rich CH_4 internal steam reforming, International Journal of Hydrogen Energy, 35 (2010) 7898-7904.

[178] I.A. Proctor, A.L. Hopkin, R.M. Ormerod, Development of anodes for direct electrocatalytic oxidation of methane in solid oxide fuel cells, Ionics, 9 (2003) 242-247.

[179] Y. Zhang, F. Yu, X. Wang, Q. Zhou, J. Liu, M. Liu, Direct operation of Ag-based anode solid oxide fuel cells on propane, Journal of Power Sources, 366 (2017) 56-64.

[180] X. Wu, X. Zhou, Y. Tian, X. Kong, J. Zhang, W. Zuo, X. Ye, K. Sun, Preparation and electrochemical performance of silver impregnated Ni-YSZ anode for solid oxide fuel cell in dry methane, International Journal of Hydrogen Energy, 40 (2015) 16484-16493.

[181] I. Gavrielatos, D. Montinaro, A. Orfanidi, S. Neophytides, Thermogravimetric and Electrocatalytic Study of Carbon Deposition of Ag-doped Ni/YSZ Electrodes under Internal CH_4 Steam Reforming Conditions, Fuel Cells, 9 (2009) 883-890.

[182] Y. Nabae, I. Yamanaka, M. Hatano, K. Otsuka, Catalytic Behavior of Pd–Ni/Composite Anode for Direct Oxidation of Methane in SOFCs, Journal of the Electrochemical Society, 153 (2006) A140-A145.

[183] Y. Nabae, I. Yamanaka, Alloying effects of Pd and Ni on the catalysis of the oxidation of dry CH_4 in solid oxide fuel cells, Applied Catalysis A: General, 369 (2009) 119-124.

[184] C.-A. Thieu, H.-I. Ji, H. Kim, K.J. Yoon, J.-H. Lee, J.-W. Son, Palladium incorporation at the anode of thin-film solid oxide fuel cells and its effect on direct utilization of butane fuel at 600 °C, Applied Energy, 243 (2019) 155-164.

[185] M. García-Diéguez, I.S. Pieta, M.C. Herrera, M.A. Larrubia, L.J. Alemany, Improved Pt-Ni nanocatalysts for dry reforming of methane, Applied Catalysis A: General, 377 (2010) 191-199.

[186] Ş. Özkara-Aydınoğlu, A.E. Aksoylu, CO2 reforming of methane over Pt–Ni/Al_2O_3 catalysts: Effects of catalyst composition, and water and oxygen addition to the feed, International Journal of Hydrogen Energy, 36 (2011) 2950-2959.

[187] T. Takeguchi, R. Kikuchi, T. Yano, K. Eguchi, K. Murata, Effect of precious metal addition to Ni-YSZ cermet on reforming of CH4 and electrochemical activity as SOFC anode, Catalysis Today, 84 (2003) 217-222.

[188] K. Park, S. Lee, G. Bae, J. Bae, Performance analysis of Cu, Sn and Rh impregnated NiO/CGO91 anode for butane internal reforming SOFC at intermediate temperature, Renewable Energy, 83 (2015) 483-490.

[189] J.J. Strohm, J. Zheng, C. Song, Low-temperature steam reforming of jet fuel in the absence and presence of sulfur over Rh and Rh–Ni catalysts for fuel cells, Journal of Catalysis, 238 (2006) 309-320.

[190] T. Bunluesin, R.J. Gorte, G.W. Graham, Studies of the water-gas-shift reaction on ceria-supported Pt, Pd, and Rh: Implications for oxygen-storage properties, Applied Catalysis B: Environmental, 15 (1998) 107-114.

[191] T. Hibino, A. Hashimoto, M. Yano, M. Suzuki, M. Sano, Ru-catalyzed anode materials for direct hydrocarbon SOFCs, Electrochimica Acta, 48 (2003) 2531-2537.

[192] M. Itome, A.E. Nelson, Methane Oxidation Over M–8YSZ and M–CeO_2/8YSZ (M = Ni, Cu, Co, Ag) Catalysts, Catalysis Letters, 106 (2006) 21-27.

[193] P. Djinović, I.G. Osojnik Črnivec, B. Erjavec, A. Pintar, Influence of active metal loading and oxygen mobility on coke-free dry reforming of Ni–Co bimetallic catalysts, Applied Catalysis B: Environmental, 125 (2012) 259-270.

[194] S.-z. Wang, J. Gao, High Performance Ni-Fe-Lanthanum Gallate Composite Anodes for Dimethyl Ether Fuel Cells, Electrochemistry and Solid State Letters, 9 (2006) A395-A398.

[195] B. Huang, S.R. Wang, R.Z. Liu, T.L. Wen, Preparation and performance characterization of the Fe–Ni/ScSZ cermet anode for oxidation of ethanol fuel in SOFCs, Journal of Power Sources, 167 (2007) 288-294.

[196] R. da Paz Fiuza, M. Aurélio da Silva, J.S. Boaventura, Development of Fe–Ni/YSZ–GDC electrocatalysts for application as SOFC anodes: XRD and TPR characterization and evaluation in the ethanol steam reforming reaction, International Journal of Hydrogen Energy, 35 (2010) 11216-11228.

[197] H. Kan, H. Lee, Enhanced stability of Ni–Fe/GDC solid oxide fuel cell anodes for dry methane fuel, Catalysis Communications, 12 (2010) 36-39.

[198] K. Li, L. Jia, X. Wang, J. Pu, B. Chi, L. Jian, Methane on-cell reforming in nickel–iron alloy supported solid oxide fuel cells, Journal of Power Sources, 284 (2015) 446-451.

[199] S. Kim, C. Kim, J.H. Lee, J. Shin, T.-H. Lim, G. Kim, Tailoring Ni-based catalyst by alloying with transition metals (M=Ni, Co, Cu, and Fe) for direct hydrocarbon utilization of energy conversion devices, Electrochimica Acta, 225 (2017) 399-406.

[200] H. Kan, S.H. Hyun, Y.-G. Shul, H. Lee, Improved solid oxide fuel cell anodes for the direct utilization of methane using Sn-doped Ni/YSZ catalysts, Catalysis Communications, 11 (2009) 180-183.

[201] J.-h. Myung, S.-D. Kim, T.H. Shin, D. Lee, J.T.S. Irvine, J. Moon, S.-H. Hyun, Nano-composite structural Ni-Sn alloy anodes for high performance and durability of direct methane-fueled SOFCs, Journal of Materials Chemistry A, 3 (2015) 13801-13806.

[202] S. McIntosh, J.M. Vohs, R.J. Gorte, An examination of lanthanide additives on the performance of Cu–YSZ cermet anodes, Electrochimica Acta, 47 (2002) 3815-3821.

[203] M. Cimenti, J.M. Hill, Direct utilization of ethanol on ceria-based anodes for solid oxide fuel cells, Asia-Pacific Journal of Chemical Engineering, 4 (2009) 45-54.

[204] Shung-Ik Lee, John M. Vohs, R.J. Gorte, A Study of SOFC Anodes Based on Cu-Ni and Cu-Co Bimetallics in CeO_2-YSZ, Journal of the Electrochemical Society, 151 (2004) A1319-A1323.

[205] M. Liu, S. Wang, T. Chen, C. Yuan, Y. Zhou, S. Wang, J. Huang, Performance of the nano-structured Cu–Ni (alloy)-CeO_2 anode for solid oxide fuel cells, Journal of Power Sources, 274 (2015) 730-735.

[206] E.W. Park, H. Moon, M.-s. Park, S.H. Hyun, Fabrication and characterization of Cu–Ni–YSZ SOFC anodes for direct use of methane via Cu-electroplating, International Journal of Hydrogen Energy, 34 (2009) 5537-5545.

[207] A. Rismanchian, J. Mirzababaei, S.S.C. Chuang, Electroless plated Cu–Ni anode catalyst for natural gas solid oxide fuel cells, Catalysis Today, 245 (2015) 79-85.

[208] S. Islam, J.M. Hill, Preparation of Cu–Ni/YSZ solid oxide fuel cell anodes using microwave irradiation, Journal of Power Sources, 196 (2011) 5091-5094.

[209] M. Li, B. Hua, J. Pu, B. Chi, L. Jian, Electrochemical performance and carbon deposition resistance of M-$BaZr_{0.1}Ce_{0.7}Y_{0.1}Yb_{0.1}O_{3-\delta}$ (M = Pd, Cu, Ni or NiCu) anodes for solid oxide fuel cells, Scientific Reports, 5 (2015) 7667.

[210] N. Nakagawa, H. Sagara, K. Kato, Catalytic activity of Ni–YSZ–CeO_2 anode for the steam reforming of methane in a direct internal-reforming solid oxide fuel cell, Journal of Power Sources, 92 (2001) 88-94.

[211] J. Qiao, K. Sun, N. Zhang, B. Sun, J. Kong, D. Zhou, Ni/YSZ and Ni–CeO_2/YSZ anodes prepared by impregnation for solid oxide fuel cells, Journal of Power Sources, 169 (2007) 253-258.

[212] J. Qiao, N. Zhang, Z. Wang, Y. Mao, K. Sun, Y. Yuan, Performance of mix-impregnated CeO_2-Ni/YSZ Anodes for Direct Oxidation of Methane in Solid Oxide Fuel Cells, Fuel Cells, 9 (2009) 729-739.

[213] M.D. McIntyre, J.D. Kirtley, A. Singh, S. Islam, J.M. Hill, R.A. Walker, Comparing in Situ Carbon Tolerances of Sn-Infiltrated and BaO-Infiltrated Ni-YSZ Cermet Anodes

in Solid Oxide Fuel Cells Exposed to Methane, The Journal of Physical Chemistry C, 119 (2015) 7637-7647.

[214] F. Wang, W. Wang, R. Ran, M.O. Tade, Z. Shao, Aluminum oxide as a dual-functional modifier of Ni-based anodes of solid oxide fuel cells for operation on simulated biogas, Journal of Power Sources, 268 (2014) 787-793.

[215] X. Song, X. Dong, M. Li, H. Wang, Effects of adding alumina to the nickel-zirconia anode materials for solid oxide fuel cells and a two-step sintering method for half-cells, Journal of Power Sources, 308 (2016) 58-64.

[216] D.R. Driscoll, M.D. McIntyre, M.M. Welander, S.W. Sofie, R.A. Walker, Enhancement of high temperature metallic catalysts: Aluminum titanate in the nickel-zirconia system, Applied Catalysis A: General, 527 (2016) 36-44.

[217] E. Ramírez-Cabrera, A. Atkinson, D. Chadwick, Catalytic steam reforming of methane over Ce0.9Gd0.1O2−x, Applied Catalysis B: Environmental, 47 (2004) 127-131.

[218] F. Matei-Rutkovska, G. Postole, C.G. Rotaru, M. Florea, V.I. Pârvulescu, P. Gelin, Synthesis of ceria nanopowders by microwave-assisted hydrothermal method for dry reforming of methane, International Journal of Hydrogen Energy, 41 (2016) 2512-2525.

[219] L.P. Teh, H.D. Setiabudi, S.N. Timmiati, M.A.A. Aziz, N.H.R. Annuar, N.N. Ruslan, Recent progress in ceria-based catalysts for the dry reforming of methane: A review, Chemical Engineering Science, 242 (2021) 116606.

[220] Y. Chen, F. Chen, W. Wang, D. Ding, J. Gao, $Sm_{0.2}(Ce_{1-x}Ti_x)_{0.8}O_{1.9}$ modified Ni–yttria-stabilized zirconia anode for direct methane fuel cell, Journal of Power Sources, 196 (2011) 4987-4991.

[221] F. Wang, H. Kishimoto, T. Ishiyama, K. Develos- Bagarinao, K. Yamaji, T. Horita, H. Yokokawa, Modification of Ni-YSZ Surface with High Carbon Tolerance Using GDC Nanoparticles, Electrochemical Society Transactions, 78 (2017) 1457-1461.

[222] B.-K. Park, R. Scipioni, D. Cox, S.A. Barnett, Enhancement of Ni–$(Y_2O_3)_{0.08}(ZrO_2)_{0.92}$ fuel electrode performance by infiltration of $Ce_{0.8}Gd_{0.2}O_{2-\delta}$ nanoparticles, Journal of Materials Chemistry A, 8 (2020) 4099-4106.

[223] W. Zhu, C. Xia, J. Fan, R. Peng, G. Meng, Ceria coated Ni as anodes for direct utilization of methane in low-temperature solid oxide fuel cells, Journal of Power Sources, 160 (2006) 897-902.

[224] D. La Rosa, A. Sin, M.L. Faro, G. Monforte, V. Antonucci, A.S. Aricò, Mitigation of carbon deposits formation in intermediate temperature solid oxide fuel cells fed with dry methane by anode doping with barium, Journal of Power Sources, 193 (2009) 160-164.

[225] L. Yang, Y. Choi, W. Qin, H. Chen, K. Blinn, M. Liu, P. Liu, J. Bai, T.A. Tyson, M. Liu, Promotion of water-mediated carbon removal by nanostructured barium oxide/nickel interfaces in solid oxide fuel cells, Nature Communications, 2 (2011) 357.

[226] M. Asamoto, S. Miyake, K. Sugihara, H. Yahiro, Improvement of Ni/SDC anode by alkaline earth metal oxide addition for direct methane–solid oxide fuel cells, Electrochemistry Communications, 11 (2009) 1508-1511.

[227] A. Yan, M. Phongaksorn, D. Nativel, E. Croiset, Lanthanum promoted NiO–SDC anode for low temperature solid oxide fuel cells fueled with methane, Journal of Power Sources, 210 (2012) 374-380.

[228] Y. Shiratori, Y. Teraoka, K. Sasaki, $Ni_{1-x-y}Mg_xAl_yO$–ScSZ anodes for solid oxide fuel cells, Solid State Ionics, 177 (2006) 1371-1380.

[229] Q. Li, X. Wang, L. Jia, B. Chi, J. Pu, J. Li, High performance and carbon-deposition resistance metal-supported solid oxide fuel cell with a nickel–manganese spinel modified anode, Materials Today Energy, 17 (2020) 100473.

[230] Z. Zhan, S.A. Barnett, An Octane-Fueled Solid Oxide Fuel Cell, Science, 308 (2005) 844.

[231] Z. Zhan, S.A. Barnett, Operation of ceria-electrolyte solid oxide fuel cells on iso-octane–air fuel mixtures, Journal of Power Sources, 157 (2006) 422-429.

[232] C. Sun, Z. Xie, C. Xia, H. Li, L. Chen, Investigations of mesoporous CeO_2–Ru as a reforming catalyst layer for solid oxide fuel cells, Electrochemistry Communications, 8 (2006) 833-838.

[233] C. Jin, C. Yang, H. Zheng, F. Chen, Intermediate temperature solid oxide fuel cells with $Cu_{1.3}Mn_{1.7}O_4$ internal reforming layer, Journal of Power Sources, 201 (2012) 66-71.

[234] B. Hua, M. Li, J. Pu, B. Chi, L. Jian, $BaZr_{0.1}Ce_{0.7}Y_{0.1}Yb_{0.1}O_{3-\delta}$ enhanced coking-free on-cell reforming for direct-methane solid oxide fuel cells, Journal of Materials Chemistry A, 2 (2014) 12576-12582.

[235] B. Hua, N. Yan, M. Li, Y.-q. Zhang, Y.-f. Sun, J. Li, T. Etsell, P. Sarkar, K. Chuang, J.-L. Luo, Novel layered solid oxide fuel cells with multiple-twinned $Ni_{0.8}Co_{0.2}$ nanoparticles: the key to thermally independent CO_2 utilization and power-chemical cogeneration, Energy & Environmental Science, 9 (2016) 207-215.

[236] X.-F. Ye, S.R. Wang, Z.R. Wang, L. Xiong, X.F. Sun, T.L. Wen, Use of a catalyst layer for anode-supported SOFCs running on ethanol fuel, Journal of Power Sources, 177 (2008) 419-425.

[237] M. Liao, W. Wang, R. Ran, Z. Shao, Development of a Ni–$Ce_{0.8}Zr_{0.2}O_2$ catalyst for solid oxide fuel cells operating on ethanol through internal reforming, Journal of Power Sources, 196 (2011) 6177-6185.

[238] X. Liu, Z. Zhan, X. Meng, W. Huang, S. Wang, T. Wen, Enabling catalysis of Ru–CeO_2 for propane oxidation in low temperature solid oxide fuel cells, Journal of Power Sources, 199 (2012) 138-141.

[239] B. Hua, M. Li, B. Chi, L. Jian, Enhanced electrochemical performance and carbon deposition resistance of Ni–YSZ anode of solid oxide fuel cells by in situ formed Ni–MnO layer for CH_4 on-cell reforming, Journal of Materials Chemistry A, 2 (2014) 1150-1158.

[240] X. Lv, H. Chen, W. Zhou, F. Cheng, S.-D. Li, Z. Shao, Direct-methane solid oxide fuel cells with an in situ formed Ni–Fe alloy composite catalyst layer over Ni–YSZ anodes, Renewable Energy, 150 (2020) 334-341.

[241] Z. Lyu, Y. Wang, Y. Zhang, M. Han, Solid oxide fuel cells fueled by simulated biogas: Comparison of anode modification by infiltration and reforming catalytic layer, Chemical Engineering Journal, 393 (2020) 124755.

[242] W. Wang, S.P. Jiang, A.I.Y. Tok, L. Luo, GDC-impregnated Ni anodes for direct utilization of methane in solid oxide fuel cells, Journal of Power Sources, 159 (2006) 68-72.

[243] D. Yoon, A. Manthiram, Ni-M (M = Sn and Sb) intermetallic-based catalytic functional layer as a built-in safeguard for hydrocarbon-fueled solid oxide fuel cells, Journal of Materials Chemistry A, 3 (2015) 21824-21831.

[244] C. Lu, W. L. Worrell, J. M. Vohs, R.J. Gorte, A Comparison of Cu-Ceria-SDC and Au-Ceria-SDC Composites for SOFC Anodes, Journal of The Electrochemical Society, 150 (2003) A1357-A1359.

[245] S. Tao, J.T.S. Irvine, A redox-stable efficient anode for solid-oxide fuel cells, Nature Materials, 2 (2003) 320-323.

[246] Tao, J.T.S. Irvine, S.M. Plint, Methane Oxidation at Redox Stable Fuel Cell Electrode $La_{0.75}Sr_{0.25}Cr_{0.5}Mn_{0.5}O_{3-\delta}$, The Journal of Physical Chemistry B, 110 (2006) 21771-21776.

[247] J.C. Ruiz-Morales, J. Canales-Vázquez, C. Savaniu, D. Marrero-López, W. Zhou, J.T.S. Irvine, Disruption of extended defects in solid oxide fuel cell anodes for methane oxidation, Nature, 439 (2006) 568-571.

[248] M.R. Pillai, I. Kim, D.M. Bierschenk, S.A. Barnett, Fuel-flexible operation of a solid oxide fuel cell with $Sr_{0.8}La_{0.2}TiO_3$ support, Journal of Power Sources, 185 (2008) 1086-1093.

[249] M. Li, B. Hua, S.P. Jiang, J. Pu, B. Chi, L. Jian, $BaZr_{0.1}Ce_{0.7}Y_{0.1}Yb_{0.1}O_{3-\delta}$ as highly active and carbon tolerant anode for direct hydrocarbon solid oxide fuel cells, International Journal of Hydrogen Energy, 39 (2014) 15975-15981.

[250] C.M. Kim, J. Kim, K. Park, Fabrication and structural properties of porous Cu–YSZ cermets for solid oxide fuel cells, Powder Technology, 254 (2014) 425-431.

[251] R. Craciun, S. Park, R.J. Gorte, J.M. Vohs, C. Wang, W.L. Worrell, A Novel Method for Preparing Anode Cermets for Solid Oxide Fuel Cells, Journal of the Electrochemical Society, 146 (1999) 4019-4022.

[252] O. Costa-Nunes, R.J. Gorte, J.M. Vohs, Comparison of the performance of Cu–CeO_2–YSZ and Ni–YSZ composite SOFC anodes with H_2, CO, and syngas, Journal of Power Sources, 141 (2005) 241-249.

[253] G. Kaur, S. Basu, Physical characterization and electrochemical performance of copper–iron–ceria–YSZ anode-based SOFCs in H2 and methane fuels, International Journal of Energy Research, 39 (2015) 1345-1354.

[254] B.J.M. Sarruf, J.-E. Hong, R. Steinberger-Wilckens, P.E.V. de Miranda, Ceria-Co-Cu-based SOFC anode for direct utilisation of methane or ethanol as fuels, International Journal of Hydrogen Energy, 45 (2020) 5297-5308.

[255] X.-F. Ye, J. Zhou, S.R. Wang, F.R. Zeng, T.L. Wen, Z.L. Zhan, Research of carbon deposition formation and judgment in Cu-CeO_2-ScSZ anodes for direct ethanol solid oxide fuel cells, International Journal of Hydrogen Energy, 37 (2012) 505-510.

[256] J.W. Fergus, Oxide anode materials for solid oxide fuel cells, Solid State Ionics, 177 (2006) 1529-1541.

[257] M.K. Rath, K.-T. Lee, Characterization of novel Ba_2LnMoO_6 (Ln = Pr and Nd) double perovskite as the anode material for hydrocarbon-fueled solid oxide fuel cells, Journal of Alloys and Compounds, 737 (2018) 152-159.

[258] J.J. Alvarado Flores, M.L. Ávalos Rodríguez, G. Andrade Espinosa, J.V. Alcaraz Vera, Advances in the development of titanates for anodes in SOFC, International Journal of Hydrogen Energy, 44 (2019) 12529-12542.

[259] L. Shu, J. Sunarso, S.S. Hashim, J. Mao, W. Zhou, F. Liang, Advanced perovskite anodes for solid oxide fuel cells: A review, International Journal of Hydrogen Energy, 44 (2019) 31275-31304.

[260] J.-J. Lee, E.-W. Park, S.-H. Hyun, Performance and Evaluation of Cu-based Nano-composite Anodes for Direct Utilisation of Hydrocarbon Fuels in SOFCs, Fuel Cells, 10 (2010) 145-155.

[261] S. Sengodan, S. Choi, A. Jun, T.H. Shin, Y.-W. Ju, H.Y. Jeong, J. Shin, J.T.S. Irvine, G. Kim, Layered oxygen-deficient double perovskite as an efficient and stable anode for direct hydrocarbon solid oxide fuel cells, Nature Materials, 14 (2015) 205-209.

[262] L. Zhao, K. Chen, Y. Liu, B. He, A novel layered perovskite as symmetric electrode for direct hydrocarbon solid oxide fuel cells, Journal of Power Sources, 342 (2017) 313-319.

[263] N.H. Menzler, J. Malzbender, P. Schoderböck, R. Kauert, H.P. Buchkremer, Sequential Tape Casting of Anode-Supported Solid Oxide Fuel Cells, Fuel Cells, 14 (2014) 96-106.

[264] X. Chen, W. Ni, X. Du, Z. Sun, T. Zhu, Q. Zhong, M. Han, Electrochemical property of multi-layer anode supported solid oxide fuel cell fabricated through sequential tape-casting and co-firing, Journal of Materials Science & Technology, 35 (2019) 695-701.

[265] C. Haering, A. Roosen, H. Schichl, M. Schnöller, Degradation of the electrical conductivity in stabilised zirconia system: Part II: Scandia-stabilised zirconia, Solid State Ionics, 176 (2005) 261-268.

[266] R.L. Grosso, E.N.S. Muccillo, Sintering, phase composition and ionic conductivity of zirconia–scandia–ceria, Journal of Power Sources, 233 (2013) 6-13.

[267] A. Escardino, A. Belda, M.-J. Orts, A. Gozalbo, Ceria-doped scandia-stabilized zirconia ($10Sc_2O_3 \cdot 1CeO_2 \cdot 89ZrO_2$) as electrolyte for SOFCs: Sintering and ionic conductivity of thin, flat sheets, International Journal of Applied Ceramic Technology, 14 (2017) 532-542.

[268] R. Knibbe, J. Hjelm, M. Menon, N. Pryds, M. Søgaard, H.J. Wang, K. Neufeld, Cathode–Electrolyte Interfaces with CGO Barrier Layers in SOFC, Journal of the American Ceramic Society, 93 (2010) 2877-2883.

[269] L. dos Santos-Gómez, J. Hurtado, J.M. Porras-Vázquez, E.R. Losilla, D. Marrero-López, Durability and performance of CGO barriers and LSCF cathode deposited by spray-pyrolysis, Journal of the European Ceramic Society, 38 (2018) 3518-3526.

[270] V. Wilde, H. Störmer, J. Szász, F. Wankmüller, E. Ivers-Tiffée, D. Gerthsen, $Gd_{0.2}Ce_{0.8}O_2$ Diffusion Barrier Layer between $(La_{0.58}Sr_{0.4})(Co_{0.2}Fe_{0.8})O_{3-\delta}$ Cathode and $Y_{0.16}Zr_{0.84}O_2$ Electrolyte for Solid Oxide Fuel Cells: Effect of Barrier Layer Sintering Temperature on Microstructure, ACS Applied Energy Materials, 1 (2018) 6790-6800.

[271] S. Molin, J. Karczewski, B. Kamecki, A. Mroziński, S.F. Wang, P. Jasiński, Processing of Ce0.8Gd0.2O2-δ barrier layers for solid oxide cells: The effect of preparation method and thickness on the interdiffusion and electrochemical performance, Journal of the European Ceramic Society, 40 (2020) 5626-5633.

[272] P. Plonczak, M. Joost, J. Hjelm, M. Søgaard, M. Lundberg, P.V. Hendriksen, A high performance ceria based interdiffusion barrier layer prepared by spin-coating, Journal of Power Sources, 196 (2011) 1156-1162.

[273] Y. Leng, S.H. Chan, Q. Liu, Development of LSCF–GDC composite cathodes for low-temperature solid oxide fuel cells with thin film GDC electrolyte, International Journal of Hydrogen Energy, 33 (2008) 3808-3817.

[274] R. Al-Gaashani, S. Radiman, N. Tabet, A.R. Daud, Optical properties of SnO_2 nanostructures prepared via one-step thermal decomposition of tin (II) chloride dihydrate, Materials Science and Engineering: B, 177 (2012) 462-470.

[275] J. Ghose, A. Kanungo, Studies on the thermal decomposition of $Cu(NO_3)_2 \cdot 3H_2O$, Journal of thermal analysis, 20 (1981) 459-462.

[276] W.K. Jóźwiak, T.P. Maniecki, Influence of atmosphere kind on temperature programmed decomposition of noble metal chlorides, Thermochimica Acta, 435 (2005) 151-161.

[277] F. Paulik, J. Paulik, M. Arnold, Examination of the decomposition of $AgNO_3$ by means of simultaneous EGA and TG method under conventional and quasi isothermal circumstances, Thermochimica Acta, 92 (1985) 787-790.

[278] S.K. Ryu, W.K. Lee, S.J. Park, Thermal Decomposition of Hydrated Copper Nitrate [$Cu(NO_3)_2$-$3H_2O$] on Activated Carbon Fibers, Carbon sciency, 5 (2004) 180-185.

[279] J. Mu, D.D. Perlmutter, Thermal decomposition of metal nitrates and their hydrates, Thermochimica Acta, 56 (1982) 253-260.

[280] A.M. Gadalla, H.-F. Yu, Thermal decomposition of Fe(III) nitrate and its aerosol, Journal of Materials Research, 5 (1990) 1233-1236.

[281] A. Faes, A. Hessler-Wyser, A. Zryd, J. Van Herle, A Review of RedOx Cycling of Solid Oxide Fuel Cells Anode, Membranes (Basel), 2 (2012) 585-664.

[282] I. Pilatowsky, R.J. Romero, C.A. Isaza, S.A. Gamboa, P.J. Sebastian, W. Rivera, Thermodynamics of Fuel Cells, in: I. Pilatowsky, R.J. Romero, C.A. Isaza, S.A. Gamboa, P.J. Sebastian, W. Rivera (Eds.) Cogeneration Fuel Cell-Sorption Air Conditioning Systems, Springer London, London, 2011, pp. 25-36.

[283] X. Huang, Z. Zhang, J. Jiang, Fuel Cell Technology for Distributed Generation: An Overview, 2006 IEEE International Symposium on Industrial Electronics, 2006, pp. 1613-1618.

[284] M.E. Orazem, B. Tribollet, Electrochemical impedance spectroscopy, New Jersey, (2008) 383-389.

[285] K. Huang, J.B. Goodenough, 9 - Performance characterization techniques for a solid oxide fuel cell (SOFC) and its components, in: K. Huang, J.B. Goodenough (Eds.) Solid Oxide Fuel Cell Technology, Woodhead Publishing2009, pp. 156-182.

[286] C.P. Canales, Electrochemical Impedance Spectroscopy and Its Applications, (2021).

[287] K. Zouhri, S.-Y. Lee, Exergy study on the effect of material parameters and operating conditions on the anode diffusion polarization of the SOFC, International Journal of Energy and Environmental Engineering, 7 (2016) 211-224.

[288] H. Schichlein, A.C. Müller, M. Voigts, A. Krügel, E. Ivers-Tiffée, Deconvolution of electrochemical impedance spectra for the identification of electrode reaction mechanisms in solid oxide fuel cells, Journal of Applied Electrochemistry, 32 (2002) 875-882.

[289] A. Leonide, V. Sonn, A. Weber, E. Ivers-Tiffée, Evaluation and Modeling of the Cell Resistance in Anode-Supported Solid Oxide Fuel Cells, Journal of The Electrochemical Society, 155 (2008) B36.

[290] A. Ploner, A. Hagen, A. Hauch, Study of Operating Parameters for Accelerated Anode Degradation in SOFCs, Fuel Cells, 17 (2017) 498-507.

[291] Q. Fang, U. de Haart, D. Schäfer, F. Thaler, V. Rangel-Hernandez, R. Peters, L. Blum, Degradation Analysis of an SOFC Short Stack Subject to 10,000 h of Operation, Journal of The Electrochemical Society, 167 (2020) 144508.

[292] J. Geng, Z. Jiao, D. Yan, L. Jia, J. Pu, J. Li, Comparative study on solid oxide fuel cell anode microstructure evolution after long-term operation, Journal of Power Sources, 495 (2021) 229792.

[293] Z. Lyu, S. Liu, Y. Wang, H. Li, Z. Liu, Z. Sun, K. Sun, S. Zhang, M. Han, Quantifying the performance evolution of solid oxide fuel cells during initial aging process, Journal of Power Sources, 510 (2021) 230432.

[294] A. Staffolani, A. Baldinelli, L. Barelli, G. Bidini, F. Nobili, Early-Stage Detection of Solid Oxide Cells Anode Degradation by Operando Impedance Analysis, Processes, 9 (2021).

[295] J. Zhang, L. Lei, H. Li, K. Sun, Z. Sun, M. Han, Experimental investigations of cell resistances to characterize the concentration polarization behavior of 10 ×10 cm^2 solid oxide fuel cells, Journal of Power Sources, 516 (2021) 230678.

[296] T.H. Wan, M. Saccoccio, C. Chen, F. Ciucci, Influence of the Discretization Methods on the Distribution of Relaxation Times Deconvolution: Implementing Radial Basis Functions with DRTtools, Electrochimica Acta, 184 (2015) 483-499.

[297] P.E.J. Flewitt, R.K. Wild, Physical Methods for Materials Characterisation, Second Edition ed., CRC Press London, 2003.

[298] N. Fleck, H. Amli, V. Dhanak, W. Ahmed, Chapter 11 - Characterization techniques in energy generation and storage, in: W. Ahmed, M. Booth, E. Nourafkan (Eds.) Emerging Nanotechnologies for Renewable Energy, Elsevier2021, pp. 259-285.

[299] Q.L. Liu, K.A. Khor, S.H. Chan, X.J. Chen, Anode-supported solid oxide fuel cell with yttria-stabilized zirconia/gadolinia-doped ceria bilalyer electrolyte prepared by wet ceramic co-sintering process, Journal of Power Sources, 162 (2006) 1036-1042.

[300] J.-H. Song, M.G. Jung, H.W. Park, H.-T. Lim, The Effect of Fabrication Conditions for GDC Buffer Layer on Electrochemical Performance of Solid Oxide Fuel Cells, Nano-Micro Letters, 5 (2013) 151-158.

[301] B. Timurkutluk, S. Celik, S. Toros, C. Timurkutluk, M.D. Mat, Y. Kaplan, Effects of electrolyte pattern on mechanical and electrochemical properties of solid oxide fuel cells, Ceramics International, 38 (2012) 5651-5659.

[302] A.L. Snowdon, Z. Jiang, R. Steinberger-Wilckens, Five-layer reverse tape casting of IT-SOFC, International Journal of Applied Ceramic Technology, 19 (2022) 289-298.

[303] A. Tsoga, A. Naoumidis, A. Gupta, D. Stöver, Microstructure and interdiffusion phenomena in YSZ-CGO composite electrolyte, Materials science forum, Trans Tech Publ, 1999, pp. 794-799.

[304] A. Tsoga, A. Gupta, A. Naoumidis, P. Nikolopoulos, Gadolinia-doped ceria and yttria stabilized zirconia interfaces: regarding their application for SOFC technology, Acta Materialia, 48 (2000) 4709-4714.

[305] S.J. Kim, G.M. Choi, Stability of LSCF electrode with GDC interlayer in YSZ-based solid oxide electrolysis cell, Solid State Ionics, 262 (2014) 303-306.

[306] A. Hussain, M.Z. Khan, R.H. Song, J.-E. Hong, S.-B. Lee, T.-H. Lim, High Performing and Durable Anode-Supported Solid Oxide Fuel Cell by Using Tape Casting, Lamination and Co-Firing Method, ECS Transactions, 91 (2019) 373-379.

[307] S. Onbilgin, B. Timurkutluk, C. Timurkutluk, S. Celik, Comparison of electrolyte fabrication techniques on the performance of anode supported solid oxide fuel cells, International Journal of Hydrogen Energy, 45 (2020) 35162-35170.

[308] X. Li, J. Lu, H. Wang, Effects of laminating and co-firing conditions on the performance of anode-supported Ce0. 8Sm0. 201.9 film electrolyte, Science of Sintering, 43 (2011) 305-312.

[309] J.-H. Song, S.-I. Park, J.-H. Lee, H.-S. Kim, Fabrication characteristics of an anode-supported thin-film electrolyte fabricated by the tape casting method for IT-SOFC, Journal of Materials Processing Technology, 198 (2008) 414-418.

[310] T. Van Gestel, D. Sebold, H.P. Buchkremer, Processing of 8YSZ and CGO thin film electrolyte layers for intermediate- and low-temperature SOFCs, Journal of the European Ceramic Society, 35 (2015) 1505-1515.

[311] Q. Dong, Z.H. Du, T.S. Zhang, J. Lu, X.C. Song, J. Ma, Sintering and ionic conductivity of 8YSZ and CGO10 electrolytes with small addition of Fe_2O_3: A comparative study, International Journal of Hydrogen Energy, 34 (2009) 7903-7909.

[312] S.U. Rehman, A. Shaur, H.-S. Kim, D.W. Joh, R.-H. Song, T.-H. Lim, J.-E. Hong, S.-J. Park, S.-B. Lee, Effect of transition metal doping on the sintering and electrochemical properties of GDC buffer layer in SOFCs, International Journal of Applied Ceramic Technology, 18 (2021) 511-524.

[313] Z. Gao, V.Y. Zenou, D. Kennouche, L. Marks, S.A. Barnett, Solid oxide cells with zirconia/ceria Bi-Layer electrolytes fabricated by reduced temperature firing, Journal of Materials Chemistry A, 3 (2015) 9955-9964.

[314] Z. Wang, J. Qian, J. Cao, S. Wang, T. Wen, A study of multilayer tape casting method for anode-supported planar type solid oxide fuel cells (SOFCs), Journal of Alloys and Compounds, 437 (2007) 264-268.

[315] C. Sun, R. Hui, J. Roller, Cathode materials for solid oxide fuel cells: a review, Journal of Solid State Electrochemistry, 14 (2010) 1125-1144.

[316] D. Kong, H. Yang, S. Wei, D. Li, J. Wang, Gel-casting without de-airing process using silica sol as a binder, Ceramics International, 33 (2007) 133-139.

[317] D. Kong, H. Yang, Y. Yang, S. Wei, J. Wang, De-stabilization mechanism and in situ solidification of alumina slurry dispersed in silica sol, Journal of Materials Processing Technology, 182 (2007) 489-497.

[318] J. Wang, Z. Lü, K. Chen, X. Huang, N. Ai, J. Hu, Y. Zhang, W. Su, Study of slurry spin coating technique parameters for the fabrication of anode-supported YSZ Films for SOFCs, Journal of Power Sources, 164 (2007) 17-23.

[319] H.J. Kim, M. Kim, K.C. Neoh, G.D. Han, K. Bae, J.M. Shin, G.-T. Kim, J.H. Shim, Slurry spin coating of thin film yttria stabilized zirconia/gadolinia doped ceria bi-layer electrolytes for solid oxide fuel cells, Journal of Power Sources, 327 (2016) 401-407.

[320] I. Jang, S. Kim, C. Kim, H. Lee, H. Yoon, T. Song, U. Paik, Interface engineering of yttrium stabilized zirconia/gadolinium doped ceria bi-layer electrolyte solid oxide fuel cell for boosting electrochemical performance, Journal of Power Sources, 435 (2019) 226776.

[321] K. Chen, Z. Lü, N. Ai, X. Huang, Y. Zhang, X. Xin, R. Zhu, W. Su, Development of yttria-stabilized zirconia thin films via slurry spin coating for intermediate-to-low temperature solid oxide fuel cells, Journal of Power Sources, 160 (2006) 436-438.

[322] X. Xu, C. Xia, S. Huang, D. Peng, YSZ thin films deposited by spin-coating for IT-SOFCs, Ceramics International, 31 (2005) 1061-1064.

[323] Y.D. Zhen, A.I.Y. Tok, S.P. Jiang, F.Y.C. Boey, Fabrication and performance of gadolinia-doped ceria-based intermediate-temperature solid oxide fuel cells, Journal of Power Sources, 178 (2008) 69-74.

[324] J. Orava, T. Kohoutek, T. Wagner, 9 - Deposition techniques for chalcogenide thin films, in: J.-L. Adam, X. Zhang (Eds.) Chalcogenide Glasses, Woodhead Publishing2014, pp. 265-309.

[325] K. Eguchi, N. Akasaka, H. Mitsuyasu, Y. Nonaka, Process of solid state reaction between doped ceria and zirconia, Solid State Ionics, 135 (2000) 589-594.

[326] C.H. Lee, G.M. Choi, Electrical conductivity of CeO_2-doped YSZ, Solid State Ionics, 135 (2000) 653-661.

[327] C. Igathinathane, L.O. Pordesimo, E.P. Columbus, W.D. Batchelor, S.R. Methuku, Shape identification and particles size distribution from basic shape parameters using ImageJ, Computers and Electronics in Agriculture, 63 (2008) 168-182.

[328] M.W. Quintero, J.A. Escobar, A. Rey, A. Sarmiento, C.R. Rambo, A.P.N.d. Oliveira, D. Hotza, Flexible polyurethane foams as templates for cellular glass–ceramics, Journal of Materials Processing Technology, 209 (2009) 5313-5318.

[329] T. Fukui, K. Murata, S. Ohara, H. Abe, M. Naito, K. Nogi, Morphology control of Ni–YSZ cermet anode for lower temperature operation of SOFCs, Journal of Power Sources, 125 (2004) 17-21.

[330] S.P.S. Shaikh, C.V. Rode, Rational synthesis of 10GDC electrolyte through a microwave irradiation GNP facile route for SOFC applications, RSC Advances, 10 (2020) 3020-3028.

[331] P.Z. Cai, D.J. Green, G.L. Messing, Constrained Densification of Alumina/Zirconia Hybrid Laminates, II: Viscoelastic Stress Computation, Journal of the American Ceramic Society, 80 (1997) 1940-1948.

[332] K.R. Mikeska, D.T. Schaefer, R.H. Jensen, Method for reducing shrinkage during firing of green ceramic bodies, U.S. Patent No. US5085720A, EIDP Inc, 1992.

[333] C. Wang, L. Luo, Y. Wu, B. Hou, L. Sun, A novel multilayer aqueous tape casting method for anode-supported planar solid oxide fuel cell, Materials Letters, 65 (2011) 2251-2253.

[334] S. Le, Y. Mao, X. Zhu, N. Zhang, K. Sun, Constrained sintering of Y_2O_3-stabilized ZrO_2 electrolyte on anode substrate, International Journal of Hydrogen Energy, 37 (2012) 18365-18371.

[335] J. Zamudio-García, L. Caizán-Juanarena, J.M. Porras-Vázquez, E.R. Losilla, D. Marrero-López, Unraveling the Influence of the Electrolyte on the Polarization Resistance of Nanostructured $La_{0.6}Sr_{0.4}Co_{0.2}Fe_{0.8}O_{3-\delta}$ Cathodes, Nanomaterials, 12 (2022) 3936.

[336] J. Kong, K. Sun, D. Zhou, N. Zhang, J. Mu, J. Qiao, Ni–YSZ gradient anodes for anode-supported SOFCs, Journal of Power Sources, 166 (2007) 337-342.

[337] C. Seok, J. Moon, M. Park, J. Hong, H. Kim, J.-W. Son, J.-H. Lee, B.-K. Kim, H.-W. Lee, K.J. Yoon, Low-temperature co-sintering technique for the fabrication of multi-layer functional ceramics for solid oxide fuel cells, Journal of the European Ceramic Society, 36 (2016) 1417-1425.

[338] P. Liu, Z. Luo, J. Kong, X. Yang, Q. Liu, H. Xu, $Ba_{0.5}Sr_{0.5}Co_{0.8}Fe_{0.2}O_{3-\delta}$-based dual-gradient cathodes for solid oxide fuel cells, Ceramics International, 44 (2018) 4516-4519.

[339] Y. Lee, J.H. Joo, G.M. Choi, Effect of electrolyte thickness on the performance of anode-supported ceria cells, Solid State Ionics, 181 (2010) 1702-1706.

[340] B.-K. Park, S.A. Barnett, Boosting solid oxide fuel cell performance via electrolyte thickness reduction and cathode infiltration, Journal of Materials Chemistry A, 8 (2020) 11626-11631.

[341] W. Pan, K. Chen, N. Ai, Z. Lü, S.P. Jiang, Mechanism and Kinetics of Ni-Y2O3-ZrO2 Hydrogen Electrode for Water Electrolysis Reactions in Solid Oxide Electrolysis Cells, Journal of The Electrochemical Society, 163 (2016) F106.

[342] T. Ivers, Eacute, E. E, A. Weber, eacute, Evaluation of electrochemical impedance spectra by the distribution of relaxation times, Journal of the Ceramic Society of Japan, 125 (2017) 193-201.

[343] D. Papurello, D. Menichini, A. Lanzini, Distributed relaxation times technique for the determination of fuel cell losses with an equivalent circuit model to identify physicochemical processes, Electrochimica Acta, 258 (2017) 98-109.

[344] I.W. Choi, W. Yu, M.S. Lee, S. Ryu, Y.H. Lee, S.W. Cha, G.Y. Cho, Tailoring 3D structured nanofibrous nickel/gadolinium-doped ceria anodes for high-performance thin-film solid oxide fuel cells, Journal of Power Sources, 531 (2022) 231320.

[345] F. Zhao, A.V. Virkar, Dependence of polarization in anode-supported solid oxide fuel cells on various cell parameters, Journal of Power Sources, 141 (2005) 79-95.

[346] T. Parhizkar, R. Roshandel, Long term performance degradation analysis and optimization of anode supported solid oxide fuel cell stacks, Energy Conversion and Management, 133 (2017) 20-30.

[347] Q. Fang, L. Blum, D. Stolten, Electrochemical Performance and Degradation Analysis of an SOFC Short Stack Following Operation of More than 100,000 Hours, Journal of The Electrochemical Society, 166 (2019) F1320-F1325.

[348] N.H. Menzler, D. Sebold, Y.J. Sohn, S. Zischke, Post-test characterization of a solid oxide fuel cell after more than 10 years of stack testing, Journal of Power Sources, 478 (2020) 228770.

[349] R. Barfod, M. Mogensen, T. Klemensø, A. Hagen, Y.-L. Liu, P. Vang Hendriksen, Detailed Characterization of Anode-Supported SOFCs by Impedance Spectroscopy, Journal of The Electrochemical Society, 154 (2007) B371.

[350] M.Z. Khan, R.-H. Song, A. Hussain, S.-B. Lee, T.-H. Lim, J.-E. Hong, Effect of applied current density on the degradation behavior of anode-supported flat-tubular solid oxide fuel cells, Journal of the European Ceramic Society, 40 (2020) 1407-1417.

[351] S. He, S.P. Jiang, Electrode/electrolyte interface and interface reactions of solid oxide cells: Recent development and advances, Progress in Natural Science: Materials International, 31 (2021) 341-372.

[352] H. Sumi, H. Shimada, Y. Yamaguchi, T. Yamaguchi, Y. Fujishiro, Degradation evaluation by distribution of relaxation times analysis for microtubular solid oxide fuel cells, Electrochimica Acta, 339 (2020) 135913.

[353] D.A. Agarkov, I.N. Burmistrov, F.M. Tsybrov, I.I. Tartakovskii, V.V. Kharton, S.I. Bredikhin, In-situ Raman spectroscopy analysis of the interfaces between Ni-based SOFC anodes and stabilized zirconia electrolyte, Solid State Ionics, 302 (2017) 133-137.

[354] J.H. Lee, H. Moon, H.W. Lee, J. Kim, J.D. Kim, K.H. Yoon, Quantitative analysis of microstructure and its related electrical property of SOFC anode, Ni–YSZ cermet, Solid State Ionics, 148 (2002) 15-26.

[355] B. Vasyliv, V. Podhurska, O. Ostash, Preconditioning of the YSZ-NiO Fuel Cell Anode in Hydrogenous Atmospheres Containing Water Vapor, Nanoscale Research Letters, 12 (2017) 265.

[356] Z. Wang, Z. Lü, B. Wei, K. Chen, X. Huang, W. Pan, W. Su, Redox of Ni/YSZ anodes and oscillatory behavior in single-chamber SOFC under methane oxidation conditions, Electrochimica Acta, 56 (2011) 6688-6695.

[357] B. Song, E. Ruiz-Trejo, A. Bertei, N.P. Brandon, Quantification of the degradation of Ni-YSZ anodes upon redox cycling, Journal of Power Sources, 374 (2018) 61-68.

[358] A. Hagen, R. Barfod, P.V. Hendriksen, Y.-L. Liu, S. Ramousse, Degradation of Anode Supported SOFCs as a Function of Temperature and Current Load, Journal of The Electrochemical Society, 153 (2006) A1165.

[359] F. Wang, M. Nishi, M.E. Brito, H. Kishimoto, K. Yamaji, H. Yokokawa, T. Horita, Sr and Zr diffusion in LSCF/10GDC/8YSZ triplets for solid oxide fuel cells (SOFCs), Journal of Power Sources, 258 (2014) 281-289.

[360] V. Wilde, H. Stormer, J. Szasz, F. Wankmuller, E. Ivers-Tiffee, D. Gerthsen, Effect of Gd0.2Ce0.8O2 Sintering Temperature on Formation of a SrZrO3 Blocking Layer between Y0.16Zr0.84O2, Gd0.2Ce0.8O2 and La0.58Sr0.4Co0.2Fe0.8O3, ECS Transactions, 66 (2015) 103-107.

[361] J.-T. Chou, Y. Inoue, T. Kawabata, J. Matsuda, S. Taniguchi, K. Sasaki, Mechanism of $SrZrO_3$ Formation at GDC/YSZ Interface of SOFC Cathode, Journal of The Electrochemical Society, 165 (2018) F959-F965.

[362] R. Gerhardt-Anderson, A.S. Nowick, Ionic conductivity of CeO_2 with trivalent dopants of different ionic radii, Solid State Ionics, 5 (1981) 547-550.

[363] M.Z. Khan, M.T. Mehran, R.-H. Song, J.-W. Lee, S.-B. Lee, T.-H. Lim, S.-J. Park, Effect of GDC interlayer thickness on durability of solid oxide fuel cell cathode, Ceramics International, 42 (2016) 6978-6984.

[364] Z. Lu, S. Darvish, J. Hardy, J. Templeton, J. Stevenson, Y. Zhong, $SrZrO_3$ Formation at the Interlayer/Electrolyte Interface during $(La_{1-x}Sr_x)_{1-\delta}Co_{1-y}Fe_yO_3$ Cathode Sintering, Journal of The Electrochemical Society, 164 (2017) F3097-F3103.

[365] S.P. Simner, M.D. Anderson, M.H. Engelhard, J.W. Stevenson, Degradation Mechanisms of La–Sr–Co–Fe–O_3 SOFC Cathodes, Electrochemical and Solid-State Letters, 9 (2006) A478.

[366] P. Tanasini, M. Cannarozzo, P. Costamagna, A. Faes, J. Van Herle, A. Hessler-Wyser, C. Comninellis, Experimental and Theoretical Investigation of Degradation Mechanisms by Particle Coarsening in SOFC Electrodes, Fuel Cells, 9 (2009) 740-752.

[367] M.S. Khan, S.-B. Lee, R.-H. Song, J.-W. Lee, T.-H. Lim, S.-J. Park, Fundamental mechanisms involved in the degradation of nickel–yttria stabilized zirconia (Ni–YSZ) anode during solid oxide fuel cells operation: A review, Ceramics International, 42 (2016) 35-48.

[368] M.Z. Khan, M.T. Mehran, R.-H. Song, J.-W. Lee, S.-B. Lee, T.-H. Lim, A simplified approach to predict performance degradation of a solid oxide fuel cell anode, Journal of Power Sources, 391 (2018) 94-105.

[369] A. Faes, A. Hessler-Wyser, D. Presvytes, C.G. Vayenas, J. Van herle, Nickel–Zirconia Anode Degradation and Triple Phase Boundary Quantification from Microstructural Analysis, Fuel Cells, 9 (2009) 841-851.

[370] M.B. Mogensen, A. Hauch, X. Sun, M. Chen, Y. Tao, S.D. Ebbesen, K.V. Hansen, P.V. Hendriksen, Relation Between Ni Particle Shape Change and Ni Migration in Ni–YSZ Electrodes – a Hypothesis, Fuel Cells, 17 (2017) 434-441.

[371] M.B. Mogensen, M. Chen, H.L. Frandsen, C. Graves, A. Hauch, P.V. Hendriksen, T. Jacobsen, S.H. Jensen, T.L. Skafte, X. Sun, Ni migration in solid oxide cell electrodes: Review and revised hypothesis, Fuel Cells, 21 (2021) 415-429.

[372] C. Comminges, Q.X. Fu, M. Zahid, N.Y. Steiner, O. Bucheli, Monitoring the degradation of a solid oxide fuel cell stack during 10,000h via electrochemical impedance spectroscopy, Electrochimica Acta, 59 (2012) 367-375.

[373] M. Torrell, A. Morata, P. Kayser, M. Kendall, K. Kendall, A. Tarancón, Performance and long term degradation of 7 W micro-tubular solid oxide fuel cells for portable applications, Journal of Power Sources, 285 (2015) 439-448.

[374] L. Holzer, B. Iwanschitz, T. Hocker, B. Münch, M. Prestat, D. Wiedenmann, U. Vogt, P. Holtappels, J. Sfeir, A. Mai, T. Graule, Microstructure degradation of cermet anodes for solid oxide fuel cells: Quantification of nickel grain growth in dry and in humid atmospheres, Journal of Power Sources, 196 (2011) 1279-1294.

[375] Z. Jiao, N. Takagi, N. Shikazono, N. Kasagi, Study on local morphological changes of nickel in solid oxide fuel cell anode using porous Ni pellet electrode, Journal of Power Sources, 196 (2011) 1019-1029.

[376] J. Sehested, N.W. Larsen, H. Falsig, B. Hinnemann, Sintering of nickel steam reforming catalysts: Effective mass diffusion constant for Ni-OH at nickel surfaces, Catalysis Today, 228 (2014) 22-31.

[377] Y. Yan, Q. Fang, L. Blum, W. Lehnert, Performance and degradation of an SOEC stack with different cell components, Electrochimica Acta, 258 (2017) 1254-1261.

[378] A. Ioselevich, A.A. Kornyshev, W. Lehnert, Degradation of Solid Oxide Fuel Cell Anodes Due to Sintering of Metal Particles: Correlated Percolation Model, Journal of The Electrochemical Society, 144 (1997) 3010-3019.

[379] Z. Jiao, N. Shikazono, N. Kasagie, Study on Degradation of Solid Oxide Fuel Cell with Pure Ni Anode, ECS Transactions, 35 (2011) 1735.

[380] Z. Jiao, N. Shikazono, Study on the effects of polarization on local morphological change of nickel at active three-phase-boundary using patterned nickel-film electrode in solid oxide fuel cell anode, Acta Materialia, 135 (2017) 124-131.

[381] J.-H. Koh, Y.-S. Yoo, J.-W. Park, H.C. Lim, Carbon deposition and cell performance of Ni-YSZ anode support SOFC with methane fuel, Solid State Ionics, 149 (2002) 157-166.

[382] A. Gunji, C. Wen, J. Otomo, T. Kobayashi, K. Ukai, Y. Mizutani, H. Takahashi, Carbon deposition behaviour on Ni–ScSZ anodes for internal reforming solid oxide fuel cells, Journal of Power Sources, 131 (2004) 285-288.

[383] K.S. Blinn, H. Abernathy, X. Li, M. Liu, L.A. Bottomley, M. Liu, Raman spectroscopic monitoring of carbon deposition on hydrocarbon-fed solid oxide fuel cell anodes, Energy & Environmental Science, 5 (2012) 7913-7917.

[384] F. Tietz, W. Fischer, T. Hauber, G. Mariotto, Structural evolution of Sc-containing zirconia electrolytes, Solid State Ionics, 100 (1997) 289-295.

[385] J.D. Kirtley, D.M. Halat, M.D. McIntyre, B.C. Eigenbrodt, R.A. Walker, High-Temperature “Spectrochronopotentiometry”: Correlating Electrochemical Performance with In Situ Raman Spectroscopy in Solid Oxide Fuel Cells, Analytical Chemistry, 84 (2012) 9745-9753.

[386] A.P. Grosvenor, M.C. Biesinger, R.S.C. Smart, N.S. McIntyre, New interpretations of XPS spectra of nickel metal and oxides, Surface Science, 600 (2006) 1771-1779.

[387] B. Farrell, S. Linic, Direct electrochemical oxidation of ethanol on SOFCs: Improved carbon tolerance of Ni anode by alloying, Applied Catalysis B: Environmental, 183 (2016) 386-393.

[388] M. Dudek, R.I. Tomov, C. Wang, B.A. Glowacki, P. Tomczyk, R.P. Socha, M. Mosiałek, Feasibility of direct carbon solid oxide fuels cell (DC-SOFC) fabrication by inkjet printing technology, Electrochimica Acta, 105 (2013) 412-418.

[389] T. Götsch, T. Schachinger, M. Stöger-Pollach, R. Kaindl, S. Penner, Carbon tolerance of Ni–Cu and Ni–Cu/YSZ sub-μm sized SOFC thin film model systems, Applied Surface Science, 402 (2017) 1-11.

[390] M.J. Escudero, C.A. Maffiotte, J.L. Serrano, Long-term operation of a solid oxide fuel cell with MoNi–CeO_2 as anode directly fed by biogas containing simultaneously sulphur and siloxane, Journal of Power Sources, 481 (2021) 229048.

[391] X. Zhao, T. Wen, J. Zhang, J. Ye, Z. Ma, H. Yuan, X. Ye, Y. Wang, Fe-Doped SnO_2 catalysts with both BA and LA sites: facile preparation and biomass carbohydrates conversion to methyl lactate MLA, RSC Advances, 7 (2017) 21678-21685.

[392] Y. Zhu, T. Liu, L. Li, S. Song, R. Ding, Nickel-based electrodes as catalysts for hydrogen evolution reaction in alkaline media, Ionics, 24 (2018) 1121-1127.

[393] B. Mo, J. Rix, U. Pal, S. Basu, S. Gopalan, Improving SOFC Anode Electrocatalytic Activity Using Nanoparticle Infiltration into MIEC Compositions, Journal of The Electrochemical Society, 167 (2020) 134506.

[394] Q. Zhang, K. Xie, Y. Luo, Y.-C. Zhang, W.-C. Jiang, Mismatch effect of material creep strength on creep damage and failure probability of planar solid oxide fuel cell, International Journal of Hydrogen Energy, 47 (2022) 2673-2684.

[395] H. Zhu, W. Wang, R. Ran, C. Su, H. Shi, Z. Shao, Iron incorporated Ni–ZrO_2 catalysts for electric power generation from methane, International Journal of Hydrogen Energy, 37 (2012) 9801-9808.

[396] W. Wang, H. Zhu, G. Yang, H.J. Park, D.W. Jung, C. Kwak, Z. Shao, A NiFeCu alloy anode catalyst for direct-methane solid oxide fuel cells, Journal of Power Sources, 258 (2014) 134-141.

[397] K.V. Kravchyk, O. Bohnke, V. Gunes, A.G. Belous, E.V. Pashkova, J. Le Lannic, F. Gouttefangeas, Ionic and electronic conductivity of 3mol% Fe_2O_3-substituted cubic Y-stabilized ZrO_2, Solid State Ionics, 226 (2012) 53-58.

[398] O. Bohnke, V. Gunes, K.V. Kravchyk, A.G. Belous, O.Z. Yanchevskii, O.I. V'Yunov, Ionic and electronic conductivity of 3mol% Fe_2O_3-substituted cubic yttria-stabilized ZrO_2 (YSZ) and scandia-stabilized ZrO_2 (ScSZ), Solid State Ionics, 262 (2014) 517-521.

[399] M.B. Pomfret, J. Marda, G.S. Jackson, B.W. Eichhorn, A.M. Dean, R.A. Walker, Hydrocarbon Fuels in Solid Oxide Fuel Cells: In Situ Raman Studies of Graphite Formation and Oxidation, The Journal of Physical Chemistry C, 112 (2008) 5232-5240.

[400] R.C. Maher, V. Duboviks, G.J. Offer, M. Kishimoto, N.P. Brandon, L.F. Cohen, Raman Spectroscopy of Solid Oxide Fuel Cells: Technique Overview and Application to Carbon Deposition Analysis, Fuel Cells, 13 (2013) 455-469.

[401] Q. Li, X. Wang, C. Liu, X. Yang, C. Li, L. Jia, J. Li, A direct-methane solid oxide fuel cell with a functionally engineered Ni–Fe metal support, Journal of Power Sources, 537 (2022) 231533.

[402] A.P. Grosvenor, B.A. Kobe, M.C. Biesinger, N.S. McIntyre, Investigation of multiplet splitting of Fe 2p XPS spectra and bonding in iron compounds, Surface and Interface Analysis, 36 (2004) 1564-1574.

[403] E. Nikolla, J. Schwank, S. Linic, Promotion of the long-term stability of reforming Ni catalysts by surface alloying, Journal of Catalysis, 250 (2007) 85-93.

[404] E. Nikolla, J. Schwank, S. Linic, Comparative study of the kinetics of methane steam reforming on supported Ni and Sn/Ni alloy catalysts: The impact of the formation of Ni alloy on chemistry, Journal of Catalysis, 263 (2009) 220-227.

[405] Q. Yang, J. Chen, C. Sun, L. Chen, Direct operation of methane fueled solid oxide fuel cells with Ni cermet anode via Sn modification, International Journal of Hydrogen Energy, 41 (2016) 11391-11398.

[406] N. Menzler, D. Sebold, S. Zischke, J. Zurek, D. Naumenko, S. Gross-Barsnick, Post-Operational Characterization of a Long-Term Operated Solid Oxide Fuel Cell Stack, ECS Transactions, 103 (2021) 1047.

[407] E. Ruiz-Trejo, A. Atkinson, N.P. Brandon, Metallizing porous scaffolds as an alternative fabrication method for solid oxide fuel cell anodes, Journal of Power Sources, 280 (2015) 81-89.

[408] G. Li, Z. You, Y. Zhang, M. Rao, P. Wen, Y. Guo, T. Jiang, Synchronous Volatilization of Sn, Zn, and As, and Preparation of Direct Reduction Iron (DRI) from a Complex Iron Concentrate via CO Reduction, JOM, 66 (2014) 1701-1710.

[409] S.-C. Wong, Y.-C. Lin, Effect of copper surface wettability on the evaporation performance: Tests in a flat-plate heat pipe with visualization, International Journal of Heat and Mass Transfer, 54 (2011) 3921-3926.

[410] G. Dai, S. Wu, X. Huang, M. Wang, X. Teng, Thermal diffusion behavior of Fe/Cu/Ni multilayer coatings: a molecular dynamics study, Modelling and Simulation in Materials Science and Engineering, 30 (2022) 065003.

[411] H.C. Park, A.V. Virkar, Bimetallic (Ni–Fe) anode-supported solid oxide fuel cells with gadolinia-doped ceria electrolyte, Journal of Power Sources, 186 (2009) 133-137.

[412] X. Lin, J. Xu, Z. Chen, N. Ai, Z. Lü, S.P. Jiang, D. Zhao, X. Wang, Y. Shao, K. Chen, Thermally driven long–distance elemental diffusion enhances the sinterability of anode and electrolyte of metal–supported solid oxide fuel cells, Journal of Power Sources, 555 (2023) 232401.

[413] Z.-P. Li, T. Mori, G.J. Aucheterlonie, J. Zou, J. Drennan, M. Miyayama, Diffusion and segregation along grain boundary at the electrolyte–anode interface in IT-SOFC, Solid State Ionics, 191 (2011) 55-60.

APPENDIX

Appendix Table 1: Ohmic resistance (R_{ohm}) and electrode polarization resistance (R_p) of the tested Cell I.

Temperature (°C)	**R_{ohm} (Ω•cm^2)**			**R_p (Ω•cm^2)**		
	Cell I-A	Cell I-B	Cell I-C	Cell I-A	Cell I-B	Cell I-C
800	0.44	0.15	0.22	2.31	0.23	0.21
750	0.65	0.22	0.34	4.04	0.39	0.41
700	0.93	0.35	0.48	7.44	0.77	0.75

Appendix Table 2: Ohmic resistance (R_{ohm}) and electrode polarization resistance (R_p) of the tested Cell II.

Temperature (°C)	**R_{ohm} (Ω•cm^2)**			**R_p (Ω•cm^2)**		
	Cell II-A	Cell II-B	Cell II-C	Cell II-A	Cell II-B	Cell II-C
800	1.24	0.64	0.63	1.32	0.85	1.24
750	1.58	1.23	0.76	3.27	1.76	2.01
700	1.95	1.87	1.11	8.71	3.99	4.34

Appendix Table 3: Ohmic resistance (R_{ohm}) and electrode polarization resistance (R_p) of the tested Cell III.

Temperature (°C)	**R_{ohm} (Ω•cm^2)**				**R_p (Ω•cm^2)**			
	Cell III-A	Cell III-B	Cell III-C	Cell III-D	Cell III-A	Cell III-B	Cell III-C	Cell III-D
800	0.051	0.063	0.065	0.054	0.129	0.125	0.123	0.135
750	0.063	0.073	0.076	0.066	0.146	0.145	0.150	0.155
700	0.081	0.087	0.092	0.086	0.198	0.194	0.191	0.203

Appendix Table 4: Electrochemical performances of the Cell III with different solid loading GDC films operated with hydrogen as fuel at 750 °C.

GDC solid loading (wt.%)	P_{max} (W•cm^{-2})	R_{ohm} (Ω•cm^2)	R_p (Ω•cm^2)
40	0.809	0.083	0.157
45	0.771	0.086	0.179
50	1.012	0.076	0.150
55	0.711	0.099	0.190

Appendix Table 5: ECM element values derived from ZView simulation for Cell III operated with hydrogen as fuel at 800 °C.

	Cell III-A	Cell III-B	Cell III-C	Cell III-D
Rs (Ω•cm^2)	0.0512	0.0638	0.0655	0.0541
R1 (Ω•cm^2)	0.0504	0.0546	0.0459	0.0605
CPE1_T (s)	0.0002	0.0002	0.0002	0.0002
CPE1_P	0.7200	0.7200	0.7400	0.7300
R2 (Ω•cm^2)	0.0017	0.0053	0.0034	0.0025
CPE2_T (s)	0.0014	0.0060	0.0018	0.0015
CPE2_P	0.7500	0.9500	1.0000	0.8700
R3 (Ω•cm^2)	0.0017	0.0066	0.0050	0.0101
CPE3_T (s)	0.0056	0.0200	0.0126	0.0229
CPE3_P	0.9000	0.8700	0.9000	0.9500
R4 (Ω•cm^2)	0.0185	0.0039	0.0067	0.0050
CPE4_T (s)	0.0438	0.2100	0.0965	0.3350
CPE4_P	0.8650	0.8200	0.8000	0.9000
R5 (Ω•cm^2)	0.0571	0.0538	0.0622	0.0571
CPE5_T (s)	1.1900	1.4000	2.1000	1.8200
CPE5_P	0.9200	0.8600	0.7400	0.8200

Appendix Table 6: ECM element values derived from ZView simulation for Cell III operated in hydrogen at 750 °C.

	Cell III-A	**Cell III-B**	**Cell III-C**	**Cell III-D**
Rs (Ω•cm^2)	0.0630	0.0729	0.0764	0.0655
R1 (Ω•cm^2)	0.0790	0.0857	0.0790	0.0890
CPE1_T (s)	0.0002	0.0002	0.0002	0.0001
CPE1_P	0.7300	0.7500	0.7500	0.7600
R2 (Ω•cm^2)	0.0034	0.0034	0.0017	0.0034
CPE2_T (s)	0.0013	0.0060	0.0016	0.0009
CPE2_P	0.7500	0.9500	0.9000	0.9200
R3 (Ω•cm^2)	0.0034	0.0049	0.0034	0.0067
CPE3_T (s)	0.0130	0.0145	0.0100	0.0100
CPE3_P	0.9000	0.8700	0.9000	1.0000
R4 (Ω•cm^2)	0.0118	0.0034	0.0089	0.0094
CPE4_T (s)	0.1240	0.3770	0.0520	0.1780
CPE4_P	0.9100	0.8200	0.7100	0.9000
R5 (Ω•cm^2)	0.0487	0.0475	0.0571	0.04603
CPE5_T (s)	1.1300	2.2900	1.4500	3.5500
CPE5_P	0.9300	0.8200	0.7500	0.8500

Appendix Table 7: ECM element values derived from ZView simulation for Cell III operated with hydrogen as fuel at 700 °C.

	Cell III-A	**Cell III-B**	**Cell III-C**	**Cell III-D**
Rs (Ω•cm^2)	0.0806	0.0869	0.0932	0.0857
R1 (Ω•cm^2)	0.1294	0.1277	0.1327	0.1142
CPE1_T (s)	0.0001	0.0001	0.0001	0.0002
CPE1_P	0.7500	0.7500	0.7500	0.7500
R2 (Ω•cm^2)	0.0101	0.0151	0.0030	0.0420
CPE2_T (s)	0.0076	0.0007	0.0085	0.0005
CPE2_P	0.7500	0.9000	1.0000	0.8600
R3 (Ω•cm^2)	0.0025	0.0027	0.0042	0.0020
CPE3_T (s)	0.0250	0.0070	0.0080	0.0047
CPE3_P	0.9000	0.9000	0.9000	1.0000
R4 (Ω•cm^2)	0.0042	0.0034	0.0067	0.0092
CPE4_T (s)	0.5710	0.3570	0.0089	0.0432
CPE4_P	1.0000	0.7700	0.8000	0.9500
R5 (Ω•cm^2)	0.0538	0.0454	0.0437	0.0360
CPE5_T (s)	3.8600	5.5300	1.9200	1.0000
CPE5_P	0.8500	0.8000	0.8200	0.9200

Appendix Table 8: ECM element values derived from ZView simulation for Cell III with 40, 45, 50, and 55wt.% GDC films operated with hydrogen as fuel at 750 °C.

	Cell III-40	**Cell III-45**	**Cell III-50**	**Cell III-55**
Rs (Ω•cm^2)	0.0832	0.0856	0.0764	0.0992
R1 (Ω•cm^2)	0.1120	0.1168	0.0790	0.1248
CPE1_T (s)	0.0001	0.0001	0.0002	0.0001
CPE1_P	0.8100	0.7100	0.7500	0.7500
R2 (Ω•cm^2)	-	0.0040	0.0017	0.0024
CPE2_T (s)	-	0.0008	0.0016	0.0007
CPE2_P	-	0.8500	0.9000	0.8700
R3 (Ω•cm^2)	0.0011	0.0056	0.0034	0.0088
CPE3_T (s)	0.0065	0.0100	0.0100	0.0066
CPE3_P	1.0000	1.0000	0.9000	0.8000
R4 (Ω•cm^2)	0.0035	0.0026	0.0089	0.0080
CPE4_T (s)	0.0522	0.1390	0.0520	0.0482
CPE4_P	0.8700	1.0000	0.7100	0.8000
R5 (Ω•cm^2)	0.0379	0.0496	0.0571	0.0448
CPE5_T (s)	1.3900	1.1200	1.4500	1.4300
CPE5_P	0.8100	0.8800	0.7500	0.9000

Appendix Table 9: ECM element values derived from ZView simulation for Cell III-200 operational stability test using hydrogen fuel at 750 °C.

Time (h)	**0**	**240**	**480**	**715**	**1200**
Rs (Ω•cm^2)	0.0688	0.0912	0.0984	0.1024	0.1264
R1 (Ω•cm^2)	0.1248	0.1600	0.1696	0.1920	0.2032
CPE1_T (s)	0.0001	0.0001	0.0001	0.0001	0.0001
CPE1_P	0.7000	0.7000	0.7000	0.7000	0.7000
R2 (Ω•cm^2)	0.0016	0.0096	0.0112	0.0112	0.0160
CPE2_T (s)	0.0006	0.0007	0.0007	0.0006	0.0005
CPE2_P	0.8500	0.8500	0.8500	0.8500	0.8500
R3 (Ω•cm^2)	0.0016	0.0208	0.0240	0.0240	0.0320
CPE3_T (s)	0.0065	0.0077	0.0088	0.0079	0.0079
CPE3_P	0.9000	0.9000	0.9000	0.9000	0.9000
R4 (Ω•cm^2)	0.0016	0.0048	0.0056	0.0144	0.0160
CPE4_T (s)	0.0070	0.1560	0.2500	0.2500	0.2500
CPE4_P	0.9500	0.9500	0.9500	0.9500	0.9500
R5 (Ω•cm^2)	0.0592	0.0416	0.0432	0.0464	0.0512
CPE5_T (s)	1.1500	1.1500	1.9100	2.0000	2.0700
CPE5_P	0.9200	0.9200	0.9200	0.9200	0.9200

Appendix Table 10: ECM element values derived from ZView simulation for Cell III-1000 operational stability test using hydrogen fuel at 750 °C.

Time (h)	**0**	**100**	**200**	**300**	**400**	**500**
Rs (Ω•cm^2)	0.0672	0.0696	0.7022	0.0717	0.0731	0.0815
R1 (Ω•cm^2)	0.0958	0.1075	0.1151	0.1193	0.1243	0.1260
CPE1_T (s)	0.0002	0.0002	0.0002	0.0002	0.0002	0.0002
CPE1_P	0.7500	0.7500	0.7500	0.7500	0.7500	0.7500
R2 (Ω•cm^2)	0.0017	0.0050	0.0064	0.0067	0.0050	0.0067
CPE2_T (s)	0.0087	0.0060	0.0060	0.0060	0.0060	0.0060
CPE2_P	0.9000	0.9000	0.9000	0.9000	0.9000	0.9000
R3 (Ω•cm^2)	0.0084	0.0084	0.0084	0.0084	0.0050	0.0042
CPE3_T (s)	0.0227	0.0575	0.0810	0.0288	0.0111	0.0111
CPE3_P	1.0000	0.7000	0.7000	0.7000	0.7000	0.7000
R4 (Ω•cm^2)	0.0034	0.0050	0.0084	0.0034	0.0050	0.0042
CPE4_T (s)	0.2513	0.1004	0.4486	0.1272	0.1638	0.1638
CPE4_P	0.8000	1.0000	0.8000	0.7000	0.7000	0.8000
R5 (Ω•cm^2)	0.0437	0.0370	0.0316	0.0336	0.0336	0.0336
CPE5_T (s)	0.7508	0.8180	1.2900	0.7578	0.8555	0.8555
CPE5_P	0.8600	0.9200	0.9000	0.8800	0.8800	0.8800

Appendix Table 11: ECM element values derived from ZView simulation for Sn1 cell.

	H_2	**Biogas**	**Biogas-120h**	**Post-biogas**
Rs (Ω•cm^2)	0.0613	0.0722	0.0756	0.0689
R1 (Ω•cm^2)	0.0907	0.0983	0.1210	0.1075
CPE1_T (s)	0.0002	0.0002	0.0002	0.0002
CPE1_P	0.7800	0.7700	0.7400	0.7500
R2 (Ω•cm^2)	0.0050	0.0092	0.0176	0.0034
CPE2_T (s)	0.0090	0.0152	0.0152	0.0100
CPE2_P	0.8000	1.0000	0.8000	0.7600
R3 (Ω•cm^2)	0.0076	0.0089	0.0101	0.0067
CPE3_T (s)	0.0350	0.0147	0.3125	0.0367
CPE3_P	0.8000	1.0000	0.7000	0.6500
R4 (Ω•cm^2)	0.0386	0.0417	0.0437	0.0403
CPE4_T (s)	1.0000	0.8650	0.6594	0.7590
CPE4_P	0.9100	0.7500	0.8300	1.0000

Appendix Table 12: ECM element values derived from ZView simulation for Sn2 cell.

	H_2	Biogas	Biogas-120h	Post-biogas
Rs (Ω•cm^2)	0.0731	0.0863	0.0928	0.0868
R1 (Ω•cm^2)	0.1327	0.1414	0.1452	0.1361
CPE1_T (s)	0.0002	0.0002	0.0007	0.0003
CPE1_P	0.7600	0.7000	0.6500	0.7400
R2 (Ω•cm^2)	0.0017	0.0074	0.0131	0.0059
CPE2_T (s)	0.0020	0.0030	0.0010	0.0005
CPE2_P	0.7000	0.7000	0.8500	0.8000
R3 (Ω•cm^2)	0.0042	0.0074	0.0020	0.0067
CPE3_T (s)	0.0500	0.0900	0.0150	0.0900
CPE3_P	0.7000	0.6000	0.7000	0.6000
R4 (Ω•cm^2)	0.0370	0.0407	0.0444	0.0403
CPE4_T (s)	1.5000	2.5000	2.5000	2.5000
CPE4_P	0.8200	0.8200	0.8000	0.8300

Appendix Table 13: Electrochemical performance of the prepared cells operated with hydrogen as fuel at 750 °C.

Cell ID	Hydrogen			Post-biogas		
	P_{max} (W•cm^{-2})	R_{ohm} (Ω•cm^2)	R_p (Ω•cm^2)	P_{max} (W•cm^{-2})	R_{ohm} (Ω•cm^2)	R_p (Ω•cm^2)
Ni1	0.847	0.069	0.210	-	-	-
Ni2	0.945	0.063	0.188	-	-	-
Sn1	0.997	0.062	0.141	0.810	0.069	0.158
Sn2	0.835	0.074	0.180	0.724	0.082	0.199
Ag1	0.965	0.064	0.126	0.159	-	-
Ag2	0.643	0.079	0.203	-	-	-
Cu1	0.819	0.083	0.173	0.681	0.092	0.198
Cu2	0.961	0.065	0.135	0.801	0.066	0.163
Fe1	0.528	0.103	0.266	0.475	0.103	0.281
Fe2	0.569	0.097	0.243	-	-	-

Appendix Table 14: Electrochemical performance of the prepared cells operated with biogas as fuel at 750 °C.

Cell ID	**Biogas 0 h**			**Biogas 120 h**		
	P_{max} (W•cm^{-2})	R_{ohm} (Ω•cm^2)	R_p (Ω•cm^2)	P_{max} (W•cm^{-2})	R_{ohm} (Ω•cm^2)	R_p (Ω•cm^2)
Ni1	0.092	0.125	-	-	-	-
Ni2	0.096	0.116	-	-	-	-
Sn1	0.963	0.071	0.154	0.786	0.076	0.190
Sn2	0.765	0.087	0.196	0.697	0.093	0.225
Ag1	0.135	0.105	-	0.016	-	-
Ag2	0.047	0.145	-	-	-	-
Cu1	0.099	0.165	-	0.082	0.190	-
Cu2	0.095	0.135	-	0.085	0.143	-
Fe1	0.107	0.133	-	0.066	0.145	-
Fe2	0.125	0.126	-	0.025	0.468	-